Magnetohydrodynamic Convective Flow Problems: Fascinating Applications of Nanofluids

Submitted to
University of Calicut
in partial fulfillment of the requirements
for the award of the Degree of

Doctor of Philosophy
in
Mathematics

By

SABU A.S.

Under the guidance of

Dr. Alphonsa Mathew

Assistant Professor



Research and Postgraduate Department of Mathematics
St. Thomas College(Autonomous)
Thrissur - 680001, Kerala
December 2022.

DECLARATION

I, **Sabu A.S**, hereby declare that the thesis entitled, **"Magnetohydrodynamic Convective Flow Problems: Fascinating Applications of Nanofluids"**, submitted to the University of Calicut in partial fulfillment of the requirements for the award of the Degree of Doctor of Philosophy in **Mathematics** is a bonafide research work done by me under the supervision and guidance of **Dr.Alphonsa Mathew**, Assistant Professor, Department of Mathematics, St. Thomas College (Autonomous), Thrissur, Kerala.

I further declare that this thesis has not previously formed the basis of any degree, diploma or any other similar title.

Thrissur **Sabu A.S.**

11 December, 2022

CERTIFICATE

This is to certify that the thesis titled **"Magnetohydrodynamic Convective Flow Problems: Fascinating Applications of Nanofluids"** submitted by **Sabu A.S.** to University of Calicut in partial fulfilment of the requirements for the award of the Degree of Doctor of Philosophy in **Mathematics** is a record of original research work carried out by him under my supervision. The content of this thesis, in full or in parts, has not been submitted by any other candidate to any other University for the award of any degree or diploma.

Thrissur
11 December, 2022

Dr. Alphonsa Mathew
Assistant Professor,
St. Thomas College(Autonomous),
Thrissur, Kerala.

CERTIFICATE

I hereby certify that, this is the revised version of the thesis entitled **"Magnetohydrodynamic Convective Flow Problems: Fascinating Applications of Nanofluids"** submitted by **Sabu A.S.**, under my guidance after incorporating the necessary corrections/suggestions made by the adjudicators. I also certify that the contents in the thesis and the soft copy are one and the same.

Thrissur
23 May, 2023

Dr. Alphonsa Mathew
Assistant Professor,
St. Thomas College(Autonomous),
Thrissur, Kerala.

ABSTRACT

Magnetohydrodynamics (MHD) is an area that discusses the coupled nature of fluid motion and magnetic field. The magnetic field induces a current on the moving conductive fluid that creates an induced magnetic field. Both the electric current and induced magnetic field generate a force namely Lorentz force on the moving fluid that can alter the velocity and magnetic effects of the fluid. Maxwell's equations for electromagnetism and Navier Stoke's equation for fluid mechanics are the basic equations that describe the governing equations of hydromagnetic fluid flows. MHD flows are widely used in metallurgy, polymer industry, plasma jet, electromagnetic pump, and aeronautics. Metal and metal oxides show higher thermal conductivity than fluids. Dispersion of these nanometer-sized (1 nm to 100 nm) particles in the conventionally used fluids like water, Ethylene glycol and oil, etc, revolutionised the area of fluid mechanics. These colloids are known as nanofluids. Hydromagnetic nanofluid flow past various geometries and its fascinating applications are discussed in this study.

CHAPTER-1: Introduction to nanofluids, classification, different types of fluid flow, and magnetohydrodynamics are addressed in this chapter. The chapter introduces various parametric effects on MHD nanofluid flow, solution methodology, and statistical tools. The chapter also examines prior studies on MHD convective flow that have been published. Further, the chapter discusses the fundamental equations and non-dimensional parameters used to describe fluid flow. Lastly the chapter elucidates the scope and objectives of the current research.

CHAPTER-2: The role of Hall current, heat source and Soret effects on MHD convective ferro-nanofluid (Fe_3O_4-water) flow through an inclined channel with porous medium has been theoretically and statistically examined. Velocity, thermal and concentration boundary layer in nanofluids are considered to be oscillatory. Heat due to radiation is induced by the huge disparity in temperature between the plates. Hall current is generated by the uniform application of a strong magnetic field perpendicular to the flow of fluid. Boundary layer equations are changed to non-dimensional type and then resolved using the perturbation approximation. The

outcomes are displayed in the form of tables and figures using MATLAB software. The outcome of pertinent parameters on concentration, temperature and velocity profiles are evaluated through graphs. Besides, wall heat, mass transfer rates and surface drag are investigated through statistical tools like regression and probable error.

CHAPTER-3: The response of MHD convective Carreau nanofluid flow over a bilateral nonlinear stretching sheet in the presence of heat source and zero mass flux condition has been analysed. The problem has been solved numerically using the MATLAB built in function bvp5c. The findings of velocity, temperature and concentration profiles based on various parameters are illustrated using graphs. Impact of various parameters on the heat transfer rate is scrutinized using statistical techniques like correlation coefficient, probable error and regression. The effect of various parameters on skin friction coefficients are studied via tables and slope of linear regression.

CHAPTER-4: The impact of multiple slip effects on the hydromagnetic Carreau nanofluid flow over an elongating cylinder considering linear heat source and exponential space based heat source has been studied. Suitable transformations are used in converting the highly nonlinear system of PDEs governing the flow into a system of ODEs and hence resolved using Runge Kutta method of order four coupled with shooting method. Parallel effect of parameters on Nusselt number is studied using surface plots and the corresponding effects are scrutinized using multiple linear regression. The consequence of different parameters on drag coefficient and mass transfer are quantified using slope of linear regression.

CHAPTER-5: The study focuses on the aggregation kinematics in the quadratic convective magneto-hydrodynamics of ethylene glycol (EG)-titania (TiO_2) nanofluid flowing through an inclined flat plate. The modified Krieger-Dougherty and Maxwell-Bruggeman models are used for the effective viscosity and thermal conductivity to account for the aggregation aspect. The effects of an exponential space-dependent heat source and thermal radiation are incorporated. The impact of pertinent parameters on the heat transfer coefficient is explored by using the Response Surface Methodology (RSM) and Sensitivity Analysis (SA). The various effects of several

parameters on the skin friction and heat transfer coefficient at the plate are displayed via surface graphs. The velocity and thermal profiles are compared for two physical scenarios: flow over a vertical plate and flow over an inclined plate. The nonlinear problem is solved using the Runge-Kutta-based shooting technique.

CHAPTER-6: Injection and suction effects play a crucial role in astronomical disciplines, fuel injection, solar collector plate, thermal protection, and aerodynamics. Therefore, the dynamics of hydromagnetic Darcy-Forchheimer hybrid nanoliquid flow over an elongated permeable sheet in the presence of hydrodynamic slip and Newtonian boundary constraints is investigated. A realistic model considering the passive control of nanoparticles and the modified Buongiorno nanoliquid model has been utilized. The modeled partial differential equations are transmuted into a system of nonlinear ordinary differential equations with the aid of apposite similarity transformations which are then resolved numerically using the finite-difference based bvp5c routine. Further, regression analysis is employed to statistically scrutinize the relationship between the pertinent parameters and the drag coefficients and a commendable agreement is noted.

CHAPTER-7: The flow of Reiner-Rivlin hydromagnetic nanoliquid passing through a rotating disk in the presence of Joule heating and a non-uniform heat source is investigated. To control the volume fraction of nanoparticles on the surface of a disk, a realistic passive control strategy is used. Nonlinear governing differential equations are solved numerically using the Bulirsch-Stoer technique and a parametric analysis is performed using graphical representations. Using the Response Surface Methodology (RSM), the interaction effects of the influential parameters on the rate of heat transfer are visualised via three-dimensional surface graphs and contours. Further, the optimum rate of the heat transfer is estimated through RSM analysis.

CHAPTER-8: The nanofluid flow considering different nanoparticle shapes (namely sphere, platelet, cylinder, and brick) and the thermo-hydrodynamic slip constraints have been modeled utilizing the modified Buongiorno model. Von Kármán's similarity transformations are exercised in the transmutation of the mathematically modeled equations into a system of first-order ODEs and treated numer-

ically using the generalized differential quadrature method. The consequence of effectual parameters on the physical quantities and the flow profiles is explained with the aid of graphs and tables.

Lastly **CHAPTER-9** presents an overall summary of the thesis followed by a few recommendations on the future scope of this work.

To My Family

ACKNOWLEDGEMENTS

First of all, I thank God Almighty for His showers of blessing throughout my research to complete the work successfully. I would also like to express my deep and sincere gratitude to my research supervisor and my mentor, Dr.Sr.Alphonsa Mathew for giving me the opportunity to do research and providing invaluable guidance throughout this research. I would always cherish this experience for the rest of my life, and it was a great privilege and honour to work and study under her guidance.

I should mention the love and great desire of two people Mr A.T Sunny and Mrs. Annamma Sunny, my parents, which made me dream about these achievements. I am very much thankful to my wife, Dr.Vidhya Thomas K, who supported me a lot to fulfil my ambition. Also, I express my thanks to my son Samuel Sabu, sister, mother in law and father in law for their cooperation.

St. Thomas College(Autonomous), Thrissur is sincerely acknowledged for providing me the resources and facelities required for the completion of my research. I express my sincere thanks to Dr. Fr Martin K.A (Principal), Dr.Joy K.L (Former Principal), Dr. Ignatius Antony (Former Principal), Dr. Jenson P.O (Former Principal) and non-teaching staffs of St. Thomas College (Autonomous), Thrissur. I am highly grateful to Dr. Saju M.I (Head of the Department), Prof Vincent Joseph Pulikkottil (Former Head of the Department) and all faculty members of the Mathematics Department. They served as a lighthouse in my journey towards the completion of this voyage.

I am forever indebted to Dr. Mahanthesh B, Associate Professor, Department of Mathematics, Christ (Deemed to be University), Bangalore for sharing his expertise and knowledge on the topic. I would like to express my sincere gratitude for the help and support rendered by my co-authors. Special thanks to Joby Mackolil and Sujesh Areekara for their constant guidance and support, which helped me greatly during the research period. I personally acknowledge the support and help rendered by my research colleagues of Mathematics and Statistics Department, St Thomas College (Autonomous), Thrissur. It was an honour to work with them.

I also recall with gratitude the support and the motivation rendered by my dear

teachers, friends and relatives. I have no valuable words to express my thanks, but my heart is still full of the favours received from every person.

Sabu A.S.

List of Symbols

r, φ, z	Cylindrical coordinates
x, y, z	Cartesian coordinates
A	Space-dependent heat source/sink parameter
a_v	Reference velocity (ms^{-1})
B	Temperature dependent heat source/sink parameter
Bi	Biot number
B_x	Strength of variable magnetic field
b_1	Velocity slip parameter
b_3	Concentration slip parameter
B_0	Strength of magnetic field
C^*	Fluid concentration in unsteady flow
C'	Dimensionless fluid concentration in unsteady flow
C_0	Nanoparticle concentration at the origin
C_∞	Ambient nanoparticle concentration
C_d	Nanoparticle concentration at the distance d
C_p	Specific heat at constant pressure
C_w	Nanoparticle concentration at the wall
D_B	Brownian diffusion coefficient (m^2s^{-1})
D_T	Thermophoretic diffusion coefficient (m^2s^{-1})
D	Fractal index
Ec	Eckert number
$f'(\zeta), g'(\zeta)$	Non-dimensional velocity components in X and Y direction (ms^{-1})
$F(\zeta), F'(\zeta)$	Axial and radial velocity components

$G(\zeta)$	Azimuthal velocity component
G_m	Modified Grashof number
G_r	Grashof number
h_f	Convective heat transfer coefficient ($WK^{-1}m^{-2}$)
H	Hall current parameter
j, o	Number of faces and factors
k^*	Rosseland mean absorption coefficient (m^{-1})
k_a	Thermal conductivity of aggregates ($Wm^{-1}\ K^{-1}$)
k_f	Thermal conductivity of fluid ($Wm^{-1}\ K^{-1}$)
K_1	Dimensionless porosity parameter
K_p	Permeability of the medium
K_r	Chemical reaction parameter
K	Reiner-Rivlin fluid parameter
κ	Curvature parameter
l	Characteristic length (m)
l'	Dimensionless velocity of unsteady flow
M	Hartmann number
m	Exponential index
Nu	Nusselt number
N_i	Slip factor ; $i = 1, 2, 3$
Nu_r	Reduced Nusselt number
Nb	Brownian motion parameter
Nt	Thermophoresis parameter
$\widetilde{n_s}$	Shape factor
n	Power law index

Pr_f	Prandtl number of the fluid
P	Pressure (Nm^{-2})
Q_1	Variable heat source parameter
Q_E	Exponential space based heat source (ESHS)
Q_T	Linear heat source (LHS)
q_R	Radiative heat flux (Wm^{-2})
$q_T, \quad q_E$	Heat source coefficients
q_w	Heat flux
Q	Volumetric rate of heat generation /absorption
R	Radiation parameter
$\mathbb{R}$	Radius of the cylinder (m)
Re	Reynolds number
Ra_x	Rayleigh number
Re_x	Local Reynolds number
$\mathcal{R}^2$	Coefficient of determination
r_a, r_p	Radii of aggregates and nanoparticles (m)
r_c	Correlation coefficient
S	Heat source/sink parameter
Sh	Sherwood number
Sc	Schmidt number
S'	Non-dimensional velocity
S_o	Soret number
T^*	Fluid temperature in unsteady flow (K)
T_0	Temperature of the fluid at the origin (K)
T_∞	Temperature of the ambient fluid (K)

T_d	Temperature of the fluid at the distance d (K)
T_w	Temperature of the fluid near the wall/disk (K)
u^*, v^*, w^*	Velocity components of unsteady flow (m/s)
$u, v, w,$	Velocity components (m/s)
U	Velocity of the palate (m/s)
U_0	Non zero constant mean velocity
We	Local Weissenberg number
w_0	Injection/suction velocity
	Greek symbols
$(\rho C_p)_f$	Fluid heat capacity $(Jm^{-3}K^{-1})$
$(\rho C_p)_p$	Nanoparticle effective heat capacity $(Jm^{-3}K^{-1})$
ϕ	Volume fraction of nanoparticles
ν	Kinematic viscosity (m^2s^{-1})
μ	Dynamic viscosity $(kgm^{-1}s^{-1})$
ζ	Similarity variable
σ	Electrical conductivity
$\theta(\zeta)$	Dimensionless temperature
θ'	Dimensionless temperature in unsteady flow
α_f	Thermal diffusivity (m^2s^{-1})
α_P	Absorption coefficient
Γ	Time material constant (s)
ρ	Density (kgm^{-3})
λ	Injection/suction parameter
β_T	Coefficient of volume expansion
β_C	Volumetric coefficient of expansion with concentration

ϕ_a	Volume fraction of nanoparticle aggregates
ϕ_m	Maximum volume fraction of nanoparticles
α	Angle of inclination
δ	Stretching ratio parameter
γ	Thermal slip parameter
τ	Effective heat capacity ratio
β^*	Viscosity ratio parameter
τ_w	Wall shear stress
μ_c	Cross-viscosity coefficient
α_1	Quadratic thermal convection parameter
β_0, β_1	First and second-order thermal expansion coefficients (K^{-1}, K^{-2})
σ^*	Stefan-Boltzmann constant $(Wm^{-2}\ K^{-4})$
ψ	Stream function
χ	Sphericity
$[\eta]$	Einstein coefficient
τ_{ij}	Stress tensors
τ_r, τ_φ	Radial and azimuthal wall stress
Ω	Angular velocity (s^{-1})
Ω^*	Rotation parameter
ω	Frequency parameter
δ_{ij}	Kronecker delta
	Subscripts
nf	Nanofluid
f	Base fluid
s	Nanoparticle

w	Quantities at wall

Abbreviations

MHD	Magnetohydrodynamic
FPSC	Flat plate solar collector
EG	Ethylene glycol
RSM	Response surface methodology
DQM	Differential quadrature method
PE	Probable Error

Contents

Declaration i
Certificate iii
Certificate v
Abstract vii
Acknowledgements xiii
List of Symbols and Abbreviations xv
List of Figures xxv
List of Tables xxx

1 **Introduction** 1
1.1 Fluid 1
1.2 Types of fluid flow 1
1.3 Viscosity 3
1.4 Newtonian fluids 4
1.5 Non-Newtonian fluids 4
1.6 Carreau fluid model 5
1.7 Reiner Rivlin fluid 5
1.8 Heat transfer 5
1.9 Mass transfer 7
1.10 Chemical reaction 7
1.11 Magnetohydrodynamics (MHD) 7
1.12 Hall current 9
1.13 Soret effect (Thermophoresis) 9
1.14 Joule heating effect 9

1.15 Porous media 10
1.16 Boussinesq approximation 11
1.17 Basic equations describing the fluid flow 12
1.18 Dimensional analysis & Non dimensional parameters 13
1.19 Nanofluid 17
1.20 Solution methodology 20
1.21 Statistical analysis 22
1.22 Response surface methodology (RSM) 23
1.23 Sensitivity analysis 23
1.24 Literature review 23
1.25 Objectives 39

2 **Statistical analysis of MHD convective ferro-nanofluid flow through an inclined channel with Hall current** 41
2.1 Introduction 41
2.2 Mathematical formulation 41
2.3 Numerical solution 45
2.4 Results and discussion 47
2.5 Conclusions 65
2.6 Appendix 66

3 **Statistical analysis on MHD convective Carreau nanofluid flow due to bilateral non linear stretching sheet with zero mass flux condition** 71
3.1 Introduction 71
3.2 Mathematical formulation 71
3.3 Numerical solution 74
3.4 Result and discussion 74
3.5 Statistical Analysis 83
3.6 Conclusions 88

4 **Effects of multi-slip and distinct heat source on MHD Carreau nanofluid flow past an elongating cylinder using statistical method** 89
4.1 Introduction 89
4.2 Mathematical formulation 90

4.3 Numerical solution 92
4.4 Result and discussion 93
4.5 Statistical Analysis 106
4.6 Conclusions 109

5 **Nanoparticle aggregation kinematics on the quadratic convective MHD flow of nanomaterial past an inclined flat plate with sensitivity analysis** 111
5.1 Introduction 111
5.2 Mathematical Formulation 112
5.3 Numerical solution 116
5.4 Results and discussion 118
5.5 Response Surface Methodology (RSM) 123
5.6 Sensitivity analysis 128
5.7 Conclusions 131

6 **MHD Darcy-Forchheimer hybrid nanoliquid flow over an elongated permeable sheet in a porous medium with hydrodynamic slip constraint** 133
6.1 Introduction 133
6.2 Mathematical formulation 134
6.3 Numerical solution 138
6.4 Results and discussion 139
6.5 Special Cases 148
6.6 Regression Analysis 152
6.7 Conclusions 156

7 **Reiner-Rivlin nanoliquid flow past a spinning disk with Joule heating and non-uniform heat source using Bulirsch-Stoer algorithm** 159
7.1 Introduction 159
7.2 Mathematical formulation 160
7.3 Numerical solution 164
7.4 Results and Discussion 165
7.5 Response Surface Methodology (RSM) 174

7.6 Conclusions 183

8 **Significance of nanoparticle shape effect on MHD convective alumina-water nanofluid flow over a rotating rigid disk** 185

8.1 Introduction 185

8.2 Mathematical formulation 185

8.3 Numerical solution 189

8.4 Results and Discussion 194

8.5 Conclusions 207

9 **Conclusive remarks and future scope** 209

Publications in journals and presentations 215

Bibliography 217

References 217

List of Figures

1.1 Laminar and turbulent flows 2
1.2 Flow chart depicting bvp5c routine 21

2.1 Physical configuration of the problem 43
2.2 Variations in Velocity $l'$with ϕ 53
2.3 Variations in temperature θ' with ϕ 54
2.4 Variations in concentration C' with ϕ 54
2.5 Variations in velocity l' with H 55
2.6 Variations in velocity l' with M 55
2.7 Variations in concentration C' with $K_r > 0$ 56
2.8 Variations in concentration C' with $(K_r < 0)$ 56
2.9 Variations in velocity l' with S 57
2.10 Variations in temperature$\theta'$with S 57
2.11 Variations in concentration C' with S 58
2.12 Variations in velocity l' with λ 58
2.13 Variations in temperature θ' with λ 59
2.14 Variations in concentration C' with S_0 59
2.15 Variations in velocity l' with α 60
2.16 Variations in velocity l' with K_1 60
2.17 Actual and estimated values of Cf 64
2.18 Actual and estimated values of Nu 64
2.19 Actual and estimated values of Sh 65

3.1 Geometry of the problem 72

3.2 Variation of $f'(\zeta)$ for various values of β^* 77
3.3 Variation of $g'(\zeta)$ for various values of β^* 77
3.4 Variation of $f'(\zeta)$ for various values of We 78
3.5 Variation of $g'(\zeta)$ for various values of We 78
3.6 Variation of $f'(\zeta)$ for various values of M 79
3.7 Variation of $g'(\zeta)$ for various values of M 79
3.8 Variation of $g'(\zeta)$ for various values of δ 80
3.9 Variation of $\theta(\zeta)$ for various values of Bi 80
3.10 Variation of $\theta(\zeta)$ for various values of S 81
3.11 Variation of $\theta(\zeta)$ for various values of Nt 81
3.12 Variation of $\phi(\zeta)$ for various values of Nb 82
3.13 Variation of $\phi(\zeta)$ for various values of Nt 82
3.14 Actual and estimated values $Re_x^{-\frac{1}{2}} Nu$ of when $n = 0.7$ 87
3.15 Actual and estimated values $Re_x^{-\frac{1}{2}} Nu$ of when $n = 1.7$ 88

4.1 Figurative representation 90
4.2 $f'(\zeta)$ for differing b_1 values 95
4.3 $\theta(\zeta)$ for differing γ values 96
4.4 $f'(\zeta)$ for differing M values 96
4.5 $f'(\zeta)$ for differing We values 97
4.6 $\theta(\zeta)$ for differing We values 97
4.7 $\theta(\zeta)$ for differing κ values 98
4.8 $\theta(\zeta)$ for differing Nb values 98
4.9 $\theta(\zeta)$ for differing Nt values 99
4.10 $\phi(\zeta)$ for differing Nb values 99
4.11 $\phi(\zeta)$ for differing Nt values 100
4.12 $\theta(\zeta)$ for differing Q_T values 100
4.13 $\theta(\zeta)$ for differing Q_E values 101
4.14 Parallel effect of Nb and Nt on $Nu(Re_x)^{\frac{-1}{2}}$ when $n = 0.5$ 102
4.15 Parallel effect of Nb and Nt on $Nu(Re_x)^{\frac{-1}{2}}$ when $n = 1.5$ 102
4.16 Parallel effect of Q_T and Q_E on $Nu(Re_x)^{\frac{-1}{2}}$ when $n = 0.5$ 103
4.17 Parallel effect of Q_T and Q_E on $Nu(Re_x)^{\frac{-1}{2}}$ when $n = 1.5$ 103
4.18 Parallel effect of γ and κ on $Nu(Re_x)^{\frac{-1}{2}}$ when $n = 0.5$ 104
4.19 Parallel effect of γ and κ on $Nu(Re_x)^{\frac{-1}{2}}$ when $n = 1.5$ 104

4.20 Estimated versus actual $Nu(Re_x)^{\frac{-1}{2}}$ when $n = 0.5$ 108
4.21 Estimated versus actual $Nu(Re_x)^{\frac{-1}{2}}$ when $n = 1.5$ 108

5.1 Physical configuration. 112
5.2 Variation of $S'(\zeta)$ for distinct values of ϕ. 119
5.3 Variation of $\theta(\zeta)$ for distinct values of ϕ. 120
5.4 Variation of $S'(\zeta)$ for distinct values of M. 120
5.5 Variation of $\theta(\zeta)$ for distinct values of M. 121
5.6 Variation of $S'(\zeta)$ for distinct values of α_1. 121
5.7 Variation of $\theta(\zeta)$ for distinct values of α_1. 122
5.8 Variation of $\theta(\zeta)$ for distinct values of Q_E. 122
5.9 Variation of $\theta(\zeta)$ for distinct values of R. 123
5.10 Surface plot of Cf_X for variation of α_1 and ϕ 124
5.11 Surface plot of Cf_X for variation of α and M 124
5.12 Surface plot of Nu_X for variation of α and M 125
5.13 Surface plot of Nu_X for variation of α_1 and ϕ 125
5.14 Residual plots for Nu_X. 127
5.15 Contour plots and Response surface plots of Nu_X for all combinations of α, Q_E and R. 129
5.15 Contour plots and Response surface plots of Nu_X for all combinations of α, Q_E and R. 130
5.16 Bar charts depicting the sensitivity of Nu_X with $X_2 = -1$,$X_2 = 0$,and $X_2 = 1$ 131

6.1 Physical configuration. 135
6.2 Change in $f'(\zeta)$ for differing ϕ_{Cu} values. 141
6.3 Change in $f'(\zeta)$ for differing M values. 142
6.4 Change in $f'(\zeta)$ for differing Fr values. 142
6.5 Change in $f'(\zeta)$ for differing K_1 values. 143
6.6 Change in $f'(\zeta)$ for differing b_1 values. 143
6.7 Change in $g'(\zeta)$ for differing M values. 144
6.8 Change in $g'(\zeta)$ for differing K_1 values. 144
6.9 Change in $g'(\zeta)$ for differing δ values. 145
6.10 Change in $\theta(\zeta)$ for differing ϕ_{Cu} values. 145

6.11 Change in $\theta(\zeta)$ for differing M values. 146
6.12 Change in $\theta(\zeta)$ for differing Bi values. 146
6.13 Change in $\phi(\zeta)$ for differing M values. 147
6.14 Change in $\phi(\zeta)$ for differing K_1 values. 147
6.15 Change in $Nu_x(Re_x)^{-\frac{1}{2}}$ for differing Nt and Bi with $\lambda = -0.1$ . . 150
6.16 Change in $Nu_x(Re_x)^{-\frac{1}{2}}$ for differing Nt and Bi with $\lambda = 0.1$. . . 150
6.17 Change in $Nu_x(Re_x)^{-\frac{1}{2}}$ for differing ϕ_{Cu} and M with $\lambda = -0.1$. . 151
6.18 Change in $Nu_x(Re_x)^{-\frac{1}{2}}$ for differing ϕ_{Cu} and M with $\lambda = 0.1$. . . 151
6.19 Change in $f'(\zeta)$ of the two-dimensional flow for differing b_1 values. 152
6.20 Change in $f'(\zeta)$ of the axisymmetric flow for differing b_1 values. . . 153
6.21 Actual $Re_x^{\frac{1}{2}}Cf_x$ versus Estimated $Re_x^{\frac{1}{2}}Cf_x$ with $\lambda = -0.1$. 154
6.22 Actual $Re_x^{\frac{1}{2}}Cf_x$ versus Estimated $Re_x^{\frac{1}{2}}Cf_x$ with $\lambda = 0.1$. 155
6.23 Actual $Re_y^{\frac{1}{2}}Cf_y$ versus Estimated $Re_y^{\frac{1}{2}}Cf_y$ with $\lambda = -0.1$. 155
6.24 Actual $Re_y^{\frac{1}{2}}Cf_y$ versus Estimated $Re_y^{\frac{1}{2}}Cf_y$ with $\lambda = 0.1$. 156

7.1 Physical configuration 160
7.2 Response in $F'(\zeta)$ for distinct M. 166
7.3 Response in $G(\zeta)$ for distinct M. 167
7.4 Response in $\theta(\zeta)$ for distinct M. 167
7.5 Response in $\phi(\zeta)$ for distinct M. 168
7.6 Response in $F'(\zeta)$ for distinct K. 168
7.7 Response in $G(\zeta)$ for distinct K. 169
7.8 Response in $\theta(\zeta)$ for distinct K. 169
7.9 Response in $\phi(\zeta)$ for distinct K. 170
7.10 Response in $\theta(\zeta)$ for distinct Ec. 171
7.11 Response in $\phi(\zeta)$ for distinct Sc. 171
7.12 Response in $\theta(\zeta)$ for distinct A & B. 172
7.13 Response in $\theta(\zeta)$ for distinct Nt. 172
7.14 Response in $\phi(\zeta)$ for distinct Nt. 173
7.15 Response in $\theta(\zeta)$ for distinct γ. 173
7.16 Surface plot of $C_f Re^{\frac{1}{2}}$ for variation of K and M. 174
7.17 Surface plot of $NuRe^{-\frac{1}{2}}$ for variation of A and B. 175
7.18 Surface plot of $NuRe^{-\frac{1}{2}}$ for variation of Sc and Ec. 175
7.19 Surface plot of $NuRe^{-\frac{1}{2}}$ for variation of Nb and Nt. 176

7.20 Residual plots for Nu_r. 179
7.21 Contour and response surface plot of Nu_r for combinations of γ, K . 180
7.22 Contour and response surface plot of Nu_r for combinations of γ, M . 180
7.23 Contour and response surface plot of Nu_r for combinations of M, K . 181
7.24 Bar charts depicting the sensitivity of Nu_r 182

8.1 Physical configuration 186
8.2 Flowchart depicting the numerical scheme. 191
8.3 Impact of $\phi_{Al_2O_3}$ on $F(\zeta)$. 195
8.4 Impact of $\phi_{Al_2O_3}$ on $G(\zeta)$. 196
8.5 Impact of $\phi_{Al_2O_3}$ on $\theta(\zeta)$. 196
8.6 Impact of M on $F(\zeta)$. 197
8.7 Impact of M on $G(\zeta)$. 197
8.8 Impact of M on $\theta(\zeta)$. 198
8.9 Impact of M on $\phi(\zeta)$. 198
8.10 Impact of b_1 on $F(\zeta)$. 199
8.11 Impact of b_1 on $G(\zeta)$. 199
8.12 Impact of b_1 on $\theta(\zeta)$. 200
8.13 Impact of b_1 on $\phi(\zeta)$. 200
8.14 Impact of γ on $\theta(\zeta)$. 201
8.15 Impact of γ on $\phi(\zeta)$. 202
8.16 Impact of Nt on $\theta(\zeta)$. 202
8.17 Impact of Nt on $\phi(\zeta)$. 203
8.18 Impact of Nb on $\phi(\zeta)$. 203
8.19 Impact of Sc on $\phi(\zeta)$. 204
8.20 Impact of $\widetilde{n_s}$ on $F(\zeta)$. 205
8.21 Impact of $\widetilde{n_s}$ on $G(\zeta)$. 205
8.22 Impact of $\widetilde{n_s}$ on $\theta(\zeta)$. 206
8.23 Impact of $\widetilde{n_s}$ on $\phi(\zeta)$. 206

List of Tables

1.1 Porosity and permeability of some common materials Based on data by (Bejan & Lage, 1991) and (Nield, Bejan, et al., 2006) 10

2.1 Thermo physical properties of base fluid and nanoparticles at 25^0 . 44

2.2 Amplitude value of the coefficient, $\frac{\varepsilon}{2}e^{it}$, in the expansion of $\left(\frac{\partial\theta'}{\partial z}\right)_{z=0}$ with $\lambda = 0, R = 0, S = 0, \phi = 0$. 48

2.3 Comparison of (τ_{0r}) and (β_0) of the steady flow in the absence of Ω^*, with $G_m = 0, R = 0, K_r = 0, K_1 \to \infty, S_0 = 0, S = 0, \phi = 0, \alpha = \pi/2$. 48

2.4 The Skin friction of Fe_3O_4-water nanofluid when $t = \frac{\pi}{4}, Pr = 6.07, K_r = 1.5,\ K_1 = 0.7,\ \ M = 3.5, S_0 = 0.5, \omega = 20, Sc = 0.22, \alpha = \frac{\pi}{4}, Re = 10.$ 50

2.5 The Nusselt number of Fe_3O_4-water nanofluid when $t = \frac{\pi}{4}, Pr = 6.07,\ G_r = 5,\ \ G_m = 5,\ \ K_r = 1.5,\ \ K_1 = 0.7,\ M = 3.5, H = 1.5,\ S_0 = 0.5,\ \omega = 20,\ \ Sc = 0.22, \alpha = \frac{\pi}{4},\ Re = 10.$ 51

2.6 The Sherwood number of Fe_3O_4-water nanofluid when $Pr = 6.07, G_r = 5,\ G_m = 5,\ K_1 = 0.7,\ M = 3.5,\ H = 1.5,\ S = 2, Sc = 0.22,\ \alpha = \frac{\pi}{4}.$ 52

2.7 Correlation coefficient (r_c), Probable error (PE) and $|\frac{r_c}{PE}|$ values of Cf with respect to the parameters $\phi, H, G_m\ , S, R, G_r$ and λ 53

2.8 Correlation coefficient (r_c), Probable error (PE) and $|\frac{r_c}{PE}|$ values of Nu with respect to the parameters ϕ, S, R and λ 61

2.9 Correlation coefficient (r_c), Probable error (PE) and $|\frac{r_c}{PE}|$ values of Sh with respect to the parameters $\phi, R, S_0, \lambda, \omega, t$ and K_r 61

2.10 Linear regression model for Cf, with Number of observations :35, Error degrees of freedom:27, Root mean square error :0.00461, $\mathcal{R}$-squared:0.989, Adjusted $\mathcal{R}$-Squared 0.986, F-statistic vs. constant model:332, p-value =1.7e-24 62

2.11 Linear regression model for Nu with number of observations :20, Error degrees of freedom:15, mean square error :0.0713, $\mathcal{R}$-squared: 0.995, Adjusted $\mathcal{R}$- Squared 0.994, F-statistic vs. constant model:773, p-value =3.59e-17 62

2.12 Linear regression model for Sh, Number of observations :35, Error degrees of freedom:27, Root mean square error :0.00753, $\mathcal{R}$-squared:0.998, Adjusted $\mathcal{R}$-Squared 0.998, F-statistic vs. constant model:2.31e+03, p-value =8.37e-36 63

3.1 Skin friction coefficients, local Nusselt number and local Sherwood number are defined as given below: 75

3.2 Comparison of $f''(0)$ and $g''(0)$ when $\beta^* = 1$ and $M = 0$ 76

3.3 Variation in local Nusselt number at $\zeta = 0$ when $m = 1$, $Nt = 1$, $S = 0.2$, $M = 0.5$, $We = 3$, $\delta = 0.8$, $\beta^* = 0.1$, $Nb = 0.5$ *and* $Bi = 0.4$ 84

3.4 Variation in Skin Friction Coefficients at $\zeta = 0$ when $m = 1$, $Nt = 1$, $S = 0.2$, $M = 0.5$, $We = 3$, $\delta = 0.8$, $\beta^* = 0.1$, $Nb = 0.5$ *and* $Bi = 0.4$ 85

3.5 Variation in Skin Friction Coefficients at $\zeta = 0$ when $m = 3$, $Nt = 1$, $S = 0.2$, $M = 0.5$, $We = 3$, $\delta = 0.8$, $\beta^* = 0.1$, $Nb = 0.5$ *and* $Bi = 0.4$ 86

3.6 Correlation Coefficient (r_c), Probable Error (PE) and $\left|\frac{r_c}{PE}\right|$ of reduced Nusselt number at $\zeta = 0$ when $Bi = 0.4$ and $Nb = 0.5$ 86

4.1 Comparison of $Nu(Re_x)^{\frac{-1}{2}}$ with $We = \kappa = M = Q_T = Q_E = Nt = b_1 = \gamma = b_3 = 0$ *and* $Nb \to 0$ 92

4.2 Comparison of $-\frac{1}{2}Cf(Re_x)^{\frac{1}{2}}$ with $M = Q_T = Q_E = Nt = b_1 = \gamma = b_3 = 0$ *and* $Nb \to 0$ 94

4.3 Variation in $-\frac{1}{2}Cf(Re_x)^{\frac{1}{2}}$ $\{at\ \zeta = 0\}$ when $\kappa = 0.2$, $We = 2$, $M = 1$, $m = 0.5$, $Q_T = 0.02$, $Q_E = 0.04$, $Nt = 0.1$, $Nb = 0.4$, $b_1 = 0.2$, $\gamma = 0.2$ and $b_3 = 0.2$ 105

4.4 Variation in $Sh(Re_x)^{-\frac{1}{2}}$ $\{at\ \zeta = 0\}$ when $\kappa = 0.2$, $We = 2$, $M = 1$, $m = 0.5$, $Q_T = 0.02$, $Nt = 0.1$ $Q_E = 0.04$, $Nb = 0.4$, $b_i = 0.2$, $\gamma = 0.2$ and $b_3 = 0.2$ 106

4.5 Probable error (PE) and correlation coefficient (r_c) of $Nu(Re_x)^{\frac{-1}{2}}$ 107

5.1 Thermophysical properties of the nanofluid with aggregation (Mackolil & Mahanthesh, 2021b) 114

5.2 Thermo physical properties of base fluid and nanoparticles at $300K$ (Mackolil & Mahanthesh, 2021b) 115

5.3 Comparison of $-\theta^{'}(0)$ values and when $\alpha_1 = \alpha = M = Q_E = R = 0$ and $\phi = 0$ with the results of (Kuznetsov & Nield, 2010) and (Mahanthesh & Mackolil, 2021) 117

5.4 Comparison of $S''(0)$ when $\alpha_1 = 0.1, m = 0.5, M = 0.1$, $Q_E = 0.2, R = 1$ and $\phi = 1\%$ 117

5.5 The effective levels of parameters 126

5.6 ANOVA table 126

5.7 The sensitivity values of the response Nu_X when $X_1 = 0$ 130

6.1 The effective thermophysical properties of the hybrid nanoliquid (with alumina as nanoparticle 1 and copper as nanoparticle 2) 137

6.2 Thermophysical properties of water, alumina, and copper (Aziz, Jamshed, Aziz, Bahaidarah, & Ur Rehman, 2021), (Aaiza, Khan, & Shafie, 2015), (Hussanan, Salleh, Khan, & Shafie, 2017) 138

6.3 Resemblance of $-Re_x^{\frac{1}{2}}\ Cf_x$ and $-Re_y^{\frac{1}{2}}\ Cf_y$ for differing values of K_1 , Fr , and δ when $M = Nt = \lambda = \phi_{Al_2O_3} = \phi_{Cu} = b_1 = Bi = 0$, $Pr = Sc = 1$, and $Nb \to 0$. 139

6.4 Resemblance of $Re_x^{-\frac{1}{2}}\ Nu_x$ for differing values of K_1 , Fr , and δ when $M = \lambda = \phi_{Al_2O_3} = \phi_{Cu} = b_1 = 0$, $Pr = Sc = 1$, $Bi = 0.3$, $Nt = 0.2$, and $Nb = 0.5$. 139

6.5 Comparison on $Re_x^{\frac{1}{2}}\ Cf_x$ for differing values of Fr, M, K_1, ϕ_{Cu}, and b_1 when $Nt = 0.5$, $Nb = 0.5, \delta = 0.1, Bi = 0.5, \phi_{Al_2O_3} = 0.02$. 148

6.6 Comparison on $Re_y^{\frac{1}{2}}\ Cf_y$ for differing values of $M,\ K_1,\ \phi_{Cu},\ b_1$ and δ when $Nt = 0.5,\ Nb = 0.5, Fr = 0.5, Bi = 0.5, \phi_{Al_2O_3} = 0.02$ . . . 149

7.1 Comparison of $F''(0), G'(0), F(\infty)$, and$-\theta'(0)$ with $K = 0,\ M = 0,\ Ec = 0,\ A = 0,\ B = 0,\ Nt = 0, Sc = 0, Nb \to 0\ , Pr_f = 0.72^a$, and $Pr_f = 6^b$. 165

7.2 The effectual levels of parameters. 177

7.3 Experimental (numerical) design. 177

7.4 ANOVA table 178

7.5 The sensitivity values of the response Nu_r when $X_1 = 0$ 183

8.1 Effective nanofluid constants see (Timofeeva, Routbort, & Singh, 2009),(Mustafa, Khan, Hayat, & Alsaedi, 2018),(Brinkman, 1952). . 188

8.2 Thermophysical Properties of water and Al_2O_3 (see (Wakif & Sehaqui, 2022)). 189

8.3 Nanoparticle shape properties of Al_2O_3 (see (Timofeeva et al., 2009)). 190

8.4 Validation for regular fluids ($Pr = 6.2,\ \phi_{Al_2O_3} = 0,\ M = 0,\ b_1 = 0,\ \gamma = 0,\ \zeta_\infty = 30,\ \tilde{N} = 100$) 193

8.5 Validation for nanofluids ($Pr = 7,\ A_1 = A_2 = A_3 = A_4 = A_5 = 1,\ Sc = 5,\ Nb = 0.5,\ Nt = 0.5,\ b_1 = 0,\ \gamma = 0,\ \zeta_\infty = 15,\ \tilde{N} = 100$) . . 193

8.6 Numerical estimation of C_{fr} for various shapes of nanoparticles ($M = 0.2,\ Sc = 5,\ Nb = 0.2,\ Nt = 0.1,\ b_1 = 0.25,\ \gamma = 0.25,\ \zeta_\infty = 30,\ \tilde{N} = 100$) 194

8.7 Numerical estimation of Nu_r for various shapes of nanoparticles ($M = 0.2,\ Sc = 5,\ Nb = 0.2,\ Nt = 0.1,\ b_1 = 0.25,\ \gamma = 0.25,\ \zeta_\infty = 30,\ \tilde{N} = 100$. 195

Chapter 1

Introduction

1.1 Fluid

Fluids are substances that are capable of flowing. Fluids can easily change their shape by rearranging their molecular structure. The main states of fluid that play a pioneering role in the earth and universe are liquid and gaseous. Moving and stationary fluids are required by nature. The movement of water in seas and rivers and the movement of air in the atmosphere are required for the existence of life in nature. Stationary fluids are also significant in our daily lives. The study of fluid's behaviour at rest (termed fluid statics) and in motion (termed fluid dynamics) is known as fluid mechanics. The major applications of fluid mechanics cover meteorology, transportation, food production, power generation, heat exchangers, nuclear reactors, biomedical equipment, air conditioning, aerospace, oil production, and hydraulics design. The important fluid flow characteristics are described as follows:

1.2 Types of fluid flow

- Steady and unsteady flows
- Laminar and turbulent flows
- Rotational and irrotational flows
- Compressible and incompressible flows
- One,two and three-dimensional flows

1.2.1 Steady and unsteady flows

Fluid properties such as pressure, velocity, and density remain constant in the steady case at any point in time. The situation can be mathematically expressed as follows:

$$\frac{dv}{dt} = 0, \ \frac{dp}{dt} = 0 \ , \ \frac{d\rho}{dt} = 0. \tag{1.2.1}$$

Where v is the velocity, p is the pressure, ρ is the density and t is the time.

1.2.2 Laminar and turbulent flows

Laminar flow refers to the parallel and regular movement of fluid layers sliding one over the other. Consider the motion of oil/water in a circular pipe that is slanted with an angle of inclination with the horizontal line. Laminar flow is observed in this case with fluid layers in the shape of concentric circular cylinders that move parallel to each other. Mixing of fluid layers or irregular fluid paths are not observed in this case. Further, fluid flow is stationary near the wall's surface and gradually increases near the pipe's center. In turbulent flow, irregular fluid paths and the mixing of fluid layers have occurred. Smoke movement near the cigarette is an example of laminar flow and the smoke movement becomes turbulent after a certain distance from the cigarette.

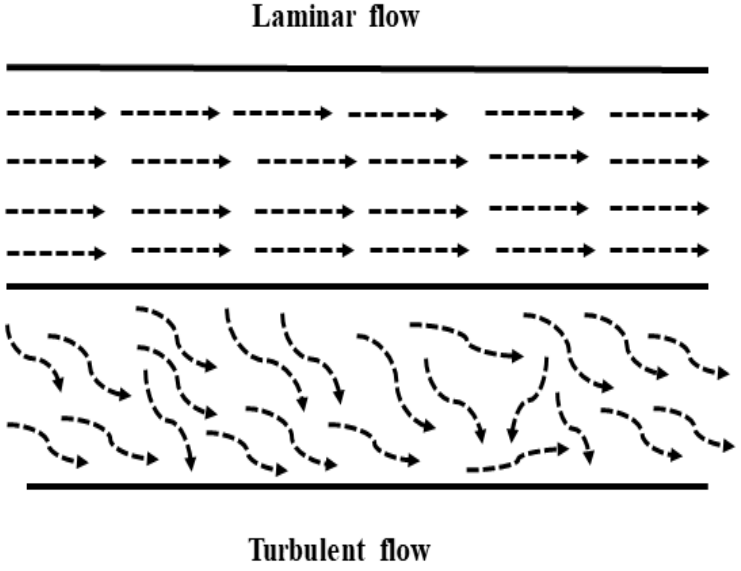

Figure 1.1: *Laminar and turbulent flows*

1.2.3 Rotational and irrotational flow

The movement of fluid particles about an axis is called rotational flow or swirling flow. $\Omega = \nabla \times V$ describes vorticity at any point of the fluid flow. Fluid particles in the flow field are rotating when $\Omega \neq 0$. Irrotational flow occurs when $\Omega = 0$.

1.2.4 Compressible and incompressible flows

Compressible fluids have a density that varies with pressure, whereas incompressible fluids have a constant density. Gases are more compressible than liquids. It is due to the larger space between gaseous molecules in the volume occupied by gases than liquids.

1.2.5 One, two and three-dimensional flows

Fluid flow can be classified as one, two, or three-dimensional depending on the number of space coordinates. The velocity, temperature, and concentration of the flow profiles in the one-dimensional form are explained with space and time coordinates whereas two-dimensional and three-dimensional flows are described with more than one space coordinate. Fluid flow past a stretching sheet with velocity varies in the x-direction forming a one-dimensional flow. In a two-dimensional flow, the velocity varies in both the x and y directions. If the velocity is a function of three space coordinates, say x, y, and z then a three-dimensional flow occurs.

1.3 Viscosity

Viscosity is an internal resistance (stress) in the movement of fluid particles. The fluid flow is degraded by viscosity. Oil, honey, and syrup have a high viscosity, whereas water, alcohol, and kerosene have a low viscosity. Viscous fluids exhibit tangential and normal stress with two contacting layers in motion. The reciprocal of viscosity is fluidity. Viscosity can be classified as follows:

- Dynamic viscosity
- Kinematic viscosity

Dynamic viscosity is the ratio of shear stress to shear rate that measures internal resistance to flow. Kinematic viscosity is defined as the ratio of dynamic viscosity to density.

1.4 Newtonian fluids

Newtonian fluids are fluids that exhibit unique viscosity with shear stress. Shear stress is a tangential force parallel to the cross-sectional area of a material. Alcohol, gasoline, and water are Newtonian fluids. These fluids obey Newton's law of viscosity and show a linear relationship between shear stress and shear rate. In other words shear stress formed by an external force is equal to the product of shear rate and fluid viscosity.

$$\tau_{yx} = \mu\dot{\gamma}_{yx} \tag{1.4.1}$$

In the relation, τ_{yx} is the shear stress due to a force on the cross-sectional area, $\dot{\gamma}_{yx}$ is the shear rate, and μ is the dynamic viscosity.

1.5 Non-Newtonian fluids

The fluid that doesn't follow Newton's law of viscosity is known as non-Newtonian fluid. Viscosity may increase or decrease depending on the shear rate and the type of fluid. Four types of non-Newtonian behavior are generally observed they are pseudoplastic, dilatant, thixotropic, and rheopectic respectively. They are further divided into time-dependent and time-independent fluids.

1.5.1 Pseudoplastic fluids

Pseudoplastic fluids show an inverse functional relationship between shear stress and viscosity. Pseudoplastic fluids are time-independent. Blood and ketchup are examples of pseudoplastic fluid. These fluids are also known as shear-thinning fluids.

1.5.2 Dilatant fluids

Dilatant fluids show high viscosity with shear stress. They are also known as shear thickening fluids. dilatant fluids are time-independent. Oobleck and quicksand are examples of dilatant fluids.

1.5.3 Thixotropic fluids

Thixotropic fluids show a negative response between shear stress and viscosity. Thixotropic fluids are time-dependent when compared with pseudoplastic fluids. The viscosity of a thixotropic fluid decreases with time at a constant shear rate. Cosmetics paint and glue are thixotropic fluids.

1.5.4 Rheopectic fluids

Rheopectic fluids show a positive response between shear stress and viscosity. Rheopectic fluids are time-dependent when compared with dilatant fluids. The Viscosity of rheopectic fluids increases with time at a constant shear rate. Cream and gypsum paste are rheopectic fluids.

1.6 Carreau fluid model

In 1972, (Carreau, 1972) introduced the following viscosity model.

$$\frac{\mu - \mu_\infty}{\mu_0 - \mu_\infty} = \left\{1 + (\Gamma\dot{\gamma}_{yx}\ )^2\ \right\}^{\frac{n-1}{2}} \tag{1.6.1}$$

where Γ is the relaxation time, $\dot{\gamma}_{yx}$ is the shear rate, n is the power law index, μ_0 and μ_∞ represent the viscosities at low and high shear rates, respectively. Shear thinning and thickening behaviour depends on n. The viscosity model with $n > 1$ show a shear thickening nature and $n < 1$ exhibits a shear thinning nature.

1.7 Reiner Rivlin fluid

Reiner and Rivlin proposed a relationship for an isotropic fluid between the stress tensor τ_{ij} and the rate of strain tensor e_{ij}. The following constitutive relation is used to model the rheological properties of the Reiner-Rivlin nanoliquid (see (Tabassum & Mustafa, 2018)).

$$\tau_{ij} = -p\delta_{ij} + \mu_f e_{ij} + \mu_c e_{ik} e_{kj}, (e_{jj} = 0). \tag{1.7.1}$$

Here, the rate of strain (deformation) tensor is denoted by $\mathrm{e_{ij}} = \frac{\partial u_i}{\partial x_j} + \frac{\partial u_j}{\partial x_i}$, Kronecker delta symbol is denoted by δ_{ij}, coefficient of viscosity is denoted by μ_f, cross-viscosity coefficient is denoted by μ_c and pressure is denoted by p. The influence of stress across velocity gradients leads to cross-viscosity, a property of the Reiner-Rivlin nanofluid considered in the study.

1.8 Heat transfer

Heat transfer occurs due to temperature differences between two regions. The transmission of heat energy from one place to another is known as heat transfer. The heat transfer mechanism improves the finishing quality of many industrial

products while reducing the risk of electronic equipment damage due to overheating. Conduction, convection, and radiation are the main modes of heat transfer.

1.8.1 Conduction

Conduction is the process of heat transfer from a hot body to a colder one that occurs through direct contact. This mode of heat transfer is usually observed in solids and liquids. The molecules in direct contact with hotter ones start vibrating and transfer the energy to nearby molecules. The molecular movement is not observed in the case while free electrons transmit energy so vacuum space does not promote conduction. Metals are good conductors than others. According to Fourier's law, the heat transfer equation is mathematically described as follows:

$$q = -k\frac{dT}{dx} \tag{1.8.1}$$

where k is the coefficient of thermal conductivity, q is the quantity of heat and $\frac{dT}{dx}$ is the temperature gradient. Here the negative sign indicates the direction of heat from higher to lower temperature.

1.8.2 Convection

The process of replacement of hotter fluid particles with the colder ones is known as convection. This process of heat transfer usually occurs in gasses and liquids by the bulk/random movement of molecules. Mainly it happens due to temperature gradient and the contact of adjacent fluid layers with a hot solid boundary. The convection phenomenon can be further classified according to the nature of the flow as free convection and forced convection. Free convection is due to buoyancy force by the density variation while forced convection is due to an external force. A fan, pump and suction devices are required for a forced convection. According to Newton's law, the heat transfer equation is mathematically described as follows:

$$q = hA\left(T_w - T_\infty\right). \tag{1.8.2}$$

where A, h, T_w and T_∞ are the heat transfer area, convection heat transfer coefficient, temperature of the surface, and reference temperature respectively.

1.8.3 Radiation

The process of heat transfer from a region to another region in the form of electromagnetic waves is known as radiation. This mode of heat transfer doesn't require any medium. Solar energy from the sun and heat energy released from the filament of a bulb are examples of radiation. The sun's energy reaches the earth without heating the space between them and a similar phenomenon is observed in the case of heat produced from the filament of a bulb.

1.9 Mass transfer

Mass transfer is the movement of mass from a higher concentration zone to a lower region. A difference in species concentration of two or more component mixtures initiates the mass transfer phenomenon. The mass transfer exists in the process of drying, adsorption, distillation, evaporation, absorption, etc. Mass transfer can be due to mass diffusion or convective mass transfer. Mass diffusion occurs due to concentration differences in adjacent fluid layers whereas a moving fluid between a boundary surface leads to convective mass transfer.

1.10 Chemical reaction

The process in which one or more reactants are converted into new products that reaction is known as a chemical reaction. It may be homogeneous or heterogeneous. if the reactants and products are in the same phase then the chemical reaction is homogeneous otherwise it is heterogeneous. In a chemical reaction either heat is absorbed or generated. Exothermic reactions evolve heat energy whereas endothermic reactions absorb heat energy. If the reaction rate is directly proportional to concentration then it is a first-order chemical reaction. Chemical reaction has an important role in the heat and mass transfer processes. Fluid flow with chemical reaction has applications in polymer production, food processing, manufacturing of ceramics, etc.

1.11 Magnetohydrodynamics (MHD)

Magnetohydrodynamics is an area that discusses the coupled nature of fluid motion and magnetic field. The magnetic field generates a current in a moving conductive fluid that creates an induced magnetic field. Both the electric current and induced

magnetic field produce a force namely Lorentz force on the moving fluid that can alter the velocity and magnetic effects of the fluid. MHD flows can be found in nature. The magnetic field is generated due to the motion of the inner liquid metal core of the earth is a shield that protects the earth from harmful radiation. Sunspots and solar flares are real-life examples of MHD flow. Fluid flows in the industrial process are greatly influenced by a magnetic field. Heated liquid metals are Stirred, pumped, and levitated by utilizing a magnetic field.

The concept of MHD flows originated from the pioneering work of Swedish Physicist Alfven (Alfvén, 1942). He was honored with the Nobel prize in physics in the year 1970. Maxwell's equations for electromagnetism and Navier Stoke's equation for fluid mechanics are the basic equations that describe the governing equations of hydromagnetic fluid flows. The Solar wind, mercury, plasmas, seawater, salt water, and electrolytes are some examples of hydromagnetic fluids. MHD flows are widely used in metallurgy, polymer industry, plasma jet, electromagnetic pump, and aeronautics. Maxwell equations are defined as follows

Gauss's law

$$\vec{\nabla}.\vec{E} = \frac{\rho_e}{\epsilon_0}. \tag{1.11.1}$$

Faraday's law of induction

$$\vec{\nabla} \times \vec{E} = -\frac{\partial \vec{B}}{\partial t}. \tag{1.11.2}$$

Ampere's law

$$\nabla \times \vec{B} = \mu_0 \vec{J} + \mu_0 \ \epsilon_0 \frac{\partial \vec{E}}{\partial t} \tag{1.11.3}$$

Lorentz force

Moving fluid particles with velocity $\vec{v}$ and charge q in the presence of an external magnetic field experiences a force known as Lorentz force.

$$\vec{F} = q \ \left(\vec{E} + \vec{v} \times \vec{B}\right). \tag{1.11.4}$$

Gauss's law for magnetism

$$\nabla.\vec{B} = 0, \vec{B} = \mu_0 \ \vec{H}. \tag{1.11.5}$$

where E is electric field intensity, ρ_e is electric charge density, ϵ_0 is the permittivity of free space, μ_0 is the permeability of free space, H is the magnetic field intensity, B is the magnetic flux density, σ is the electric conductivity and J is the electric current density.

1.12 Hall current

Electrically conducting fluid in the presence of a strong magnetic field induces a current known as Hall current which is normal to both electric and magnetic fields. It was observed by Edwin Herbert Hall in 1879 (Hall et al., 1879). Hall effect causes a drift in the movement of charged particles due to gyration. Fluid flow with hall current has a significant role in micromixing of physiological samples, Nuclear reactor cooling, meteorological studies, MHD power generators, etc.
Ohm's law with Hall current can be described as follows

$$J + \frac{\omega_e \tau_e}{B_0} \ (J \times B) = \sigma \ \left(\vec{E} + \mu_e \overrightarrow{v} \times \vec{B}\right). \tag{1.12.1}$$

where v is the velocity vector, B is the magnetic field, B_0 is the strength of the magnetic field, J is the electric current density, μ_e is the magnetic permeability, ω_e is the cyclotron frequency and τ_e is the electron collision time. $\omega_e \tau_e$ is the Hall parameter.

1.13 Soret effect (Thermophoresis)

Hot or high-energy level fluid particles migrate towards the cold/low energy level region. Physically this is due to the temperature gradient. This force is known as thermophoresis force which accelerates the heat transfer process. This phenomenon is observed in a suspended mixture of fluid particles.

1.14 Joule heating effect

The physical effect of a current passing through an electrical conductor producing thermal energy is known as Joule heating. This thermal energy is then manifested as an increase in the temperature of the conductor material. The process of Joule

heating effect can be seen in electric oven, electric kettle and room heaters etc.

1.15 Porous media

A porous medium is a solid matrix with enough open space or voids which enable the movement of fluid particles. Rock, soil, sand, biological tissues, and sponge are some examples of porous media. A porous media is usually characterized by its porosity and permeability. Porosity is the ratio of the volume of open space to the volume of the solid matrix including open space. The value usually lies between 0 and 1. Permeability depends on the geometry or structure of the medium. Fuel cells, petroleum engineering, filtration, and soil mechanics utilize the concept of porous media.

1.15.1 Darcy's Law

Fluid filtration through a porous medium can be mathematically expressed by the Darcy law. Oil, gas, and water flow through petroleum reservoirs are described with the help of the Darcy law. It is valid for laminar and low viscous cases. Darcy's law (1856) found a proportionality between the applied pressure and flow rate. In the case of the isotopic medium, Darcy's law is mathematically expressed as $\nabla P = -\frac{\mu}{K_p}\, v$, (see (Nield et al., 2006)) where μ is the dynamic viscosity of fluid, K_p (a scaler in isotropic medium) is the permeability of the medium, v is the velocity and P is the pressure.

Table 1.1: *Porosity and permeability of some common materials Based on data by (Bejan & Lage, 1991) and (Nield et al., 2006)*

Material	**Porosity**	**Permeability,**$K_p(cm^2)$
Brick	0.12 -0.34	$4.8 \times 10^{-11} - 2.2 \times 10^{-9}$
Soil	0.43-0.54	$2.9 \times 10^{-9} - 1.4 \times 10^{-7}$
Sand	0.37-0.50	$2 \times 10^{-7} - 1.8 \times 10^{-6}$
Leather	0.56-0.59	$9.5 \times 10^{-10} - 1.2 \times 10^{-9}$

1.15.2 Brinkman's equation

Brinkman (Brinkman, 1949) modified Darcy's law in 1949 using a Laplace term which is significant for the flow around a particle submerged in a porous medium with the no-slip condition. It is suitable for a high porous medium (porosity $>$ 0.6) with negligible convective inertia. Porosity is normally less than 0.6 in a naturally occurring porous medium. Brinkman's equation is mathematically expressed as

$$\nabla P = -\frac{\mu}{K_p} v + \mu \nabla^2 v \tag{1.15.1}$$

where μ is the effective viscosity.

1.15.3 Darcy Forchheimer flow

Darcy-Forchheimer flow is a fluid flow through a porous medium satisfying the Darcy-Forchheimer relation that subsumes inertial properties and boundary characteristics. A Laminar flow observed in the low fluid velocity through porous medium with Reynolds number is less than or equal to 1. A sudden transition of laminar to turbulent flow does not happen when the Reynolds number is augmented between 1 to 10. In such a case surface drag due to solid obstacles is comparable with surface drag due to friction (see (Nield et al., 2006)). Darcy Forchheimer equation is mathematically expressed as (see (Joseph, Nield, & Papanicolaou, 1982))

$$\nabla P = -\frac{\mu}{K_p} v - \frac{C_f}{\sqrt{K_p}} \rho_f \ |v| \, v \tag{1.15.2}$$

where C_f is drag constant and ρ_f is density. The last term in the expression is called the Forchheimer term.

1.16 Boussinesq approximation

The Boussinesq approximation is a significant method utilized in nonisothermal problems and natural convection processes. The approximation is more accurate in low-density variations. It accounts for the importance of density variation in the buoyancy term (ρg). If ρ_0 is the reference density then

$$(\rho - \rho_0) \, g = -\rho_0 \ \beta_T \, (T - T_0) \, g. \tag{1.16.1}$$

Where T is the temperature, T_0 is the reference temperature and β_T is the coefficient of thermal expansion. When heat and mass transfer effects co-exists in a system then the Boussinesq approximation is

$$(\rho - \rho_0)\, g = -\rho_0\ \beta_T\ \ (T - T_0)\, g - \rho_0\ \beta_C\, (C - C_0)\, g \tag{1.16.2}$$

Where β_C is the coefficient of species expansion and C_0 is the reference Concentration.

1.17 Basic equations describing the fluid flow

1.17.1 Equation of continuity (Conservation of mass)

Equation of continuity is based on the principle of law of conservation of mass which is defined as the rate of generation of mass within a given volume is equal to the difference between the rate of mass entering into a volume and the rate of mass out of the volume. Continuity equation can be mathematically expressed as

$$\frac{\partial \rho}{\partial t} + div\,(\rho V) = 0. \tag{1.17.1}$$

where $V = (u, v, w)$ are the components of velocity in x, y, and z directions. $div\,(\rho V) = 0$, if the fluid is steady and compressible. $div\,(V) = 0$, if the fluid is steady and incompressible.

1.17.2 Navier -Stoke's equations (Conservation of momentum)

Navier -Stoke's equation is based on Newtons' second law of motion which states that the total force is equal to the rate of change of linear momentum.

$$\rho \frac{DV}{Dt} = \rho\ F + \mu\ \nabla^2 V - \nabla P. \tag{1.17.2}$$

$\frac{D}{Dt} \cong \frac{\partial}{\partial t} + (V.\nabla)$ is know as the material derivative.

1.17.3 Conservation of energy

The equation of energy is based on the law of conservation of energy which states that the total energy in an isolated system is constant. Rate of increase of energy in a volume is equal to the difference of rate at which heat is produced by the work (due to surface stress & external agencies) and rate of energy loss (due to conduction & convection).

$$\rho C_p \frac{DT}{Dt} = \frac{\partial Q}{\partial t} + k \frac{\partial}{\partial x_i} \left(\frac{\partial T}{\partial x_i} \right) + \varphi_v. \tag{1.17.3}$$

where $\varphi_v = \mu \left(\frac{\partial v_i}{\partial x_j} + \frac{\partial v_j}{\partial x_i} \right) \frac{\partial v_i}{\partial x_j}$ is the dissipation function, a heat generation function due to frictional forces.

1.18 Dimensional analysis & Non dimensional parameters

Dimensional analysis is a mathematical tool for obtaining the qualitative behaviour of a physical problem. In dimensional analysis, basic equations are converted into dimensionless forms involving non-dimensional parameters. The ratio of one force to the other force yields a dimensionless number known as the non dimensional parameter. The dimensionless parameter (non dimensional parameters) aids us in comprehending the physical significance of a specific phenomenon associated with the problem. Major non dimensional parameters in the thesis are

1.18.1 Magnetic parameter or Hartmann number

Hartmann number is a dimensionless number that is defined as the ratio of an electromagnetic force to viscous force. Lorentz force generates due to an increase in Hartmann number that influences the flow profiles of an electrically conducting fluid passing through a magnetic field. Mathematically it can be denoted as.

$$M = B_0 l \sqrt{\frac{\sigma}{\mu}} \tag{1.18.1}$$

where B_0 is magnetic field intensity, l is the characteristic length scale, σ is the electrical conductivity and μ is dynamic viscosity.

1.18.2 Schmidt number

Schmidt number is a dimensionless number that is defined as the ratio of momentum diffusivity to mass diffusivity. It is used to characterize fluid flows that have both momentum and mass diffusion convection processes going on at the same time. Mathematically it can be represented as.

$$Sc = \frac{\nu}{D} \tag{1.18.2}$$

where ν is the kinematic viscosity and D is the mass diffusivity.

1.18.3 Reynolds number

Reynolds number is a dimensionless number that is defined as the ratio of inertial force to viscous force. Reynolds number determines the flow pattern. A high Reynolds number enhances the inertial force and produces a turbulent flow pattern. Laminar flow takes place at a low Reynolds number. Viscous forces dominate in the case of small Reynolds numbers. Mathematically, it can be expressed as

$$Re = \frac{ul}{\nu} \tag{1.18.3}$$

where u is the flow speed, l is the characteristic length scale and ν is the kinematic viscosity

1.18.4 Eckert number

Eckert number is a dimensionless number that is defined as the ratio of advective mass transfer to the heat dissipation potential. It characterizes the Self- heating of a fluid due to viscous dissipation. Mathematically, it can be represented as

$$Ec = \frac{U_W^2}{C_p\left(T_w - T_\infty\right)} \tag{1.18.4}$$

where U_W is the velocity at the wall, C_p is the specific heat at constant pressure, (T_w, T_∞) denotes temperatures at the wall and away from the wall, respectively.

1.18.5 Prandtl number

Prandtl number is a dimensionless number that is defined as the ratio of momentum diffusivity to thermal diffusivity. Pr is connected with the heat convection process. For example, $Pr = 0.015$ is for liquid mercury and Pr varies between 100 & 40000 for Engine oil. Liquid mercury show more thermal diffusivity than engine oil. In addition, heat convection is more effective in engine oil than liquid mercury. Mathematically, it can be expressed as

$$\mathrm{Pr} = \frac{\mu C_p}{k} \tag{1.18.5}$$

where μ is the dynamic viscosity, C_p is the specific heat at constant pressure and k is the thermal conductivity.

1.18.6 Grashof number

Grashof number is a dimensionless number that is defined as the ratio of the buoyancy to viscous force. The number occurs in the natural convection process. In the presence of buoyancy force, thermal and solutal Grashof numbers are significant. As the temperature increases, the density decreases and the fluid rises. The motion is caused by the buoyancy force. Thermal and solutal Grashof numbers emerge due to temperature and concentration gradient, respectively. Mathematically, thermal and solutal Grashof numbers are described as follows

$$G_r = \frac{\nu g \beta \left(T_0 - T_d\right)}{U_0 {w_0}^2}. \tag{1.18.6}$$

$$G_m = \frac{\nu g \beta \left(C_0 - C_d\right)}{U_0 {w_0}^2}, \tag{1.18.7}$$

where β is the volume expansion coefficient, g is the acceleration due to gravity, ν is the kinematic viscosity, (T_0, T_d) is the temperature of the fluid near the origin and at d respectively. (C_0, C_d) is the concentration of the fluid near the origin and at d respectively.

1.18.7 Biot number

Biot number is a dimensionless number that is defined as the ratio of thermal resistance inside a body and at the surface of the body. The number describes the temperature variations inside a body during the heating and cooling process over the surface. Mathematically it can be expressed as

$$Bi = \frac{h}{k}\, l \tag{1.18.8}$$

where h is convective heat transfer coefficient, k is the thermal conductivity, and l is the characteristic length scale.

1.18.8 Soret number

Soret number is a dimensionless number that is defined as the ratio of thermal diffusion coefficient and the normal diffusion coefficient. It measures the degree of separation of the species. Mathematically, it can be expressed as

$$S_0 = \frac{D_m K_T \left(T_W - T_\infty\right)}{T_m \nu_f \left(C_W - C_\infty\right)} \tag{1.18.9}$$

where $D_m, K_T, T_W, T_\infty,\ C_\infty$ and ν_f are mass diffusivity, thermal diffusion ratio, temperature near the solid boundary, temperature far away the solid boundary, free stream concentration and kinematic viscosity, respectively.

1.18.9 Weissenberg number

Weissenberg number is a dimensionless number that is defined as the ratio of the elastic force to the viscous force. Elastic effects dominate the viscous force if the time scale of flow is less than the relaxation time and vice versa. So, the Weissenberg number has a significant role in the study of viscoelastic flows. Mathematically, it can be described as

$$We = \frac{\tau_{xx} - \tau_{yy}}{\tau_{xy}} \tag{1.18.10}$$

1.18.10 Nusselt number

The conductive and convective heat transfer phenomenon occurs through a fluid layer of thickness l. According to Newton's law, the mathematical notation of heat flux (in the case of convection) is

$$q_{conv} = h\delta T. \tag{1.18.11}$$

where h is the convective heat transfer coefficient and δT is the temperature difference of the fluid layer.

According to Fourier's law, the mathematical expression of heat flux (in the case of conduction) is

$$q_{cond} = \frac{k\delta T}{l} \tag{1.18.12}$$

where k is thermal conductivity.

A Nusselt number is a dimensionless number that is defined as the ratio of convective to conductive heat transfer. The Nusselt number can be used to estimate the effectiveness of heat convection at the surface. Mathematically, it can be expressed as

$$Nu = \frac{hl}{k} \tag{1.18.13}$$

where h is convective heat transfer coefficient, l is the characteristic length and k is thermal conductivity.

1.18.11 Sherwood number

Sherwood number is a dimensionless number that is defined as the ratio of convective mass transfer to diffusive mass transfer rate. The Sherwood number can be used to estimate the effectiveness of mass convection at the surface. Mathematically, it can be represented as

$$Sh = \frac{k_m l}{D_m}, \tag{1.18.14}$$

where k_m is the convective mass transfer coefficient, l is the characteristic length scale and D_m is the mass diffusivity.
Solution diffuses from a higher concentration to a lower concentration region and the diffusion flux is proportional to the concentration gradient. According to Fick's law, diffusion flux is given by

$$J = -D\frac{dC}{dx} \tag{1.18.15}$$

where D is the diffusion coefficient, C is the concentration and x is the position.

1.18.12 Skin friction coefficient

The fluid velocity at the touching surface is zero whereas it is maximum in the main stream of the flow. The boundary layer of the flow is the region where the fluid velocity starts from zero to maximum. A skin friction coefficient is a non-dimensional number that estimates the tangential shear force of a moving fluid against the surface. Tangential shear force is due to no-slip conditions caused by viscosity, geometry, and the type of fluid flow. Mathematically, it can be expressed as

$$c_f = \frac{\tau_w}{\rho U_\infty^2} \tag{1.18.16}$$

where τ_w is the local shear wall stress, U_∞ is the free stream velocity.

1.19 Nanofluid

The performance of a fluid in the heat transfer phenomenon significantly depends on the thermophysical properties of the fluid. Metal and metal oxides show higher thermal conductivity than fluids. Dispersion of these nanometer-sized (1 nm to 100 nm) particles in the conventionally used fluids like water, Ethylene glycol and

oil, etc, revolutionised the area of fluid mechanics. These colloids are known as nanofluids. Nanoparticles can be metal-based (Cu, Ag, Au, Zn), metal oxide-based (Fe_3O_4, Al_2O_3, TiO, ZnO, CUO), carbide based (Calcium carbide, Silicon carbide) Nitride based (Aluminium nitride, Silicon nitride), Sulfide based (Zinc sulfide, Silver sulfide), carbon-based (Graphene, Carbon nanotubes), or polymer-based (Polystyrene). Nanofluid is prepared by dispersing a small quantity of nanoparticles in base fluid which can significantly alter the properties of the base fluid. Water-based, Glycol-based, oil-based (vegetable oil, gasoline, kerosene, and lubricating oil) or Refrigerant-based (R134a , R600a, R141b) base fluids are commonly used in Engineering and industrial applications. Further, the performance of a nanofluid is influenced by the volume fraction of nanoparticles, particle shape, particle size and temperature.

1.19.1 Volume fraction of nanoparticles

The nanoparticle volume fraction is the ratio between the volume of nanoparticles and the volume of all constituents of the mixture. Mathematically, nanoparticle volume fraction is expressed as $\phi = \frac{V_{np}}{V_{nf}} = \frac{V_{np}}{V_{np}+V_{bf}}$ where V_{np}, V_{nf}, and V_{bf} represent the volume of nanoparticle, nanofluid, and base fluid respectively (see (A. R. I. Ali & Salam, 2020)). Metals and metal oxides show larger thermal conductivity in comparison with fluids. Nanofluid was first discovered by Choi (Choi & Eastman, 1995) for its exceptional cooling performance and heat transfer ability. Base fluid and nanoparticles in nanofluid exhibit unique chemical and physical properties.
Major applications of nanofluids are

- Magnetic liquid rotatory seal utilizes the properties of magnetic nanoliquids and operates with low maintenance in the industry.
- The efficiency of solar thermal collectors enhances with the use of nanofluid as the absorption media.
- Nanofluids can reduce friction and grinding force with the help of a dense slurry layer in the grinding process of cast iron.
- Non-toxic nanoparticles(like gold nanoparticles) can work as a drug delivery agent.

- Nanoparticles can cross the cell membrane of the bacteria and work as an antibacterial agent.
- Nanofluids can reduce the size of submarines, fighter jets, etc. by contributing towards smaller and efficient cooling system.
- Apart from these nanofluids are used in vehicle brake fluids, heat exchangers, nuclear reactors, transformer oil, refrigeration and electronics equipment.

1.19.2 Thermophysical properties of nanofluid

Density of nanofluid

The ratio of mass to volume is the density. According to classical mixture law, the density of nanofluid is

$$\rho_{nf} = \rho_s \phi + (1 - \phi)\, \rho_f. \tag{1.19.1}$$

Specific heat of nanofluid

Specific heat of a substance is the quantity of heat required to change the temperature by one degree. Specific heat of nanofluid is (see (Xuan & Roetzel, 2000))

$$(\rho C_p)_{nf} = (\rho C_p)_s \phi + (1 - \phi)\, (\rho C_p)_f. \tag{1.19.2}$$

Thermal conductivity of nanofluid

The Maxwell model for spherical shape nanoparticles and the Hamilton-Crosser model for non-spherical shape nanoparticles are the two most commonly used models for thermal conductivity in the literature.
The Maxwell model predicts that the thermal conductivity of nanofluid is

$$\frac{k_{nf}}{k_f} = \frac{k_s + 2k_f + 2\phi\,(k_s - k_f)}{k_s + 2k_f - \phi\,(k_s - k_f)} \tag{1.19.3}$$

The Hamilton-Crosser model (Hamilton & Crosser, 1962) for thermal conductivity of nanofluids is

$$\frac{k_{nf}}{k_f} = \frac{k_s + (\mathcal{H} - 1)\, k_f - (\mathcal{H} - 1)\, \phi\, (k_f - k_s)}{k_s + (\mathcal{H} - 1)\, k_f + \phi\, (k_f - k_s)} \tag{1.19.4}$$

. where $\mathcal{H} = \frac{3}{\psi}$ where ψ is the sphericity and $\mathcal{H}$ is the empirical shape factor.

Dynamic viscosity of nanofluid

Two of the most commonly used effective dynamic viscosity models are the Brinkman and Einstein models. The Brinkman model (Brinkman, 1952) is $\frac{\mu_{nf}}{\mu_f} = \frac{1}{(1-\phi)^{2.5}}$ and the Einstein model is $\frac{\mu_{nf}}{\mu_f} = 1 + 2.5\ \phi$ (see (Drew & Passman, 2006)).

1.19.3 Shape and size of nanoparticles

Effective dynamic viscosity and thermal conductivity of nanofluid depend on the shape and size of nanoparticles. The shape of nanoparticles may be spherical, cylindrical, brick, platelet, or blade. (Timofeeva et al., 2009) studied particle shape effect on the rheological properties of Al_2O_3/EG-water. In a similar way size of nanoparticles influenced the thermal conductivity and viscosity of nanofluids. (Teng, Hung, Teng, Mo, & Hsu, 2010) found an enhanced thermal conductivity of Al_2O_3/water nanofluid with a decrease in particle size of nanoparticles.

1.20 Solution methodology

In the research, the following tools have been opted for the numerical computation

1.20.1 Perturbation technique

Perturbation technique is an analytical method for finding approximate solution of nonlinear differential equations. They are more suitable for recurring solutions of vibrating systems involving nonlinear effects and complex boundary conditions. In the perturbation technique a small parameter $\epsilon < 1$ is added to the mathematical description of the solvable problem. Analytical solution can be expressed as $u(x,t) = u_0(x) + \sum_{i=1}^{\infty} \epsilon^i u_i(x,t)$. The higher order terms are known as perturbation terms. The series is a convergent series that converges to a limit as ϵ tends to zero (see (Singh & Kumar, 2009)).

1.20.2 Finite difference method based bvp5c Routine

The bvp5c solver integrates simultaneous differential equations of the form $y' = f(x,y)$ with initial/boundary conditions. It starts with an initial guess and works with an algorithm based on the four-stage finite difference code Lobatto IIIa formula (see (Kierzenka & Shampine, 2008)). The flowchart of the numerical simulation is given in the Figure 1.2.

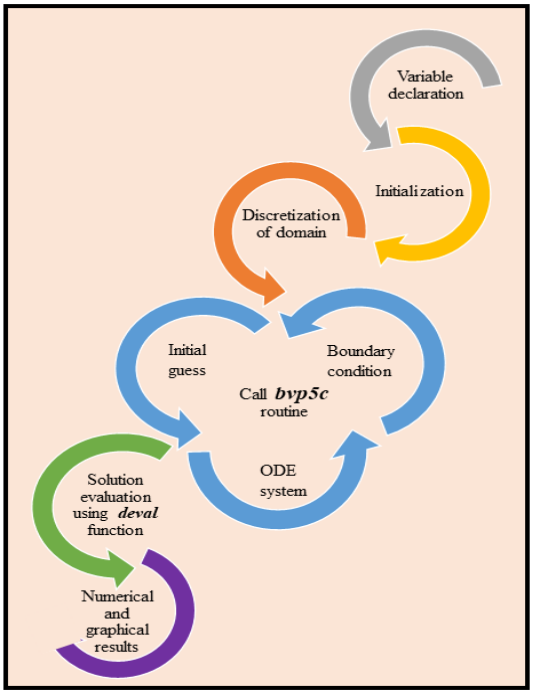

Figure 1.2: *Flow chart depicting bvp5c routine*

1.20.3 Runge–Kutta method

The fourth order Runge–Kutta method is used to find an approximated value of y at x. Nonlinear ordinary differential equations are converted to a system of first order ODEs for the solution procedure. The Runge–Kutta algorithm is described as follows:- $x_i = x_{i-1} + h$.

$y_{i+1} = y_i + \frac{1}{6}(K_1 + 2K_2 + 2K_3 + K_4)$.

$K_1 = h\ f(x_i, y_i)$.

$K_2 = hf\left(x_i + \frac{h}{2}, y_i + \frac{K_1}{2}\right)$.

$K_3 = hf\left(x_i + \frac{h}{2}, y_i + \frac{K_2}{2}\right)$.

$K_4 = hf(x_i + h\ , y_i + K_3)$.

1.20.4 Shooting method

The shooting method is a numerical technique that solves a boundary value problem (BVP) by reducing it into an initial value problem (IVP). For this, an initial guess value is assumed for the unknown initial conditions. The newly derived IVP is solved and checked for accuracy by comparing the solution with the existing boundary conditions. If the accuracy of the solution is less than the desired accuracy level, the process is repeated by choosing a new guess value. For this, methods like the

midpoint rule, Newton-Raphson method, etc. are utilized.

1.20.5 Bulirsch-Stoer method

The Bulirsch-Stoer algorithm is a numerical procedure based on the Richardson extrapolation and the midpoint method (See (Kiusalaas, 2005) and (Bulirsch, Stoer, & Stoer, 2002)). The midpoint formula $y(x+h) = y(x-h) + 2hf[x, y(x)]$ of the numerical integration of $y' = f(x, y)$ is the basis of the Bulirsch-Stoer method. The midpoint method is initially applied in two steps. With each successive integration, the number of steps is increased by two, and each integration is followed by Richardson extrapolation. When two successive solutions differ by less than a prescribed tolerance, the procedure is terminated. For improved efficiency, the automated step size modification has been removed from the classical Bulirsch and Stoer technique algorithm. The Bulirsch-Stoer method is advantageous in computations that require high accuracy solutions for smooth functions. The high accuracy, simplistic approach, easy execution, and improved efficiency provide an upper hand for the Bulirsch-Stoer method over the existing numerical techniques.

1.21 Statistical analysis

1.21.1 Correlation with probable error and regression analysis

Correlation is a statistical technique that quantifies the nature of the association of two variables. The relation between two variables is a positive or a negative correlation depending on their sign. A positive correlation means that an increment in one variable leads to an increase in the other. The magnitude of r_c indicates the intensity of this relationship. Correlation is said to be significant if $\left|\frac{r_c}{PE}\right| > 6$; where $PE = 0.6745\ \left(\frac{1-{r_c}^2}{\sqrt{\tilde{n}}}\right)$ and $\tilde{n}$ is the total observation number (see (Fisher et al., 1921)). PE is known as probable error. It establishes the reliability of the correlation coefficient. The probable error gives an idea of how to generalise the correlation coefficient calculated from the sample to the population.

Regression analysis is a statistical modelling technique used to establish a relationship between a dependent and one or more independent variables. The following elements are included in a multilinear regression model: independent variables, dependent variables, unknown parameters and error terms. Mathematically, it can be expressed as: $Y = r_i X_i + e\ ,\ i = 1\ to\ n$ where Y is dependent variable, X_i are independent

variables and e is the error term.

1.22 Response surface methodology (RSM)

RSM is an experimental design-based statistical technique that illustrates the impact of influential parameters (independent variables) and their interactive effects on the physical quantity of choice (dependent or response variable). Experimental trials are time-consuming and costly whereas RSM reduces the number of trials and optimizes the response variable. RSM using the Central Composite Design (CCD) is a suitable sequential experimentation method which is incorporated in the present study with 20 ($2^j + 2j + o,\ j\ = 3, o = 6$) runs, here o denotes the number of faces and j denotes the number of factors. The relation involves 2^3 factorial 6 center and 6 axial points (see (Mahanthesh, Mackolil, & Mallikarjunaiah, 2021)). A full quadratic 3 level factorial design is adopted in the study as follows

$$\begin{aligned} \textit{Response}\ (Y) = \ & L_1X_1 + L_2X_2 + L_3X_3 + L_4X_1X_2 + L_5X_2X_3 + L_6X_1X_3 \\ & + L_7X_1^2 + L_8X_2^2 + L_9X_3^2 + L_{10}. \end{aligned} \tag{1.22.1}$$

where, L_i ($i = 1,\ 2,\ \ldots,\ 10$) denote the regression coefficients. The RSM technique becomes advantageous in finding the levels of the parameters that optimize the response. ANOVA table as described evaluates the quality of the fitted quadratic model reliably. The significance of linear, quadratic, and interactive regression terms are computed statistically using F and p values. All the regression terms with a high F and p-value < 0.05 in the fitted model are significant.

1.23 Sensitivity analysis

Sensitivity is a measurement that interprets the level of change in response variables with variation in independent variables. The positive or negative sign in the sensitivity function indicates the nature of the sensitivity and its magnitude delineates the intensity of the relationship (see (Mackolil & Mahanthesh, 2021a)).

1.24 Literature review

1.24.1 Magnetohydrodynamics

The concept of magnetohydrodynamics (MHD) was introduced by Hannes Alfven in 1942. Naturally convected magnetohydrodynamic flow has been studied by

many researchers theoretically and experimentally having applications in scientific, engineering, industrial and medical fields. It plays a pivotal role in the field of microelectronics, solar technology, glass fibers, hot rolling, paper production, and plasma studies (see (Vinita & Poply, 2020), (Rabbi et al., 2020) and (Alsagri, Hassanpour, & Alrobaian, 2019)). (Naga Santoshi, Venkata Ramana Reddy, & Padma, 2019) studied Magneto Carreau nanofluid numerically under slip and obtained suppressed velocity profiles through augmented values of Hartmann number. (Abbas, Rehman, Shah, Idrees, & Qayyum, 2020) analysed magneto hydrodynamic flow on a stretching sheet using Carreau fluid. They deployed a Runge-Kutta 4th order method for solving the problem numerically. (Gholinia, Armin, Ranjbar, & Ganji, 2019) studied the influence of magnetic field over an expanding cylinder utilizing CNT nanofluids. With increasing magnetic field parameter a decrease in the surface drag was observed. (Bilal, Sagheer, & Hussain, 2018) numerically examined the MHD flow over a lengthening cylinder on Williamson fluid and noticed a decline in velocity profile due to an augmentation in magnetic field parameter. (Sohail & Naz, 2020) incorporated a revised mass and heat transmission model in MHD flow over a stretched cylinder and attained the numerical solutions using OHAM method. Further, Magnetohydrodynamics (MHD), has relevance in drug targeting, metallurgy, polymer industry, plasma jet, electromagnetic pump, aeronautics, fusion reactors, crystal growth, and MHD flow meters. (Hayat, Riaz, Aziz, & Alsaedi, 2020) scrutinized the hydromagnetic nanoliquid flow past a lengthening surface. They noticed an elevation in the thermal profile and a decline in the velocity profile with augmented values of Hartmann number. The consequence of uniform magnetic force and ellipse-shaped obstacle on the nanoparticle migration within a porous cubic cavity was elucidated by (Sheikholeslami, Shah, Shafee, Khan, & Tlili, 2019). (Shehzad, Sheikholeslami, et al., 2020) illustrated that mounting values of the Hartmann number declined the heat transfer characteristics by 11.97 %. Magnetic nanoparticles have applications in cancer therapy, drug delivery, magnetic cell separation, and magnetic resonance imaging (see (P. S. A. Reddy & Chamkha, 2018) and (Salehi, Nori, Hosseinzadeh, & Ganji, 2020)). (O. D. Makinde et al., 2018) analyzed the significance of radiation and heat sources on the MHD flow over a rotating disk involving aluminium and titanium alloy nanoparticles. (Ouyang et al., 2020) remarked an enhancement in the drag coefficient with increasing magnetic

field parameter. (Salahuddin, Sakinder, Alharbi, & Abdelmalek, 2021) deliberated a hydromagnetic nanofluid flow towards a heated sphere and observed a decline in the nanofluid velocity with augmenting values of magnetic field parameter.

1.24.2 Nanofluid

In the 19th century, there was a high demand for innovative methodologies in finding an efficient thermal conducting fluid due to its various industrial applications. Low thermal conductivity of conventional fluids like water, ethylene-glycol, biological fluids, glycol, and oil limited their functionality. Metals and metal oxides show larger thermal conductivity in comparison with fluids. Nanofluid was first discovered by (Choi & Eastman, 1995) for its exceptional cooling performance and heat transfer ability in 1995. The researchers investigated a new class of fluids by suspending nanometer-sized (1 nm to 100 nm) copper metallic particles in water. Later, researchers investigated different nanofluids by suspending various nanoparticles (metalic or non metalic) in conventional fluids. Base fluid and nanoparticles in nanofluid exhibit unique chemical and physical properties (see (Chamkha, Jena, & Mahapatra, 2015)). Concerning the heat transfer property of nanofluid, (Eastman, Choi, Li, Thompson, & Lee, 1996) observed that when 5% of Copper Oxide nanoparticles was used in water, the heat transfer property increased by 60 %. Nanofluids are used in solar thermal collectors, heat pipes, automotive radiators and tube heat exchangers (see (Leong et al., 2018)). Further, nanofluids exhibited a higher thermal conductivity when compared with the traditional fluids. Nanofluids play a crucial role in cooling systems, hydraulic systems, biomedical equipment, and nuclear reactors (see (Ho, Cheng, Yang, Rashidi, & Yan, 2021), (Sheriff, Mir, Ahmad, & Rafiq, 2021), (Deymi-Dashtebayaz et al., 2021), (Abdo & Saidani-Scott, 2021) and (Erkan, Tüccar, Tosun, & Özgür, 2021)).

1.24.3 Hybrid nanofluid

Hybrid nanofluid is a colloidal suspension of base fluid with more than one distinct nanoparticle. Hybrid nanoliquids due to their superior heat transfer capabilities have applications in solar collectors, heat exchangers, nanomedicines, and electronic cooling devices. (Tahat & Benim, 2017) experimentally analyzed the thermal conductivity and viscosity of Al_2O_3-CuO/ethylene glycol hybrid nanoliquid and observed a significant increase in these parameters with respect to volume fraction of

nanoparticles. (Shahul Hameed, Suresh, & Singh, 2019) reported that a 0.3% volume fraction of Al_2O_3-Cu/water nanofluid enhanced the heat transfer coefficient by 20.48 % when compared with water. Further, a thermal enhancement of 6-11% for CuO-Al_2O_3/water nanofluid in comparison with alumina nanoliquid was experimentally derived by (Plant, Hodgson, Impellizzeri, & Saghir, 2020). More studies concerning hybrid nanoliquid flow can be seen in (Khashi'ie, Arifin, Merkin, Yahaya, & Pop, 2021), (Gangadhar, Bhargavi, Kannan, Venkata Subba Rao, & Chamkha, 2020) and (Mathew, Neethu, & Areekara, 2021).

1.24.4 Channel flow

(Sheikholeslami, Hatami, & Ganji, 2013) conducted an analytical study of hydromagnetic flow in a porous channel and discovered an inverse relationship between the thickness of the velocity boundary layer and the Reynolds number. (Gul, Khan, Shafie, Khalid, & Khan, 2015) investigated the flow of ferro nanofluid through a vertical channel and its heat transfer effects. The researchers also conducted a velocity comparison between Al_2O_3/water and Fe_3O_4/water nanofluids. (Raza, Rohni, & Omar, 2016) investigated MHD flow through a porous channel with stretching effects. Skin friction decreased as the volume fraction increased, according to the researchers. MHD convective flow through an inclined channel can be found in (Malashetty & Umavathi, 1997), (Said, Habib, Badr, & Anwar, 2005), (Hasnain, Abbas, & Sajid, 2015) and (S. Hussain, Mehmood, Sagheer, & Farooq, 2017).
(S. Das, Jana, & Makinde, 2016) reviewed the transient free convection nanofluid flow through a vertical channel in the presence of thermal radiation. Convection flow through the vertical channel is decisive in the cooling systems of heat exchangers and solar cells. Warm blood circulation in mammals and engine cooling are examples of convection. Forced and free convections are very important in the convection flows. Enforced convection with heat transfer properties in a porous channel is evaluated by (Maghrebi, Nazari, & Armaghani, 2012). An oscillatory MHD flow through a rotating channel in the presence of Hall current has been analyzed previously by (Pal & Talukdar, 2013). Electrically conducting fluid flow through a rotating porous channel has wide industrial uses like nuclear reactors, geothermal systems and filtration etc. (See (Sulochana et al., 2014)).

1.24.5 Flow past a flat plate

Flow past a flat plate frequently occurs in the field of aerodynamics, plasma studies, and cooling systems. Fluid flow over an inclined/vertical flat plate encounters buoyancy forces which significantly affect the convective flow and heat transfer. Free and forced convection is important in such flows. Free convective flow past a vertical plate is discussed in (Krishna & Chamkha, 2019), (Nandi & Kumbhakar, 2020), (Krishna, Swarnalathamma, & Chamkha, 2019) and (Akcay, Akdag, & Palancioglu, 2020). (Krishna et al., 2019) studied the mixed convective flow over a flat plate and found that frictional force at the plate was decreased due to an increase in the applied magnetic field. (Akcay et al., 2020) experimentally investigated the mixed convective fluid flow over a vertical flat plate. The researchers observed that heat flux on the plate significantly affected the performance of heat transfer. (Khademi, Razminia, & Shiryaev, 2020) studied the mixed convective fluid flow over an inclined plate. They implemented the Differential Quadrature Method (DQM) for solving the nonlinear differential equations. (Mondal, Pal, Chatterjee, & Sibanda, 2018) explored the MHD mixed convective fluid flow over an inclined plate. It is found that the velocity profile is declined due to an increase in the inclination angle. (Rashed, Ahmed, & Sheremet, 2019) investigated the MHD flow over an inclined plate in the presence of solar radiation. The researchers noticed an enhancement in the temperature field by the increment in the angle of inclination.

1.24.6 Flow past a stretching sheet

Stretching surface has intrigued many researchers due to its diverse applications in industrial and engineering fields like production of plastic and rubber plates, cooling of metallic plate in a bath, metal extrusion, etc. (J. A. Khan, Mustafa, Hayat, & Alsaedi, 2014) studied the heat transfer over a bilateral stretched nonlinear surface numerically with the aid of OHAM and Runge-Kutta coupled with shooting method. (Z. Hussain, Hayat, Alsaedi, & Ahmad, 2018) analysed the effect of heat generation of CNTs nanofluids over a nonlinear bilateral stretched surface. A reduced thermal layer due to the rate of stretching was noted. (M. Nandeppanavar & Siddalingappa, 2013) analysed the consequence of thermal radiation and viscous dissipation on heat transfer over a nonlinear stretching sheet through a porous medium and inferred a positive and negative effect on temperature due to Eckert number and

thermal radiation parameter, respectively. (Tlili, Bilal, Qureshi, & Abdelmalek, 2020) investigated three dimensional flow over a stretched surface using Williamson fluid and they had established that the velocity along Y direction enhanced due to stretching. (Hayat, Aziz, Muhammad, & Alsaedi, 2019) investigated the Carreau nanofluid flow induced by a bilateral stretched surface. They tackled the nonlinear differential equations using NDsolve. (Shakunthala & Nandeppanavar, 2019) studied the boundary layer flow and Cattaneo-Christov heat flux of a nonlinear stretching sheet with suspended carbon nanotubes.

1.24.7 Flow past a stretching cylinder

Viscous fluid flow over an expanding cylinder has important applications in industry and engineering fields. Production of plastic films, rubber, copper wires, and paper are some industrial applications of viscous fluid flows. The heat transfer rate and stretching determines the quality and finishing of a product. Nanofluid flow over a lengthening cylinder with shape factor is considered in the study of (Shaiq, Maraj, & Iqbal, 2019). Heat transfer via a stretched cylinder utilizing nanofluids is important in food processing, glass fibre production and metal spinning. (Shojaei, Amiri, Ardahaie, Hosseinzadeh, & Ganji, 2019) analysed second-grade non-Newtonian fluid flow over a stretched cylinder and observed an elevated temperature profile due to large curvature parameter values. (Z. Hussain, Hayat, Alsaedi, & Ahmed, 2018) conducted a simultaneous study on the nanofluid flow over an elongating cylinder and a flat sheet. They noticed an increase in the velocity profile due to flow over a flat sheet when collated with flow over an expanding cylinder.

1.24.8 Flow past a rotating disk

Following (Von Kármán, 1921) pioneering work, the fluid motion caused by disc spinning has stimulated the interest of many researchers due to its wide application in engineering and industry. Von Kármán flow delineates a swirling flow by the uniform rotation of a disk. Centrifugal pumps, polymer extrusion, disk drives, electrochemistry, petroleum processes, evaporators, and lubrication are some applications that utilize the concept of rotational fluid flow (see (M. I. Khan, 2021) and (Shehzad, Mabood, Rauf, & Tlili, 2020)). (S. Mandal & Shit, 2021) scrutinized the mechanism of nanoliquid flow past a rotating disk and the researchers noticed a strong relationship between the rate of heat transfer and rotation of the disk.

(Tassaddiq et al., 2020) explored nanoliquid flow past a rotating disk and they found enhanced velocity and temperature profiles by rotation of the disk. (Ibrahim, 2020) numerically analyzed viscous fluid (time-dependent) flow over a rotating disk and observed a decrease in volume fraction of nanoparticles as the Schmidt number increased.

1.24.9 Heat source

Heat source/sink parameter has a key role in medical and industrial field. Heat pumps, heat exchangers and filtration device are a few examples exploiting the effect of various heat sources. Nanofluid flow over an elongating cylinder with heat source is reviewed in (A. Ahmed, Khan, Hafeez, & Ahmed, 2020) and (M. Ali, Shahzad, Sultan, & Khan, 2020). (Gireesha, Nagaraja, Sindhu, & Sowmya, 2020) studied about the CNT nanofluid flow on top of a curved elongating sheet and noticed an increase in temperature due to exponential space-based heat source (ESHS). (Mahanthesh, Shashikumar, & Lorenzini, 2021) scrutinized the simultaneous effect of ESHS and linear heat source (LHS) parameter on the nanofluid flow over a stretchable rotating disk. They discovered an elevated heat transfer rate due to ESHS parameter than the LHS parameter. Non-Newtonian and Newtonian fluid flow considering ESHS for different scenarios are studied by (Mahanthesh, Shashikumar, Gireesha, & Animasaun, 2019) and (Nagaraja & Gireesha, 2021). Heat sources have a remarkable role in the regulation of heat fluctuations in thermal systems. (Pattnaik, Mishra, Mahanthesh, Gireesha, & Rahimi-Gorji, 2020) numerically computed the effect of the exponential heat source (EHS) on fluid flow over a plate and compared it with thermal based-heat source (THS).

Heat source parameters can regulate heat transfer effects which have a key role in space heating, air conditioning, and industries including rubber, polymer, food, oil production, etc. Heat source from a high surface area naturally generates an irregular (non-uniform) heat distribution (Fauzan, Muyeen, & Islam, 2021). Temperature-dependent and space-dependent heat source models are described in the previous studies (Mabood, Ibrahim, Rashidi, Shadloo, & Lorenzini, 2016) and (Raju, Sandeep, & Malvandi, 2016). The non-uniform heat source model is a combination of temperature and space-dependent heat sources. (Sravanthi, 2019) studied nanoliquid flow over a rotating disk with the non-uniform heat source and recorded a negative

impact in the heat transfer rate with augmentation in space-dependent heat source parameters. (Song et al., 2022) noticed an enhanced temperature profile with increment in the space and temperature dependant heat generation parameters whereas entropy production is minimized due to the non-uniform heat source (see (Unyong, Vadivel, Govindaraju, Anbuvithya, & Gunasekaran, 2022)).

1.24.10 Carreau nanofluid

Carreau nanofluid model includes low and high shear rates which is an attracting aspect in non-Newtonian studies. It is used to represent many manufacturing and chemical engineering flows. (Eid, Mahny, Dar, & Muhammad, 2020) studied Carreau nanofluid flow on top of an expanding sheet and found out that power law index promotes velocity. The Carreau fluid flow on top of an elongating cylinder was numerically investigated by (I. Khan, Ullah, Malik, & Hussain, 2018). They noticed a reverse relationship in the drag force due to Weissenberg number. (Salahuddin, Hussain, Malik, Awais, & Khan, 2017) analysed the slip effects of Carreu nanofluid over an elongated cylinder and observed a high-velocity profile for dilatant fluid due to augmentation in Weissenberg number.
(Hayat, Ahmed, Alsaedi, & Abbasi, 2018) numerically studied the flow of Carreau-Yasuda nanofluid in the presence of mixed convection and hall current and observed an inverse effect for concentration profiles under thermophoresis and Brownian motion parameters. (M. Khan, Azam, & Alshomrani, 2017) investigated about the unsteady slip flow of Carreau nanofluid over a wedge. (M. M. Nandeppanavar, Kemparaju, & Shilpa, 2019) scrutinized the Carreau nanofluid flow over an exponentially stretching sheet in a saturated porous medium using fourth order Runge-Kutta shooting method. (M. Khan, Hussain, Malik, Salahuddin, & Aly, 2019) numerically analysed the Carreau fluid flow for generalized Fourier's and Fick's laws. They observed that the horizontal velocity enhances with an increase in wall thickness parameter, power-law index, Weissenberg number, thermal Grashof parameter and bioconvection Rayleigh number.

1.24.11 Reiner-Rivlin fluid

Non-Newtonian fluids are classified as shear thinning, shear thickening, rheopectic, and thixotropic. Many viscoelastic non-Newtonian fluids like power-law fluids, Ellis fluids, Prandtl fluids, and Reiner-Rivlin fluids have fascinated researchers

owing to their applicability. Non-Newtonian fluids possess an elastic and viscous nature. Reiner-Rivlin nanoliquid is a non-Newtonian fluid that exhibits the dilatancy phenomenon. Dilatancy is the ability associated with the volume of a material. Dilatant material acquires a higher volume by stirring. Some important non-Newtonian fluids such as food products, biological fluids, and polymers, can be effectively analyzed by Reiner-Rivlin's nanofluid model (see (Lv, Gul, Ramzan, Chung, & Bilal, 2021), (Rashid & Mustafa, 2021) and (Rafiq, Mustafa, & Khan, 2022)). (Tabassum & Mustafa, 2018) investigated the Reiner-Rivlin slip flow on a rotating rough disk. They observed that the skin friction and resisting torque were increased with an increment in parameters of wall roughness. (A. Das & Sahoo, 2018) analyzed heat transfer between rotating coaxial disks by using Reiner-Rivlin fluid. (Sahoo & Shevchuk, 2019) investigated the rotating Reiner-Rivlin fluid flow on a stretching surface. They concluded that a significant decrease in the thermal boundary layer occurred due to increased radial stretching. (Naqvi, Kim, Muhammad, Mallawi, & Ullah, 2020) examined the Reiner-Rivlin liquid flow on a spinning disk including slip conditions. They observed that a higher torque was required to preserve consistent disk rotation with high wall slip. (Abdal et al., 2021) implemented bioconvection on Reiner-Rivlin nanoliquid flow past a rotating disk and they reported that intensified values of Reiner-Rivlin fluid parameter decremented both the radial and azimuthal wall stress. (Sadiq & Hayat, 2022) addressed the Reiner-Rivlin nanoliquid flow due to an elongated rotating disk. The researchers constructed a convergent solution using the ND-solve method and observed an improvement in tangential velocity with an increase in Reiner-Rivlin fluid parameter.

1.24.12 Quadratic/non linear convection

Nonlinear thermal convection play a significant role in solar collectors, the manufacturing of electronic equipment, and the process of doping. In these situations, a linear approximation of the density variation with temperature may incur significant errors. (Vajravelu & Sastri, 1977) introduced nonlinear thermal convection which drew the attention of many researchers as seen in ((Mahanthesh & Mackolil, 2021), (Elshehabey, Raizah, Öztop, & Ahmed, 2020) and (Basha, Sivaraj, Prasad, & Beg, 2021)). (Raju, Saleem, Al-Qarni, & Upadhya, 2019) studied the nonlinear

convective fluid flow past a stretching sheet utilizing Eyring–Powell fluid model with the suspension of dust and graphene particles. The researchers found an inverse relationship between the Nusselt number and the nonlinear convection parameter. (Jha & Sarki, 2020) investigated the nonlinear convection near a moving plate and studied the heat and mass transfer effects. An increased fluid velocity in the case of nonlinear convection was reported.

1.24.13 Nanoparticle aggregation

Nanoparticles tend to form clusters known as nanoparticle aggregates. Rapid and moderate aggregation occurs depending on the interparticle characteristics of the nanoparticles and the chemistry of the base fluid. Aggregated nanoparticles possess different properties when compared to independently dispersed particles. (Ganguly, Basu, & Sikdar, 2012) investigated the cluster of nanoparticles from an aqueous suspension of Al_2O_3 with a volume fraction of 0.005 and observed an agglomeration size varying in the range 100-500 nm. Nanoparticle aggregates of stable nanofluids can significantly alter the heat transfer capacity of the working fluids (see (Wensel et al., 2008) and (Parameshwaran & Kalaiselvam, 2013)). The aggregation structure is described by the fractal dimensions which quantitatively measures the degree of openness or compactness of the aggregate structure (W. Zhang, 2014). (B.-X. Wang, Zhou, & Peng, 2003) described a fractal model and successfully predicted the thermal conductivity for low volume fractions of metallic oxide nanoparticles in the base fluid. (Chen, Ding, He, & Tan, 2007) effectively estimated the nanofluid thermal conductivity using aggregation of titanium dioxide (TiO_2) in EG base fluid. TiO_2 nanoparticles are widely used in cosmetics, toothpastes, plastics, paints and solar collectors and their aggregation characteristics have been discussed by researchers as seen in (Zhu, Wang, Keller, Wang, & Li, 2014), (Hu et al., 2018) and (V. K. Sharma, 2009). (Sindhu & Gireesha, 2020) studied the kinematics of nanofluid flow with nanoparticle aggregation through a microchannel. The researchers observed a high-temperature profile for the aggregation model when compared to the conventional models. (Mackolil & Mahanthesh, 2021b) analyzed the nanoparticle aggregation factor in the Marangoni convective flow of a nanofluid and scrutinized the sensitivity of the heat transfer rate. It is noticed that a lowered velocity profile due to aggregation effects.

1.24.14 Porous medium

Porous material includes voids and is characterized by porosity parameters. Studies relating to petroleum engineering, filtration, soil mechanics, and biological tissues utilize the idea of porous media. (Jafar, Shafie, & Ullah, 2020) analyzed nanofluid flow in a porous medium and they investigated an enhanced temperature profile with high porous parameter values. (Eid & Nafe, 2022) found a retarded velocity profile with incremented porous parameter values. Additionally, studies involving porous medium are discussed in (Krishna, Ahamad, & Chamkha, 2020) and (Z. Khan, Makinde, Hamid, Haq, & Khan, 2020).

1.24.15 Injection/suction

A permeable medium allows fluid penetration in the presence of more connected voids. The injection and suction effects due to the influence of permeability have a potential application in astronomical disciplines, fuel injection thermal protection and aerodynamics (see (Ganapathirao, Chamkha, & Srinivasa Rao, 2019), and (S. Rana, Mehmood, & Bhatti, 2021)). (Acharya, Maity, & Kundu, 2020) observed an amplified temperature profile in the presence of injection. (Nadeem, Abbas, & Malik, 2020) noticed an elevated boundary layer thickness in the presence of injection effects and the trend reversed with suction.

1.24.16 Convective boundary condition

Convective boundary condition creates a significant relation between thermal difference and heat flux at the surface (Zhao, Li, Wang, & Wang, 2022). (Sreedevi, Reddy, & Chamkha, 2018) found an enhanced heat transfer effect and (Saif, Muhammad, Sadia, & Ellahi, 2020) noticed an increment in the thermal boundary layer with elevation in the Biot number. (Patel & Singh, 2019) studied micropolar fluid flow over a stretched sheet with convective boundary conditions in the presence of Brownian motion and thermophoresis effects. An improvement in heat transfer due to increased Biot numbers was observed. (Ray, Vasu, Murthy, & Gorla, 2020) studied the non-similar solution of Eyring-Powell fluid flow and heat transfer with convective boundary conditions using HAM.

1.24.17 Radiation

(S. Das et al., 2016) reviewed the transient free convection nanofluid flow through a vertical channel in the presence of thermal radiation. MHD flow past a cosinusoidally fluctuating heated plate with radiation was researched by (Ram, Singh, Kumar, Kumar, & Joshi, 2017). (Nayak, Shaw, Pandey, & Chamkha, 2018) studied the combined effects of slip and convective boundary conditions on MHD three-dimensional stretched flow of nanofluid through porous media under nonlinear thermal radiation. (Kumar, Sood, Shehzad, & Sheikholeslami, 2017) investigated the non -Newtonian fluid flow past a Riga plate and the researchers found an elevation in the heat transfer rate with an increase in radiation parameter. (Mohammadein & El-Amin, 2000) investigated the influence of radiation on power-law fluid flow past a plate in a porous medium and the researchers noticed an increased temperature profile with radiation. Nanofluid flow with radiation effects are studied in (K. Das, Duari, & Kundu, 2014), (Hossain & Takhar, 1996) and (Sekhar et al., 2017)

1.24.18 Chemical reaction

(Haile & Shankar, 2014) examined the MHD nanofluid flow with heat and mass transfer through a porous medium with thermal radiation, viscous dissipation, and chemical reaction effects. The study showed that the effect of heat and mass transfer with chemical reaction has a significant role in processes like the transfer of energy in a wet cooling tower, drying, the flow in desert coolers, and electric power generation. Chemical reaction effect has a major role in industrial processes like the fabrication of ceramics or glassware and the production of polymers (Haile & Shankar, 2014). Nanofluid flow with chemical reaction can be found in (Kameswaran, Narayana, Sibanda, & Murthy, 2012), (Tarakaramu & Narayan, 2017), (C. Zhang, Zheng, Zhang, & Chen, 2015) and (Kumar, Sood, Sheikholeslami, & Shehzad, 2017).

1.24.19 Hall current

Hall current is developed in the flow of a conducting fluid normal to the strong magnetic field. (Hall et al., 1879) introduced the concept in 1879. Hall current has attracted many researchers due to its application in Hall accelerators, Hall sensors, magnetic resonance imaging, etc. (Lv, Shaheen, et al., 2021). An oscillatory MHD flow through a rotating channel in the presence of a Hall current has been analyzed previously by (Pal & Talukdar, 2013). (Tlili, Ramzan, Kadry, Kim, &

Nam, 2020) analyzed Hall effect on hydromagnetic flow past a moving thin needle and the researchers noticed an enhanced velocity profile with an increase in the Hall parameter.

1.24.20 Soret effect

Whenever there are different chemical species present under a strong temperature gradient, the Soret effect is significant. (Hayat, Aslam, Khan, Khan, & Alsaedi, 2019) studied the Soret effect on peristalsis flow through an inclined channel utilizing pseudoplastic fluid and the researchers addressed a declined concentration profile with an increase in Soret number. Hydromagnetic flow with Soret effect can be found in the studies of (S. A. Khan, Hayat, Khan, & Alsaedi, 2020), (S. A. Khan et al., 2020), (Krishna et al., 2019) and (Hayat, Shehzad, & Alsaedi, 2012).

1.24.21 Joule heating

The Joule heating process can be seen in food processing equipment, soldering irons, electric kettles, and electric stoves. On the other hand, excess heat during the procedure is harmful to numerous systems. Therefore Joule heating is crucial. (Gayatri, Jayarami Reddy, & Jayachandra Babu, 2020) studied the influence of Joule heating on a two-dimensional Carreau fluid flow past a stretching sheet. (Kempannagari, Buruju, Naramgari, & Vangala, 2020) discussed Joule heating effect on hydromagnetic non-Newtonian flow past a curved surface. Hydromagnetic flow with joule heating effect is discussed in (Gireesha et al., 2019), (Iqbal, Khan, Ahmed, & Nadeem, 2020) and (Wakif et al., 2020).

1.24.22 Various models depicting nanofluid flow

Buongiorno presented a model in 2006 based on seven slip mechanisms such as gravity, Magnus effect, fluid drainage, thermophoresis, diffusiophoresis, Brownian random motion, and inertia. Among them, thermophoresis and Brownian diffusion were found to be the most imperative. (Kho, Hussanan, Mohamed, & Salleh, 2019) utilized the Buongiorno model to analyze the heat transfer properties of the Williamson nanofluid considering thermophoresis and Brownian motion. They reported enhanced concentration and temperature profiles with the increment in the Williamson parameter. (S. E. Ahmed & Rashed, 2019) explained the thermophoretic and random motion effects in a wavy porous enclosure. (Sheikholeslami, Chamkha, Rana, & Moradi, 2017) scrutinized the impact of nanoparticles via Brownian random

motion and thermophoretic effect in the free convection through an enclosure of L-shape. They incorporated the CVFEM method for the computations. Rotating disk fluid transport of an Oldroyd-B nanofluid was explored by (Hafeez, Khan, & Ahmed, 2020). A drop in the heat transfer rate was observed in their study with the variations in Brownian random motion and thermophoretic parameters. Nanofluid flow over various attributes utilizing Buongiorno model can be found in (De, 2019b), (S. Reddy, Bala Anki Reddy, & Rashad, 2020), (De, 2019a), (Roşca, Roşca, Pop, & Merkin, 2020) and (De & Gorji, 2020). (Zeeshan, Maskeen, & Mehmood, 2018) presented MHD flow over a stretched cylinder using Buongiorno's model and observed that the concentration profile declined due to Brownian motion.

However, the Buongiorno model excludes the augmentation in the effective thermophysical properties of nanomaterial. In 2003, (Khanafer, Vafai, & Lightstone, 2003) developed a nanoliquid transport model considering the nanoparticle dispersion. Later, (Tiwari & Das, 2007) developed a simpler nanofluid model considering the effective thermophysical properties of a nanofluid. (Kumar, Kumar, Shehzad, & Sheikholeslami, 2018) utilized the Tiwari-Das nanofluid model to investigate the influence of vibrational rotations and multiple slip conditions on the hydromagnetic nanomaterial flow over an elongating surface. They observed a rise in the Nusselt number for augmenting nanoparticle volume fraction.

Modified Buongiorno nanoliquid model (MBNM) extends the traditional Buongiorno model by considering the effectual slip mechanisms along with the effective properties of a nanofluid. (Yang, Li, & Nakayama, 2013) modified the Buongiorno model for the impact of volume fraction of nanoparticles in the equations describing the fluid flow. The heat transfer of a nanoliquid over an elongated sheet involving MBNM was studied by (P. Rana, Shukla, Bég, & Bhardwaj, 2021). (Mahanthesh, Shashikumar, & Lorenzini, 2021) utilized MBNM to model the nanoliquid flow over a wedge. Higher sensitivity towards the heat transfer rate was exhibited by the Brownian motion parameter. Further discussions on the flow problems modelled using MBNM can be seen in (Ray, Vasu, Bég, Gorla, & Murthy, 2019), (Wakif, Chamkha, Thumma, Animasaun, & Sehaqui, 2021), (Mahanthesh & Mackolil, 2021), (Areekara, Mackolil, Mahanthesh, Mathew, & Rana, 2022) and (P. Rana, Srikantha, Muhammad, & Gupta, 2021).

1.24.23 Nanofluid flow with slip effects

At microscopic interfaces, the velocity of the fluid (near the wall) may not be always considered zero due to the occurrence of a relative movement between the wall and the fluid. In these situations, the velocity of the fluid at the interface is assumed to be a constant multiple of wall shear stress and this constant multiple (measured in length) that extrapolates velocity is named the velocity slip parameter (or hydrodynamic slip parameter). Slip flow plays a significant role in engineering and medical field. Micro valves, hard disk drives, internal cavities and nozzles are a few examples where the slip flow is utilized. (Ramya, Raju, Rao, & Chamkha, 2018) investigated a decreased velocity profile with augmented values of velocity slip. The significance of hydrodynamic slip and viscous dissipation over a stretching/shrinking surface was studied by (Aly & Pop, 2020). A comparative analysis between the hybrid and traditional nanofluid on the effect of slip parameter showcased the superior cooling capability of the hybrid nanoliquid. Further studies exploring velocity slip effects are discussed in (S. U. Khan, Waqas, Muhammad, Imran, & Aly, 2020), (M. I. Khan, Alzahrani, Hobiny, & Ali, 2020) and (I. C. Mandal, Mukhopadhyay, & Vajravelu, 2021). (Vinita & Poply, 2020) studied slip flow past a stretched cylinder and found a reduced velocity profile due to the slip parameter. Non-Newtonian and Newtonian fluids with slip effects are reviewed by numerous researchers. Effect of thermal slip and velocity slip past a stretching cylinder are found in (Ogunseye, Sibanda, & Mondal, 2019), (Mishra & Kumar, 2020) and (Usman, Soomro, Haq, Wang, & Defterli, 2018). (Sadiq, Haider, Hayat, & Alsaedi, 2020) illustrated the effects of thermal slip in Darcy-Forchheimer nanofluid flow by a rotating disk. They observed that the heat transfer rate is an increasing function of the thermal slip parameter. In addition, (Ramzan et al., 2021) noticed a decline in the thermal boundary layer due to the increasing thermal slip parameter. Thermo-hydrodynamic (thermal and velocity) slip plays a major role in the applications like polishing of surfaces, micro devices, and mechanical heart valves (see (Mishra & Kumar, 2020)).

1.24.24 Zero mass flux condition/Passive control approach

(Kuznetsov & Nield, 2013) introduced a physically more realistic model which involves the passive control of the nanoparticle volume fraction at the boundary. Nanofluid flow past a stretching sheet with zero mass flux condition is discussed in

(Sudarsana Reddy & Sreedevi, 2021) and (Faisal, Ahmad, & Javed, 2021). Mass flux corresponds to the rate of mass flow per unit area perpendicular to the direction of flow. Zero mass flux is the condition when the normal flux of nanoparticles is zero at the boundary. (Ramzan, Sheikholeslami, Saeed, & Chung, 2019) examined the flow of couple stress nanofluid past an exponential stretched surface and observed that for growing values of Brownian motion and thermophoresis parameters, the concentration profile exhibits decreasing and increasing behaviour respectively. (Uddin et al., 2018) investigated the characteristics of buoyancy forces on stagnation point flow under magneto-nanoparticles and zero mass flux condition. Characteristics of a thermally stratified flow of Sutterby nanofluid along with zero mass flux condition was analysed by (Mir et al., 2020).

1.24.25 Darcy-Forchheimer flow

Darcy's law corresponds to an equation that explains the capability of a fluid to flow via a porous medium. Darcy-Forchheimer flow is a fluid flow through a porous medium satisfying the Darcy-Forchheimer relation that subsumes inertial properties and boundary characteristics. The Darcy-Forchheimer nanoliquid flow due to a curved lengthening sheet has been numerically examined by (Hayat, Qayyum, Alsaedi, & Ahmad, 2020). They noted a decline in the velocity profile for mounting values of the Forchheimer number. (Alzahrani, Ullah, Alshomrani, & Gul, 2021) elucidated the significance of Darcy-Forchheimer hybrid nanoliquid flow over an inclined solar collector plate. Studies discussing the three-dimensional Darcy-Forchheimer flow over a lengthening sheet can be seen in (Kumar, Sharma, Kumar, Sheikholeslami, & Vajravelu, 2021), (Ullah, Muhammad, & Mallawi, 2021), (Jawad, Saeed, Khan, & Islam, 2021), (Shankaralingappa, Gireesha, Prasannakumara, & Nagaraja, 2021), (Xiong, Chu, Khan, Khan, & Abbas, 2021) and (Joshi, Upreti, & Pandey, 2022).

1.24.26 Nanofluids with various shapes of nanoparticles

Nanofluids with various nanoparticle shape exhibits differing thermal and physical properties. In 2009, (Timofeeva et al., 2009) discussed the consequence of different shaped alumina nanoparticles (platelet, blade, brick, and cylinder) on its thermo-physical properties and predicted a model for effective thermal conductivity and effective dynamic viscosity based on the experimental data. In addition, (Kim, Lee, Lee, & Jang, 2015) experimentally concluded that the liquid suspension with

brick-shaped alumina nanoparticles showcased the highest thermal conductivity. Recently, the fluid characteristics and heat transfer capabilities of nanofluid flow through a horizontal tube with various nanoparticle shapes were investigated by (Benkhedda, Boufendi, Tayebi, & Chamkha, 2020) and observed higher heat rates for the platelet-shaped nanoparticles. In addition, (Bahiraei, Monavari, & Moayedi, 2020) noticed that the maximum frictional entropy generation belonged to the platelet-shaped nanoparticles and the minimum frictional entropy generation belonged to the Os-shaped nanoparticles.
(Mahanthesh, Gireesha, Shehzad, Rauf, & Kumar, 2018) explored the effects of various nanoparticles of column, lamina, sphere, hexahedron, and tetrahedron-shaped nanoparticles in a magnetohydrodynamic flow due to a rotating disk and detected an increased nanofluid temperature for sphere-shaped nanoparticles. (Saranya & Al-Mdallal, 2021) examined the effect of nanoparticle shapes (sphere, cylinder, brick, blade, and platelet) on the alumina-silicon oil nanofluid flow due to a rotating disk. They observed that the blade-shaped nanoparticles displayed the highest thermal conductivity followed by platelet, cylinder, brick, and sphere-shaped nanoparticles. Further, (Waqas, Farooq, Naseem, Hussain, & Alghamdi, 2021) analyzed the impact of the sphere, platelet, and cylindrical-shaped nanoparticles on the hybrid nanofluid flow due to a rotating disk.

1.25 Objectives

The main objectives of the present work are to investigate

- Various mathematical models describing hydromagnetic flows
- Numerical methods to solve MHD convective nanofluids
- The effectiveness of heat transfer enhancement in different nano fluids with different parameters
- The applicability of nanofluids in optimizing drag coefficient
- The comparison of theoretical findings with statistical results

Chapter 2

Statistical analysis of MHD convective ferro-nanofluid flow through an inclined channel with Hall current *

2.1 Introduction

Molecule transport in a slanted rectangular channel is usual in designing applications, e.g. molecule transport in micro channels. Slanted pipe and channels have extensive applications in automobile industry for designing equipments. Nanoparticles can considerably reduce the size of equipments and show a better performance than the existing ones. Convection flow through the vertical channel is decisive in the cooling system of heat exchangers and solar cells. Warm blood circulation in mammals and engine cooling are examples of convection. Forced and free convections are very important in the convection flows. Chemical reaction and radiation impacts on MHD convective nanofluid flow through an inclined channel with Hall current, heat source and Soret effect are analyzed using ferro-nanofluid. In addition, the resultant thermal conductivity is found using the Hamilton-Crosser model. Besides, wall heat, mass transfer rates and surface drag are investigated through statistical tools like regression and probable error.

2.2 Mathematical formulation

An unsteady free convective, incompressible and electrically conducting ferro-nanofluid flow through an inclined channel packed with porous medium is considered. The problem is studied under the following assumptions:

*Published in: Thermal Science and Engineering Progress (Elsevier), 2021; 22; 100816

1. Ferro-nanofluid flow is observed in the X^* direction.
2. Two infinite electrically non-conducting and permeable parallel plates at a distance d apart inclined at an angle α are considered (see Fig. 2.1).
3. One plate is held stationary while the other is oscillating in its own plane with a velocity $U^*(t^*)$.
4. Ferro-nanofluid is injected into the stationary plate with a velocity w_0 and is sucked by the oscillating plate with a velocity w_0.
5. A uniform magnetic field of strength B_0 is exerted in the Z^* axis (orthogonal to the flow) and Hall current is generated due to this magnetic field.
6. Effect of induced electric and magnetic field are ignored due to small magnetic Reynolds number.
7. Temperature and concentration at the stationary plate periodically varies with time t^*.
8. Plates are maintained at high-temperature variation to induce heat transfer via radiation. The radiative heat flux is considered in the Z^* direction.
9. Density variation with temperature and concentration in body force term is considered and all other fluid properties are assumed to be constant.
10. Additional heat source (Q) and the order of reactive species in an irreversible chemical reaction are considered.
11. Viscous dissipation, Joule heating, electric and polarisation effects are ignored (Balvinder, Krishan, & Bansal, 2014).

Using Boussinesq's approximation, the flow is described (Singh & Mathew, 2012), (Pal & Talukdar, 2013), (Sureshkumar & Muthtamilselvan, 2016)as:

$$\begin{aligned}\rho_{nf}\left(\tfrac{\partial u^*}{\partial t^*}+w_0\tfrac{\partial u^*}{\partial z^*}\right) &= -\tfrac{\partial P}{\partial x^*}+\mu_{nf}\tfrac{\partial^2 u^*}{\partial z^{*2}} \ +(\rho\beta_T)_{nf}g\,(T^*-T_d)\,sin\alpha \\ &+(\rho\beta_C)_{nf}g\,(C^*-C_d)\sin\alpha \ +\tfrac{\sigma {B_0}^2(Hv^*-u^*)}{1+H^2}-\tfrac{\mu_{nf}}{K_p}u^*\end{aligned} \tag{2.2.1}$$

$$\rho_{nf}\left(\frac{\partial v^*}{\partial t^*}+w_0\frac{\partial v^*}{\partial z^*}\right)=-\frac{\partial P}{\partial y^*}+\mu_{nf}\frac{\partial^2 v^*}{\partial z^{*2}}-\frac{\sigma {B_0}^2\,(Hu^*+v^*)}{1+H^2}-\frac{\mu_{nf}}{K_p}v^* \tag{2.2.2}$$

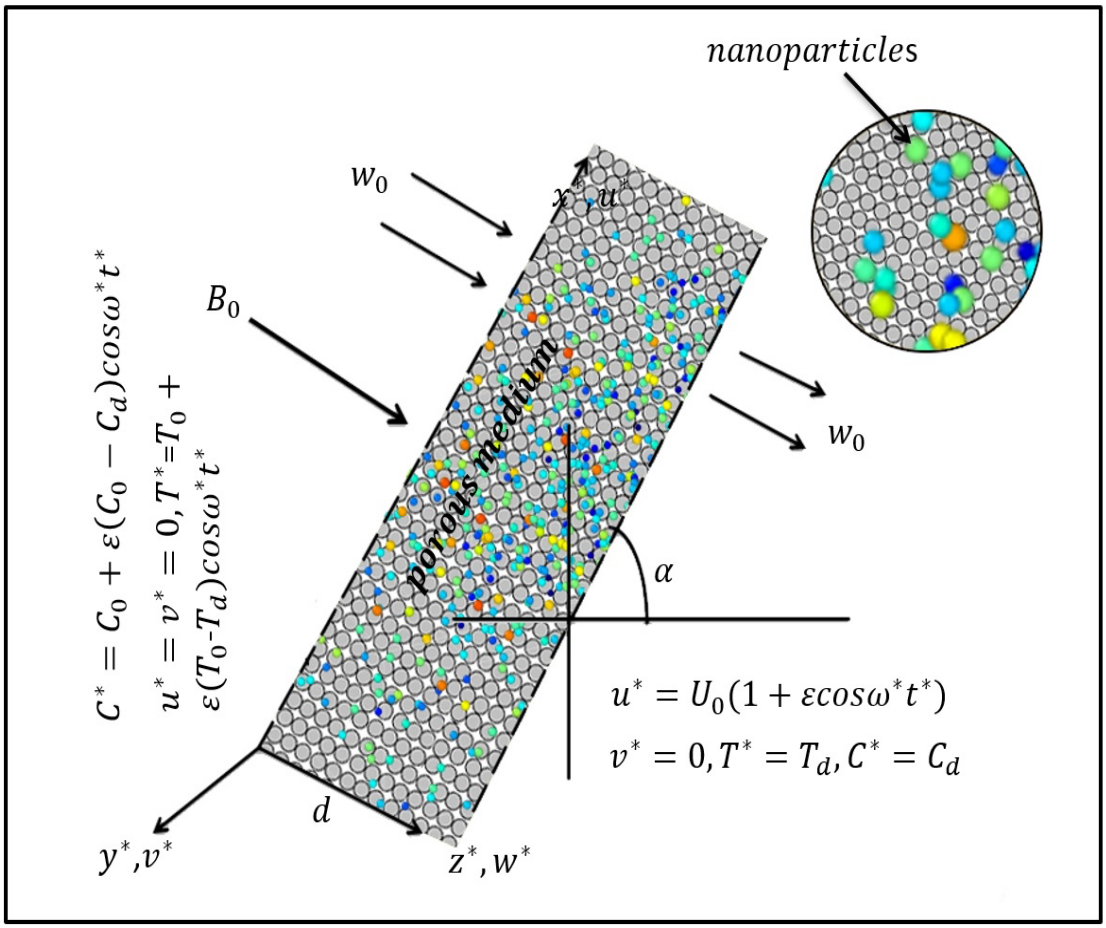

Figure 2.1: *Physical configuration of the problem*

$$(\rho C_p)_{nf}\left(\frac{\partial T^*}{\partial t^*} + w_0\frac{\partial T^*}{\partial z^*}\right) = k_{nf}\frac{\partial^2 T^*}{\partial z^{*2}} - \frac{\partial q_R}{\partial z^*} + Q\,(T^* - T_d) \tag{2.2.3}$$

$$\frac{\partial C^*}{\partial t^*} + w_0\frac{\partial C^*}{\partial z^*} = D_B\frac{\partial^2 C^*}{\partial z^{*2}} + D_T\frac{\partial^2 T^*}{\partial z^{*2}} - K_l\,(C^* - C_d) \tag{2.2.4}$$

where the terms are explained in nomenclature.

Optically thin nanofluid has been considered and hence radiative heat flux (Balvinder et al., 2014) is taken as

$$\frac{\partial q_R}{\partial z^*} = 4{\alpha_P}^2\,(T_0 - T_d) \tag{2.2.5}$$

Corresponding boundary conditions are:

$$\left.\begin{gathered} u^* = v^* = 0,\ T^* = T_0 + \epsilon\,(T_0 - T_d)\,cos\omega^* t^*,\ C^* = C_0 + \epsilon\,(C_0 - C_d)\,cos\omega^* t^*,\ z^* = 0 \\ u^* = U_0\,(1 + \epsilon cos\omega^* t^*)\,,\quad v^* = 0,\quad T^* = T_d,\ C^* = C_d,\quad z^* = d \end{gathered}\right\} \tag{2.2.6}$$

Following quantities are used to make equations (2.2.1) to (2.2.4) in dimensionless form:

$$\begin{gathered} K_r = \frac{K_l \nu}{{w_0}^2}, D_B = \frac{\nu}{Sc},\ R = \frac{2\alpha_P d}{\sqrt{K}},\ Re = \frac{U_0 d}{\nu},\ \lambda = \frac{w_0 d}{\nu}, M = B_0 d\sqrt{\frac{\sigma}{\mu}}, \\ z = \frac{z^*}{d},\ x = \frac{x^*}{d}, t = t^*\omega^*, u = \frac{u^*}{U_0}, v = \frac{v^*}{U_0}\ , \omega = \frac{\omega^* d^2}{\nu}, \\ U = \frac{U^*}{U_0}, K_1 = \frac{K_p}{d^2},\ S = \frac{Qd^2}{K}, Pr = \frac{\mu C_p}{K}, G_m\ = \frac{\nu g\beta(C_0 - C_d)}{U_0 {w_0}^2} \\ S_0 = \frac{D_T(T_0 - T_d)}{(C_0 - C_d)\nu}, \theta' = \frac{T^* - T_d}{(T_0 - T_d)}, C' = \frac{C^* - C_d}{(C_0 - C_d)}, G_r = \frac{\nu g\beta(T_0 - T_d)}{U_0 {w_0}^2} \end{gathered} \tag{2.2.7}$$

The nanofluid constants are stated (O. Makinde & Animasaun, 2016) as follows:

$$\begin{gathered} \rho_{nf} = (1-\phi)\,\rho_f + \phi\rho_s, \mu_{nf} = \frac{\mu_f}{(1-\phi)^{2.5}}, \\ (\rho C_p)_{nf} = (1-\phi)\,(\rho C_p)_f + \phi(\rho C_p)_s, \\ \lambda_n = \frac{k_{nf}}{k_f} = \frac{k_s + (h-1)k_f - (h-1)\left(k_f - k_s\right)\phi}{k_s + (h-1)k_f + \left(k_f - k_s\right)\phi}, \\ \frac{\sigma_{nf}}{\sigma_f} = 1 + \frac{3\left(\frac{\sigma_s}{\sigma_f} - 1\right)\phi}{\frac{\sigma_s}{\sigma_f} - 2 - \left(\frac{\sigma_s}{\sigma_f} - 1\right)\phi}, \\ (\rho\beta_T)_{nf} = (1-\phi)\,(\rho\beta_T)_f + \phi(\rho\beta_T)_s, \end{gathered} \tag{2.2.8}$$

Let $\beta_T = \beta_C$ and assume that

$$\begin{gathered} \phi_1 = 1 - \phi + \phi\frac{\rho_s}{\rho_f},\ \phi_2 = \frac{1}{(1-\phi)^{2.5}}, \\ \phi_3 = 1 - \phi + \phi\frac{(\rho\beta_T)_s}{(\rho\beta_T)_f}, \\ \phi_4 = 1 - \phi + \phi\frac{(\rho C_p)_s}{(\rho C_p)_f}, \\ \phi_5 = \frac{\sigma_{nf}}{\sigma_f}, \end{gathered} \tag{2.2.9}$$

Let $l' = u + iv$ and $h = 3$, then the equations (2.2.1) to (2.2.4) along with condition

Table 2.1: *Thermo physical properties of base fluid and nanoparticles at* 25^0

Model	$\rho\,(kgm^{-3})$	$C_p\,(Jkg^{-1}K^{-1})$	$k\,(Wm^{-1}K^{-1})$	$\beta \times 10^{-5}\,(K^{-1})$	$\sigma\,(s/m)$
Water	997.1	4179	0.613	21	0.05
Fe_3O_4	5180	670	9.7	1.3	25000

(2.2.6) are transformed into the non-dimensional form given by:

$$\begin{aligned}\phi_1\left(\omega\frac{\partial l'}{\partial t}+\lambda\frac{\partial l'}{\partial z}\right)=\phi_1\omega\frac{\partial U}{\partial t}+\phi_2\frac{\partial^2 l'}{\partial z^2}+\phi_3\lambda^2 sin\alpha\,(Gr\;\theta'+Gm\;C')\\-(l'-U)\left(\frac{\phi_2}{K_1}+\frac{\phi_5 M^2}{1+H^2}\,(1+iH)\right)\end{aligned}\tag{2.2.10}$$

$$\phi_4\left(\omega\frac{\partial\theta'}{\partial t}+\lambda\frac{\partial\theta'}{\partial z}\right)=\frac{1}{Pr}\left(\lambda_n\frac{\partial^2\theta'}{\partial z^2}-R^2\theta'+S\theta'\right)\tag{2.2.11}$$

$$\omega\frac{\partial C'}{\partial t}+\lambda\frac{\partial C'}{\partial z}=\frac{1}{Sc}\frac{\partial^2 C'}{\partial z^2}+S_0\frac{\partial^2\theta'}{\partial z^2}-K_r\lambda^2 C'\tag{2.2.12}$$

The corresponding boundary conditions are:

$$\left.\begin{aligned}l'=0,\quad \theta'=C'=1+\epsilon cost,\quad z=0\\ l'=1+\epsilon cost,\quad \theta'=0,\quad C'=0,\quad z=1\end{aligned}\right\}\tag{2.2.13}$$

2.3 Numerical solution

Solutions of equation (2.2.10) to (2.2.13) are approximated (Telionis & Telionis, 1981) as:

$$\delta'=\delta'_0(z)+\frac{\epsilon}{2}\left(\delta'_1(z)\,e^{(it)}+\delta'_2(z)\,e^{(-it)}\right)\tag{2.3.1}$$

Replacing δ' by the terms l', θ' and C' and applying in equations (2.2.10)-(2.2.13) we have:

$$\theta'_0=m_1e^{(\eta_1 z)}+m_2e^{(\eta_2 z)}\tag{2.3.2}$$

$$\theta'_1=m_3e^{(\eta_3 z)}+m_4e^{(\eta_4 z)}\tag{2.3.3}$$

$$\theta'_2=m_5e^{(\eta_5 z)}+m_6e^{(\eta_6 z)}\tag{2.3.4}$$

$$C'_0=\zeta_1e^{(q_1 z)}+\zeta_2e^{(q_2 z)}+A_{11}e^{(\eta_1 z)}+A_{12}e^{(\eta_2 z)}\tag{2.3.5}$$

$$C'_1=\zeta_3e^{(q_3 z)}+\zeta_4e^{(q_4 z)}+A_{21}e^{(\eta_3 z)}+A_{22}e^{(\eta_4 z)}\tag{2.3.6}$$

$$C'_2=\zeta_5e^{(q_5 z)}+\zeta_6e^{(q_6 z)}+A_{31}e^{(\eta_5 z)}+A_{32}e^{(\eta_6 z)}\tag{2.3.7}$$

$$\begin{aligned}l'_0=h_1e^{(\chi_1 z)}+h_2e^{(\chi_2 z)}+D_{11}+D_{12}e^{(\eta_1 z)}+D_{13}e^{(\eta_2 z)}\\+D_{14}e^{(q_1 z)}+D_{15}e^{(q_2 z)}+D_{16}e^{(\eta_1 z)}+D_{17}e^{(\eta_2 z)}\end{aligned}\tag{2.3.8}$$

$$\begin{aligned}l'_1=h_3e^{(\chi_3 z)}+h_4e^{(\chi_4 z)}+D_{21}+D_{22}e^{(\eta_3 z)}+D_{23}e^{(\eta_4 z)}\\+D_{24}e^{(q_3 z)}+D_{25}e^{(q_4 z)}+D_{26}e^{(\eta_3 z)}+D_{27}e^{(\eta_4 z)}\end{aligned}\tag{2.3.9}$$

$$\begin{aligned} l'_2 = h_5 e^{(\chi_5 z)} + h_6 e^{(\chi_6 z)} + D_{31} + D_{32} e^{(\eta_5 z)} + D_{33} e^{(\eta_6 z)} \\ + D_{34} e^{(q_5 z)} + D_{35} e^{(q_6 z)} + D_{36} e^{(\eta_5 z)} + D_{37} e^{(\eta_6 z)} \end{aligned} \tag{2.3.10}$$

$$\left.\begin{array}{c} \text{Local Nusselt number } Nu = \frac{x^* q_w}{K_f(T_0 - T_d)} \\ \text{local Sherwood number } \ Sh = \frac{x^* q_m}{D_B(C_0 - C_d)} \\ \text{Skin friction coefficient } \ Cf = \frac{\tau_w}{\rho_f U_0^2} \end{array}\right\} \tag{2.3.11}$$

where

$$q_w = -k_{nf}\frac{\partial T^*}{\partial z^*}, \quad q_m = -D_B\frac{\partial C^*}{\partial z^*}, \quad \tau_w = \mu_{nf}\frac{\partial u^*}{\partial z^*} \tag{2.3.12}$$

Using the non-dimensional quantities (2.2.7), the above expressions are transformed into:

$$Nu = -\lambda_n\frac{\partial \theta'}{\partial z}, \quad Sh = -\frac{\partial C'}{\partial z}, \qquad Cf = \frac{\phi_2}{Re}\frac{\partial l'}{\partial z} \tag{2.3.13}$$

Nusselt Number Nu at z = 1

$$Nu = -\lambda_n\left(\frac{\partial \theta'}{\partial z}\right)_{z=1} \tag{2.3.14}$$

$$Nu = -\lambda_n\left(Nu_0 + \frac{\varepsilon}{2}\left(Nu_1 e^{(it)} + Nu_2 \mathrm{e}^{(-\mathrm{it})}\right)\right) \tag{2.3.15}$$

where

$$Nu_0 = \eta_1 m_1 \mathrm{e}^{(\eta_1)} + \eta_2 m_2 \mathrm{e}^{(\eta_2)} \tag{2.3.16}$$

$$Nu_1 = \eta_3 m_3 \mathrm{e}^{(\eta_3)} + \eta_4 m_4 \mathrm{e}^{(\eta_4)} \tag{2.3.17}$$

$$Nu_2 = \eta_5 m_5 \mathrm{e}^{(\eta_5)} + \eta_6 m_6 \mathrm{e}^{(\eta_6)} \tag{2.3.18}$$

Sherwood Number Sh at $z = 1$

$$Sh = -\left(\frac{\partial C'}{\partial z}\right)_{z=1} \tag{2.3.19}$$

$$Sh = -\left(Sh_0 + \frac{\varepsilon}{2}\left(Sh_1 e^{(it)} + Sh_2 \mathrm{e}^{(-\mathrm{it})}\right)\right) \tag{2.3.20}$$

where

$$Sh_0 = q_1\zeta_1 \mathrm{e}^{(\mathrm{q}_1)} + q_2\zeta_2 \mathrm{e}^{(\mathrm{q}_2)} + \eta_1 A_{11} e^{(\eta_1)} + \eta_2 A_{12} \mathrm{e}^{(\eta_2)} \tag{2.3.21}$$

$$Sh_1 = q_3\zeta_3 \mathrm{e}^{(\mathrm{q}_3)} + q_4\zeta_4 \mathrm{e}^{(\mathrm{q}_4)} + \eta_3 A_{21} \mathrm{e}^{(\eta_3)} + \eta_4 A_{22} \mathrm{e}^{(\eta_4)} \tag{2.3.22}$$

$$Sh_2 = q_5\zeta_5 \mathrm{e}^{(\mathrm{q}_5)} + q_6\zeta_6 \mathrm{e}^{(\mathrm{q}_6)} + \eta_5 A_{31} \mathrm{e}^{(\eta_5)} + \eta_6 A_{32} \mathrm{e}^{(\eta_6)} \tag{2.3.23}$$

Skin friction Coefficient C_f at $z = 1$

$$Cf = \frac{\phi_2}{Re}\left(\frac{\partial l'}{\partial z}\right)_{z=1} \tag{2.3.24}$$

$$Cf = \frac{\phi_2}{Re}\left(Cf_0 + \frac{\varepsilon}{2}\left(Cf_1 e^{(it)} + Cf_2 e^{(-it)}\right)\right) \tag{2.3.25}$$

where

$$\begin{gathered} Cf_0 = \chi_1 h_1 e^{(\chi_1)} + \chi_2 h_2 e^{(\chi_2)} \quad + \eta_1 D_{12}\mathrm{e}^{(\eta_1)} + \eta_2 D_{13} e^{(\eta_2)} + \\ q_1 D_{14} e^{(q_1)} + q_2\ D_{15}\mathrm{e}^{(\mathrm{q}_2)} + \eta_1 D_{16}\mathrm{e}^{(\eta_1)} + \eta_2 D_{17}\mathrm{e}^{(\eta_2)} \end{gathered} \tag{2.3.26}$$

$$\begin{gathered} Cf_1 = \chi_3 h_3 e^{(\chi_3)} + \chi_4 h_4 \mathrm{e}^{(\chi_4)} \\ + \eta_3 D_{22}\mathrm{e}^{(\eta_3)} + \eta_4 D_{23}\mathrm{e}^{(\eta_4)} + q_3 D_{24}\mathrm{e}^{(\mathrm{q}_3)} + q_4 D_{25}\mathrm{e}^{(\mathrm{q}_4)} + \eta_3 D_{26}\mathrm{e}^{(\eta_3)} + \eta_4 D_{27}\mathrm{e}^{(\eta_4)} \end{gathered} \tag{2.3.27}$$

$$\begin{gathered} Cf_2 = \chi_5 h_5 \mathrm{e}^{(\chi_5)} + \chi_6 h_6 \mathrm{e}^{(\chi_6)} + \eta_5 D_{32}\mathrm{e}^{(\eta_5)} + \eta_6 D_{33}\mathrm{e}^{(\eta_6)} + q_5\ D_{34}\mathrm{e}^{(\mathrm{q}_5)} \\ + q_6 D_{35}\mathrm{e}^{(\mathrm{q}_6)} + \eta_5 D_{36}\mathrm{e}^{(\eta_5)} + \eta_6 D_{37}\mathrm{e}^{(\eta_6)} \end{gathered} \tag{2.3.28}$$

The amplitude (τ_{0r}) and phase difference (β_0) of shear stress at $z = 0$ in the case of steady flow is defined as $\tau_{0r} = \sqrt{\tau_{0x}^2 + \tau_{0y}^2}$ and $\beta_o = \tan^{-1}\left(\frac{\tau_{0y}}{\tau_{0x}}\right)$; where $\left(\frac{\partial l_0'}{\partial z}\right)_{z=0} = \tau_{0x} + i\tau_{0y}$,

$$\left(\frac{\partial l_0'}{\partial z}\right)_{z=0} = \chi_1 h_1 + \chi_2 h_2 \quad + \eta_1 D_{12} + \eta_2 D_{13} + D_{14} q_1 + D_{15} q_2 + D_{16}\eta_1 + D_{17}\eta_2. \tag{2.3.29}$$

The arbitrary constants appearing in the solutions are given in the appendix section. To validate the numerical values, comparison study has been carried out in Table 2.2 and Table 2.3 with previously published papers (P. K. Sharma, Sharma, & Chaudhary, 2007) and (Pal & Talukdar, 2013). The numerical values are found to be in excellent agreement.

2.4 Results and discussion

Fluid profiles for l', θ' and $C'$of ferro-nanofluid are plotted by choosing the following values:

$t = \frac{\pi}{4}, Pr = 6.07,\ \ G_r = 5,\ \ G_m = 5,\ \lambda = 1,\ R = 0.5,\ K_r = 1,\ K_1 = 0.7,\ M = 3,\ \ H = 0.5,\ S_0 = 1,\ S = 3,\ \omega = 10,\ Sc = 0.22,\ \phi = 0.04,\ h = 3,\ \alpha = 45^0,\ \ Re = 10,\ \epsilon = 0.01$

Table 2.2: *Amplitude value of the coefficient, $\frac{\varepsilon}{2}e^{it}$, in the expansion of $\left(\frac{\partial\theta'}{\partial z}\right)_{z=0}$ with $\lambda = 0, R = 0, S = 0, \phi = 0$.*

ω	(P. K. Sharma et al., 2007) $\left\|\left(\frac{\partial\theta_1}{\partial y}\right)_{y=0}\right\|$		Present Study $\left\|\left(\frac{\partial\theta_1'}{\partial z}\right)_{z=0}\right\|$	
	$Pr = 0.71$	$Pr = 7$	$Pr = 0.71$	$Pr = 7$
2	1.144	3.762	1.1438	3.7623
4	1.474	5.293	1.4745	5.2937
6	1.857	6.479	1.8575	6.4794
8	2.228	7.483	2.2289	7.4832
10	2.568	8.366	2.5668	8.3667

Table 2.3: *Comparison of (τ_{0r}) and (β_0) of the steady flow in the absence of Ω^*, with $G_m = 0, R = 0, K_r = 0, K_1 \to \infty, S_0 = 0, S = 0, \phi = 0, \alpha = \pi/2$.*

G_r	M	H	λ	Pr	(Pal & Talukdar, 2013)		Present Study	
					τ_{0r}	β_0	τ_{0r}	β_0
5	2	1	0.5	0.71	1.829935	0.265883	1.829935	0.265883
10	2	1	0.5	0.71	2.167691	0.20624	2.167692	0.20624
5	4	1	0.5	0.71	3.344788	0.370293	3.344789	0.370293
5	2	3	0.5	0.71	1.364854	0.255192	1.364854	0.255192
5	2	1	1	0.71	2.613122	0.142007	2.613122	0.142006
5	2	1	0.5	7	1.907705	0.246677	1.907705	0.246677

Thermophysical properties (Sheikholeslami & Ganji, 2014),(Kumar et al., 2018), (Aminfar, Mohammadpourfard, & Mohseni, 2012) of nanoparticles and base fluid at 25^0 are shown in the Table 2.1. Values of Cf, Nu and Sh are given in Tables 2.4-2.6. The effect of volume fraction and non-dimensional parameters has been studied using spherical shape Fe_3O_4 nano particles.

Figures 2.2 to 2.4 illustrate the impact of ϕ on l', θ' and C' profiles. It is understood from the plots that l' and θ'diminishes with increase in ϕ while concentration

increases. Figures 2.5 to 2.16 display the hold of diverse non-dimensional parameters on θ', l' and C' profiles. These profiles have been drawn according to the variation in z. The l' profile increases with rise in Hall current parameter (Figure 2.5) but velocity is diminishing with rise in M (Figure 2.6). The movement of ferro-nanofluid perpendicular to B_0 induces a Lorentz force against the fluid flow which retards the fluid velocity. Also, B_0 induces a Hall current which acts in the direction of the fluid flow and thus it accelerates the fluid velocity.

Concentration of ferro-nanofluid with variation in chemical reaction parameter is depicted in figures 2.7 and 2.8. The sign of chemical reaction parameter determines whether the chemical reaction is destructive or constructive (Sarma & Pandit, 2018). As $K_r(K_r > 0)$ increases, a destructive chemical reaction enhances and thus concentration of the nanofluid decreases. As K_r $(K_r < 0)$ decreases, a constructive chemical reaction enhances and hence concentration increases.

The profiles for l', θ' and C' of ferro-nanofluid with changes in heat source parameter are illustrated in the figures 2.9 to 2.11. A rise in S enhances the fluid temperature and increases the kinetic energy level in molecules of nanofluid. Consequently, l' of the ferro-nanofluid goes up and C' comes down.

l' *and* θ' profiles of the ferro-nanofluid with variation in injection/suction parameter are shown in figures 2.12 and 2.13. l' *and* θ' of the nanofluid near the oscillatory plate increases with increasing injection/suction parameter. As λ $(\lambda > 0)$ increases, heated fluid particles enter into the channel and cold fluid particles disappear from the channel increasing the velocity and temperature inside the channel. The process is reversed in the case λ $(\lambda < 0)$. Concentration profile of ferro- nanofluid with variation in Soret number is depicted in figure 2.14. Concentration decreases due to the increase in S_0. A step up in S_0 indicates the enhancement in $\theta^{'}$ difference and therefore C' is diminished. Figure 2.15 reveals that velocity of ferro-nanofluid increases with rise in α. This is due to the effect of increased gravitational force. Figure 2.16 depicts the level of enhancement in velocity profile with increasing porosity parameter.

Table 2.4: *The Skin friction of Fe_3O_4-water nanofluid when $t = \frac{\pi}{4}, Pr = 6.07, K_r = 1.5,\ K_1 = 0.7,\ \ M = 3.5, S_0 = 0.5, \omega = 20, Sc = 0.22, \alpha = \frac{\pi}{4}, Re = 10$.*

ϕ	H	G_m	S	R	G_r	λ	$-Cf$	Enhancement(%)
0.05	1.5	5	2	0.5	5	1.4	0.203108111	
0.0525	1.5	5	2	0.5	5	1.4	0.201751152	-0.668
0.055	1.5	5	2	0.5	5	1.4	0.200389459	-0.675
0.0575	1.5	5	2	0.5	5	1.4	0.199023038	-0.682
0.06	1.5	5	2	0.5	5	1.4	0.197651889	-0.689
Slope							-0.54562232	
0.04	1	5	2	0.5	5	1.4	0.189942907	
0.04	1.125	5	2	0.5	5	1.4	0.194262629	2.274
0.04	1.25	5	2	0.5	5	1.4	0.198388724	2.124
0.04	1.375	5	2	0.5	5	1.4	0.202275413	1.959
0.04	1.5	5	2	0.5	5	1.4	0.20589929	1.792
Slope							0.03194044	
0.04	1.5	3	2	0.5	5	1.4	0.177751404	
0.04	1.5	3.5	2	0.5	5	1.4	0.184788376	3.959
0.04	1.5	4	2	0.5	5	1.4	0.191825347	3.808
0.04	1.5	4.5	2	0.5	5	1.4	0.198862319	3.668
0.04	1.5	5	2	0.5	5	1.4	0.20589929	3.539
Slope							0.014073943	
0.04	1.5	5	2.5	0.5	5	1.4	0.214495149	
0.04	1.5	5	2.625	0.5	5	1.4	0.216330949	0.856
0.04	1.5	5	2.75	0.5	5	1.4	0.218190236	0.859
0.04	1.5	5	2.875	0.5	5	1.4	0.220073412	0.863
0.04	1.5	5	3	0.5	5	1.4	0.221980887	0.867
Slope							0.014971151	
0.04	1.5	5	2	0.1	5	1.4	0.22571289	
0.04	1.5	5	2	0.125	5	1.4	0.225624356	-0.039
0.04	1.5	5	2	0.15	5	1.4	0.225516217	-0.048
0.04	1.5	5	2	0.175	5	1.4	0.225388517	-0.057
0.04	1.5	5	2	0.2	5	1.4	0.225241303	-0.065
Slope							-0.004716052	
0.04	1.5	5	2	0.5	3	1.4	0.126386072	
0.04	1.5	5	2	0.5	3.5	1.4	0.15109988	19.554
0.04	1.5	5	2	0.5	4	1.4	0.175813688	16.356
0.04	1.5	5	2	0.5	4.5	1.4	0.200527496	14.057
0.04	1.5	5	2	0.5	5	1.4	0.225241303	12.324
Slope							0.049427616	
0.04	1.5	5	2	0.5	5	1	0.061783952	
0.04	1.5	5	2	0.5	5	1.1	0.092068285	49.017
0.04	1.5	5	2	0.5	5	1.2	0.126548023	37.45
0.04	1.5	5	2	0.5	5	1.3	0.165346706	30.659
0.04	1.5	5	2	0.5	5	1.4	0.208586679	26.151
Slope							0.366883875	

Table 2.5: *The Nusselt number of Fe_3O_4-water nanofluid when $t = \frac{\pi}{4}, Pr = 6.07,\ G_r = 5,\quad G_m = 5,\quad K_r = 1.5,\quad K_1 = 0.7,\ M = 3.5, H = 1.5,\ S_0 = 0.5,\ \omega = 20,\quad Sc = 0.22, \alpha = \frac{\pi}{4},\ Re = 10.$*

ϕ	S	R	λ	Nu	Enhancement(%)
0.05	2	0.5	1.4	10.47453	
0.0525	2	0.5	1.4	10.46772	-0.065
0.055	2	0.5	1.4	10.4609	-0.065
0.0575	2	0.5	1.4	10.45407	-0.065
0.06	2	0.5	1.4	10.44724	-0.065
Slope				-2.72878	
0.04	2.8	0.5	1.4	11.1924	
0.04	2.85	0.5	1.4	11.24113	0.435
0.04	2.9	0.5	1.4	11.29012	0.436
0.04	2.95	0.5	1.4	11.33938	0.436
0.04	3	0.5	1.4	11.3889	0.437
Slope				0.982513	
0.04	2	0.1	1.4	11.6304	
0.04	2	0.125	1.4	11.62467	-0.049
0.04	2	0.15	1.4	11.61767	-0.06
0.04	2	0.175	1.4	11.6094	-0.071
0.04	2	0.2	1.4	11.59987	-0.082
Slope				-0.30535	
0.04	2	0.5	1	8.354338	
0.04	2	0.5	1.1	9.018292	7.947
0.04	2	0.5	1.2	9.673948	7.27
0.04	2	0.5	1.3	10.32214	6.7
0.04	2	0.5	1.4	10.96381	6.216
Slope				6.5228	

2.4.1 Statistical analysis

The impact of different parameters on Cf, Nu and Sh (z = 1) are established using r_c (Correlation coefficient) and PE (Probable error) described in the tables 2.7 to 2.9. The sign of r_c determines the nature of relationship and the magnitude of r_c indicates the intensity of relationship (Mackolil & Mahanthesh, 2019). The significance in the precision of correlation coefficient is verified using PE of r_c and the correlation is said to be significant if $|r_c| > 6.|PE|$ (Fisher et al., 1921) Probable error is calculated using the formula, PE = $(\ \frac{1-{r_c}^2}{\sqrt{\tilde{n}}})$ 0.6745; where $\tilde{n}$ is the number of observations. From Table 2.7, it is observed that Cf has high positive correlation with ϕ and R and high negative correlation with H, G_m, S, G_r and λ. All the values

p

Table 2.6: *The Sherwood number of Fe_3O_4-water nanofluid when $Pr = 6.07, G_r = 5,\ G_m = 5,\ K_1 = 0.7,\ M = 3.5,\ H = 1.5,\ S = 2, Sc = 0.22,\ \alpha = \frac{\pi}{4}$.*

ϕ	R	S_0	λ	ω	t	K_r	Sh	Enhancement(%)
0.05	0.5	0.5	1.4	20	0.785	1	0.21135492	
0.0525	0.5	0.5	1.4	20	0.785	1	0.21771996	3.012
0.055	0.5	0.5	1.4	20	0.785	1	0.22403398	2.9
0.0575	0.5	0.5	1.4	20	0.785	1	0.23029753	2.796
0.06	0.5	0.5	1.4	20	0.785	1	0.23651114	2.698
Slope							2.51559988	
0.04	0.1	0.5	1.4	20	0.785	1	0.12563614	
0.04	0.125	0.5	1.4	20	0.785	1	0.12617555	0.429
0.04	0.15	0.5	1.4	20	0.785	1	0.12683434	0.522
0.04	0.175	0.5	1.4	20	0.785	1	0.12761224	0.613
0.04	0.2	0.5	1.4	20	0.785	1	0.1285089	0.703
Slope							0.02872886	
0.04	0.5	0.1	1.4	20	0.785	1	0.86984265	
0.04	0.5	0.2	1.4	20	0.785	1	0.68450921	-21.307
0.04	0.5	0.3	1.4	20	0.785	1	0.49917578	-27.075
0.04	0.5	0.4	1.4	20	0.785	1	0.31384234	-37.128
0.04	0.5	0.5	1.4	20	0.785	1	0.1285089	-59.053
Slope							-1.85333436	
0.04	0.5	0.5	1	20	0.785	1	0.38038438	
0.04	0.5	0.5	1.1	20	0.785	1	0.31760915	-16.503
0.04	0.5	0.5	1.2	20	0.785	1	0.25475175	-19.791
0.04	0.5	0.5	1.3	20	0.785	1	0.19174312	-24.733
0.04	0.5	0.5	1.4	20	0.785	1	0.1285089	-32.979
Slope							-0.62961697	
0.04	0.5	0.5	1.4	25	0.785	1	0.1281293	
0.04	0.5	0.5	1.4	25.25	0.785	1	0.12810759	-0.017
0.04	0.5	0.5	1.4	25.5	0.785	1	0.12808535	-0.017
0.04	0.5	0.5	1.4	25.75	0.785	1	0.12806256	-0.018
0.04	0.5	0.5	1.4	26	0.785	1	0.12803922	-0.018
Slope							-9.01E-05	
0.04	0.5	0.5	1.4	20	1	1	0.12798591	
0.04	0.5	0.5	1.4	20	1.125	1	0.12774596	-0.187
0.04	0.5	0.5	1.4	20	1.25	1	0.12735648	-0.305
0.04	0.5	0.5	1.4	20	1.375	1	0.12682355	-0.418
0.04	0.5	0.5	1.4	20	1.5	1	0.12615547	-0.527
Slope							-0.00366663	
0.04	0.5	0.5	1.4	20	0.785	0.5	0.1888454	
0.04	0.5	0.5	1.4	20	0.785	0.625	0.18065067	-4.339
0.04	0.5	0.5	1.4	20	0.785	0.75	0.17256179	-4.478
0.04	0.5	0.5	1.4	20	0.785	0.875	0.16457699	-4.627
0.04	0.5	0.5	1.4	20	0.785	1	0.15669457	-4.79
Slope							-0.06430027	

p

Table 2.7: *Correlation coefficient (r_c), Probable error (PE) and $|\frac{r_c}{PE}|$ values of Cf with respect to the parameters ϕ, H, G_m , S, R, G_r and λ*

Parameter	r_c	PE	$\lvert\frac{r_c}{PE}\rvert$
ϕ	0.999997896	1.27E-06	787896.2218
H	-0.99940294	0.000360093	2775.399238
G_m	-1	0	Inf
S	-0.999971478	1.72E-05	58114.63519
R	0.995217965	0.002878061	345.7945854
G_r	-1	1.34E-16	7.47E+15
λ	-0.997583808	0.001455906	685.1977823

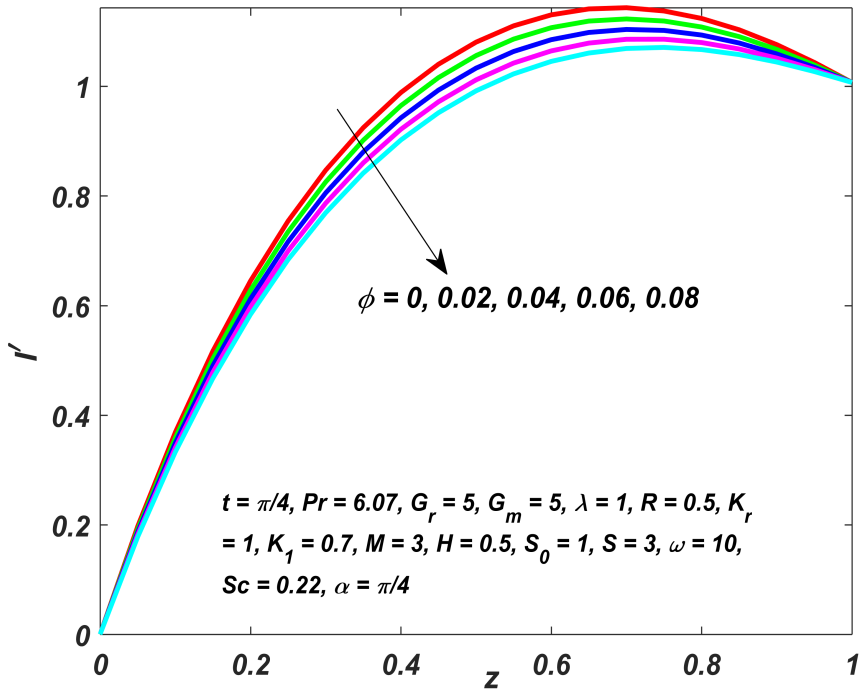

Figure 2.2: *Variations in Velocity l' with ϕ*

of $\left|\frac{r_c}{PE}\right|$ for Cf are greater than 6 meaning that the parameters described in the table are significant. Table 2.8 proposes that Nu is highly negatively correlated with ϕ and R and positively correlated with S and λ. From table 2.9, it can be inferred that Sh is highly positively correlated with ϕ and R and highly negatively correlated with S_0, λ, ω, t and K_r .

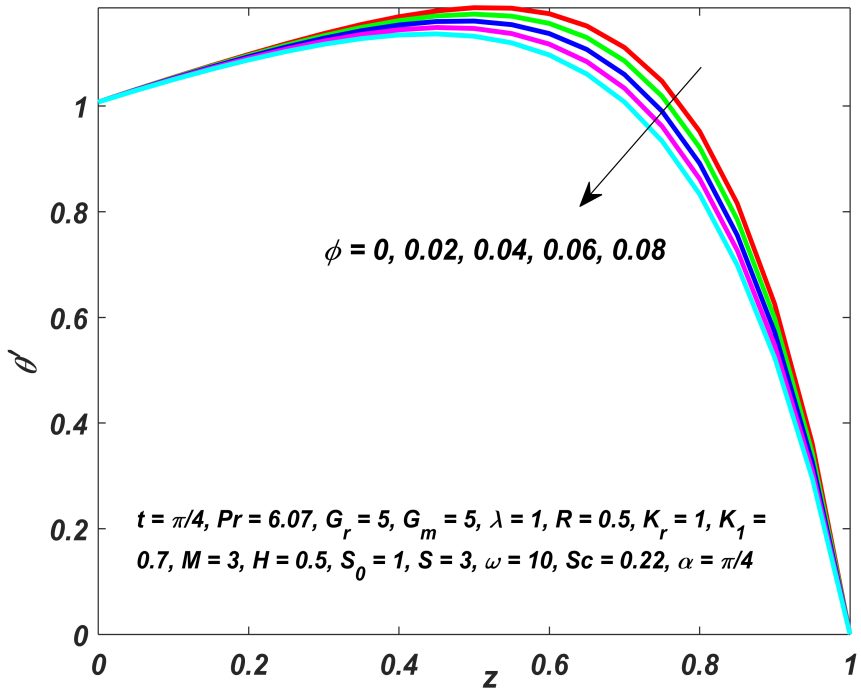

Figure 2.3: *Variations in temperature θ' with ϕ*

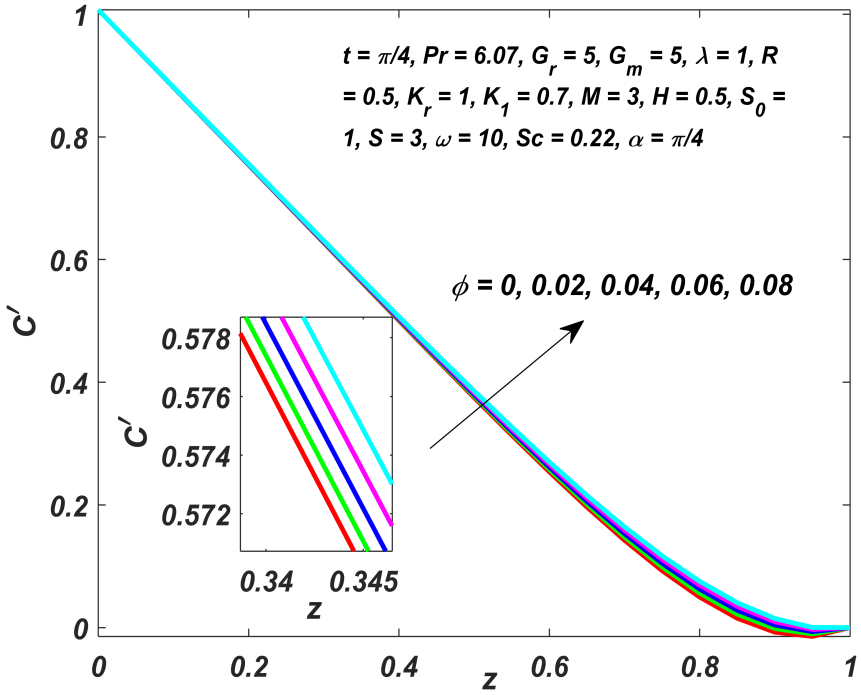

Figure 2.4: *Variations in concentration C' with ϕ*

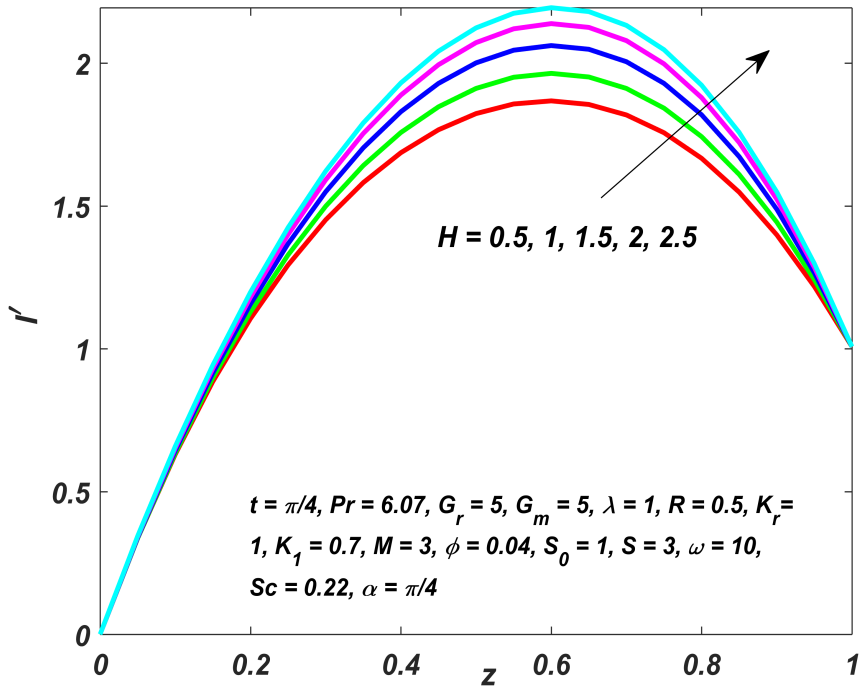

Figure 2.5: *Variations in velocity l' with H*

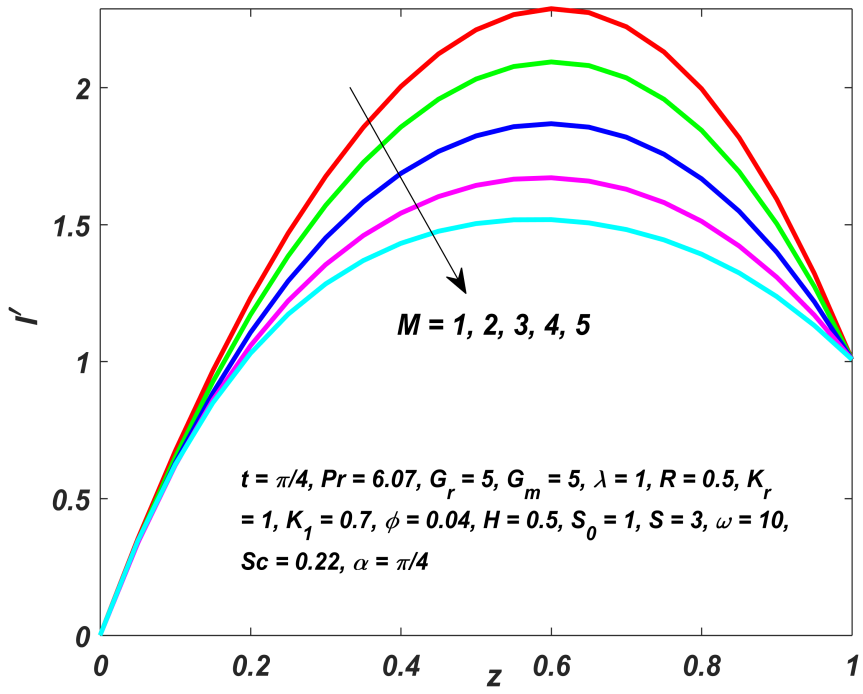

Figure 2.6: *Variations in velocity l' with M*

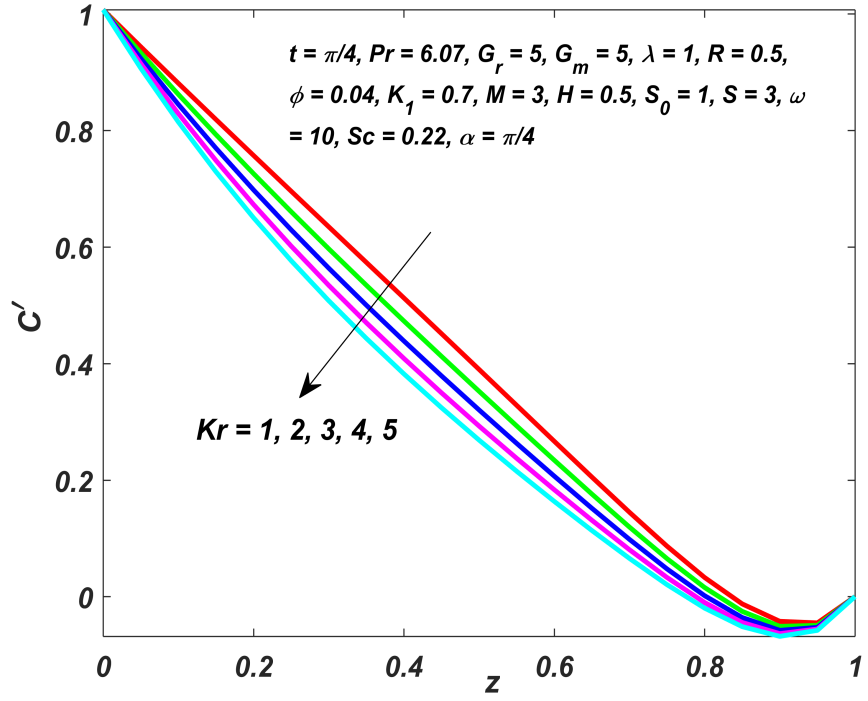

Figure 2.7: *Variations in concentration* C' *with* $K_r > 0$

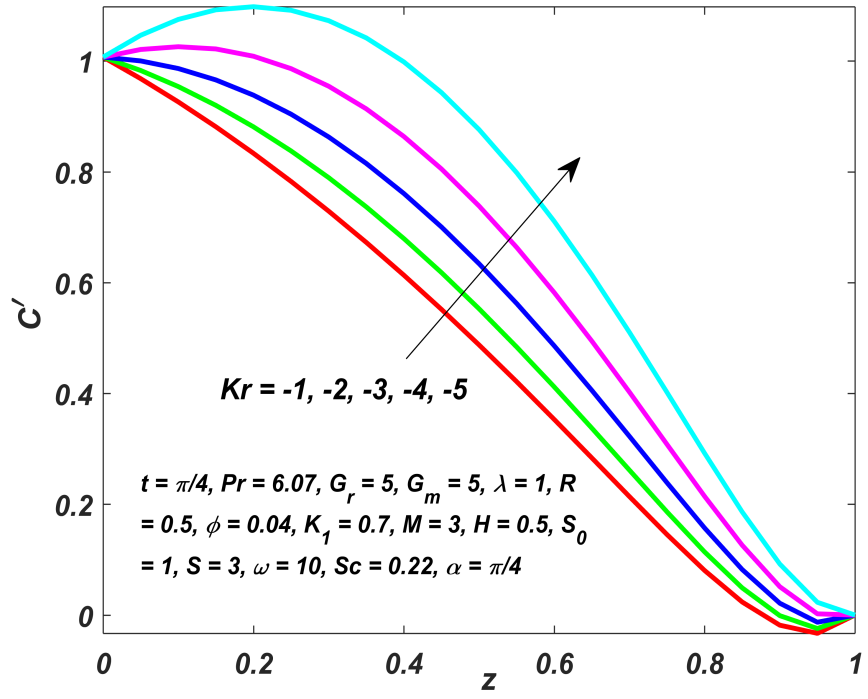

Figure 2.8: *Variations in concentration* C' *with* $(K_r < 0)$

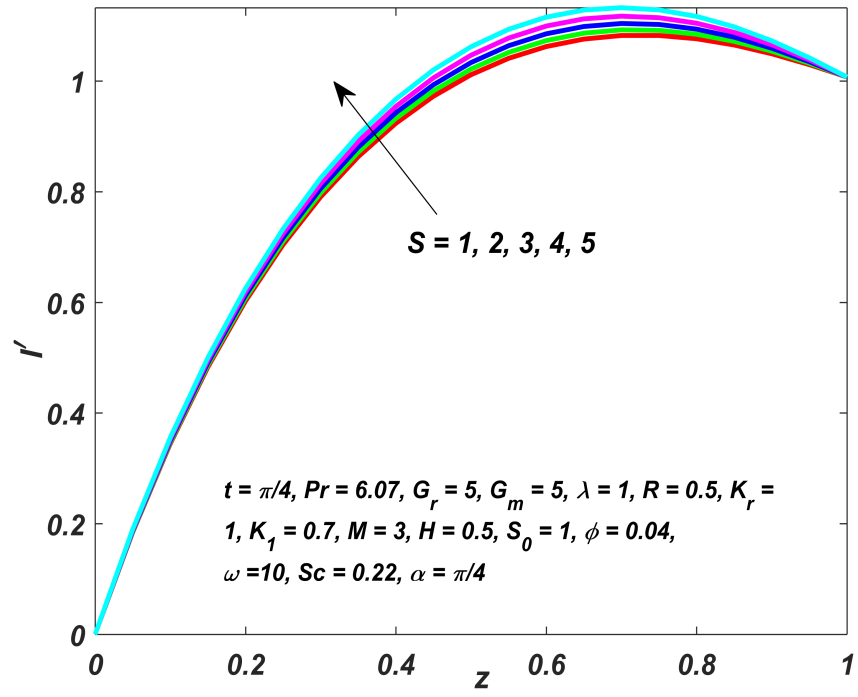

Figure 2.9: *Variations in velocity l' with S*

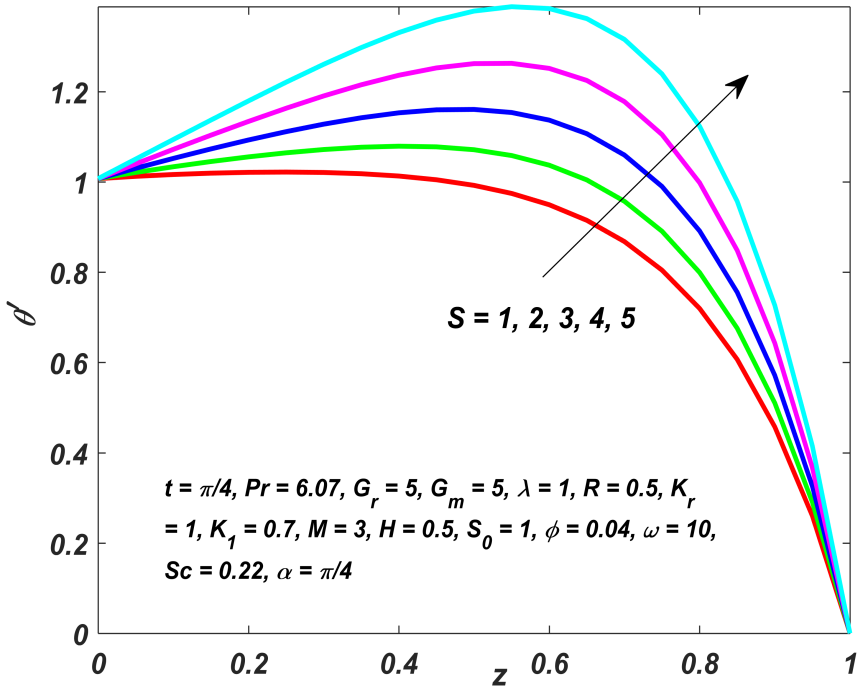

Figure 2.10: *Variations in temperature$\theta'$with S*

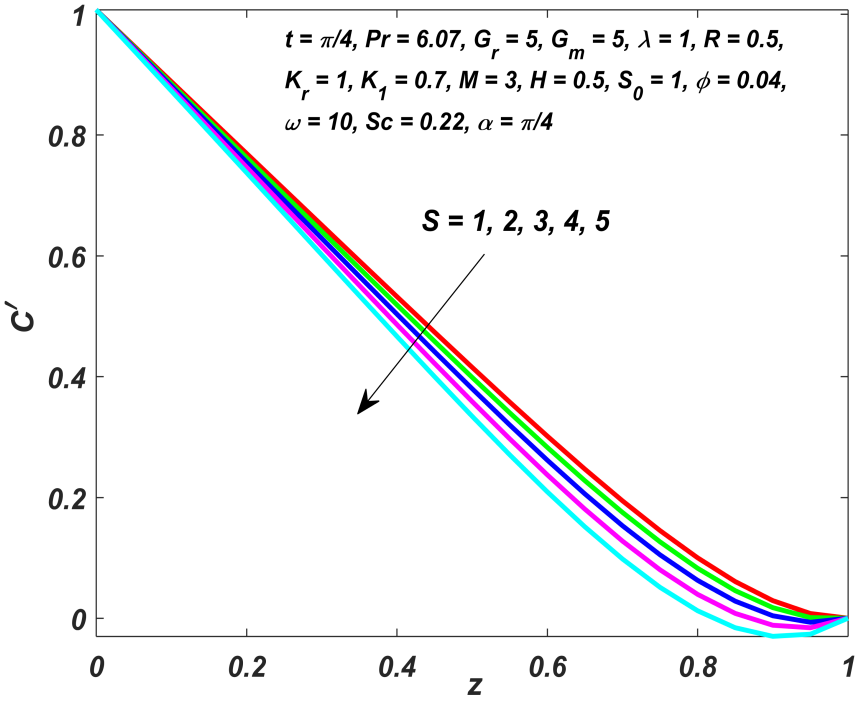

Figure 2.11: *Variations in concentration C' with S*

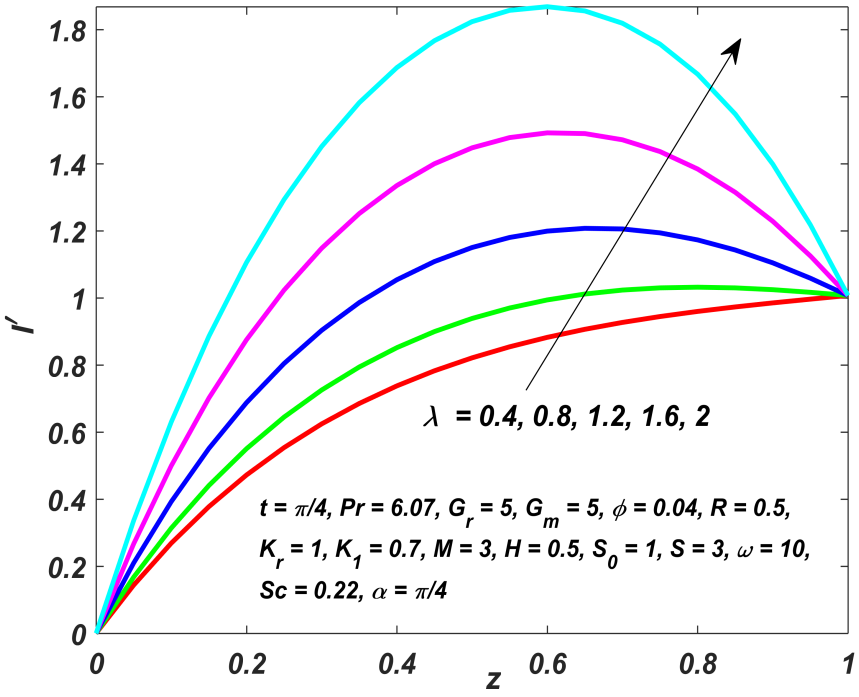

Figure 2.12: *Variations in velocity l' with λ*

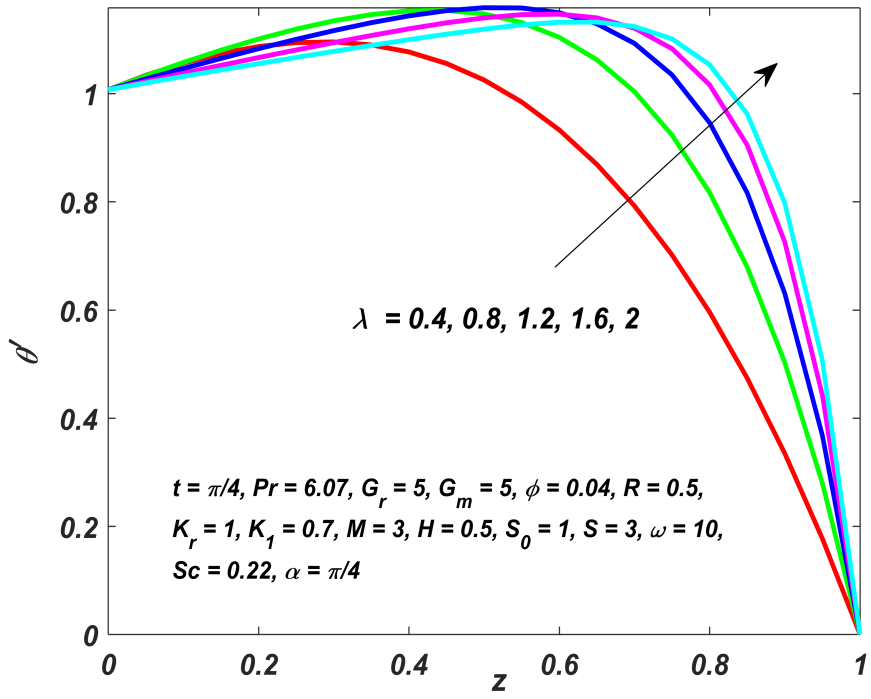

Figure 2.13: *Variations in temperature θ' with λ*

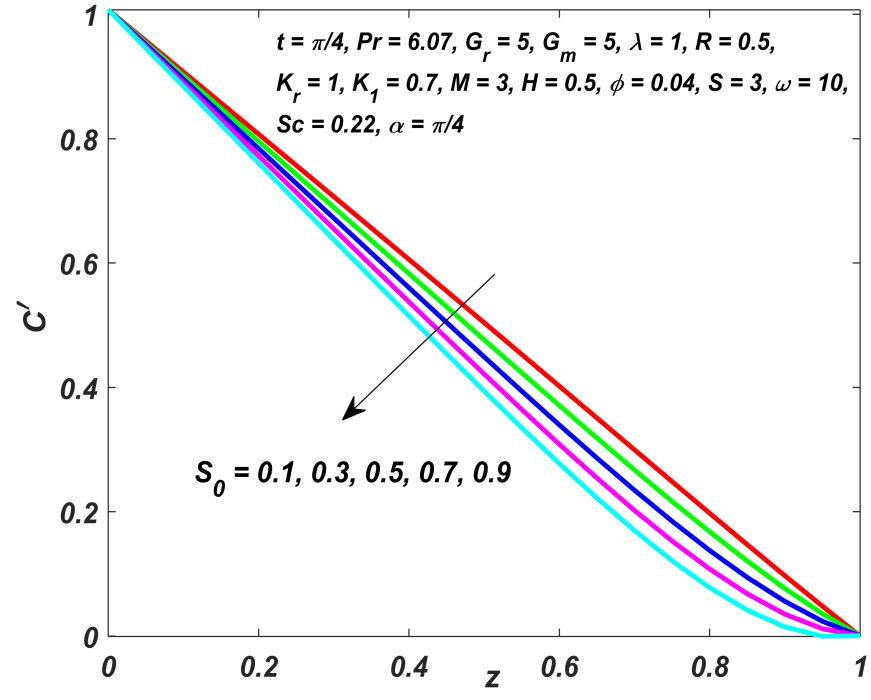

Figure 2.14: *Variations in concentration C' with S_0*

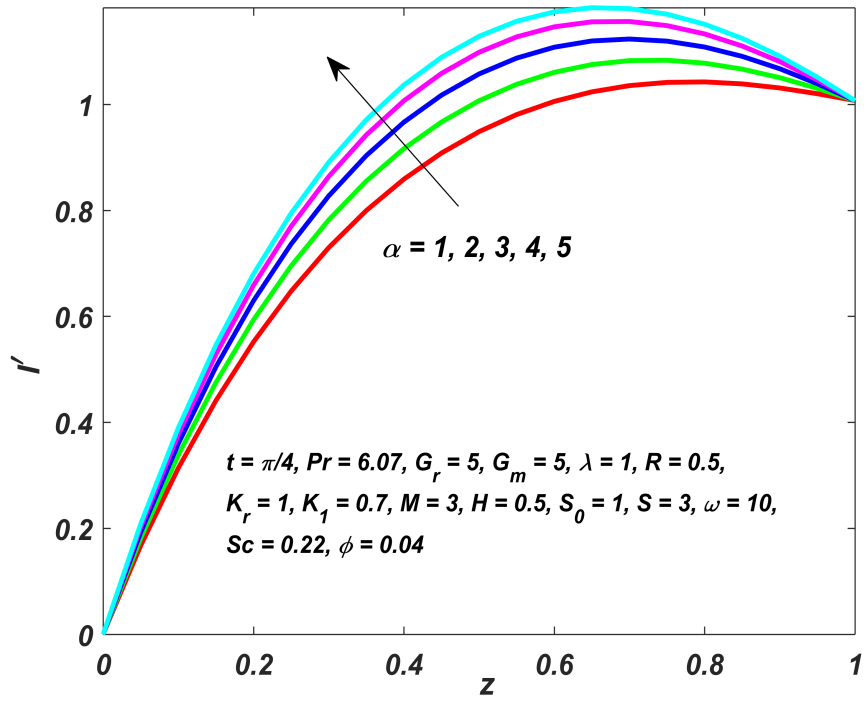

Figure 2.15: *Variations in velocity l' with α*

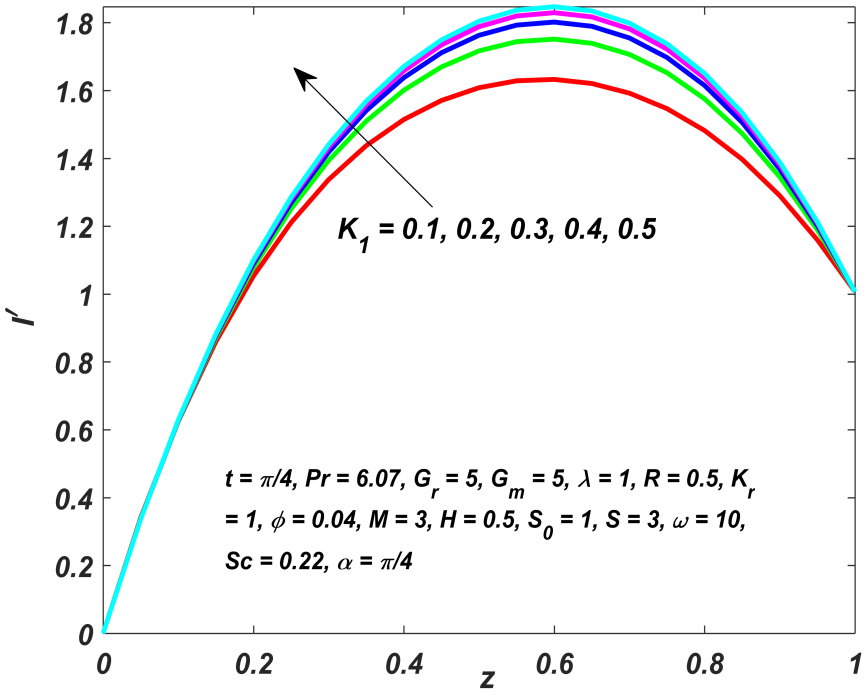

Figure 2.16: *Variations in velocity l' with K_1*

Table 2.8: *Correlation coefficient (r_c), Probable error (PE) and $|\frac{r_c}{PE}|$ values of Nu with respect to the parameters ϕ, S, R and λ*

parameter	r_c	PE	$\lvert\frac{r_c}{PE}\rvert$.
ϕ	-0.999999812	1.13E-07	8835395.319
S	0.999994883	3.09E-06	323962.1929
R	-0.995220189	0.002876726	345.9558435
λ	0.999977238	1.37E-05	72822.19318

Table 2.9: *Correlation coefficient (r_c), Probable error (PE) and $|\frac{r_c}{PE}|$ values of Sh with respect to the parameters $\phi, R, S_0, \lambda, \omega, t$ and K_r*

parameter	r_c	PE	$\left\lvert\frac{r_c}{PE}\right\rvert$
ϕ	0.999988727	6.80E-06	147044.3608
R	0.995223125	0.002874963	346.1690028
S_0	-1	0	Inf
λ	-0.999998944	6.37E-07	1569871.63
ω	-0.999897527	6.18E-05	16174.89232
t	-0.983424825	0.009916783	99.16772636
K_r	-0.999970646	1.77E-05	56468.14162

2.4.2 Regression analysis

Regression analysis is a statistical modelling technique used to establish a relationship between a dependent and one or more independent variables. Tables 2.7 to 2.9 reflect the nature of relationship with single variable whereas in regression analysis the quantity of relationship is obtained with more than one independent variable. $Cf,\ Nu$ and Sh are estimated using multiple linear regression models given by the form:

$$Cf_{est} = c + b_\phi\ \phi + b_H H + b_{G_m} G_m + b_S\ S + b_R\ R + b_{Gr} G_r + b_\lambda\ \lambda \tag{2.4.1}$$

$$Nu_{est} = c + b_\phi\ \phi + b_S\ S + b_R R + b_\lambda\ \lambda \tag{2.4.2}$$

$$Sh_{est} = c + b_\phi\ \phi + b_R\ R + b_{S_0} S_0 + b_\lambda \lambda + b_\omega\ \omega + b_t\ t + b_{K_r} K_r \tag{2.4.3}$$

where $c, b_\phi, b_H, b_{G_m}\ , b_S, b_R, b_{G_r}, b_\lambda, b_{S_0}, b_\omega, b_t$ and b_{K_r} are the estimated regression coefficients. These values are estimated from the table (2.4-2.6) values using MATLAB

software. It can be noted from tables 2.10-2.12 that all Sig. value < 0.05 (p Value) proving that the calculated regression coefficients are significant. From tables 2.10 to 2.12 it is observed that the R-squared values are approximately equal to 1 and also error is negligibly small (close to 0) meaning that the test is effective. The estimated Cf, Nu and Sh are:

Table 2.10: *Linear regression model for Cf, with Number of observations :35, Error degrees of freedom:27, Root mean square error :0.00461, $\mathcal{R}$-squared:0.989, Adjusted $\mathcal{R}$-Squared 0.986, F-statistic vs. constant model:332, p-value =1.7e-24*

Variables	Estimate	SE	tStat	p Value
Intercept	0.652031	0.027974	23.31551	2.02E-19
ϕ	0.654027	0.171889	3.804932	0.00074
H	-0.043	0.008129	-5.28944	1.40E-05
G_m	-0.017	0.002032	-8.36414	5.65E-09
S	-0.0108	0.003438	-3.14246	0.004041
R	0.043069	0.007597	5.669406	5.08E-06
G_r	-0.03946	0.002032	-1.4154	2.16E-17
λ	-0.38702	0.010161	-38.0881	5.25E-25

Table 2.11: *Linear regression model for Nu with number of observations :20, Error degrees of freedom:15, mean square error :0.0713, $\mathcal{R}$-squared: 0.995, Adjusted $\mathcal{R}$- Squared 0.994, F-statistic vs. constant model:773, p-value =3.59e-17*

Variables	Estimate	SE	tStat	p Value
Intercept	3.350136	0.217599	15.39591	1.34E-10
ϕ	-28.7968	3.787674	-7.60277	1.60E-06
S	0.42104	0.065763	6.402399	1.19E-05
R	-1.98807	0.168527	-11.7967	5.46E-09
λ	6.334471	0.212077	29.86876	8.87E-15

$$Cf_{est} = 0.652231 + 0.654027\ \phi - 0.043\ H - 0.017\ G_m - 0.0108\ S + 0.043069\ R - 0.03946\ G_r - 0.38702\ \lambda \tag{2.4.4}$$

$$Nu_{est} = 3.350136 - 28.7968\ \phi + 0.42104\ S - 1.98807\ R + 6.334471\ \lambda \tag{2.4.5}$$

$$Sh_{est} = 1.812674 + 5.495754\ \phi + 0.034541\ R - 1.818151\ S_0 - 0.594991\lambda \\ -0.001988\ \omega - 0.022729\ t - 0.111039\ K_r \tag{2.4.6}$$

It is understood from the regression equations that H, G_m, S, G_r and λ have a negative impact on Cf whereas R and ϕ has a positive impact on Cf. The mounting values of R and ϕ creates a significant increase in the values of Cf while it reverses in the case of negatively impacted parameters.These results coincide with the results described in table 2.7. Enhancing the value of ϕ and R diminishes the value of Nu while an increase in S and λ increases the value of Nu. These results are in perfect synchronization with the observations in Table 2.8. Similarly, from the regression equation for Sh, it is understood that ϕ and R have a positive impact on Sh whereas S_0, λ, ω, t and K_r have a negative impact on Sh. This is in agreement with the findings in Table 2.9. Figures 2.17 -2.19 illustrates the accuracy of the regression model for the chosen sample. A commendable agreement is noted between the numerically calculated values and regression values.

Table 2.12: *Linear regression model for Sh, Number of observations :35, Error degrees of freedom:27, Root mean square error :0.00753, $\mathcal{R}$-squared:0.998, Adjusted $\mathcal{R}$-Squared 0.998, F-statistic vs. constant model:2.31e+03, p-value =8.37e-36*

Variables	Estimate	SE	tStat	p value
Intercept	1.812674817	0.02908886	62.31508568	1.03E-30
ϕ	5.495754491	0.292700432	18.77603823	5.02E-17
R	0.034541513	0.012949556	2.667389769	0.012762683
S_0	-1.818151624	0.017165431	-105.9193681	6.57E-37
λ	-0.594991434	0.017165431	-34.66218983	6.36E-24
ω	-0.001988324	0.000827683	-2.402277412	0.023439152
t	-0.022729364	0.00891019	-2.550940334	0.01672498
K_r	-0.111039183	0.013732345	-8.08595936	1.09E-08

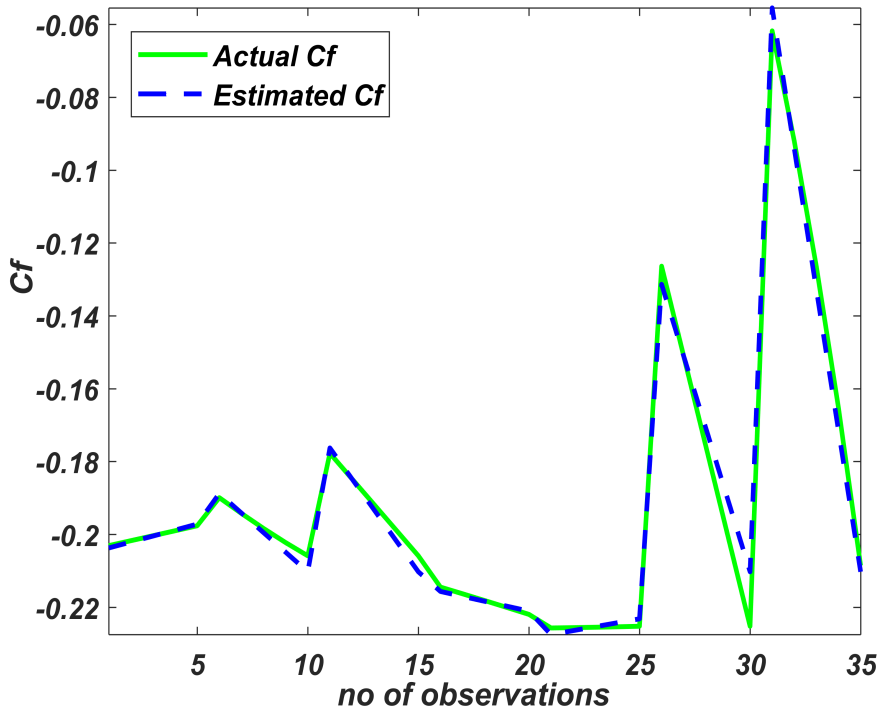

Figure 2.17: *Actual and estimated values of Cf*

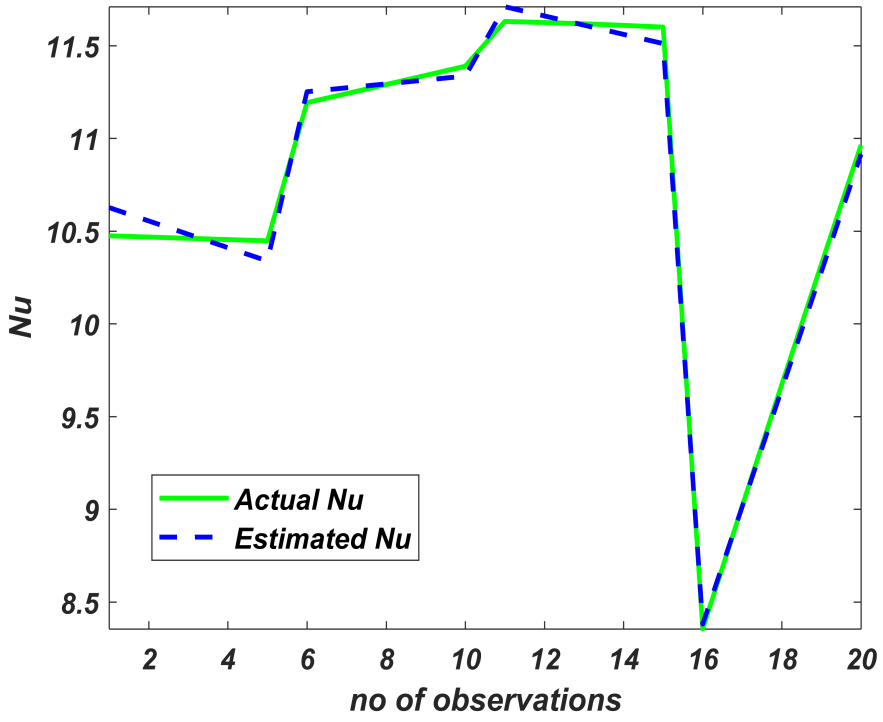

Figure 2.18: *Actual and estimated values of Nu*

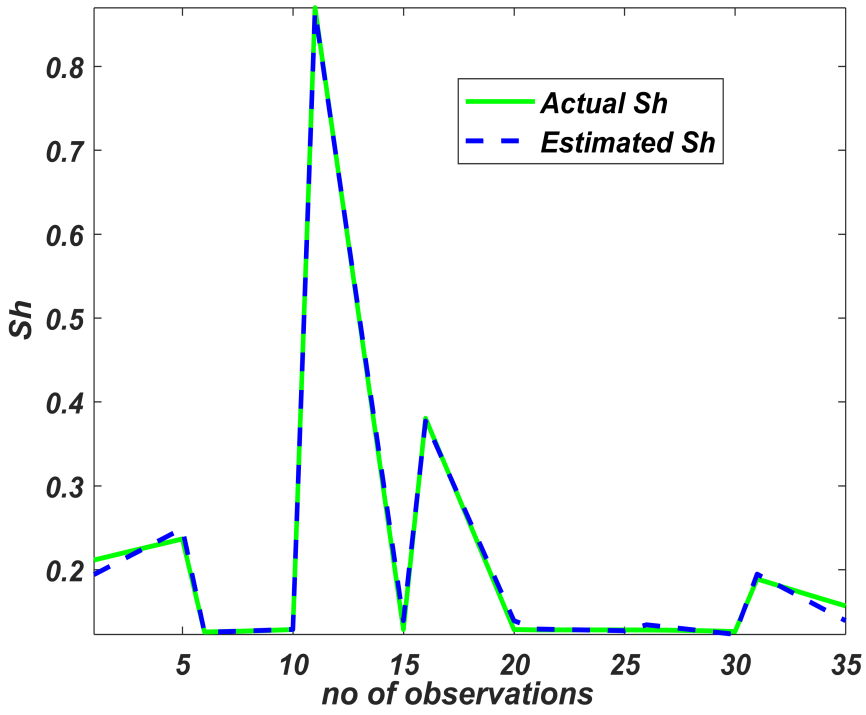

Figure 2.19: *Actual and estimated values of Sh*

2.5 Conclusions

The influence of heat source and hall current on magneto-hydrodynamic ferro-nanoflow in an inclined porous channel with radiation and chemical reaction has been theoretically analysed. The major conclusions drawn from the current analysis are given below:

- Hall current and injection/suction parameter play a crucial role in amplifying the velocity profile.
- The temperature and velocity profiles are directly proportional to the heat source parameter, S.
- Angle of inclination, α has a constructive effect on the velocity profiles.
- The volume fraction of the nanoparticles, ϕ enhances the concentration profiles but reduces the temperature and velocity profiles.
- Increase in Hartmann number accounts for a reduction in velocity profile.
- The Soret effect has a destructive impact on concentration profiles.

- Heat source and hall current has a negative impact on skin friction.

- An increase of 0.982513 per unit S (heat source) is noted due to the impact of heat source on Nusselt number.

- Soret number has a negative impact (a decrease of 1.853334359 per unit S_o) on Sherwood number.

Our future aim is to extend the present study by incorporating viscous dissipation, Joule heating and entropy generations which are decisive in heat and mass transfer rates.

2.6 Appendix

$$\eta_1 = \frac{\phi_4\lambda + \sqrt{(\phi_4\lambda)^2 - 4\lambda_n \frac{(-R^2+S)}{(P_r)^2}}}{2\left(\frac{\lambda_n}{P_r}\right)} \tag{2.6.1}$$

$$\eta_2 = \frac{\phi_4\lambda - \sqrt{(\phi_4\lambda)^2 - 4\lambda_n \frac{(-R^2+S)}{(P_r)^2}}}{2\left(\frac{\lambda_n}{P_r}\right)} \tag{2.6.2}$$

$$\eta_3 = \frac{\phi_4\lambda + \sqrt{(\phi_4\lambda)^2 - 4\frac{\lambda_n}{P_r}\left(\frac{S}{P_r} - \frac{R^2}{P_r} - \omega i\phi_4\right)}}{2\left(\frac{\lambda_n}{P_r}\right)} \tag{2.6.3}$$

$$\eta_4 = \frac{\phi_4\lambda - \sqrt{(\phi_4\lambda)^2 - 4\frac{\lambda_n}{P_r}\left(\frac{S}{P_r} - \frac{R^2}{P_r} - \omega i\phi_4\right)}}{2\left(\frac{\lambda_n}{P_r}\right)} \tag{2.6.4}$$

$$\eta_5 = \frac{\phi_4\lambda + \sqrt{(\phi_4\lambda)^2 - 4\frac{\lambda_n}{P_r}\left(\frac{S}{P_r} - \frac{R^2}{P_r} + \omega i\phi_4\right)}}{2\left(\frac{\lambda_n}{P_r}\right)} \tag{2.6.5}$$

$$\eta_6 = \frac{\phi_4\lambda - \sqrt{(\phi_4\lambda)^2 - 4\frac{\lambda_n}{P_r}\left(\frac{S}{P_r} - \frac{R^2}{P_r} + \omega i\phi_4\right)}}{2\left(\frac{\lambda_n}{P_r}\right)} \tag{2.6.6}$$

$$q_1 = \frac{\lambda + \sqrt{\lambda^2 + 4K_r\frac{\lambda^2}{S_c}}}{\frac{2}{S_c}} \tag{2.6.7}$$

$$q_2 = \frac{\lambda - \sqrt{\lambda^2 + 4K_r\frac{\lambda^2}{S_c}}}{\frac{2}{S_c}} \tag{2.6.8}$$

$$q_3 = \frac{\lambda + \sqrt{\lambda^2 + \frac{4}{S_c}\left(K_r\lambda^2 + \omega i\right)}}{\frac{2}{S_c}} \tag{2.6.9}$$

$$q_4 = \frac{\lambda - \sqrt{\lambda^2 + \frac{4}{S_c}\left(K_r\lambda^2 + \omega i\right)}}{\frac{2}{S_c}} \tag{2.6.10}$$

$$q_5 = \frac{\lambda + \sqrt{\lambda^2 + \frac{4}{S_c}\left(K_r\lambda^2 - \omega i\right)}}{\frac{2}{S_c}} \tag{2.6.11}$$

$$q_6 = \frac{\lambda - \sqrt{\lambda^2 + \frac{4}{S_c}\left(K_r\lambda^2 - \omega i\right)}}{\frac{2}{S_c}} \tag{2.6.12}$$

$$\chi_1 = \frac{\phi_1\lambda + \sqrt{\left(\phi_1\lambda\right)^2 + 4\phi_2 p'}}{2\phi_2} \tag{2.6.13}$$

$$\chi_2 = \frac{\phi_1\lambda - \sqrt{\left(\phi_1\lambda\right)^2 + 4\phi_2 p'}}{2\phi_2} \tag{2.6.14}$$

$$\chi_3 = \frac{\phi_1\lambda + \sqrt{\left(\phi_1\lambda\right)^2 + 4\phi_2 q'}}{2\phi_2} \tag{2.6.15}$$

$$\chi_4 = \frac{\phi_1\lambda - \sqrt{\left(\phi_1\lambda\right)^2 + 4\phi_2 q'}}{2\phi_2} \tag{2.6.16}$$

$$\chi_5 = \frac{\phi_1\lambda + \sqrt{\left(\phi_1\lambda\right)^2 + 4\phi_2 r'}}{2\phi_2} \tag{2.6.17}$$

$$\chi_6 = \frac{\phi_1\lambda - \sqrt{\left(\phi_1\lambda\right)^2 + 4\phi_2 r'}}{2\phi_2} \tag{2.6.18}$$

$$A_{11} = \frac{-S_0(\eta_1)^2 m_1}{\frac{1}{S_c}(\eta_1)^2 - \lambda\eta_1 - K_r\lambda^2} \tag{2.6.19}$$

$$A_{12} = \frac{-S_0(\eta_2)^2 m_2}{\frac{1}{S_c}(\eta_2)^2 - \lambda\eta_2 - K_r\lambda^2} \tag{2.6.20}$$

$$A_{21} = \frac{-S_0(\eta_3)^2 m_3}{\frac{1}{S_c}(\eta_3)^2 - \lambda\eta_3 - \left(K_r\lambda^2 + \omega i\right)} \tag{2.6.21}$$

$$A_{22} = \frac{-S_0(\eta_4)^2 m_4}{\frac{1}{S_c}(\eta_4)^2 - \lambda\eta_4 - (K_r\lambda^2 + \omega i)} \tag{2.6.22}$$

$$A_{31} = \frac{-S_0(\eta_5)^2 m_5}{\frac{1}{S_c}(\eta_5)^2 - \lambda\eta_5 + (-K_r\lambda^2 + \omega i)} \tag{2.6.23}$$

$$A_{32} = \frac{-S_0(\eta_6)^2 m_6}{\frac{1}{S_c}(\eta_6)^2 - \lambda\eta_6 + (-K_r\lambda^2 + \omega i)} \tag{2.6.24}$$

$$D_{11} = 1 \tag{2.6.25}$$

$$D_{12} = \frac{-\phi_3 G_r(\lambda)^2 m_1 sin\alpha}{\phi_2(\eta_1)^2 - \phi_1\lambda\eta_1 - p'} \tag{2.6.26}$$

$$D_{13} = \frac{-\phi_3 G_r(\lambda)^2 m_2 sin\alpha}{\phi_2(\eta_2)^2 - \phi_1\lambda\eta_2 - p'} \tag{2.6.27}$$

$$D_{14} = \frac{-\phi_3 G_m(\lambda)^2 \zeta_1 sin\alpha}{\phi_2(q_1)^2 - \phi_1\lambda q_1 - p'} \tag{2.6.28}$$

$$D_{15} = \frac{-\phi_3 G_m(\lambda)^2 \zeta_2 sin\alpha}{\phi_2(q_2)^2 - \phi_1\lambda q_2 - p'} \tag{2.6.29}$$

$$D_{16} = \frac{-\phi_3 G_m(\lambda)^2 A_{11} sin\alpha}{\phi_2(\eta_1)^2 - \phi_1\lambda\eta_1 - p'} \tag{2.6.30}$$

$$D_{17} = \frac{-\phi_3 G_m(\lambda)^2 A_{12} sin\alpha}{\phi_2(\eta_2)^2 - \phi_1\lambda\eta_2 - p'} \tag{2.6.31}$$

$$D_{21} = 1 \tag{2.6.32}$$

$$D_{22} = \frac{-\phi_3 G_r(\lambda)^2 m_3 sin\alpha}{\phi_2(\eta_3)^2 - \phi_1\lambda\eta_3 - q'} \tag{2.6.33}$$

$$D_{23} = \frac{-\phi_3 G_r(\lambda)^2 m_4 sin\alpha}{\phi_2(\eta_4)^2 - \phi_1\lambda\eta_4 - q'} \tag{2.6.34}$$

$$D_{24} = \frac{-\phi_3 G_m(\lambda)^2 \zeta_3 sin\alpha}{\phi_2(q_3)^2 - \phi_1\lambda q_3 - q'} \tag{2.6.35}$$

$$D_{25} = \frac{-\phi_3 G_m(\lambda)^2 \zeta_4 sin\alpha}{\phi_2(q_4)^2 - \phi_1\lambda q_4 - q'} \tag{2.6.36}$$

$$D_{26} = \frac{-\phi_3 G_m(\lambda)^2 A_{21} sin\alpha}{\phi_2(\eta_3)^2 - \phi_1\lambda\eta_3 - q'} \tag{2.6.37}$$

$$D_{27} = \frac{-\phi_3 G_m(\lambda)^2 A_{22} sin\alpha}{\phi_2(\eta_4)^2 - \phi_1\lambda\eta_4 - q'} \tag{2.6.38}$$

$$D_{31} = 1 \tag{2.6.39}$$

$$D_{32} = \frac{-\phi_3 G_r(\lambda)^2 m_5 sin\alpha}{\phi_2(\eta_5)^2 - \phi_1 \lambda \eta_5 - r'} \tag{2.6.40}$$

$$D_{33} = \frac{-\phi_3 G_r(\lambda)^2 m_6 sin\alpha}{\phi_2(\eta_6)^2 - \phi_1 \lambda \eta_6 - r'} \tag{2.6.41}$$

$$D_{34} = \frac{-\phi_3 G_m(\lambda)^2 \zeta_5 sin\alpha}{\phi_2(q_5)^2 - \phi_1 \lambda q_5 - r'} \tag{2.6.42}$$

$$D_{35} = \frac{-\phi_3 G_m(\lambda)^2 \zeta_6 sin\alpha}{\phi_2(q_6)^2 - \phi_1 \lambda q_6 - r'} \tag{2.6.43}$$

$$D_{36} = \frac{-\phi_3 G_m(\lambda)^2 A_{31} sin\alpha}{\phi_2(\eta_5)^2 - \phi_1 \lambda \eta_5 - r'} \tag{2.6.44}$$

$$D_{37} = \frac{-\phi_3 G_m(\lambda)^2 A_{32} sin\alpha}{\phi_2(\eta_6)^2 - \phi_1 \lambda \eta_6 - r'} \tag{2.6.45}$$

$$m_1 = \frac{-\mathrm{e}^{(\eta_2)}}{e^{(\eta_1)} - \mathrm{e}^{(\eta_2)}} \tag{2.6.46}$$

$$m_2 = 1 - m_1 \tag{2.6.47}$$

$$m_3 = \frac{-\mathrm{e}^{(\eta_4)}}{e^{(\eta_3)} - \mathrm{e}^{(\eta_4)}} \tag{2.6.48}$$

$$m_4 = 1 - m_3 \tag{2.6.49}$$

$$m_5 = \frac{-e^{(\eta_6)}}{e^{(\eta_5)} - e^{(\eta_6)}} \tag{2.6.50}$$

$$m_6 = 1 - m_5 \tag{2.6.51}$$

$$\zeta_1 = \frac{e^{(q_2)} - A_{11}\left(e^{(q_2)} - e^{(\eta_1)}\right) + A_{12}\left(e^{(\eta_2)} - e^{(q_2)}\right)}{e^{(q_2)} - e^{(q_1)}} \tag{2.6.52}$$

$$\zeta_2 = 1 - \zeta_1 - A_{11} - A_{12} \tag{2.6.53}$$

$$\zeta_3 = \frac{e^{(q_4)} - A_{21}\left(e^{(q_4)} - e^{(\eta_3)}\right) + A_{22}\left(e^{(\eta_4)} - e^{(q_4)}\right)}{e^{(q_4)} - e^{(q_3)}} \tag{2.6.54}$$

$$\zeta_4 = 1 - \zeta_3 - A_{21} - A_{22} \tag{2.6.55}$$

$$\zeta_5 = \frac{e^{(q_6)} - A_{31}\left(e^{(q_6)} - e^{(\eta_5)}\right) + A_{32}\left(e^{(\eta_6)} - e^{(q_6)}\right)}{e^{(q_6)} - e^{(q_5)}} \tag{2.6.56}$$

$$\zeta_6 = 1 - \zeta_5 - A_{31} - A_{32} \tag{2.6.57}$$

$$h_1 = \frac{\begin{array}{r} -1 + \mathrm{D}_{11}(1 - \mathrm{e}^{(\chi_2)}) - D_{12}\left(e^{(\chi_2)} - e^{(\eta_1)}\right) \\ -D_{13}\left(e^{(\chi_2)} - e^{(\eta_2)}\right) + D_{14} \quad \left(e^{(q_1)} - e^{(\chi_2)}\right) + D_{15}\left(e^{(q_2)} - e^{(\chi_2)}\right) \\ +D_{16}\left(e^{(\eta_1)} - e^{(\chi_2)}\right) + D_{17}\left(e^{(\eta_2)} - e^{(\chi_2)}\right) \end{array}}{e^{(\chi_2)} - e^{(\chi_1)}} \tag{2.6.58}$$

$$h_2 = -h_1 - D_{11} - D_{12} - D_{13} - D_{14} - D_{15} - D_{16} - D_{17} \tag{2.6.59}$$

$$h_3 = \frac{\begin{array}{r} -1 + \mathrm{D}_{21}(1 - \mathrm{e}^{(\chi_4)}) - D_{22}\left(e^{(\chi_4)} - e^{(\eta_3)}\right) \\ -D_{23}\left(e^{(\chi_4)} - e^{(\eta_4)}\right) + D_{24}\left(e^{(q_3)} - e^{(\chi_4)}\right) + D_{25}\left(e^{(q_4)} - e^{(\chi_4)}\right) \\ +D_{26}\left(e^{(\eta_3)} - e^{(\chi_4)}\right) + D_{27}\left(e^{(\eta_4)} - e^{(\chi_4)}\right) \end{array}}{e^{(\chi_4)} - e^{(\chi_3)}} \tag{2.6.60}$$

$$h_4 = -h_3 - D_{21} - D_{22} - D_{23} - D_{24} - D_{25} - D_{26} - D_{27} \tag{2.6.61}$$

$$h_5 = \frac{\begin{array}{r} -1 + \mathrm{D}_{31}(1 - e^{(\chi_6)}) - D_{32}\left(e^{(\chi_6)} - e^{(\eta_5)}\right) \\ -D_{33}\left(e^{(\chi_6)} - e^{(\eta_6)}\right) + D_{34}\left(e^{(q_5)} - e^{(\chi_6)}\right) + D_{35}\left(e^{(q_6)} - e^{(\chi_6)}\right) \\ +D_{36}\left(e^{(\eta_5)} - e^{(\chi_6)}\right) + D_{37}\left(e^{(\eta_6)} - e^{(\chi_6)}\right) \end{array}}{e^{(\chi_6)} - e^{(\chi_5)}} \tag{2.6.62}$$

$$h_6 = -h_5 - D_{31} - D_{32} - D_{33} - D_{34} - D_{35} - D_{36} - D_{37} \tag{2.6.63}$$

$$p' = \frac{\phi_2}{K_1} + \frac{\phi_5 M^2}{1 + H^2} + \frac{\phi_5 M^2 i H}{1 + H^2} \tag{2.6.64}$$

$$q' = \frac{\phi_2}{K_1} + \frac{\phi_5 M^2}{1 + H^2} + \frac{\phi_5 M^2 i H}{1 + H^2} + \phi_1 \omega i \tag{2.6.65}$$

$$r' = \frac{\phi_2}{K_1} + \frac{\phi_5 M^2}{1 + H^2} + \frac{\phi_5 M^2 i H}{1 + H^2} - \phi_1 \omega i \tag{2.6.66}$$

Chapter 3

Statistical analysis on MHD convective Carreau nanofluid flow due to bilateral non linear stretching sheet with zero mass flux condition *

3.1 Introduction

Stretching surface has intrigued many researchers due to its diverse applications in industrial and engineering fields like production of plastic and rubber plates, cooling of metallic plate in a bath, metal extrusion, etc. Both Newtonian and Non-Newtonian fluid flow over a bilateral non-linear stretching sheet has been studied by many researchers. MHD Carreau nanofluid flow over a bilateral stretching non-linear surface with zero mass flux condition has been studied in the chapter. Magnetic and heat source effects are accounted to analyse the effects of velocity and heat transport of Carreau nanofluid over a non linear stretching sheet. Effects of various parameters on skin friction coefficients and heat transfer rate are scrutinized using statistical techniques like slope of linear regression, correlation coefficient, probable error and regression.

3.2 Mathematical formulation

Three dimensional steady MHD Carreau nanofluid flow due to a bilateral stretching sheet with velocities $u_W = a(x+y)^m,\ v_W = b(x+y)^m;\ a,\ b,\ m > 0$ along the X and Y directions respectively is considered. Velocity, temperature and concentration equations are investigated with convective and zero mass flux condition at the

*Published in: Heat Transfer (Wiley), 2021; 50 (4) 3641-3660

surface. A non-uniform magnetic field $B = B_0(x+y)^{\frac{m-1}{2}}$ is applied along the Z direction (see Figure 3.1). In addition, a non-uniform heat generation or absorption $Q = Q_0(x+y)^{m-1}$ is implemented. The boundary layer equations (J. A. Khan et al., 2014), (Hayat, Aziz, et al., 2019) (M. Khan, Sardar, et al., 2018) are given by:

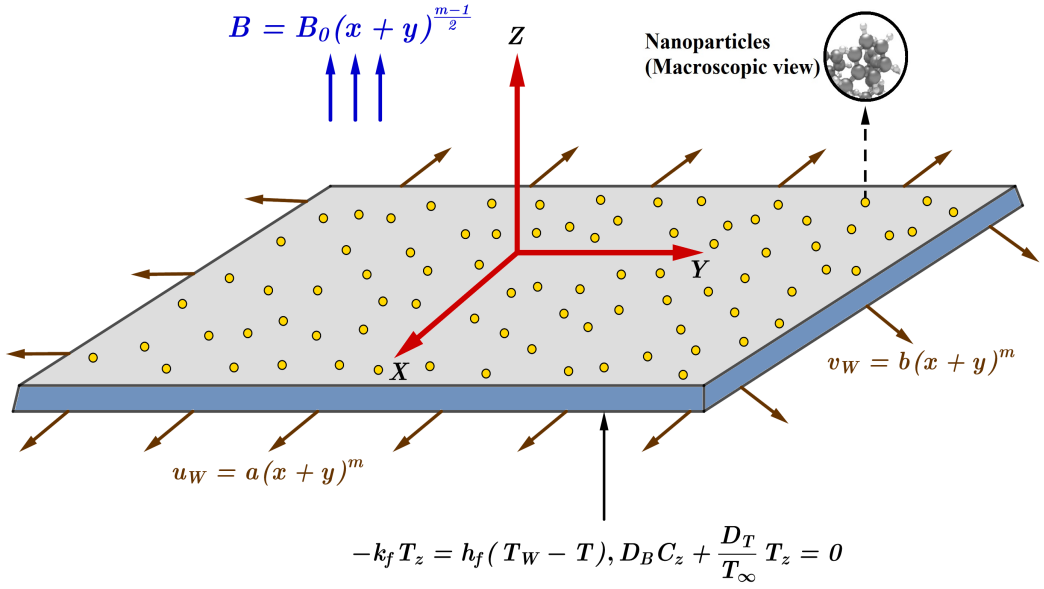

Figure 3.1: *Geometry of the problem*

$$u_x + v_y + w_z = 0 \tag{3.2.1}$$

$$\begin{aligned} uu_x + vu_y + wu_z = \nu_f u_{zz}\left[\beta^* + (1-\beta^*)\left\{1+\Gamma^2(u_z)^2\right\}^{\frac{n-1}{2}}\right] \\ +\nu_f(n-1)(1-\beta^*)\Gamma^2 u_{zz}(u_z)^2\left\{1+\Gamma^2(u_z)^2\right\}^{\frac{n-3}{2}} - \frac{\sigma B^2 u}{\rho} \end{aligned} \tag{3.2.2}$$

$$\begin{aligned} uv_x + vv_y + wv_z = \nu_f v_{zz}\left[\beta^* + (1-\beta^*)\left\{1+\Gamma^2(v_z)^2\right\}^{\frac{n-1}{2}}\right] \\ +\nu_f(n-1)(1-\beta^*)\Gamma^2 v_{zz}(v_z)^2\left\{1+\Gamma^2(v_z)^2\right\}^{\frac{n-3}{2}} - \frac{\sigma B^2 v}{\rho} \end{aligned} \tag{3.2.3}$$

$$uT_x + vT_y + wT_z = \alpha_f T_{zz} + \frac{Q}{(\rho c)_f}(T - T_\infty) + \tau\left[D_B T_z C_z + \frac{D_T}{T_\infty}(T_z)^2\right] \tag{3.2.4}$$

$$uC_x + vC_y + wC_z = D_B C_{zz} + \frac{D_T}{T_\infty} T_{zz} \tag{3.2.5}$$

The respective boundary conditions are given as:

$$\left.\begin{array}{c} u = u_W = a(x+y)^m, \quad v = v_W = b(x+y)^m, \quad w = 0 \\ -k_f T_z = h_f \left(T_W - T\right), \quad D_B C_z + \frac{D_T}{T_\infty} T_z = 0 \end{array}\right\} \text{ at } z = 0 \tag{3.2.6}$$

$$u \to 0, \quad v \to 0, \quad T \to T_\infty, \quad C \to C_\infty \quad \text{at } z \to \infty \tag{3.2.7}$$

The following similarity variables are implemented in converting the above system of partial differential equations into a system of ordinary differential equations:

$$\left.\begin{array}{c} u = a(x+y)^m \quad f'(\zeta) \\ v = a(x+y)^m \quad g'(\zeta) \\ w = -\sqrt{a\nu_f}\,(x+y)^{\frac{m-1}{2}} \quad \left[\ \frac{m+1}{2}\ (f(\zeta)+g(\zeta))\ +\ \frac{m-1}{2}\ \zeta\ (f'(\zeta)+g'(\zeta))\ \right] \end{array}\right\} \tag{3.2.8}$$

$$\theta(\zeta) = \frac{T - T_\infty}{T_W - T_\infty}, \quad \phi(\zeta) = \frac{C - C_\infty}{C_\infty}, \quad \zeta = \sqrt{\frac{a}{\nu_f}}\ z\ (x+y)^{\frac{m-1}{2}} \tag{3.2.9}$$

The transformed boundary layer equations are given below:

$$\begin{array}{c} f'''\left[\beta^* + (1-\beta^*)\left(1 + We^2 (f'')^2\right)^{\frac{n-3}{2}}\left(1 + nWe^2 (f'')^2\right)\right] - Mf' \\ -m(f')^2 - mf'g' + \frac{m+1}{2} f''(f+g) = 0 \end{array} \tag{3.2.10}$$

$$\begin{array}{c} g'''\left[\beta^* + (1-\beta^*)\left(1 + We^2 (g'')^2\right)^{\frac{n-3}{2}}\left(1 + nWe^2 (g'')^2\right)\right] \\ -Mg' - m(g')^2 - mf'g' + \frac{m+1}{2} g''(f+g) = 0 \end{array} \tag{3.2.11}$$

$$\theta'' + Pr\left[S\theta + Nb\phi'\theta' + Nt(\theta')^2 + \left(\frac{m+1}{2}\right)(f+g)\,\theta'\right] = 0 \tag{3.2.12}$$

$$\phi'' + \frac{Nt}{Nb}\theta'' + Sc\phi'\left(\frac{m+1}{2}\right)(f+g) = 0 \tag{3.2.13}$$

The corresponding boundary conditions are given by:

$$\left.\begin{array}{c} f(0) = 0, \quad g(0) = 0, \quad f'(0) = 1, \quad g'(0) = \delta \\ \theta'(0) = -Bi\left(1 - \theta(0)\right), \quad \phi'(0) + \frac{Nt}{Nb}\theta'(0) = 0 \end{array}\right\} \text{ at } z = 0 \tag{3.2.14}$$

$$f'(\infty) \to 0, \quad g'(\infty) \to 0, \quad \theta(\infty) \to 0, \quad \phi(\infty) \to 0 \tag{3.2.15}$$

where the non-dimensional parameters are taken as following:

$$\left.\begin{array}{c} We=\sqrt{\frac{\Gamma^2 a^3(x+y)^{3m-1}}{\gamma}},\quad M=\frac{\sigma B_o^2}{\rho_f a},\quad Pr=\frac{\nu_f}{\alpha_f},\quad Sc=\frac{\nu_f}{D_B},\quad \delta=\frac{b}{a} \\ Nt=\frac{\tau D_T(T_W-T_\infty)}{T_\infty \nu_f},\quad Nb=\frac{\tau D_B C_\infty}{\nu_f},\quad \tau=\frac{(\rho c)_p}{(\rho c)_f},\quad S=\frac{Q_0}{a(\rho c)_f} \end{array}\right\} \tag{3.2.16}$$

Skin friction coefficients, local Nusselt number and local Sherwood number measures the surface drag, heat transfer rate and mass transfer rate, respectively. They are defined (M. Khan et al., 2018), (Mahanthesh, Gireesha, & Gorla, 2017) as given below:(see Table 3.1)

3.3 Numerical solution

The equations (3.2.10) – (3.2.13) with boundary conditions (3.2.14)-(3.2.15) are solved numerically using bvp5c solver, a MATLAB built in function. To accomplish this, we choose:

$f=y_1,\quad f'=y_2,\quad f''=y_3,\quad g=y_4,\quad g'=y_5,$

$g''=y_6,\quad \theta=y_7,\quad \theta'=y_8,\quad \phi=y_9,\quad \phi'=y_{10}$

Accordingly, the equations (3.2.10) – (3.2.15) takes the form:

$$\begin{array}{c} y_1^{'}=y_2,\quad y_2^{'}=y_3,\quad y_3^{'}=\frac{my_2^2+my_2y_5-\left(\frac{m+1}{2}\right)y_3(y_1+y_4)+My_2}{\beta^*+(1-\beta^*)\left(1+We^2y_3^2\right)^{\frac{n-3}{2}}\left(1+nWe^2y_3^2\right)} \\ y_4^{'}=y_5,\quad y_5^{'}=y_6,\quad y_6^{'}=\frac{my_5^2+my_2y_5-\left(\frac{m+1}{2}\right)y_6(y_1+y_4)+My_5}{\beta^*+(1-\beta^*)\left(1+We^2y_6^2\right)^{\frac{n-3}{2}}\left(1+nWe^2y_6^2\right)} \\ y_7^{'}=y_8,\quad y_8^{'}=-\Pr\left[Sy_7+Nby_8y_{10}+Nt(y_8)^2+\left(\frac{m+1}{2}\right)(y_1+y_4)\,y_8\right],\quad y_9^{'}=y_{10} \\ y_{10}^{'}=\left\{\frac{Nt}{Nb}\ \Pr\left[Sy_7+Nby_8y_{10}+Nt(y_8)^2+\left(\frac{m+1}{2}\right)(y_1+y_4)\,y_8\right]-Scy_{10}\left(\frac{m+1}{2}\right)(y_1+y_4)\right\} \\ y_1(0)=0,\quad y_2(0)=1,\quad y_2(\infty)=0,\quad y_4(0)=0,\quad y_5(0)=\delta,\quad y_5(\infty)=0 \\ y_7(\infty)=0,\quad y_8(0)=-Bi\,(1-y_7(0)),\quad y_9(\infty)=0,\quad y_{10}(0)+\frac{Nt}{Nb}y_8(0)=0 \end{array} \tag{3.3.1}$$

Accuracy of the code and the validation of the current problem have been accounted through a restrictive comparison of the present work with prior published (J. A. Khan et al., 2014) results and is found to be in good agreement (described in Table 3.2).

3.4 Result and discussion

The impact of viscosity ratio parameter (β^*), Weisssenberg number (We), Hartmann number (M), heat generation/absorption parameter (S), power law index (n), Biot number (Bi), stretching ratio parameter (δ), Brownian motion parameter (Nb),

Table 3.1: *Skin friction coefficients, local Nusselt number and local Sherwood number are defined as given below:*

Local Nusselt number	$Nu = \frac{(x+y)q_w}{k_f(T_w - T_\infty)}$ where $q_w = -k_f\left(\frac{\partial T}{\partial z}\right)_{z=0}$
Reduced form of Nusselt number	$Re_x^{-\frac{1}{2}}\ Nu = -\theta'(0)$ where $Re_x = \frac{u_w(x+y)}{\nu_f}$ is the local Reynolds number along the x direction
Local Sherwood Number	$Sh = \frac{(x+y)m_w}{D_B(C_w - C_\infty)}$ where $m_w = -D_B\left(\frac{\partial C}{\partial z}\right)_{z=0}$
Reduced form of Sherwood number	$Re_x^{-\frac{1}{2}}\ Sh = -\phi'(0)$
Skin Friction Coefficients	$Cf_x = \frac{\tau_{zx}}{\rho_f u_w^2}$ where $\tau_{zx} = \mu_f\left(\frac{\partial u}{\partial z}\right)\left[\beta^* + (1-\beta^*)\left(1 + \Gamma^2\left(\frac{\partial u}{\partial z}\right)^2\right)^{\frac{n-1}{2}}\right]$
	$Cf_y = \frac{\tau_{zy}}{\rho_f v_w^2}$ where $\tau_{zy} = \mu_f\left(\frac{\partial v}{\partial z}\right)\left[\beta^* + (1-\beta^*)\left(1 + \Gamma^2\left(\frac{\partial v}{\partial z}\right)^2\right)^{\frac{n-1}{2}}\right]$
Reduced form of Skin Friction	$Re_x^{\frac{1}{2}} Cf_x = f''(0)\left[\beta^* + (1-\beta^*)\left(1 + We^2(f''(0))^2\right)^{\frac{n-1}{2}}\right]$
	$Re_y^{\frac{1}{2}} Cf_y = \delta^{-1.5}\ g''(0) \times \left[\beta^* + (1-\beta^*)\left(1 + We^2(g''(0))^2\right)^{\frac{n-1}{2}}\right]$ where $Re_y = \frac{v_w(x+y)}{\nu_f}$ is the local Reynolds number along y direction

thermophoresis parameter (Nt) on the X direction velocity ($f'(\zeta)$), Y direction velocity ($g'(\zeta)$), temperature ($\theta(\zeta)$) and concentration ($\phi(\zeta)$) profiles are carefully analysed through Figs. 3.2 - 3.13. The Prandtl number (Pr) and Schmidt numbers (Sc) are fixed at 5 and 2 respectively.

Table 3.2: *Comparison of* $f''(0)$ *and* $g''(0)$ *when* $\beta^* = 1$ *and* $M = 0$

m	δ	$f''(0)$ [Present paper]	$f''(0)$ (J. A. Khan et al., 2014)	$g''(0)$ [Present paper]	$g''(0)$ (J. A. Khan et al., 2014)
1	0	-1.000172394	-1	0	0
1	0.5	-1.22478775	-1.224745	-0.612393875	-0.612372
1	1	-1.414226121	-1.414214	-1.414226121	-1.414214
3	0	-1.624368157	-1.624356	0	0
3	0.5	-1.989423631	-1.989422	-0.994711816	-0.994711
3	1	-2.297186414	-2.297186	-2.297186414	-2.297186

Figs. 3.2 and 3.3 depict the variation of $f'(\zeta)$ and $g'(\zeta)$ due to the increment in β^*. The analysis has been carried out for shear-thinning n ($n < 1$) and shear thickening n ($n > 1$) cases. Both $f'(\zeta)$ and $g'(\zeta)$ exhibit an increase (shear-thinning case) with an increase in β^* whereas the results are reversed for the shear thickening case. The effect of We on $f'(\zeta)$ and $g'(\zeta)$ are elucidated in Figs. 3.4 and 3.5. A contrasting behaviour is observed on the velocity profiles for different values of n. An increase in We improves the elastic forces which hence causes a reduction in the velocity profiles in a shear-thinning fluid. Fig. 3.6 and 3.7 illustrates the variation of M on $f'(\zeta)$ and $g'(\zeta)$. An increment in M generates Lorentz force which retards $f'(\zeta)$ and $g'(\zeta)$ profiles. Fig. 3.8 exhibits the influence of δ on $g'(\zeta)$. As δ increases, $g'(\zeta)$ also increases since the vertical downward flow is accelerated due to the bi-directional stretching of the sheet.

With a rise in the magnitude of Bi, temperature profile is enhanced, shown in Fig. 3.9. Physically, this can be attributed to the fact that increase in Biot number enhances the heat transfer coefficient which in turn increases θ. Fig. 3.10 displays the effect of S on $\theta(\zeta)$. $\theta(\zeta)$ is observed to increase as S is increased. Fig. 3.11 reveals the change in $\theta(\zeta)$ with increasing Nt. Nt is found to have a positive effect. The mounting of Nt promotes an increment in the thermophoresis force which enforces the movement of nanoparticles from a hot region to a cold region and hence $\theta(\zeta)$ is increased. Fig. 3.12 describes the variation of $\phi(\zeta)$ with Nb. Nb shows a negative influence with $\phi(\zeta)$. Physically, an increase in Nb improves the random motion of nanoparticles which in return lowers the concentration of nanofluid. Fig. 3.13 shows that $\phi(\zeta)$ increases when Nt is increased.

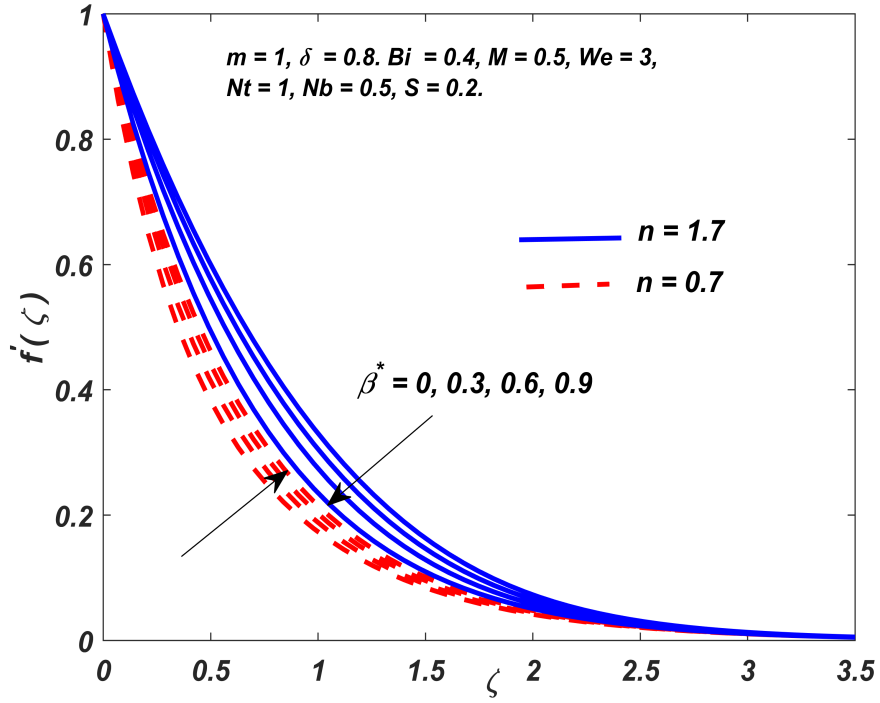

Figure 3.2: *Variation of* $f'(\zeta)$ *for various values of* β^*

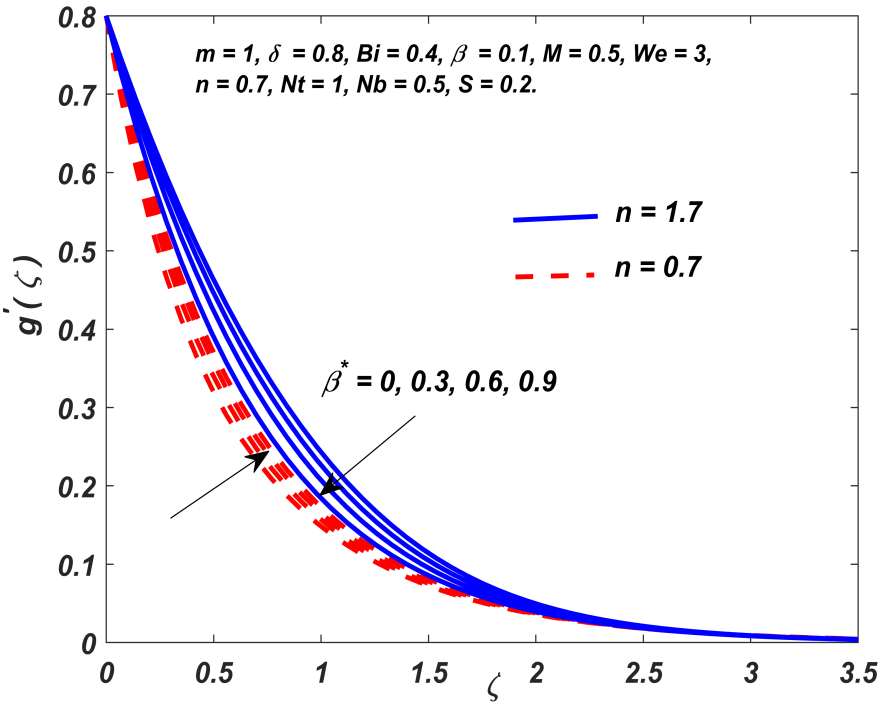

Figure 3.3: *Variation of* $g'(\zeta)$ *for various values of* β^*

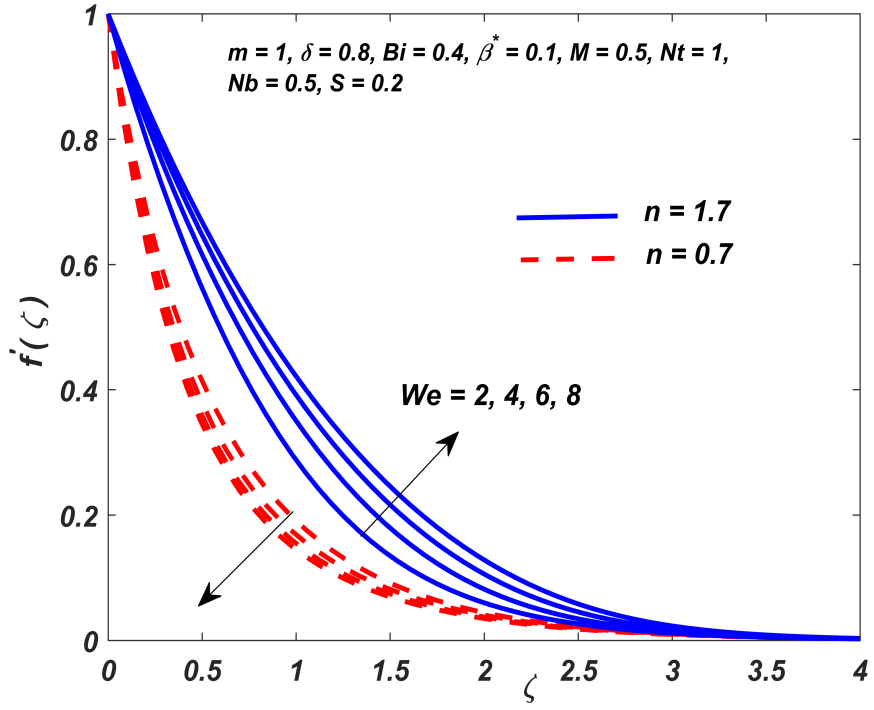

Figure 3.4: *Variation of* $f'(\zeta)$ *for various values of* We

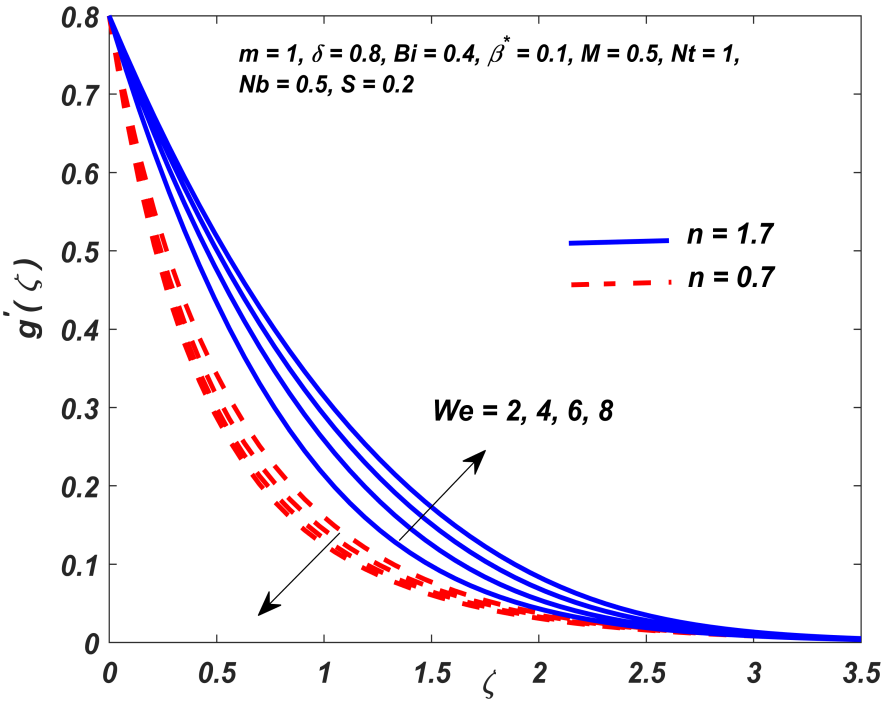

Figure 3.5: *Variation of* $g'(\zeta)$ *for various values of* We

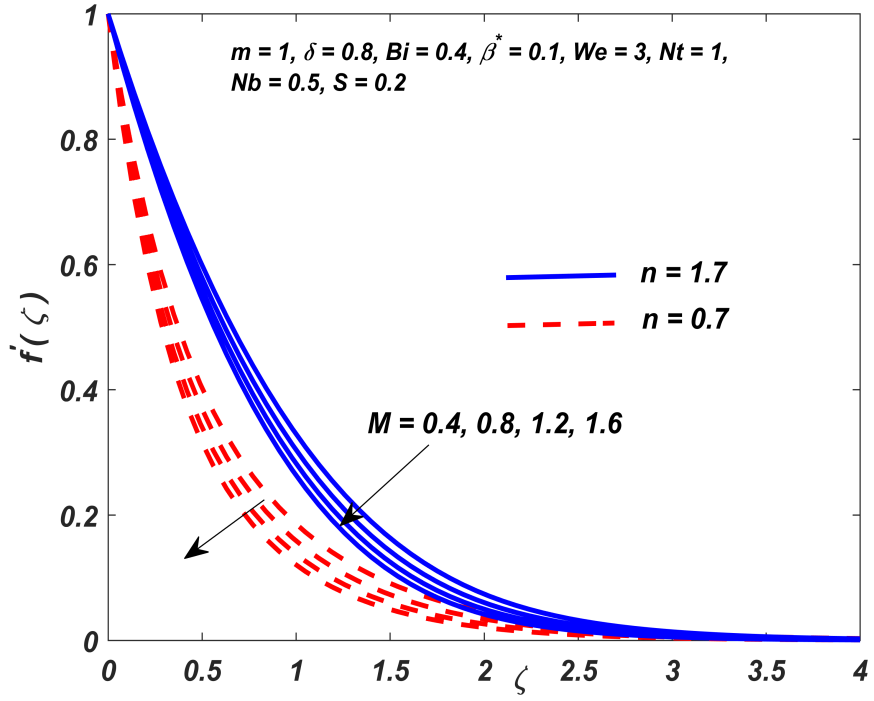

Figure 3.6: *Variation of* $f'(\zeta)$ *for various values of* M

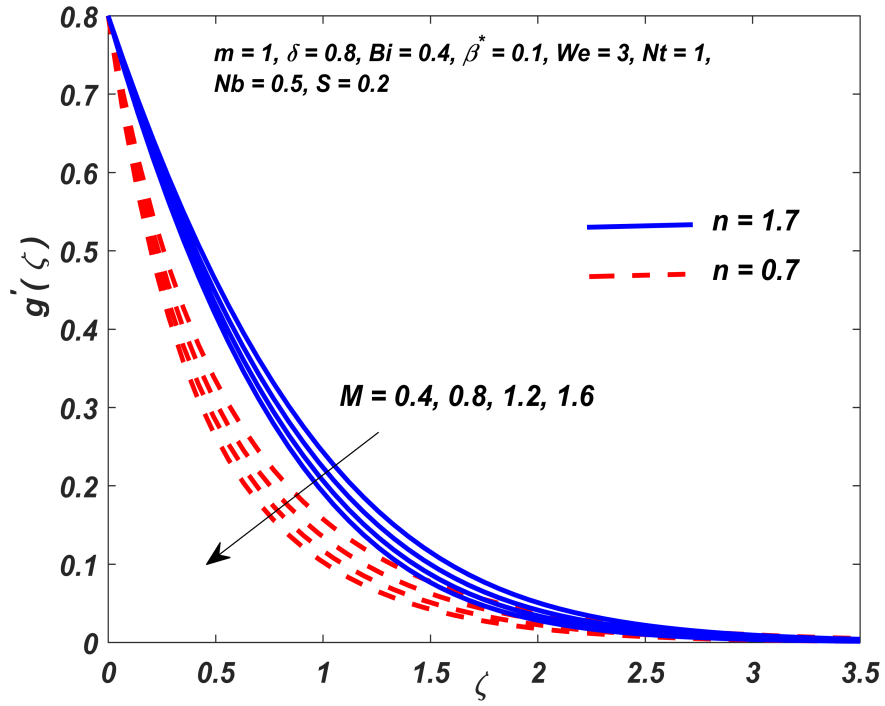

Figure 3.7: *Variation of* $g'(\zeta)$ *for various values of* M

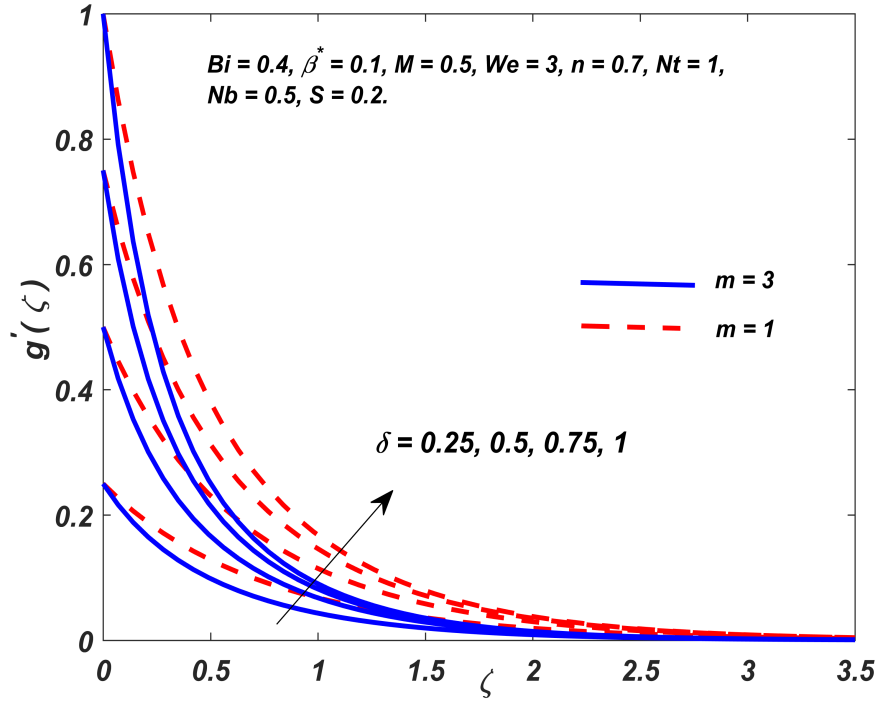

Figure 3.8: *Variation of* $g'(\zeta)$ *for various values of* δ

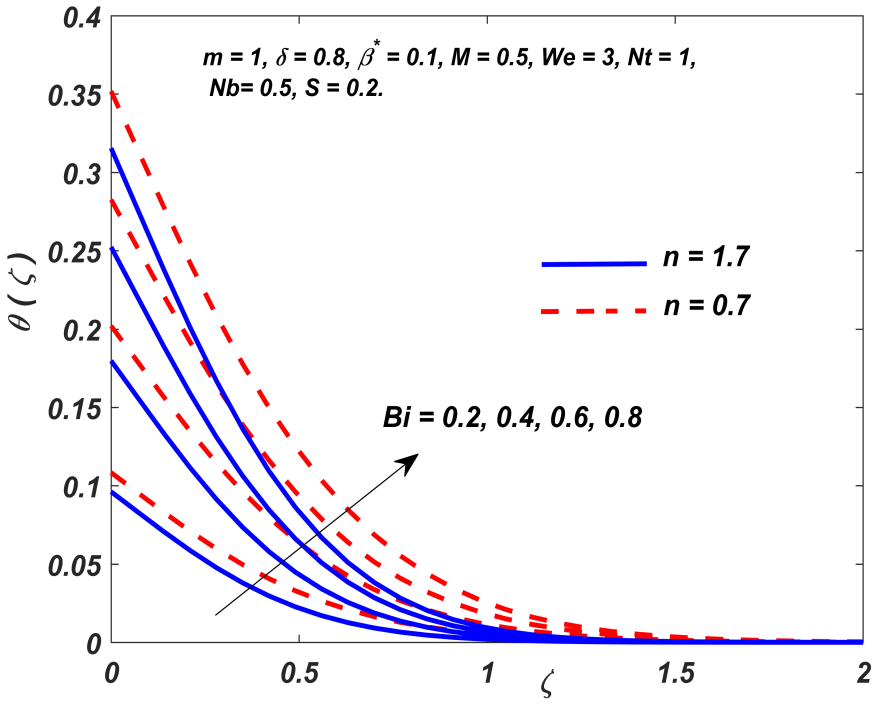

Figure 3.9: *Variation of* $\theta(\zeta)$ *for various values of* Bi

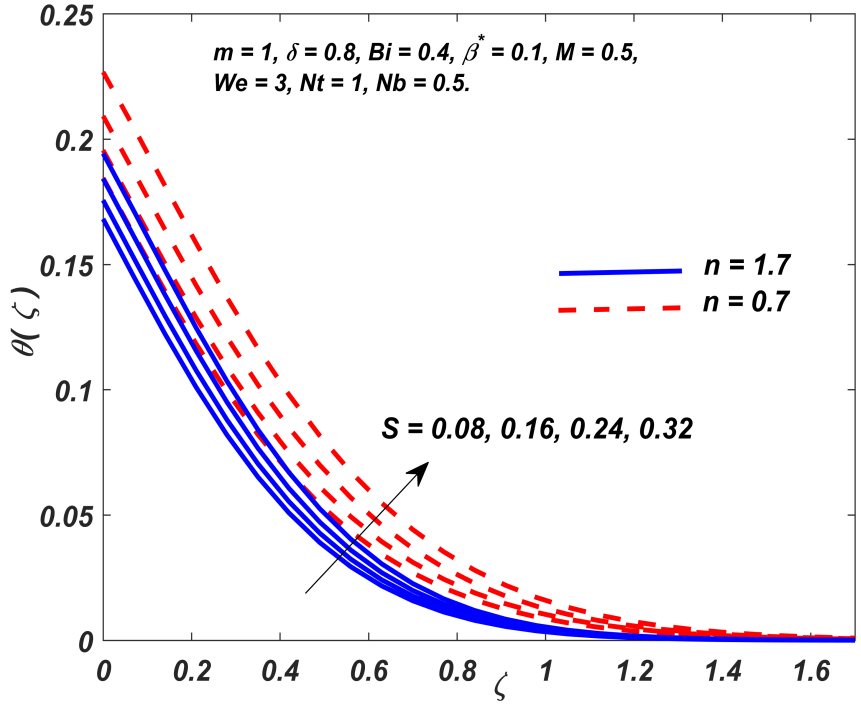

Figure 3.10: *Variation of* $\theta(\zeta)$ *for various values of* S

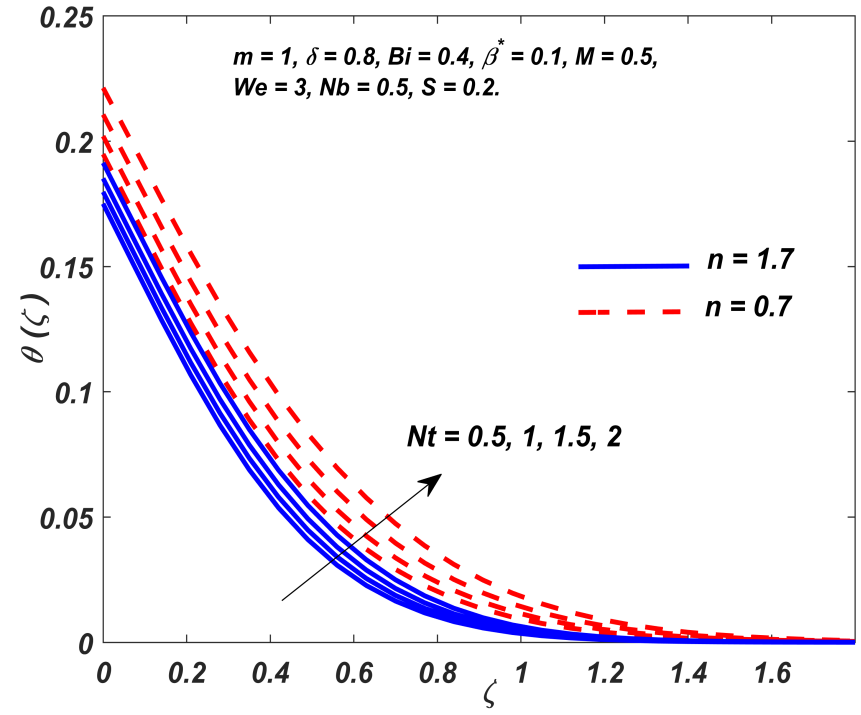

Figure 3.11: *Variation of* $\theta(\zeta)$ *for various values of* Nt

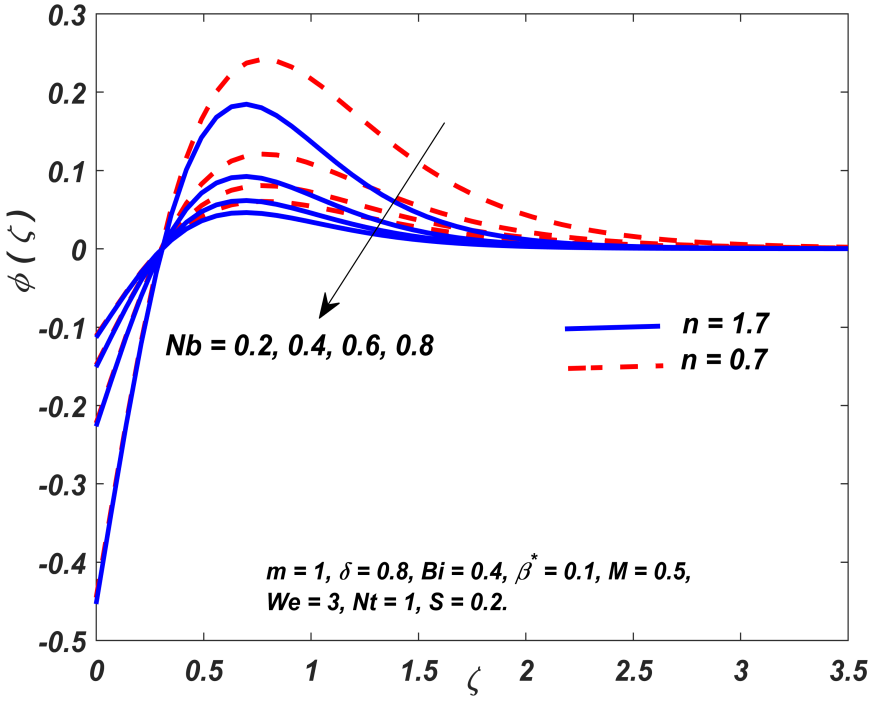

Figure 3.12: *Variation of $\phi(\zeta)$ for various values of Nb*

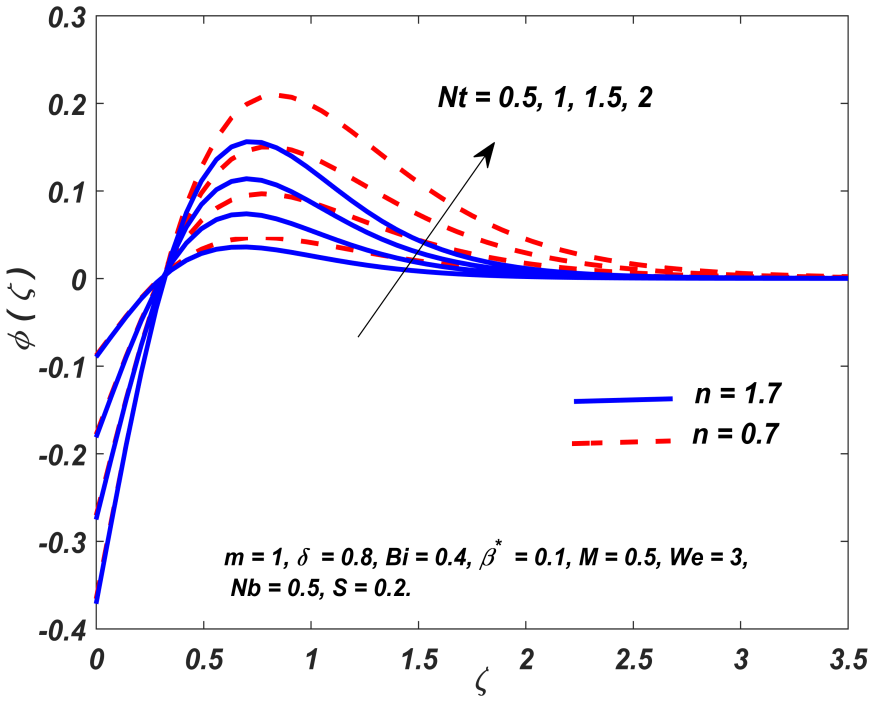

Figure 3.13: *Variation of $\phi(\zeta)$ for various values of Nt*

The effect of various parameters on local Nusselt number for $n = 0.7$ *and* 1.7 is studied using table 3.3. Increment/decrement rate denotes the percentage change of current value with respect to the previous value of local Nusselt number. A positive sign represents an increment while a negative sign represents decrement in heat transfer rate. From table 3.3, it is deduced that $Re_x^{-\frac{1}{2}} Nu$ (*both cases*) increases with δ and decreases for $Nt,\ S\ \&\ M$. It is further noted that $Re_x^{-\frac{1}{2}} Nu\ (n = 0.7)$ increases with β^* and decreases with We whereas the results are reversed for $Re_x^{-\frac{1}{2}} Nu\ (n = 1.7)$. Slope of linear regression is used to study the trend of variation in skin friction coefficient. A negative slope with respect to a parameter indicates that the parameter has a negative effect on skin friction meaning, an increase in that parameter will diminish the surface drag. Magnitude of slope represents the rate of change of skin friction coefficient per unit value of the corresponding parameter. The impact of various parameters on skin friction coefficients for $m = 1 \quad \& \quad 3$ at $n = 0.7 \quad \& \quad 1.7$ is illustrated in table 3.4 and 3.5.

From tables 3.4 and 3.5, it is inferred that We has a positive and negative impact on both skin friction coefficients $\left\{ Re_x^{\frac{1}{2}} Cf_x \quad \& \quad Re_y^{\frac{1}{2}} Cf_y \right\} (m = 1 \quad \& \quad m = 3)$ when $n = 0.7 \quad \& \quad 1.7$, respectively and β^* has a reversed impact on skin friction coefficients when compared with We. It is observed that M has a reducing effect on the surface drag. It is also observed that the skin friction coefficient decreases with increasing δ (for $Re_x^{\frac{1}{2}} Cf_x$) and increases with increasing δ (for $Re_y^{\frac{1}{2}} Cf_y$). The respective rate of change (slope) for each parameters are shown in tables 3.4 and 3.5.

3.5 Statistical Analysis

Statistical techniques like correlation and regression are widely used by researchers to identify the nature of impact of independent variables (various parameters) on the dependent variable (physical quantities like Nusselt number, drag coefficient or Sherwood number). Regression analysis helps in quantifying the variation of dependent variable due to the change in independent variables. Regression analysis eliminates the need for solving the problem repeatedly and thereby simplifying the calculation process. An approximate value of dependent variable can be faultlessly predicted for the chosen range of independent variables.

Table 3.3: *Variation in local Nusselt number at* $\zeta = 0$ *when* $m = 1$, $Nt = 1$, $S = 0.2$, $M = 0.5$, $We = 3$, $\delta = 0.8$, $\beta^* = 0.1$, $Nb = 0.5$ *and* $Bi = 0.4$

Nt	S	M	δ	We	β^*	$Re_x^{-\frac{1}{2}} Nu$		Increment Rate	
						$n = 0.7.$	$n = 1.7$	$n = 0.7$	$n = 1.7.$
0.5						0.3220801	0.3299969		
0.875						0.3199708	0.3286018	-0.655%	-0.423%
1.25						0.3175703	0.3270705	-0.750%	-0.466%
1.625						0.3147927	0.325376	-0.875%	-0.518%
2						0.3115088	0.3234827	-1.043%	-0.582%
	0.08					0.326205	0.3327401		
	0.14					0.32297	0.3305449	-0.992%	-0.660%
	0.2					0.3192066	0.3281077	-1.165%	-0.737%
	0.26					0.3147406	0.3253792	-1.399%	-0.832%
	0.32					0.3092984	0.3222934	-1.729%	-0.948%
		0.4				0.319804	0.3282712		
		0.7				0.3180105	0.3277891	-0.561%	-0.147%
		1				0.3162062	0.3273291	-0.567%	-0.140%
		1.3				0.3143798	0.3268877	-0.578%	-0.135%
		1.6				0.3125207	0.3264619	-0.591%	-0.130%
			0.25			0.2972953	0.3094536		
			0.4375			0.3071497	0.3172612	3.315%	2.523%
			0.625			0.3141479	0.3234272	2.278%	1.944%
			0.8125			0.3195285	0.3284102	1.713%	1.541%
			1			0.3238713	0.3325305	1.359%	1.255%
				2		0.320498	0.3271069		
				3.5		0.3186733	0.3284715	-0.569%	0.417%
				5		0.3173661	0.3292629	-0.410%	0.241%
				6.5		0.3163448	0.3297959	-0.322%	0.162%
				8		0.3155017	0.3301881	-0.266%	0.119%
					0.1	0.3192066	0.3281077		
					0.3	0.3205573	0.3276043	0.423%	-0.153%
					0.5	0.3216038	0.3269473	0.326%	-0.201%
					0.7	0.3224475	0.3260304	0.262%	-0.280%
					0.9	0.3231473	0.3245935	0.217%	-0.441%

3.5.1 Correlation and Probable Error

Correlation is a statistical technique which helps in determining the degree of relationship between two variables. The sign of correlation coefficient (r_c) determines the nature of relationship while magnitude of r_c indicates the magnitude of the relationship. Positive value of correlation coefficient implies that an increase in independent variable will fuel an increase in the dependent variable and negative value of correlation coefficient indicates that an increase in independent variable

Table 3.4: *Variation in Skin Friction Coefficients at* $\zeta = 0$ *when* $m = 1$, $Nt = 1$, $S = 0.2$, $M = 0.5$, $We = 3$, $\delta = 0.8$, $\beta^* = 0.1$, $Nb = 0.5$ *and* $Bi = 0.4$

We	β^*	M	δ	$-Re_x^{\frac{1}{2}} Cf_x$		$-Re_y^{\frac{1}{2}} Cf_y$	
				$n = 0.7$	$n = 1.7$	$n = 0.7$	$n = 1.7$
2				1.33511	1.86889	1.52449	2.02782
4				1.22088	2.15347	1.39943	2.32086
6				1.1555	2.36256	1.32533	2.54024
8				1.11123	2.52993	1.2746	2.71707
Slope				-0.03685	0.10961	-0.04119	0.11436
	0.2			1.30295	1.98544	1.48571	2.14815
	0.4			1.365	1.90031	1.54612	2.06399
	0.6			1.42028	1.80114	1.60037	1.9667
	0.8			1.47045	1.67999	1.64987	1.84939
Slope				0.27889	-0.50776	0.27337	-0.49678
		0.4		1.24376	1.97236	1.42361	2.13213
		0.8		1.33935	2.17465	1.53495	2.34492
		1.2		1.42665	2.3659	1.63649	2.54627
		1.6		1.50737	2.54804	1.73028	2.73812
Slope				0.21953	0.47958	0.25539	0.50483
			0.25	1.12977	1.70474	2.51655	2.89424
			0.5	1.19716	1.84841	1.81195	2.36941
			0.75	1.25722	1.99478	1.49662	2.20445
			1	1.31215	2.14103	1.31215	2.14103
Slope				0.24288	0.58209	-1.57142	-0.96983

will reduce the dependent variable. The reliability of the calculated correlation coefficient values is guaranteed using probable error (PE). Correlation is said to be significant (Fisher et al., 1921) if $\left|\frac{r_c}{PE}\right| > 6$; where $PE = \left(\frac{1-{r_c}^2}{\sqrt{\tilde{n}}}\right) 0.6745$ and $\tilde{n}$ is the number of observations.

From table 3.6, it is inferred that $Re_x^{-\frac{1}{2}} Nu$ (*both cases*) is positively correlated with δ and negatively correlated with S , M and Nt. It is observed that We exhibits negative and β^* exhibits positive correlation for $Re_x^{-\frac{1}{2}} Nu$ $(n = 0.7)$. It is also noted that the nature of correlation for We and β^* is reversed when $Re_x^{-\frac{1}{2}} Nu$ $(n = 1.7)$. Using $\left|\frac{r}{PE}\right|$ values, it can be concluded that all parameters of $Re_x^{-\frac{1}{2}} Nu$ (*both cases*) are significant.

Table 3.5: *Variation in Skin Friction Coefficients at* $\zeta = 0$ *when* $m = 3$, $Nt = 1$, $S = 0.2$, $M = 0.5$, $We = 3$, $\delta = 0.8$, $\beta^* = 0.1$, $Nb = 0.5$ *and* $Bi = 0.4$

We	β^*	M	δ	$-Re_x^{\frac{1}{2}} Cf_x$		$-Re_y^{\frac{1}{2}} Cf_y$	
				$n = 0.7$	$n = 1.7$	$n = 0.7$	$n = 1.7$
2				1.91894	3.054	2.1954	3.30479
4				1.74778	3.56384	2.00299	3.83948
6				1.65419	3.92644	1.89571	4.2241
8				1.59169	4.21322	1.82361	4.52954
Slope				-0.05377	0.19201	-0.06113	0.20294
	0.2			1.88497	3.25976	2.14958	3.52184
	0.4			2.00493	3.09201	2.2704	3.35199
	0.6			2.11052	2.89401	2.37747	3.15268
	0.8			2.20561	2.64641	2.47432	2.9061
Slope				0.53376	-1.01903	0.54065	-1.02327
		0.4		1.80207	3.29733	2.06412	3.55888
		0.8		1.86302	3.44808	2.13524	3.7165
		1.2		1.9213	3.59477	2.20316	3.87005
		1.6		1.97723	3.73779	2.26826	4.01989
Slope				0.14593	0.36702	0.17009	0.38415
			0.25	1.58658	2.71252	3.59345	4.50058
			0.5	1.69935	2.9938	2.58371	3.81117
			0.75	1.79885	3.27865	2.14315	3.61699
			1	1.88932	3.56095	1.88932	3.56095
Slope				0.40309	1.13206	-2.22118	-1.20522

Table 3.6: *Correlation Coefficient* (r_c)*, Probable Error* (PE) *and* $\left|\frac{r_c}{PE}\right|$ *of reduced Nusselt number at* $\zeta = 0$ *when* $Bi = 0.4$ *and* $Nb = 0.5$

Parameter	$Re_x^{-\frac{1}{2}} Nu$ when $n = 0.7$			$Re_x^{-\frac{1}{2}} Nu$ when $n = 1.7$		
	r_c	PE	$\left\|\frac{r_c}{PE}\right\|$	r_c	PE	$\left\|\frac{r_c}{PE}\right\|$
S	-0.9947	0.0032	311.6281	-0.9977	0.0014	732.2152
M	-1	0	63550.21	-0.9997	0.0002	5508.991
δ	0.9866	0.008	122.7986	0.992	0.0048	207.3562
We	-0.9879	0.0072	136.5306	0.9689	0.0185	52.4026
β^*	0.9915	0.0051	194.3342	-0.978	0.0131	74.4632
Nt	-0.9962	0.0023	430.4705	-0.9982	0.0011	909.9878

3.5.2 Multiple Linear Regression

Regression analysis is a statistical modelling technique used to establish a relationship between a dependent (Nusselt number) and one or more independent (various parameters considered) variables. Local Nusselt number for $n = 0.7$ and 1.7 is estimated using multiple linear regression models (as all correlations are significant). The estimated models are:

$$Nu_{est}^{n=0.7} = -0.07007S - 0.00566M + 0.03556\delta - 0.00072We + 0.00583\beta^* \\ -0.00697Nt + 0.31579 \tag{3.5.1}$$

$$Nu_{est}^{n=1.7} = -0.04343S - 0.00128M + 0.03116\delta + 0.00051We - 0.00352\beta^* \\ -0.00428Nt + 0.31540 \tag{3.5.2}$$

The accuracy of the estimated regression model is illustrated using Fig. 3.14 and 3.15. It is conclusive that δ and β^* have a positive impact whereas $S,\ M,\ We\ and\ Nt$ have negative impact on Nusselt number when $n = 0.7$. It can also be concluded that δ and We have a positive impact while $S,\ M,\ \beta^*\ and\ Nt$ have negative impact on Nusselt number when $n = 1.7$. This is in agreement with the results seen in table 3.3.

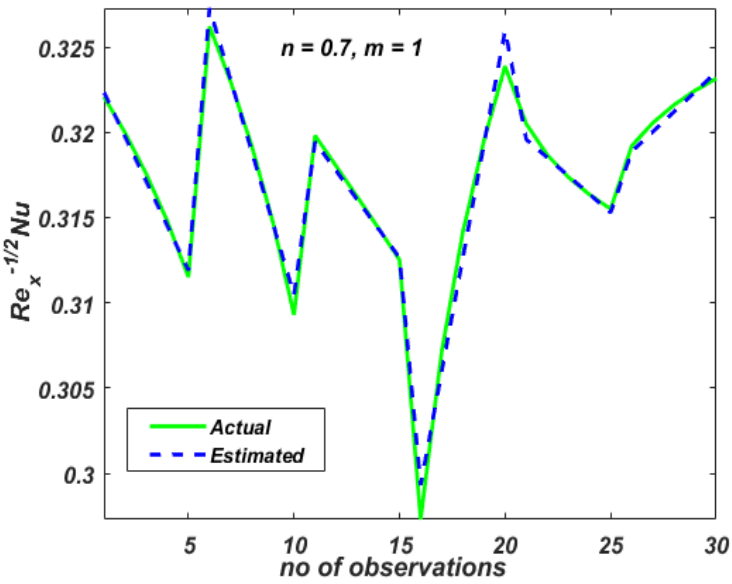

Figure 3.14: *Actual and estimated values* $Re_x^{-\frac{1}{2}}\ Nu$ *of when* $n = 0.7$

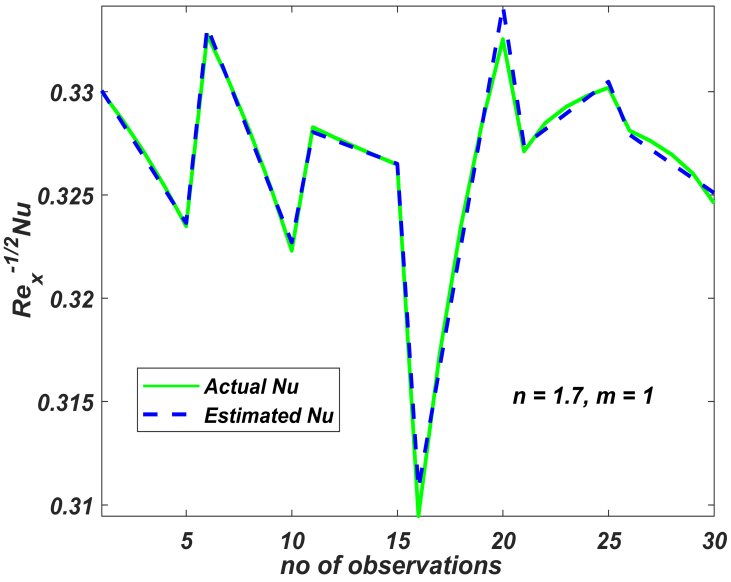

Figure 3.15: *Actual and estimated values* $Re_x^{-\frac{1}{2}}\,Nu$ *of when* $n = 1.7$

3.6 Conclusions

The major conclusions drawn from the current analysis are given below:

- The velocity profiles are directly proportional to the viscosity ratio parameter in shear thinning case and inversely proportional in shear thickening case.
- Weissenberg number enhances the velocity profiles in case of shear thickening fluids and retards the velocity profiles for shear thinning fluids.
- An exponential increase is observed in the temperature profile due to an increase in Biot number, heat generation/absorption and thermophoresis parameters.
- Hartmann number has a destructive effect on surface drag and the velocity profiles.
- Increase in the stretching ratio parameter improves the Y directional velocity profile.
- The concentration profile is enhanced and depleted with increasing thermophoresis and Brownian motion effects, respectively.
- The regression models are found to be in synchronization with the numerical results for the chosen values of parameters.

Chapter 4

Effects of multi-slip and distinct heat source on MHD Carreau nanofluid flow past an elongating cylinder using statistical method *

4.1 Introduction

Viscous fluid flow over an expanding cylinder has important applications in industry and engineering fields. Production of plastic films, rubber, copper wires, and paper are some industrial applications of viscous fluid flows. The heat transfer rate and stretching determines the quality and finishing of a product. Slip flow plays a significant role in engineering and medical field. Micro valves, hard disk drives, internal cavities and nozzles are a few examples where the slip flow is utilized. Carreau nanofluid fluid flow over an elongating cylinder with multiple slip effects has been investigated in the chapter. ESHS and LHS effects are incorporated in the current study. Numerical solutions of the problem are obtained by transforming the system of PDEs into a system of ODEs and hence solving the transformed system using fourth order Runge Kutta coupled with shooting. The consequence of various parameters on heat transfer rate for pseudo-plastic and dilatant fluids are inspected using multiple linear regression Furthermore, the response of different parameters on drag coefficient and mass transfer is quantified using slope of linear regression via data points.

*Published in: Heat Transfer (Wiley), 2021; 50 (6) 5652-5673

4.2 Mathematical formulation

A steady, incompressible two-dimensional flow of an electrically conducting Carreau nanofluid over an elongating cylinder with radius $r = \mathbb{R}$ is considered. A uniform magnetic field (of strength B_0) is administered along the r direction. Let the cylinder be fixed at origin, O and stretched with a velocity $\frac{a_v x}{l}$ along the x direction (see Figure 4.1). Simultaneous effects of LHS and ESHS are considered. C_w and T_w are the constant values of concentration and temperature at the stretching cylinder whereas the ambient values are denoted by T_∞ and C_∞ with r tending to infinity. The governing equations take the form ((I. Khan, Malik, Hussain, Khan, et al., 2017)):

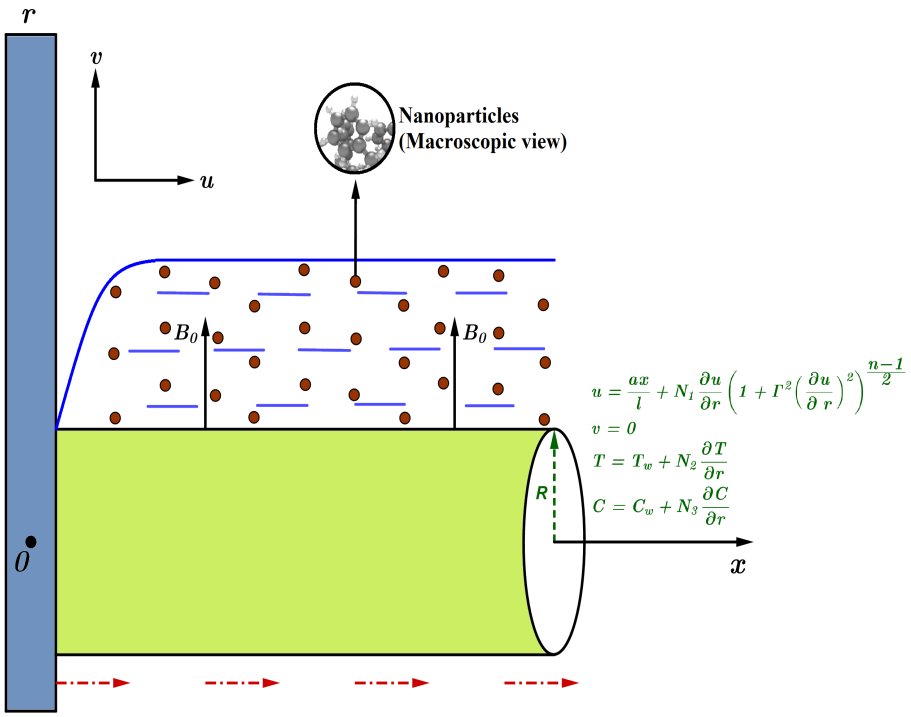

Figure 4.1: *Figurative representation*

$$\frac{\partial}{\partial x}(ru) + \frac{\partial}{\partial r}(rv) = 0 \tag{4.2.1}$$

$$u\frac{\partial u}{\partial x}+v\frac{\partial u}{\partial r}=\frac{\nu_f}{r}\frac{\partial u}{\partial r}\left(1+\Gamma^2\left(\frac{\partial u}{\partial r}\right)^2\right)^{\frac{n-1}{2}}+\nu_f\frac{\partial^2 u}{\partial r^2}\left(1+\Gamma^2\left(\frac{\partial u}{\partial r}\right)^2\right)^{\frac{n-1}{2}}$$
$$+\nu_f\left(n-1\right)\Gamma^2\left(\frac{\partial u}{\partial r}\right)^2\frac{\partial^2 u}{\partial r^2}\left(1+\Gamma^2\left(\frac{\partial u}{\partial r}\right)^2\right)^{\frac{n-3}{2}}-\frac{\sigma_f B_0^2 u}{\rho_f} \tag{4.2.2}$$

$$u\frac{\partial T}{\partial x}+v\frac{\partial T}{\partial r}=\alpha_f\left(\frac{\partial^2 T}{\partial r^2}+\frac{1}{r}\frac{\partial T}{\partial r}\right)+\frac{\left(\rho C_p\right)_p}{\left(\rho C_p\right)_f}\left(D_B\frac{\partial C}{\partial r}\frac{\partial T}{\partial r}+\frac{D_T}{T_\infty}\left(\frac{\partial T}{\partial r}\right)^2\right)$$
$$+\frac{q_T}{\left(\rho C_p\right)_f}\left(T-T_\infty\right)+\frac{q_E}{\left(\rho C_p\right)_f}\left(T_w-T_\infty\right)\ e^{\frac{-m\left(r^2-\mathbb{R}^2\right)}{2\mathbb{R}}\sqrt{\frac{a}{l\nu_f}}} \tag{4.2.3}$$

$$u\frac{\partial C}{\partial x}+v\frac{\partial C}{\partial r}=D_B\left(\frac{\partial^2 C}{\partial r^2}+\frac{1}{r}\frac{\partial C}{\partial r}\right)+\frac{D_T}{T_\infty}\left(\frac{\partial^2 T}{\partial r^2}+\frac{1}{r}\frac{\partial T}{\partial r}\right) \tag{4.2.4}$$

with

$$\left.\begin{array}{c} u=\frac{a_v x}{l}+N_1\frac{\partial u}{\partial r}\left(1+\Gamma^2\left(\frac{\partial u}{\partial r}\right)^2\right)^{\frac{n-1}{2}},\quad v=0,\\ T=T_w+N_2\frac{\partial T}{\partial r},\quad C=C_w+N_3\frac{\partial C}{\partial r}\quad when\ r=\mathbb{R}\\ u\to 0,\quad T\to T_\infty\ ,\quad C\to C_\infty\quad when\quad r\to\infty \end{array}\right\} \tag{4.2.5}$$

The following similarity variables ((Salahuddin et al., 2017)) are implemented in converting the above system of PDEs into a system of ODEs:

$$\left.\begin{array}{c} u=\frac{1}{r}\frac{\partial \psi}{\partial r},\quad v=\frac{-1}{r}\frac{\partial \psi}{\partial x},\quad \psi=\sqrt{\frac{a_v\nu_f}{l}}x\mathbb{R}f\left(\zeta\right),\\ \zeta=\left(\frac{r^2-\mathbb{R}^2}{2\mathbb{R}}\right)\sqrt{\frac{a_v}{l\nu_f}},\quad \theta=\frac{T-T_\infty}{T_w-T_\infty},\quad \phi=\frac{C-C_\infty}{C_w-C_\infty} \end{array}\right\} \tag{4.2.6}$$

The transformed equations are:

$$ff''+\left(n-1\right)We^2\kappa(f'')^3\left(1+We^2(f'')^2\right)^{\frac{n-3}{2}}+2\kappa f''\left(1+We^2(f'')^2\right)^{\frac{n-1}{2}}$$
$$-Mf'-\left(f'\right)^2+\left(1+2\kappa\zeta\right)f'''\left(1+We^2(f'')^2\right)^{\frac{n-1}{2}}$$
$$+\left(n-1\right)We^2\left(1+2\kappa\zeta\right)\left(f''\right)^2f'''\left(1+We^2(f'')^2\right)^{\frac{n-3}{2}}=0 \tag{4.2.7}$$

$$\left(1+2\kappa\zeta\right)\theta''+2\kappa\theta'+Pr\ f\ \theta'+\mathrm{Pr}\ \ \left(1+2\kappa\zeta\right)\left[Nb\phi'\theta'+Nt\ \left(\theta'\right)^2\right]+Pr\ Q_T\ \theta$$
$$+Pr\ Q_E\ e^{-m\zeta}=0 \tag{4.2.8}$$

$$\left(1+2\ \kappa\ \zeta\right)\ \phi''+\frac{Nt}{Nb}\ \left(1+2\ \kappa\ \zeta\right)\ \theta''+2\ \kappa\left[\phi'+\frac{Nt}{Nb}\ \theta'\right]+Sc\ f\ \phi'=0 \tag{4.2.9}$$

with

$$\left.\begin{array}{c} f\left(0\right)=0,\quad f'\left(0\right)=1+b_1f''\left(0\right)\left[1+We^2f''(0)^2\right]^{\frac{n-1}{2}},\quad \theta\left(0\right)=1+\gamma\theta'\left(0\right),\\ \phi\left(0\right)=1+b_3\phi'\left(0\right),\quad f'\left(\infty\right)\to 0,\quad \theta\left(\infty\right)\to 0,\quad \phi\left(\infty\right)\to 0 \end{array}\right\} \tag{4.2.10}$$

where the nondimensional parameters are taken as follows:

$$\left.\begin{array}{c} We^2 = \frac{\Gamma^2\ {a_v}^3\ x^2\ r^2}{\nu_f\ l^3\ \mathbb{R}^2},\quad \kappa = \frac{1}{\mathbb{R}}\sqrt{\frac{\nu_f\ l}{a_v}}\ ,\quad Sc = \frac{\nu_f}{D_B},\ M = \frac{\sigma_f\ B_0^2\ l}{a_v\ \rho_f},\quad Pr = \frac{\nu_f}{\alpha_f} \\ Nb = \frac{(\ \rho C_p\ )_p\ D_B\ (C_w - C_\infty)}{\nu_f\ (\ \rho C_p\ )_f},\ Nt = \frac{(\ \rho C_p\ )_p\ D_T\ (T_w - T_\infty)}{T_\infty\ \nu_f\ (\ \rho C_p\ )_f}, Q_T = \frac{q_T\ l}{a_v\ (\ \rho C_p\ )_f}, Q_E = \frac{q_E\ l}{a_v\ (\ \rho C_p\ )_f} \end{array}\right\} \tag{4.2.11}$$

Drag coefficient (Cf), mass transfer rate (Sh) and heat transfer rate (Nu) are defined as follows ((I. Khan et al., 2017)):

$$Cf = \frac{\tau_{rx}}{\frac{1}{2}\rho_f\left(\frac{a_v x}{l}\right)^2}\quad ,\quad Sh = \frac{x q_m}{D_B\left(C_w - C_\infty\right)}\quad ,\quad Nu = \frac{x q_w}{k_f\left(T_w - T_\infty\right)} \tag{4.2.12}$$

where

$$\tau_{rx} = \left(\mu_f\left(\frac{\partial u}{\partial r}\right)\left[1 + \Gamma^2\left(\frac{\partial u}{\partial r}\right)^2\right]^{\frac{n-1}{2}}\right)_{r\ =\ \mathbb{R}},\quad q_m = -D_B\left(\frac{\partial C}{\partial r}\right)_{r\ =\ \mathbb{R}}\ , \qquad q_w = -k_f\left(\frac{\partial T}{\partial r}\right)_{r\ =\ \mathbb{R}} \tag{4.2.13}$$

The reduced physical quantities (using (4.2.6)) take the form:

$$\frac{Cf(Re_x)^{\frac{1}{2}}}{2} = f''(0)\left(1 + We^2(f''(0))^2\right)^{\frac{n-1}{2}},\quad Sh(Re_x)^{-\left(\frac{1}{2}\right)} = -\phi'(0)\ , \qquad Nu(Re_x)^{-\left(\frac{1}{2}\right)} = -\theta'(0) \tag{4.2.14}$$

4.3 Numerical solution

Table 4.1: *Comparison of* $Nu(Re_x)^{\frac{-1}{2}}$ *with* $We = \kappa = M = Q_T = Q_E = Nt = b_1 = \gamma = b_3 = 0$ *and* $Nb \to 0$

Pr	$Nu(Re_x)^{-\frac{1}{2}}$	
	(W. Khan & Pop, 2010)	RK4
0.7	0.4539	0.453932
2	0.9113	0.911359
7	1.8954	1.895428
20	3.3539	3.354174

The highly nonlinear coupled ODE (4.2.7) to (4.2.9) with corresponding boundary conditions (4.2.10) are solved by engaging Runge-Kutta method of fourth order together with shooting technique with an accuracy of 10^{-6}. For the numerical computation we have restricted infinity to 15 and a step size of 0.1 is chosen. The

accuracy of the numerical method is guaranteed by performing a restrictive study with the already published results of (W. Khan & Pop, 2010) and an excellent agreement (discussed in Table 4.1) is noted. Additionally, the numerical values computed using Runge-Kutta of fourth order (RK4) is compared with BVP5C and RKF45 which are presented in Table 4.2 and four-digit accuracy is obtained. To accomplish this, we assume:

$$f = h_1, \quad f' = h_2, \quad f'' = h_3, \quad \theta = h_4, \quad \theta' = h_5, \quad \phi = h_6, \quad \phi' = h_7 \tag{4.3.1}$$

Accordingly, equation (4.2.7)-(4.2.10) takes the form:

$$\begin{gathered} h_1^{'} = h_2, \quad h_2^{'} = h_3, \\ h_3^{'} = \frac{-2\ \kappa\ h_3\left(1+We^2\ h_3^2\right)^{\frac{n-1}{2}} -(n-1)We^2\ \kappa\ h_3^3\left(1+We^2\ h_3^2\right)^{\frac{n-3}{2}} +M\ h_2+h_2^2-h_1h_3}{\left[(1+2\ \kappa\ \zeta)\left(1+We^2\ h_3^2\right)^{\frac{n-1}{2}} +(n-1)We^2(1+2\ \kappa\ \zeta)h_3^2\left(1+We^2\ h_3^2\right)^{\frac{n-3}{2}}\right]} \\ h_4^{'} = h_5, \\ h_5^{'} = \frac{-2\ \kappa\ h_5-Pr\ h_1\ h_5-\mathrm{Pr}\ (1+2\ \kappa\ \zeta)\left[Nb\ h_5\ h_7+Nt\ h_5^2\ \right]-Pr\ Q_T\ h_4-Pr\ Q_E\ e^{-m\zeta}}{1+2\ \kappa\ \zeta} \\ h_6^{'} = h_7,\ h_7^{'} = \frac{-\frac{Nt}{Nb}(1+2\ \kappa\ \zeta)\ h_5^{'}-2\ \kappa\left[h_7+\frac{Nt}{Nb}\ h_5\right]-Sc\ h_1\ h_7}{1+2\ \kappa\ \zeta} \end{gathered} \tag{4.3.2}$$

The following initial conditions are considered:

$$\begin{gathered} h_1(0) = 0, \quad h_2(0) = 1 + b_1\ s_1[1 + We^2\ {s_1}^2]^{\frac{n-1}{2}}, \quad h_3(0) = s_1 \\ h_4(0) = 1 + \gamma\ s_2, \quad h_5(0) = s_2, \quad h_6(0) = 1 + b_3\ s_3, \quad h_7(0) = s_3 \end{gathered} \tag{4.3.3}$$

where $s_1,\ s_2,\ s_3$ are unknowns and are found using Newton-Raphson method with a suitable initial guess.

4.4 Result and discussion

The impact of velocity slip (b_1), thermal slip (γ), concentration slip (b_3), Weissenberg number (We), linear heat source parameter (Q_T), thermophoresis parameter (Nt), Hartmann number (M), exponential heat source parameter (Q_E), curvature parameter (κ), Brownian motion parameter (Nb) on concentration $(\phi(\zeta))$, temperature $(\theta(\zeta))$ and velocity $\left(f'(\zeta)\right)$ profiles are carefully studied through Figures 4.2 - 4.13. The Schmidt number (Sc) and Prandtl number (Pr) are fixed at 1 and 3 respectively.

The discrepancy in $f'(\zeta)$ due to an increase in b_1 is depicted in Figure 4.2. Augmentation in b_1 shows a reduction in $f'(\zeta)$ for both dilatant and pseudo-plastic

Table 4.2: *Comparison of* $-\frac{1}{2}Cf(Re_x)^{\frac{1}{2}}$ *with* $M = Q_T = Q_E = Nt = b_1 = \gamma = b_3 = 0$ *and* $Nb \to 0$

n	We	κ	$-\frac{1}{2}Cf(Re_x)^{\frac{1}{2}}$		
			BVP5C	RKF45	RK4
0.5	1	0.2	0.989702	0.989709	0.989709
	1	0.4	1.03995	1.039965	1.039965
	1	0.6	1.088334	1.088361	1.088361
	2	0.2	0.867191	0.867198	0.867198
	2	0.4	0.901331	0.901343	0.901343
	2	0.6	0.934526	0.934545	0.934545
	3	0.2	0.777193	0.777201	0.777201
	3	0.4	0.80436	0.804374	0.804374
	3	0.6	0.830948	0.830972	0.830972
1.5	1	0.2	1.145708	1.145708	1.145708
	1	0.4	1.239624	1.239625	1.239625
	1	0.6	1.332933	1.332936	1.332936
	2	0.2	1.247964	1.247965	1.247965
	2	0.4	1.367059	1.367061	1.367061
	2	0.6	1.485123	1.485127	1.485127
	3	0.2	1.335538	1.335539	1.335539
	3	0.4	1.474373	1.474375	1.474375
	3	0.6	1.61158	1.611585	1.611585

fluids. Mounting values of b_1 causes a reduction in the movement of fluid particles and hence $f'(\zeta)$ decreases. Figure 4.3 delineates the decrease in $\theta(\zeta)$ with increasing γ values. Physically, augmenting thermal slip parameter minimises the sensitivity of the fluid flow within the boundary layer which diminishes the amount of heat produced and thus reduces the temperature. It is further noted that the thermal boundary layer thickness of pseudo-plastic fluid is greater than dilatant fluid.

Figure 4.4 depicts the variation of $f'(\zeta)$ due to the enhancement in M. An augmentation in M produces Lorentz force and hence a resistance force acts in the direction opposite to the fluid flow which retards the velocity of both fluids. An increase in We escalates the relaxation time of Carreau nanofluid and the fluid thickness grows which implies that the velocity profile of shear thinning fluid reduces whereas $f'(\zeta)$ enhances in the case of shear-thickening fluid (shown in Figure 4.5). Figure 4.6 depicts the effect of We on $\theta(\zeta)$. An opposite nature is observed on $\theta(\zeta)$ for shear thinning and thickening fluid. Variation in $\theta(\zeta)$ concerning κ is described in Figure 4.7. Physically, an increase in κ reduces the cylinder's radius

and surface area associated with the fluid which declines the heat transfer rates and hence $\theta(\zeta)$ rises. Figure 4.8 elucidates the consequence of Nb on $\theta(\zeta)$. An increase in Nb promotes the random motion of nanoparticles which enhances the temperature profile. Growing Nt values causes the hot fluid particles to move towards the cold region increasing $\theta(\zeta)$ (illustrated in Figure 4.9).

Figures 4.10 and 4.11 describe the variation of $\phi(\zeta)$ due to a rise in Nb and Nt, respectively. An increase in Nb reduces the concentration profile whereas an increase in Nt increases $\phi(\zeta)$. Figures 4.12 and 4.13 illustrate the variation in $\theta(\zeta)$ with increasing Q_T and Q_E values. Both parameters enhance $\theta(\zeta)$. It is also noted that temperature profile due to variation in Q_E has faster convergence than the temperature profile due to varying Q_T. The simultaneous impact of differing

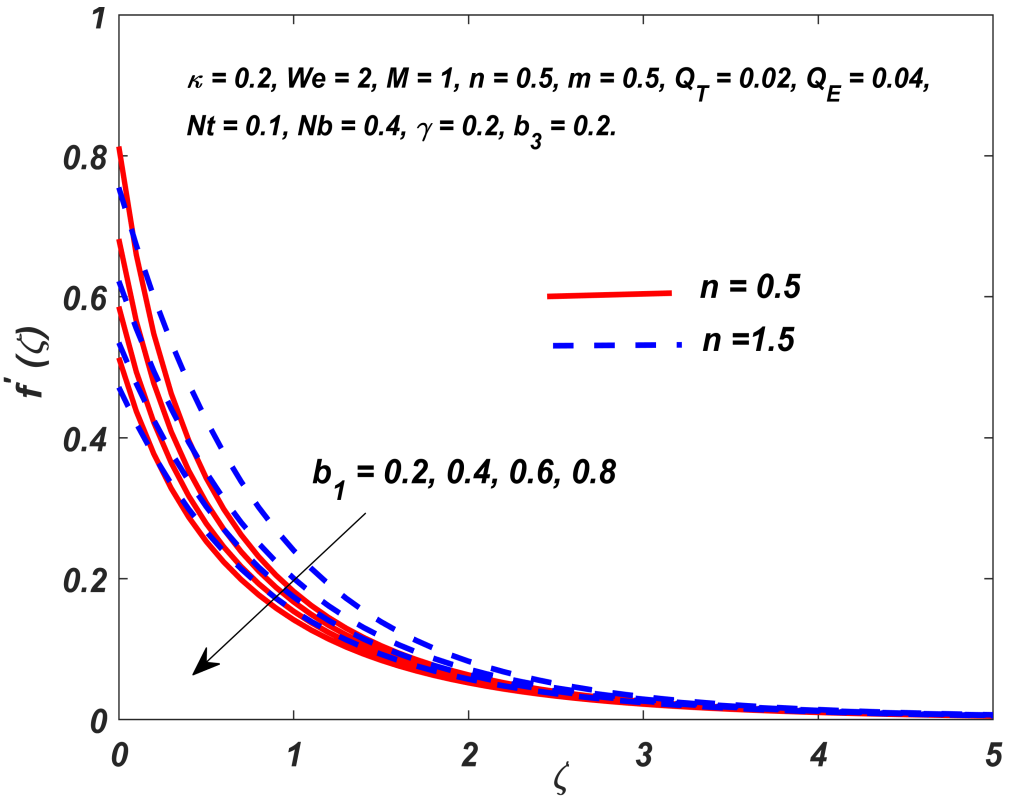

Figure 4.2: *$f'(\zeta)$ for differing b_1 values*

parameters on $Nu(Re_x)^{\frac{-1}{2}}$ is studied using surface plots which have been graphed in Figures $4.14 - 4.19$. The 4.14, 4.16, and 4.18 figures analyses the effects in case of shear thinning fluids while 4.15,4.17 and 4.19 figures examines the effects for

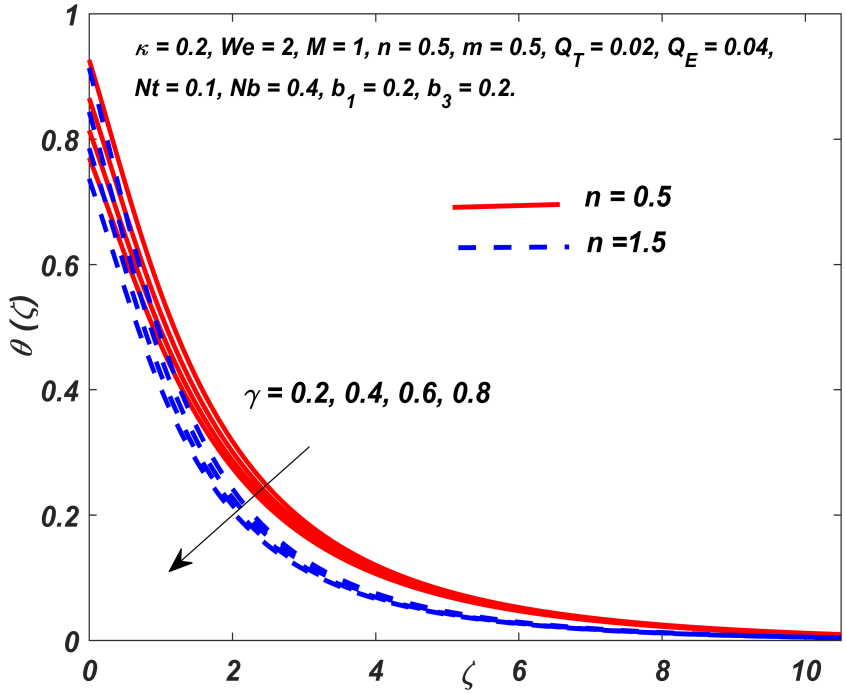

Figure 4.3: $\theta(\zeta)$ *for differing* γ *values*

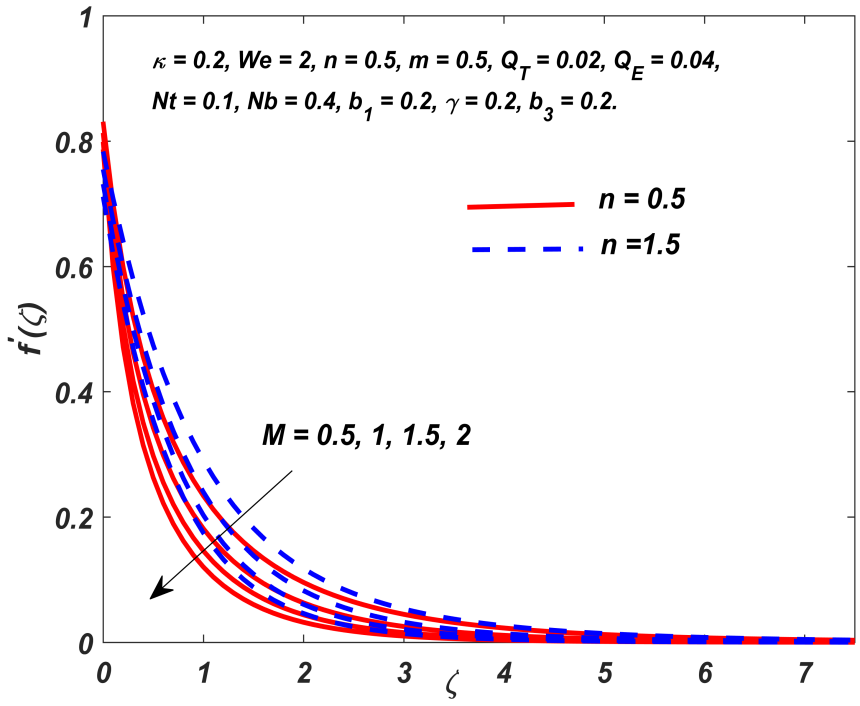

Figure 4.4: $f'(\zeta)$ *for differing* M *values*

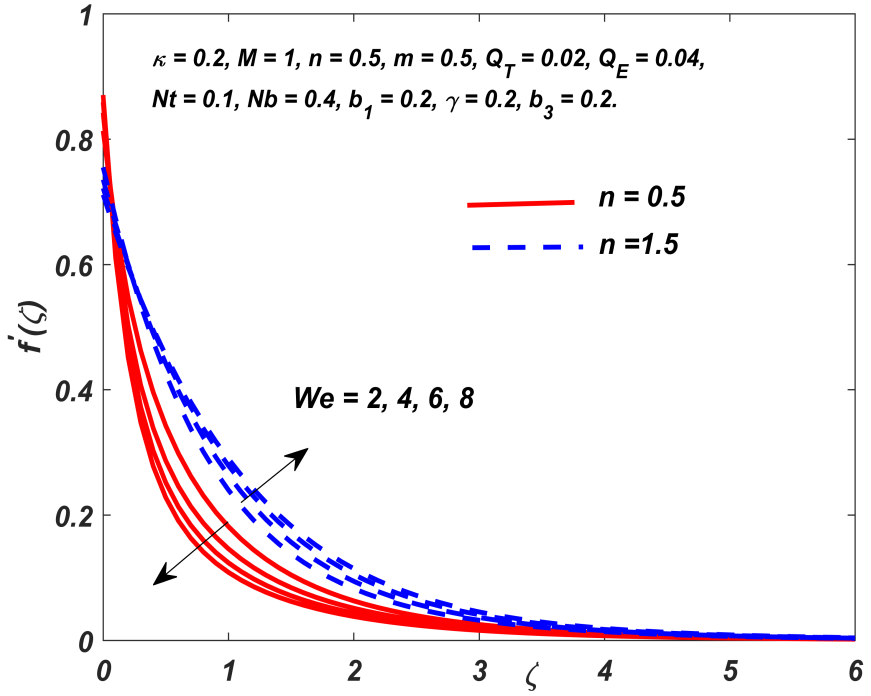

Figure 4.5: *$f'(\zeta)$ for differing We values*

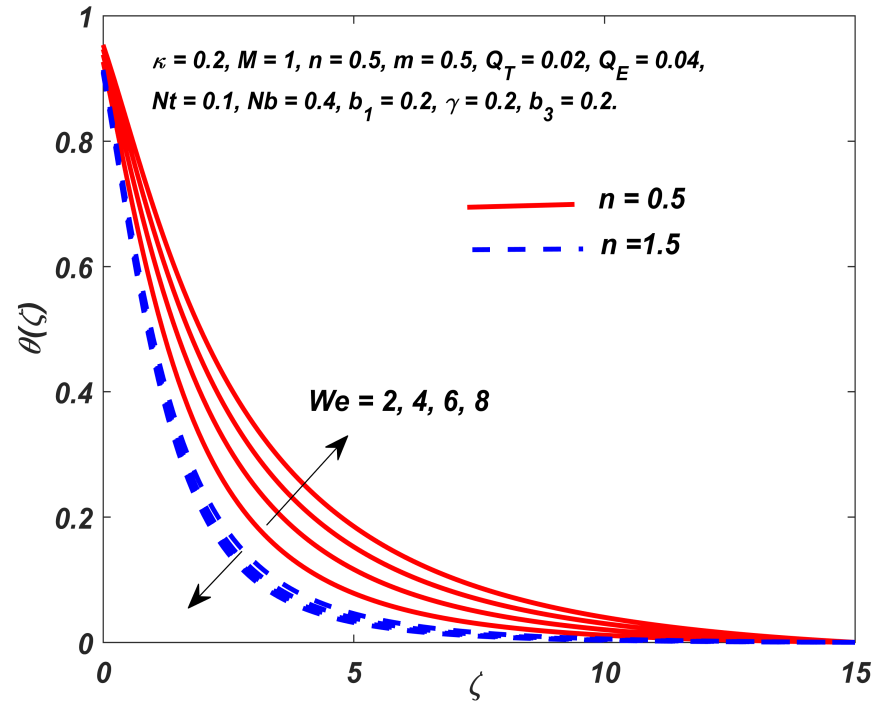

Figure 4.6: *$\theta(\zeta)$ for differing We values*

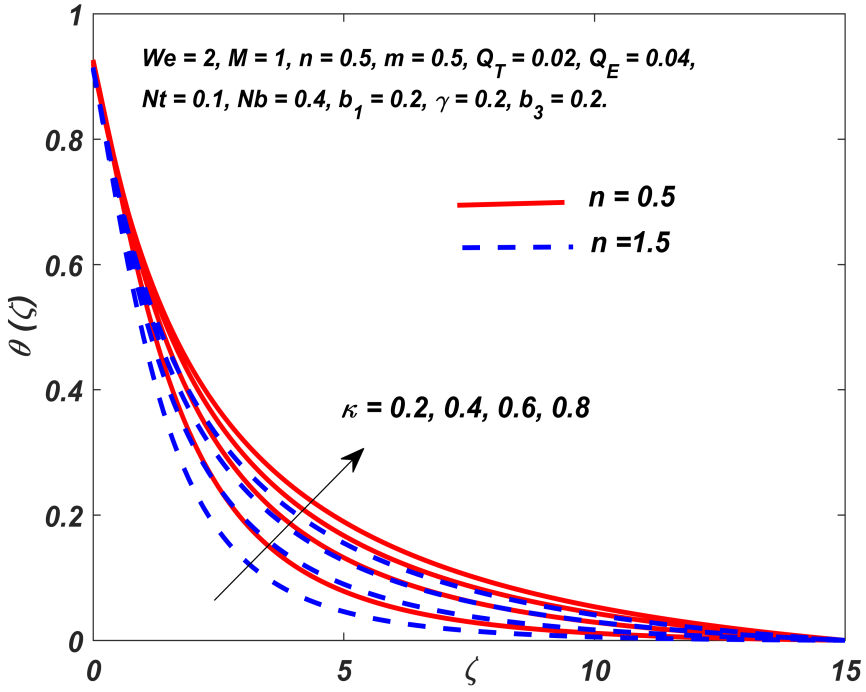

Figure 4.7: $\theta(\zeta)$ *for differing* κ *values*

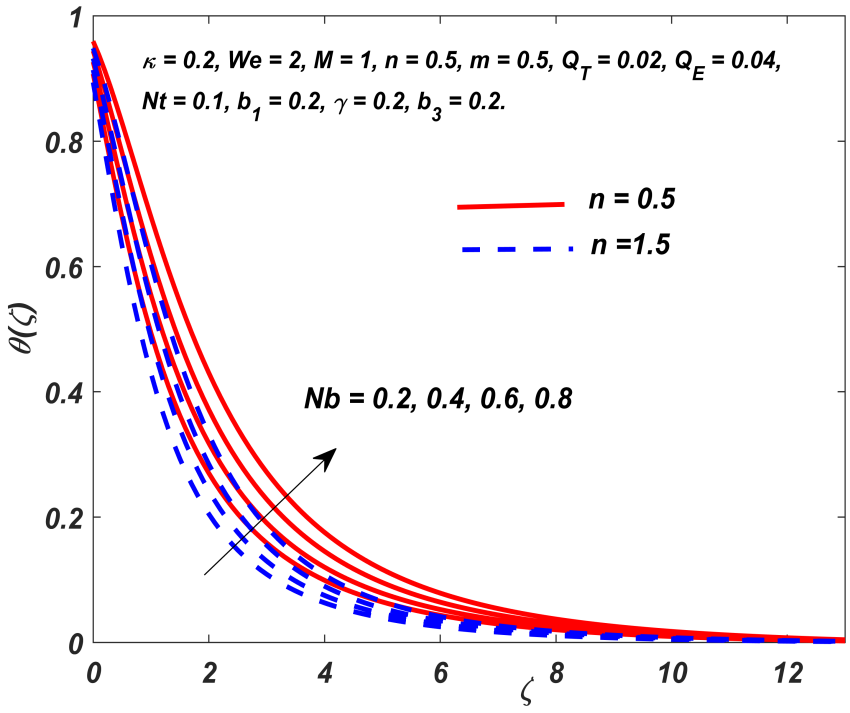

Figure 4.8: $\theta(\zeta)$ *for differing* Nb *values*

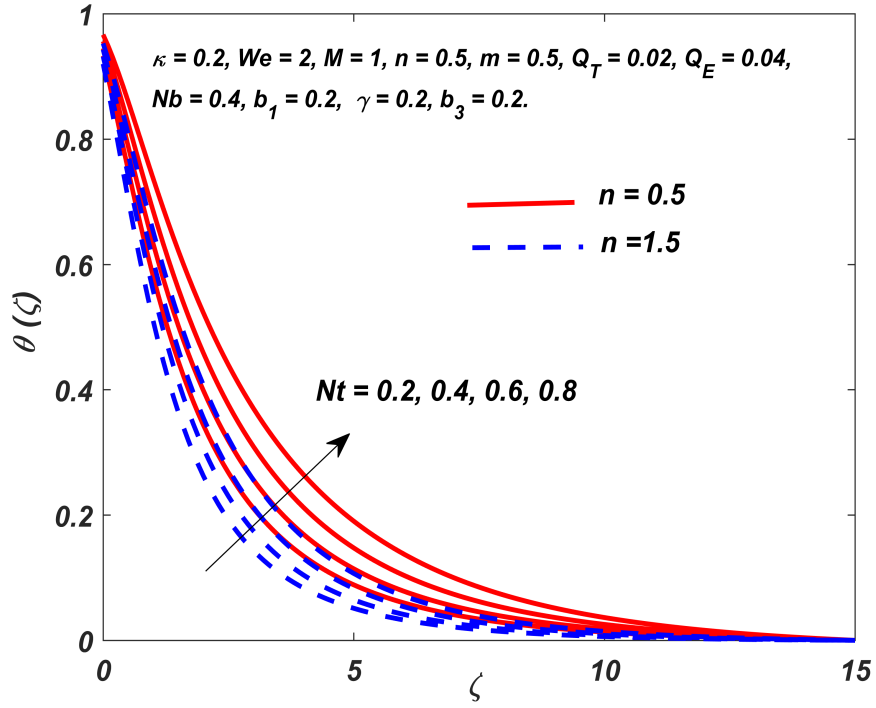

Figure 4.9: $\theta(\zeta)$ *for differing* Nt *values*

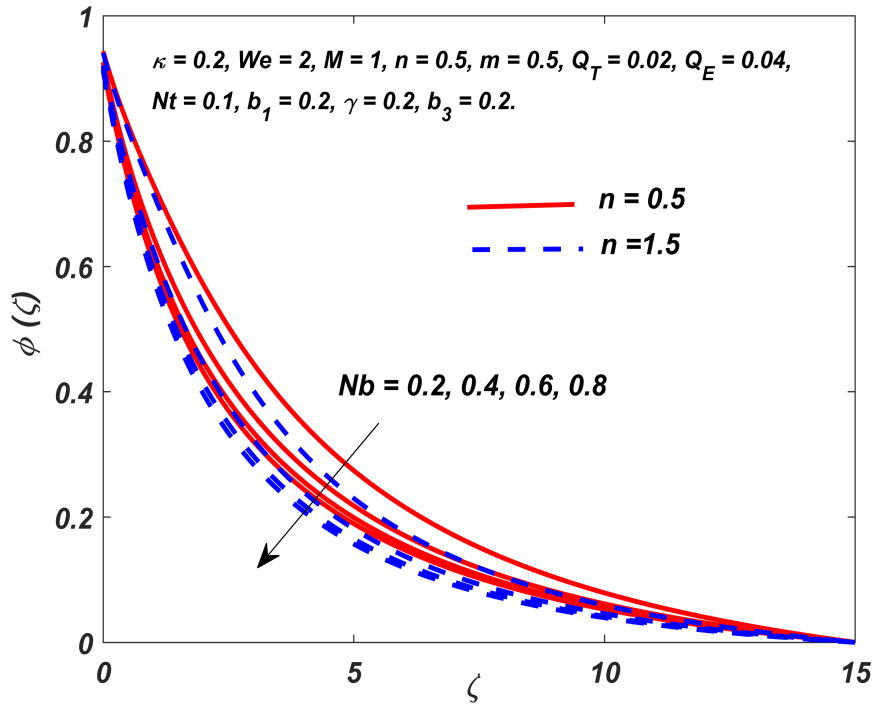

Figure 4.10: $\phi(\zeta)$ *for differing* Nb *values*

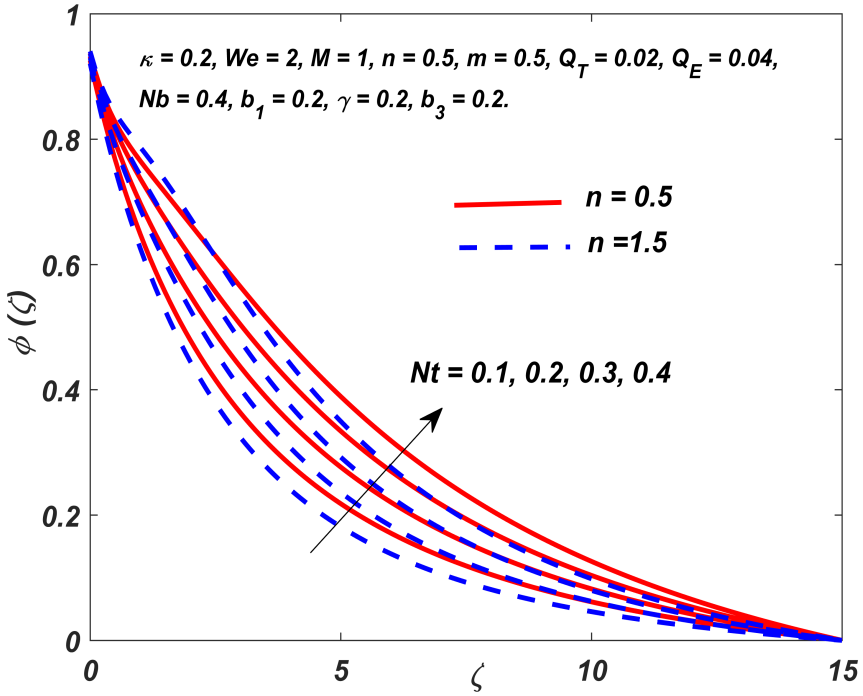

Figure 4.11: *$\phi(\zeta)$ for differing Nt values*

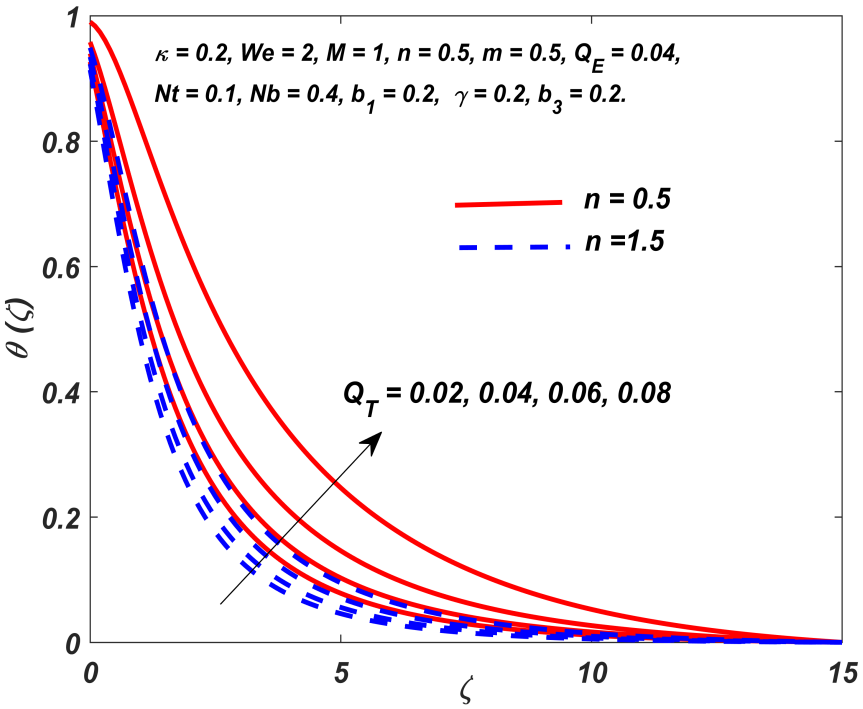

Figure 4.12: *$\theta(\zeta)$ for differing Q_T values*

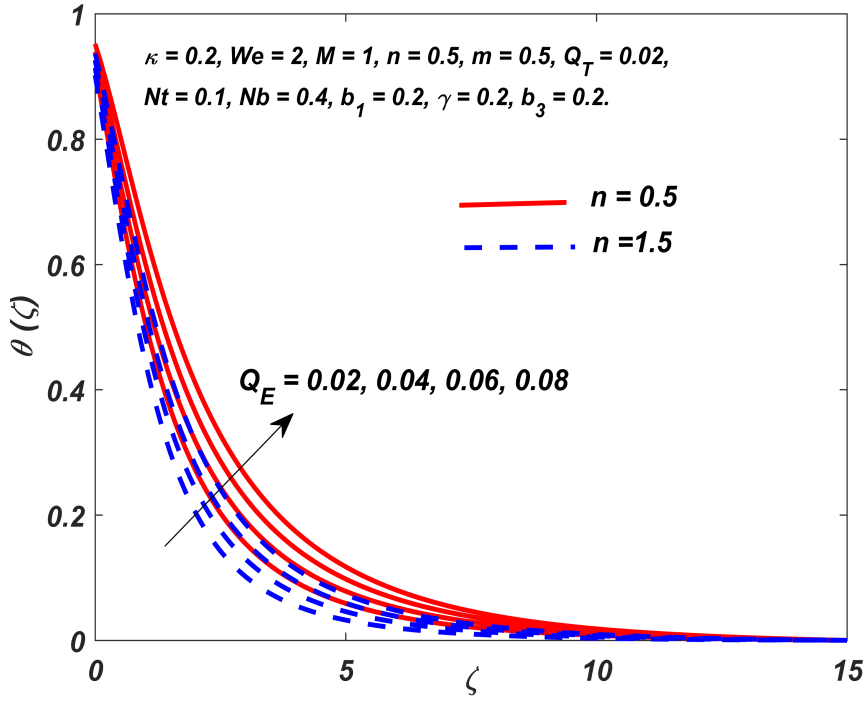

Figure 4.13: $\theta(\zeta)$ *for differing* Q_E *values*

shear thickening fluids. The impact of Nt and Nb on the heat transfer rate is described in Figures 4.14 and 4.15 with $\kappa = 0.2,\ We = 2,\ M = 1,\ m = 0.5,\ Q_E = 0.04,\ Q_T = 0.02$ and $b_1 = \gamma = b_3 = 0.2$. $Nu(Re_x)^{\frac{-1}{2}}$ diminishes for greater values of Nb and Nt in both cases ($n = 0.5$ and $n = 1.5$).

$Nu(Re_x)^{\frac{-1}{2}}$ is elevated with lower Q_T and Q_E values as shown in Figures 4.16 and 4.17 with $\kappa = 0.2,\ We = 2,\ M = 1,\ m = 0.5,\ Nb = 0.4,\ Nt = 0.1$ and $b_1 = \gamma = b_3 = 0.2$. The parallel effect of γ and κ on the heat transfer coefficient with $We = 2,\ M = 1, m = 0.5,\ Q_E = 0.04,\ Q_T = 0.02,\ Nb = 0.4,\ Nt = 0.1$ and $b_1 = b_3 = 0.2$ is explained in Figures 4.18 and 4.19. A rise in κ values enhances $Nu(Re_x)^{\frac{-1}{2}}$ whereas the heat transfer rate diminishes due to high thermal slip values. Hence, it can be concluded that $Nu(Re_x)^{\frac{-1}{2}}$ is directly proportional to κ and inversely proportional to Nt , Nb , Q_T , Q_E *and* γ. The consequence of different parameters on drag coefficient and Sherwood number when $n = 0.5$ and $n = 1.5$ is described in the table 4.3 and 4.4. Increment/decrement rate indicates the percentage change in the current value with respect to the previous value (preceding entry in the table). A positive sign denotes an increment while a negative sign indicates a decrement.

From table 4.3, it is understood that $-\frac{1}{2}Cf(Re_x)^{\frac{1}{2}}$ $\{for\ both\ cases\}$ increases with

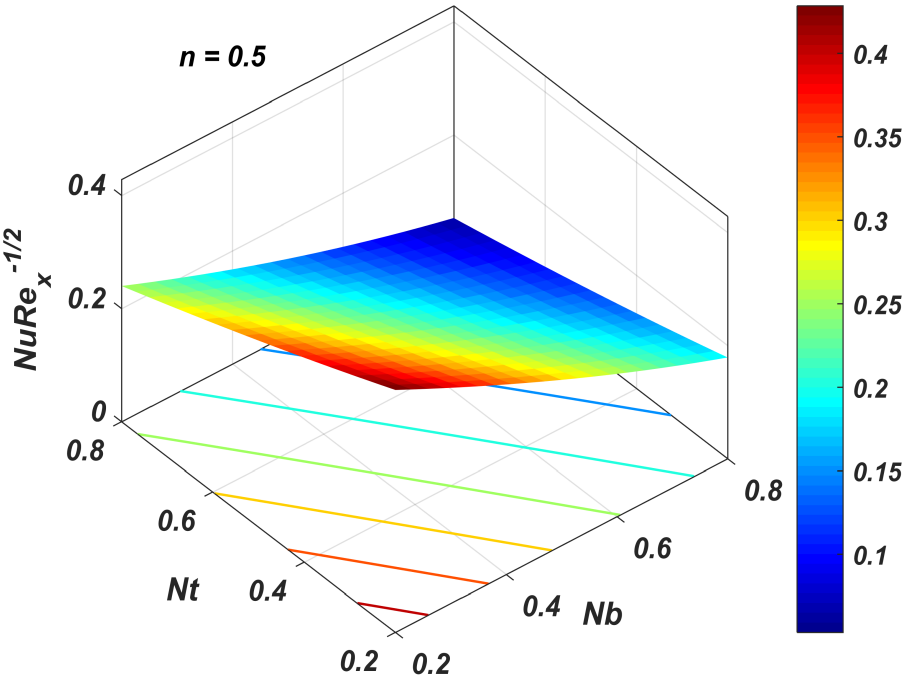

Figure 4.14: *Parallel effect of* Nb *and* Nt *on* $Nu(Re_x)^{\frac{-1}{2}}$ *when* $n = 0.5$

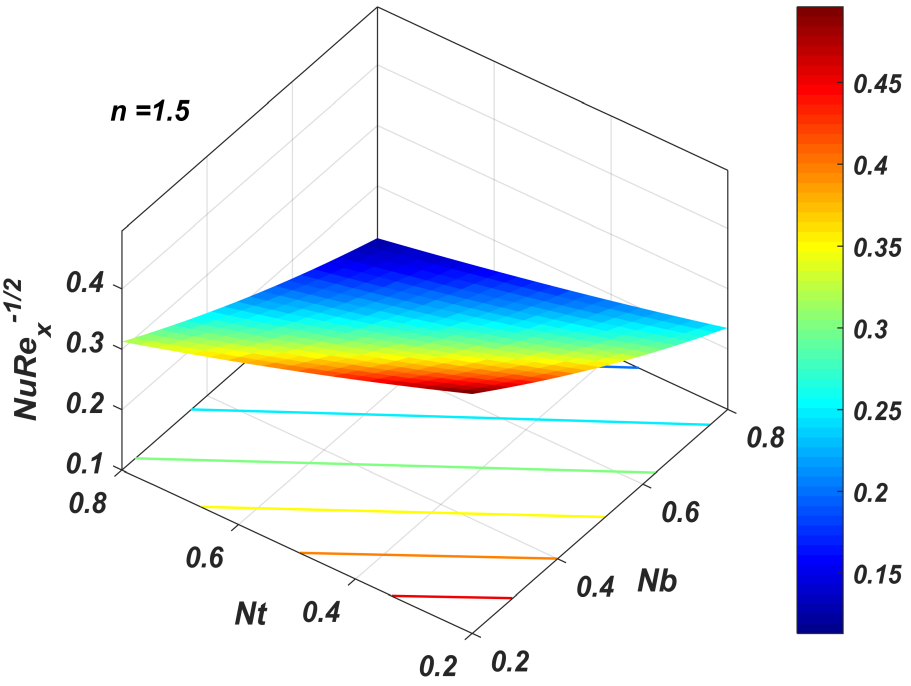

Figure 4.15: *Parallel effect of* Nb *and* Nt *on* $Nu(Re_x)^{\frac{-1}{2}}$ *when* $n = 1.5$

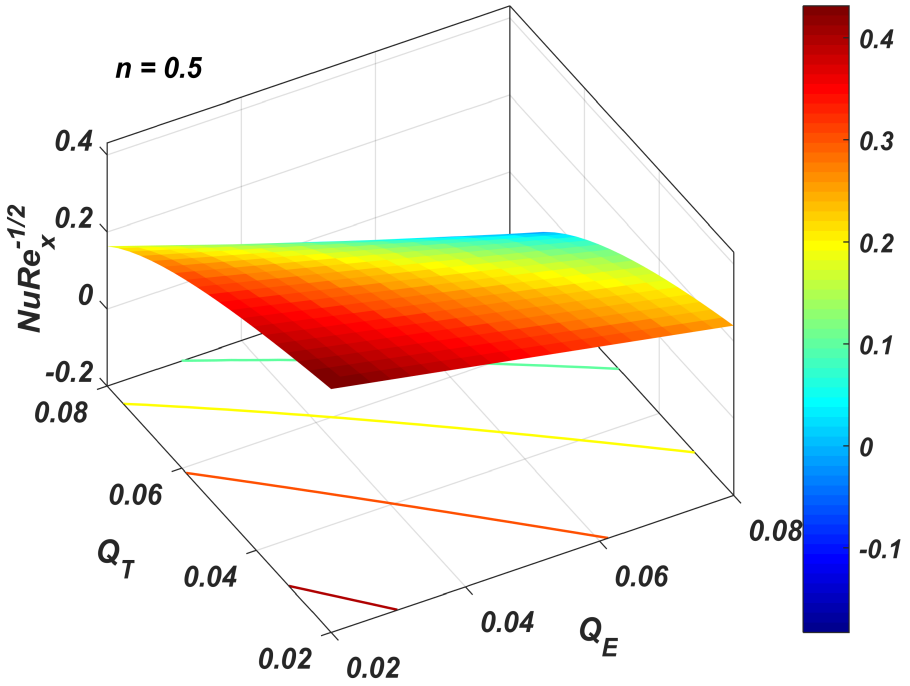

Figure 4.16: *Parallel effect of* Q_T *and* Q_E *on* $Nu(Re_x)^{\frac{-1}{2}}$ *when* $n = 0.5$

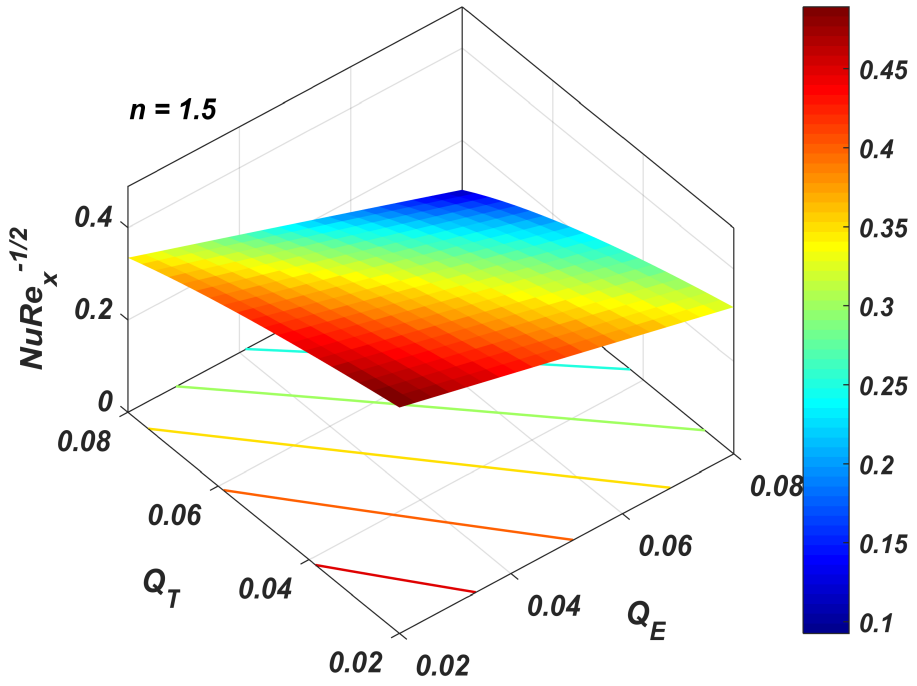

Figure 4.17: *Parallel effect of* Q_T *and* Q_E *on* $Nu(Re_x)^{\frac{-1}{2}}$ *when* $n = 1.5$

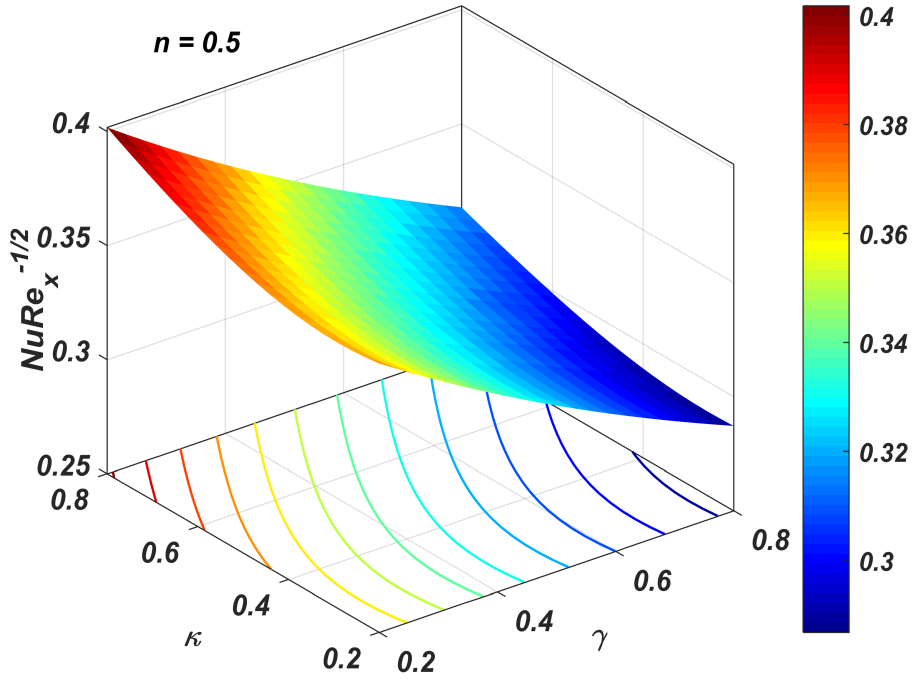

Figure 4.18: *Parallel effect of* γ *and* κ *on* $Nu(Re_x)^{\frac{-1}{2}}$ *when* $n = 0.5$

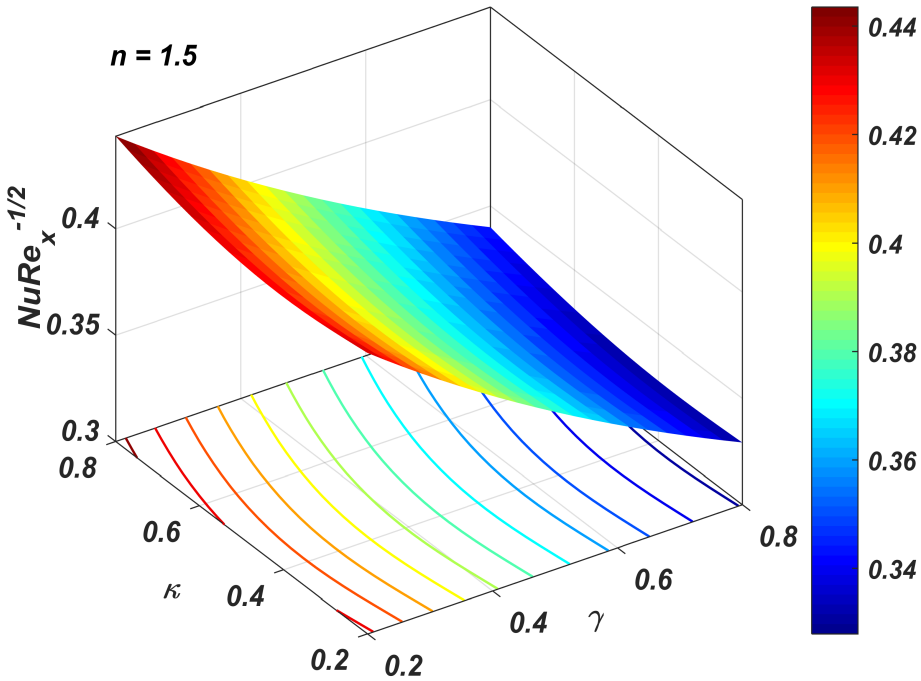

Figure 4.19: *Parallel effect of* γ *and* κ *on* $Nu(Re_x)^{\frac{-1}{2}}$ *when* $n = 1.5$

increase in κ and M values and decreases for increasing values of b_1. It is also seen that We has a negative response on $-\frac{1}{2}Cf(Re_x)^{\frac{1}{2}}$ $(when\ n = 0.5)$ and it is also seen that the result is reversed for $-\frac{1}{2}Cf(Re_x)^{\frac{1}{2}}$ $(when\ n = 1.5)$. From table 4.4, it is understood that κ and Nb enhances and Nt and b_3 diminishes the mass transfer rate.

The nature of variation in Sherwood number and skin friction coefficients due to different parameters has been quantified in table 4.3 and 4.4 using slope of linear regression. Positive slope implies that the corresponding parameter enhances the Sherwood number/drag coefficient. The magnitude of slope represents the rate of increase/decrease of drag coefficient/Sherwood number per unit value of the corresponding parameters.

Table 4.3: *Variation in* $-\frac{1}{2}Cf(Re_x)^{\frac{1}{2}}$ $\{at\ \zeta = 0\ \}$ *when* $\kappa = 0.2$, $We = 2$, $M = 1$, $m = 0.5$, $Q_T = 0.02$, $Q_E = 0.04$, $Nt = 0.1$, $Nb = 0.4$, $b_1 = 0.2$, $\gamma = 0.2$ *and* $b_3 = 0.2$

				$-\frac{1}{2}Cf(Re_x)^{\frac{1}{2}}$		**Increment(%)**	
We	κ	M	b_1	$n = 0.5$	$n = 1.5$	$n = 0.5$	$n = 1.5$
2				0.93454	1.225294		
4				0.789978	1.323258	-15.469	7.995
6				0.705486	1.391796	-10.695	5.18
8				0.648771	1.444318	-8.039	3.774
Slope				-0.04709	0.03628		
	0.2			0.93454	1.225294		
	0.4			0.960097	1.29569	2.735	5.745
	0.6			0.984375	1.361064	2.529	5.045
	0.8			1.007556	1.422289	2.355	4.498
Slope				0.121664	0.328178		
		0.5		0.845765	1.082917		
		1		0.93454	1.225294	10.496	13.148
		1.5		1.00619	1.342749	7.667	9.586
		2		1.066699	1.443231	6.014	7.483
Slope				0.146891	0.239679		
			0.2	0.93454	1.225294		
			0.4	0.795551	0.944656	-14.872	-22.904
			0.6	0.690287	0.775479	-13.232	-17.909
			0.8	0.608344	0.660741	-11.871	-14.796
Slope				-0.54193	-0.93142		

Table 4.4: *Variation in* $Sh(Re_x)^{-\frac{1}{2}}$ $\{at\ \zeta = 0\}$ *when* $\kappa = 0.2$, $We = 2$, $M = 1$, $m = 0.5$, $Q_T = 0.02$, $Nt = 0.1$ $Q_E = 0.04$, $Nb = 0.4$, $b_i = 0.2$, $\gamma = 0.2$ *and* $b_3 = 0.2$

				$Sh(Re_x)^{-\frac{1}{2}}$		Increment(%)	
κ	Nt	Nb	b_3	$n = 0.5$	$n = 1.5$	$n = 0.5$	$n = 1.5$
0.2				0.371478	0.396258		
0.4				0.459318	0.472917	23.646	19.346
0.6				0.541304	0.549809	17.849	16.259
0.8				0.616713	0.622549	13.931	13.23
Slope				0.408845	0.377883		
	0.1			0.371478	0.396258		
	0.2			0.339432	0.352109	-8.627	-11.142
	0.3			0.320597	0.320201	-5.549	-9.062
	0.4			0.314358	0.299672	-1.946	-6.411
Slope				-0.190197	-0.321665		
		0.2		0.28382	0.296854		
		0.4		0.371478	0.396258	30.885	33.486
		0.6		0.399384	0.428064	7.512	8.027
		0.8		0.412213	0.442835	3.212	3.451
Slope				0.206541	0.234875		
			0.2	0.371478	0.396258		
			0.4	0.340335	0.360624	-8.384	-8.993
			0.6	0.313986	0.330844	-7.742	-8.258
			0.8	0.291408	0.305591	-7.191	-7.633
Slope				-0.133281	-0.150891		

4.5 Statistical Analysis

4.5.1 Correlation and Probable Error

A statistical technique which helps in predicting the nature and quantity of relationship between two variables is known as correlation coefficient (r_c). The nature of relationship is elucidated using sign of r_c and its magnitude predicts the quantity of relationship. Nature of relationship is identified as positive or negative based on the relation. A positive value in r_c reflects that an increase in one variable correspondingly increases the other variable and a reverse nature is observed for a negative r_c value. Probable error (PE) guarantees the reliability of r_c and correlation is ought to be important ((Fisher et al., 1921)) when $\left|\frac{r_c}{PE}\right| > 6$; where $\tilde{n}$ denotes the number of observations and $PE = \left(\frac{1-{r_c}^2}{\sqrt{\tilde{n}}}\right) 0.6745$.

It is evident from table 4.5 that b_1, γ, M, Nb, Nt, Q_T and Q_E are negatively corre-

lated while κ exhibits a positive correlation with $Nu(Re_x)^{\frac{-1}{2}}$ $\{both\ cases\}$. It is also noted that We shows a differing nature on the heat transfer rate, i.e., r_c is positive in case of $Nu(Re_x)^{\frac{-1}{2}}$ $\{\text{n} = 1.5\}$ and negative for $Nu(Re_x)^{\frac{-1}{2}}$ $\{0.5\}$. From $\left|\frac{r_c}{PE}\right|$ values, it can be concluded that all the parameter of $Nu(Re_x)^{\frac{-1}{2}}$ $\{both\ cases\}$ are significant.

Table 4.5: *Probable error* (PE) *and correlation coefficient* (r_c) *of* $Nu(Re_x)^{\frac{-1}{2}}$

Parameter	$Nu(Re_x)^{\frac{-1}{2}}$ $(n = 0.5)$			$Nu(Re_x)^{\frac{-1}{2}}$ $(n = 1.5)$		
	r_c	PE	$\left\|\frac{r_c}{PE}\right\|$	r_c	PE	$\left\|\frac{r_c}{PE}\right\|$
Q_E	-1	0	2350568	-1	0	2572632.69
b_1	-0.99878	0.00073	1361.92	-0.99527	0.00284	349.98
γ	-0.99756	0.00147	678.85	-0.99705	0.00178	560.3
M	-0.99953	0.00028	3516.14	-0.99971	0.00017	5789.53
We	-0.99382	0.00372	267.47	0.96969	0.01801	53.85
κ	0.93349	0.03879	24.06	0.99667	0.002	497.15
Nb	-0.99886	0.00069	1453.69	-0.99903	0.00058	1712.46
Nt	-0.99948	0.00031	3183.46	-0.99918	0.0005	2012.09
Q_T	-0.97908	0.01249	78.41	-0.99531	0.00282	352.67

4.5.2 Regression Analysis

Multiple linear regression model of heat transfer rate (for n =0.5 and 1.5) is estimated using 45 set of values within the range $[0.2, 0.8]$ for b_1, γ, N_b, κ and Nt, $[0.02, 0.08]$ for Q_T and Q_E, $[0.5, 2]$ for M and $[2, 8]$ for We. The estimated model is given by:

$$Nu_{est}\,(n) = c + a_M\,M + a_{We}\,We + a_\kappa\,\kappa + a_{Nb}\,Nb + a_{Nt}\,Nt + a_{b_1}\,b_1 + a_\gamma\,\gamma + a_{Q_T}\,Q_T + a_{Q_E}\,Q_E \tag{4.5.1}$$

where c, a_{b_1}, a_γ, a_M, a_{We}, a_κ, a_{Nb}, a_{Nt}, a_{Q_T} and a_{Q_E} are the estimated regression coefficients. Nusselt number is estimated individually for $n = 0.5$ and $n = 1.5$ with the aid of MATLAB software. The estimated regression models are:

$$\begin{aligned} Nu_{est}\,(0.5) = {} & 1.03641 - 0.26072\,b_1 - 0.14210\,\gamma - 0.12386\,M - 0.02418\,We \\ & + 0.04218\,\kappa - 0.42863\,Nb - 0.29557\,Nt - 4.69465\,Q_T - 3.20600\,Q_E \end{aligned} \tag{4.5.2}$$

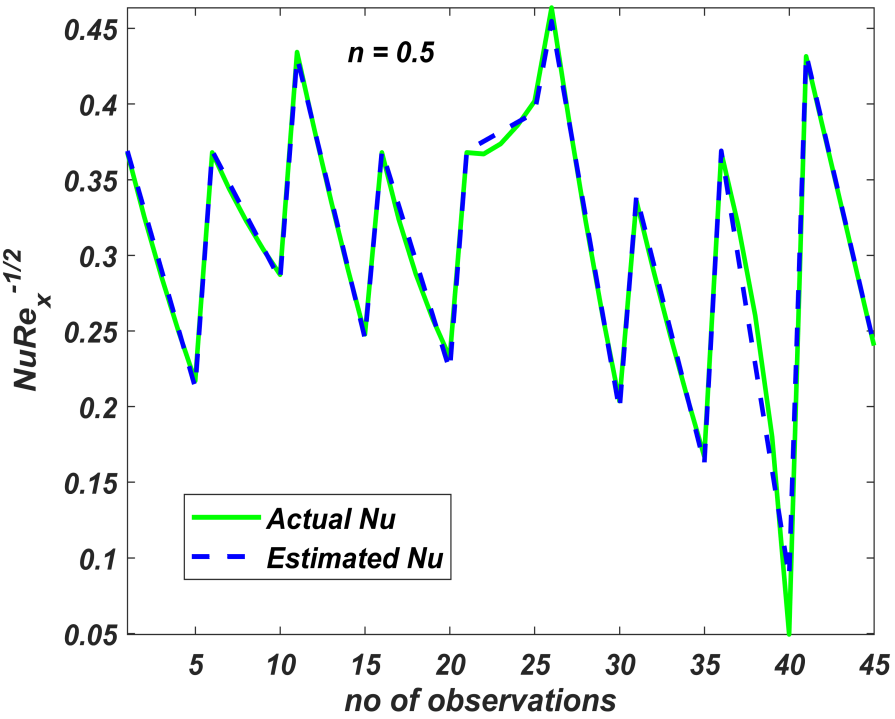

Figure 4.20: *Estimated versus actual* $Nu(Re_x)^{\frac{-1}{2}}$ *when* $n = 0.5$

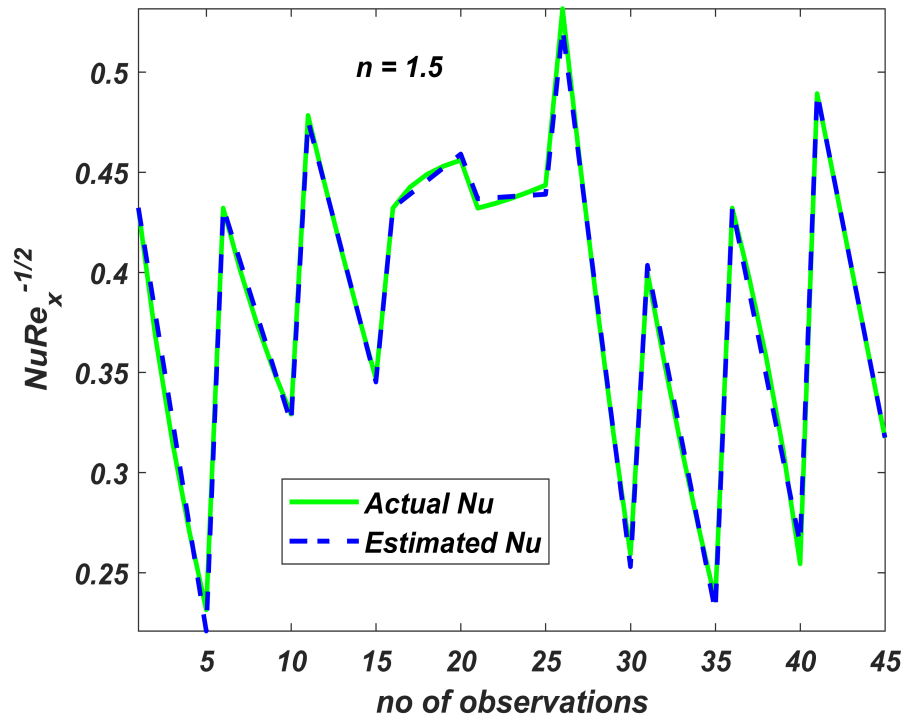

Figure 4.21: *Estimated versus actual* $Nu(Re_x)^{\frac{-1}{2}}$ *when* $n = 1.5$

$$Nu_{est}\,(1.5) = 0.99305 - 0.35222\ b_1 - 0.17913\ \gamma - 0.08699\ M + 0.00446\ We$$
$$+0.01121\kappa - 0.44799\ Nb - 0.28786\ Nt - 2.79750\ Q_T - 2.86966\ Q_E \tag{4.5.3}$$

The estimated regression coefficients are significant; since all p-values < 0.05. The accuracy of estimated regression models is described in Figure 4.20 and 4.21. It is understood that $b_1,\ \gamma,\ Nb,\ Nt,\ Q_T,\ Q_E$ and M have a negative response on the estimated $Nu\ \{both\ cases\}$. The estimated regression model predicts that the corresponding parameter induces a decreasing effect on Nu meaning that Nu decreases upon increasing parameter values. An increase in κ enhances the heat transfer coefficient $\{for\ both\ cases\}$. A reverse nature is observed due to increasing values of We for $n = 0.5\ and\ \ n = 1.5$. These results are in perfect synchronisation with the results discussed in table 4.5.

4.6 Conclusions

The key results of the current study are listed below:

- Hartmann number has a destructive effect on the velocity profile.
- Exponential space-based heat source (ESHS) and linear heat source (LHS) parameters exhibit a constructive behaviour on the temperature profile.
- Slip effect decreases the velocity and temperature profiles.
- Weissenberg number exhibits a differing nature on the velocity profile based on the nature of fluid; velocity is reduced when $n < 1$ and increased when $n > 1$.
- Velocity slip increases the drag coefficient whereas Hartmann number decreases the drag coefficient.
- Heat transfer rate lowers with ESHS, LHS and temperature slip parameters.
- Mass transfer rate is inversely proportional to concentration slip parameter.
- Nusselt number has been faultlessly estimated using multiple linear regression.

Chapter 5

Nanoparticle aggregation kinematics on the quadratic convective MHD flow of nanomaterial past an inclined flat plate with sensitivity analysis *

5.1 Introduction

Ethylene glycol-based nanofluid containing titanium dioxide is frequently used in cooling processes, solar collectors, and nuclear reactors. Oxides are chemically more stable than metal nanoparticles as metals oxidise easily. Also, ethylene glycol is more preferable since it can be used over a wide temperature range. Furthermore, TiO_2 is a harmless material and is widely available making the nanoparticle suitable for various thermal applications. Motivated by experimental results and practical applicability, a nanofluid prepared by dispersing TiO_2 nanoparticles in ethylene glycol is used for this theoretical study. The main objectives of the current study are to:

- Study the quadratic convective flow of nanofluid over an inclined plate.
- Investigate the significance of aggregation of nanoparticles on the heat transfer.
- Compare the results for two different geometries, viz., vertical plate and inclined plate.
- Analyze and optimize the heat transfer rate using the Response Surface Methodology.
- Explore the sensitivity of heat transfer rate with respect to the governing

*Published in: Proceedings of the Institution of Mechanical Engineers, Part E (Sage Publications Ltd), 2021; 236 (3)

operational parameters.

5.2 Mathematical Formulation

The physical model of the present problem is described in Fig. 5.1. Consider a two-dimensional steady flow of ethylene glycol-based titania nanofluid past a flat plate at $y = 0$ with an angle of inclination α towards the vertical. The constant value of temperature is chosen as T_w, at the plate ($y = 0$) and the ambient value is T_∞, far from the plate ($y \to \infty$). The aggregation kinematics of the nanoparticles is included in the model. A variable magnetic field of intensity ${B_x}^2 = B_0^2 x^{-0.5}$ (B_0-uniform magnetic field) is applied perpendicular to the fluid flow. An exponential space-based heat source ($Q_1 = Q_e x^{-0.5}$) and radiative heat flux are accounted in the system. The viscous and Joule heating effects are negligible and hence are not considered. Under nonlinear Boussinesq and boundary layer approximations, the flow can be described by the following governing equations (Kuznetsov & Nield, 2014),(Acharya, Das, & Kundu, 2017),(Goyal & Bhargava, 2018):

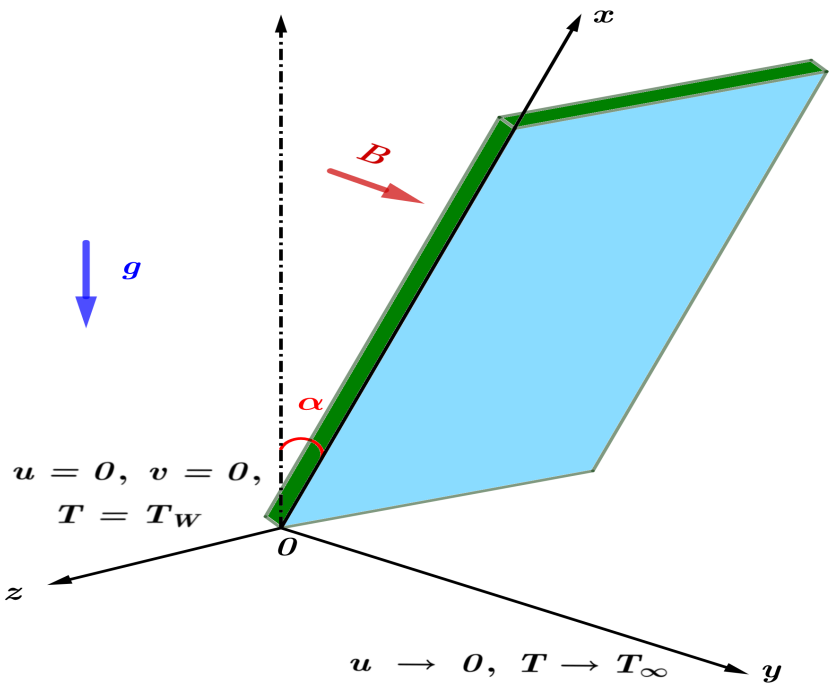

Figure 5.1: *Physical configuration.*

$$\frac{\partial u}{\partial x} + \frac{\partial v}{\partial y} = 0 \tag{5.2.1}$$

$$\rho_{nf}\left(u\frac{\partial u}{\partial x}+v\frac{\partial u}{\partial y}\right)= \mu_{nf}\frac{\partial^2 u}{\partial y^2}+\rho_{nf}g\left\{(\beta_0)_{nf}(T-T_\infty)+(\beta_1)_f(T-T_\infty)^2\right\}\cos\alpha -\sigma_{nf}B^2u \tag{5.2.2}$$

$$(\rho C_p)_{nf}\left(u\frac{\partial T}{\partial x}+v\frac{\partial T}{\partial y}\right)=k_{nf}\frac{\partial^2 T}{\partial y^2}-\frac{\partial q_R}{\partial y} +Q_1(T_w-T_\infty)\exp\left[-m\left\{\frac{(\beta_0)_f g(T_w-T_\infty)}{v_f\alpha_f}\right\}^{\frac{1}{4}}\frac{y}{x^{\frac{1}{4}}}\right] \tag{5.2.3}$$

Appropriate boundary conditions are

$$\begin{aligned}\text{At } y=0: &\quad u=0,\quad v=0,\quad T=T_w\\ \text{As } y\to\infty: &\quad u\to 0,\quad T\to T_\infty.\end{aligned} \tag{5.2.4}$$

where, u, v are the velocity components in the x and y directions, T is the temperature of the liquid. $T_w,\ T_\infty$- are the temperatures at the plate and ambient conditions, g is the acceleration due to gravity, α is the inclination of the plate, B is the magnetic flux, q_R is the radiative heat flux, Q_1 is the exponential heat source coefficient, m is the exponential index, ρ, μ and k are respectively the density, dynamic viscosity and thermal conductivity. β_0 and β_1 are the first and second order thermal expansion coefficients, α_f, C_p, and ν_f are respectively the thermal diffusivity, specific heat and kinematic viscosity.

The radiative heat flux for the optically thick fluid in this study is approximated using the Rosseland equation as follows:

$$q_R=-\frac{4\sigma^*}{3k^*}\frac{\partial T^4}{\partial y},\qquad T^4\approx 4T_\infty^3T-3T_\infty^4. \tag{5.2.5}$$

Here σ^* is the Stefan-Boltzmann constant and k^* is the mean absorption factor. The conventional Maxwell model for thermal conductivity and the Brinkman model for viscosity deviate significantly from the experimental data and hence lack accuracy. Therefore, thermophysical properties of nanofluid with the influence of nanoparticle aggregation are used as described in Table 5.1 and thereafter. Nanofluids are characterized by higher viscosity and thermal conductivity which is due to the aggregation kinematics of nanoparticles. A more suitable and realistic model including aggregation effects for the viscosity of $EG-TiO_2$ nanofluid is the modified

Table 5.1: *Thermophysical properties of the nanofluid with aggregation (Mackolil & Mahanthesh, 2021b)*

Effective density	$\frac{\rho_{nf}}{\rho_f} = (1-\phi_a) + \phi_a \frac{\rho_s}{\rho_f} = A_1$
Effective heat capacity	$\frac{(\rho C_p)_{nf}}{(\rho C_p)_f} = (1-\phi_a) + \phi_a \frac{(\rho C_p)_s}{(\rho C_p)_f} = A_2$
Effective thermal expansion	$\frac{(\rho \beta_0)_{nf}}{(\rho \beta_0)_f} = (1-\phi_a) + \phi_a \frac{(\rho \beta_0)_s}{(\rho \beta_0)_f} = A_3$
Effective electrical conductivity	$\frac{\sigma_{nf}}{\sigma_f} = 1 + \frac{3\left(\frac{\sigma_s}{\sigma_f}-1\right)\phi_a}{\left(\frac{\sigma_s}{\sigma_f}+2\right)-\left(\frac{\sigma_s}{\sigma_f}-1\right)\phi_a} = A_4$

Krieger-Dougherty model (Chen et al., 2007) as given below:

$$\frac{\mu_{nf}}{\mu_f} = \left(1 - \frac{\phi_a}{\phi_m}\right)^{[\eta]\phi_m} = A_5, \quad \phi_a = \phi\left(\frac{r_a}{r_p}\right)^{3-D}, \tag{5.2.6}$$

An experimentally agreed value of the relative radii of the aggregates to the individual nanoparticle, $\frac{r_a}{r_p}$ is 3.34 by assuming the shape of the aggregate as spherical and D is 1.8. The value of ϕ_m is 0.605 and $[\eta]$ is 2.5 (see (Chen et al., 2007)).
The effective thermal conductivity is modeled by combining the Maxwell and Bruggeman models to incorporate the aggregation aspect for $EG - TiO_2$ nanofluid (Chen et al., 2007). The model is given below:

$$\frac{k_{nf}}{k_f} = \frac{(k_a + 2k_f) - 2\phi_a (k_f - k_a)}{(k_a + 2k_f) + \phi_a (k_f - k_a)} = A_6, \tag{5.2.7}$$

$$\frac{k_a}{k_f} = \frac{1}{4}\left\{(3\phi_{in}-1)\frac{k_s}{k_f} + (3(1-\phi_{in})-1) + \left[\left((3\phi_{in}-1)\frac{k_s}{k_f} + (3(1-\phi_{in})-1)\right)^2 + 8\frac{k_s}{k_f}\right]^{\frac{1}{2}}\right\} \tag{5.2.8}$$

, $\phi_{in} = \left(\frac{r_a}{r_p}\right)^{D-3}$,where ϕ_{in} denotes the solid volume fraction of aggregates.
Thermophysical properties of nanoparticles and base fluid at 300 K are shown in the table 5.2

The following similarity variables (Kuznetsov & Nield, 2010) are used in the computation procedure:

$$\left.\begin{aligned} \zeta = \frac{y}{x} Ra_x^{\frac{1}{4}}, Ra_x = \frac{(\beta_0)_f \; g(T_w - T_\infty)x^3}{\nu_f \alpha_f}, \\ S(\zeta) = \frac{\psi}{\alpha_f Ra_x^{\frac{1}{4}}}, \theta(\zeta) = \frac{T - T_\infty}{T_w - T_\infty}. \end{aligned}\right\} \tag{5.2.9}$$

Table 5.2: *Thermo physical properties of base fluid and nanoparticles at* $300K$ *(Mackolil & Mahanthesh, 2021b)*

Model	$\rho\,(kgm^{-3})$	$C_p\,(Jkg^{-1}K^{-1})$	$k\,(Wm^{-1}K^{-1})$	$\beta\times10^{-5}\,(K^{-1})$	$\sigma\,(s/m)$
TiO_2	4250	686.2	8.9538	0.9	2.38×10^{6}
EG	1114	2415	0.252	57	1.07×10^{-6}

Here, ψ is the stream function with

$$u=\frac{\partial\psi}{\partial y}\quad,\quad v=-\frac{\partial\psi}{\partial x}. \tag{5.2.10}$$

Using the similarity variables, Eqns. (5.2.1) to (5.2.3) become,

$$S'''-\frac{1}{4Pr_f}\frac{A_1}{A_5}\left(2(S')^2-3SS''\right)+\frac{1}{A_5}\left\{A_3\theta+A_1\alpha_1\theta^2\right\}cos\alpha-\frac{A_4}{A_5}MS'=0, \tag{5.2.11}$$

$$\theta''\left(1+\frac{4}{3}\frac{R}{A_6}\right)+\frac{Q_E}{A_6}\exp\left(-m\zeta\right)+\frac{3}{4}\frac{A_2}{A_6}\,S\theta'=0, \tag{5.2.12}$$

The reduced boundary conditions are

$$\left.\begin{aligned}S'(0)=0, S(0)=0, \theta(0)=1.\\ S'(\infty)\to0, \theta(\infty)\to0.\end{aligned}\right\} \tag{5.2.13}$$

The non-dimensional parameters are given below:

$$\begin{aligned}\alpha_1=\frac{\beta_{1f}}{\beta_{0f}}\left(T_w-T_\infty\right), Pr_f=\frac{\nu_f}{\alpha_f},\ R=\frac{4\sigma^*T_\infty^3}{k^*k_f},\\ M=\frac{\sigma_f B_0^2\left(\nu_f\alpha_f\right)^{0.5}}{\mu_f\left(g(\beta_0\ )_f(T_w-T_\infty)\right)^{0.5}},\ Q_E=\frac{Q_e\left(\nu_f\alpha_f\right)^{0.5}}{k_f\left(g(\beta_0\ )_f(T_w-T_\infty)\right)^{0.5}}.\end{aligned} \tag{5.2.14}$$

where, α_1 (quadratic thermal convection parameter), Pr_f (Prandtl number), R (radiation parameter), M (Hartmann number), and Q_E (exponential heat source parameter).

Thermal nanofluidic devices depend on the physical quantities such as skin friction and the rate of heat transfer. The information regarding these physical quantities plays a crucial part for designing highly efficient nanofluidic devices. The local

skin friction coefficient and local Nusselt number is defined as follows (Kandasamy, Dharmalingam, & Prabhu, 2018),(Kuznetsov & Nield, 2010),(Aladdin, Bachok, & Pop, 2020):

$$C_f = \frac{\tau_w}{\rho_f u_w^2}, Nu = \frac{x q_w}{k_f \left(T_w - T_\infty\right)}. \tag{5.2.15}$$

where τ_w and q_w are the wall shear stress and the heat flux respectively which are defined as follows:

$$\tau_w = \mu_{nf}\left(\frac{\partial u}{\partial y}\right)_{y=0}, q_w = -\left(k_{nf}\frac{\partial T}{\partial y} - q_R\right)_{y=0}. \tag{5.2.16}$$

The reduced skin friction coefficient (Cf_X) and local Nusselt number (Nu_X) are respectively:

$$Cf_X = Cf(Ra_x)^{\frac{1}{4}} = A_5 Pr_f S''(0), \quad Nu_X = NuRa_x^{-\left(\frac{1}{4}\right)} = -\left(A_6 + \frac{4R}{3}\right)\theta'(0). \tag{5.2.17}$$

5.3 Numerical solution

The nonlinear ordinary differential system in Eqns. (5.2.11)-(5.2.12) with corresponding boundary conditions (5.2.13) are solved by employing the Runge-Kutta method of fourth-order with shooting technique. Refined values of initial guesses are found by the Newton-Raphson method with an accuracy of 10^{-6}. The domain of the present study is fixed to [0, 20] as a larger value for ∞ had no significant effect. Numerical values of the present study are compared with previously published results of (Kuznetsov & Nield, 2010) and (Mahanthesh & Mackolil, 2021) as described in Table 5.3. Furthermore, in Table 5.3, the results are also validated with the numerical results obtained by Fehlberg method and the bvp5c routine, a built-in solver in MATLAB. A commendable agreement of the present results with previously published results and the results from the bvp5c routine is noted. In addition, the numerical values of wall shear stress for various values of angle of inclination show an excellent agreement with bvp5c (see Table 5.4). To arrive at the numerical solutions, the following substitution is made:

$$S = y_1, S' = y_2, S'' = y_3, \theta = y_4, \theta' = y_5. \tag{5.3.1}$$

Accordingly, the equations (5.2.11)-(5.2.12) with boundary condition (5.2.13) takes the form as given below:

$$\begin{gathered} y_1^{'} = y_2, \\ y_2^{'} = y_3, \\ y_3^{'} = \frac{1}{4Pr_f}\frac{A_1}{A_5}\ \left(2(y_2)^2 - 3y_1y_3\right) - \frac{1}{A_5}\left\{A_3y_4 + A_1\alpha_1y_4^2\right\}\ cos\alpha + \frac{A_4}{A_5}My_2, \\ y_4^{'} = y_5, \\ y_5^{'} = \frac{-\frac{Q_E}{A_6}\exp(-m\zeta) - \frac{3}{4}\frac{A_2}{A_6}\ y_1y_5}{\left(1+\frac{4}{3}\frac{R}{A_6}\right)}, . \end{gathered} \tag{5.3.2}$$

with

$y_1(0) = 0, y_2(0) = 0, y_3(0) = K_1, y_4(0) = 1, y_5(0) = K_2.$

where, K_1 and K_2 are estimated using the Newton-Raphson method, a numerical procedure that aids in computing the roots of a real valued function. This method is governed by the idea that an analytic function can be estimated by approximating a straight-line tangent to it.

Table 5.3: *Comparison of $-\theta^{'}(0)$ values and when $\alpha_1 = \alpha = M = Q_E = R = 0$ and $\phi = 0$ with the results of (Kuznetsov & Nield, 2010) and (Mahanthesh & Mackolil, 2021)*

P_r	Kuznetsov & Nield	Mahanthesh & Mackolil	Present study		
			RK4	RKF45	Bvp5c
1	0.401	0.401	0.4010118	0.4010117	0.4010118
10	0.463	0.4633	0.4632903	0.4632903	0.4632903
100	0.481	0.4811	0.4810727	0.4810727	0.4810727
1000	0.484	0.4836	0.4836079	0.4836078	0.4836079

Table 5.4: *Comparison of $S''(0)$ when $\alpha_1 = 0.1, m = 0.5, M = 0.1$, $Q_E = 0.2, R = 1$ and $\phi = 1\%$*

α	Runge-Kutta method	bvp5c algorithm	Increment rate (%)
	$S''(0)$	$S''(0)$	
0^0	1.3974581543	1.3974581546	–
15^0	1.3597001912	1.3597001914	-2.7019
30^0	1.2472074728	1.2472074729	-8.2733
45^0	1.0619645094	1.0619645094	-14.8526
60^0	0.8056606724	0.8056606723	-24.1349
75^0	0.4742217598	0.4742217598	-41.1388
90^0	0.0000000000	0.0000000000	-100

5.4 Results and discussion

The impact of different parameters namely volume fraction of nanoparticles (ϕ), Hartmann number (M), quadratic thermal convection parameter (α_1), exponential heat source parameter (Q_E), radiation parameter (R), and exponential index (m) on velocity profile ($S'(\zeta)$), and temperature profile ($\theta(\zeta)$) of an inclined plate is explored through Figs. 5.2-5.9. The blue and red lines delineate the fluid flow past vertical and inclined plates respectively. A medium angle of inclination ($\alpha = 45^0$) has been chosen for the inclined plate case. The calculated value of the Prandtl number (Pr_f) for ethylene glycol (EG) at 300 K is 150.4583. The effect of differing inclination angles on drag force is tabulated in Table 5.4. It can be noticed that an increase in the angle of inclination exhibits a negative impact on the physical quantity. Further the rate (%) of decrements in wall shear stress is shown in Table 5.4. A decrement rate of 41.1388 % in wall shear stress is observed when the plate is inclined from 60^0 to 75^0. Physically, this occurs due to a depreciation in the fluid velocity (see (Goyal & Bhargava, 2018)).

Figs. 5.2-5.3 delineate the impact of the parameter ϕ on $S'(\zeta)$, and $\theta(\zeta)$ respectively. The liquid velocity retards by the augmented values of ϕ. The velocity profile starts from zero and attains a maximum peak then asymptotically converges to zero satisfying the conditions at the boundaries (see (Aziz & Khan, 2012)). Nanofluid flow past a vertical and an inclined plate cases are compared in this study. Nanoparticles tend to form aggregates (see (Chen et al., 2007)). Augmentation in the volume fraction of nanoparticles promotes more aggregation and enhances the viscosity of nanofluid which in turn depreciates the velocity profile. The temperature profile enhances by incremented values of ϕ. The addition of nanoparticles enhances the thermal conductivity of nanofluid (see (Chen et al., 2007),(Acharya, Das, & Kundu, 2019)) which raises the temperature profile. Figs. 5.4-5.5 display the variation of $S'(\zeta)$, and $\theta(\zeta)$ profiles with M. The distance covered by the nanofluid per unit time decreases when M is incremented. An increment in M induces a drag force (namely Lorentz force) against the fluid flow which decelerates the velocity profile (see (Goyal & Bhargava, 2018)). The temperature profile increases as shown in Fig. 5.5. This is due to an increase in friction. This is in agreement with findings of (Goyal & Bhargava, 2018). Figs 5.6-5.7 display the effect of α_1 on $S'(\zeta)$ and $\theta(\zeta)$

profiles. An increment in α_1 heightens the $S'(\zeta)$ profile. Physically, the enhancement in α_1 exhibits a force on the fluid due to a boost in the temperature gradient at the wall which accelerates fluid flow as a result of which the velocity increases and the temperature decreases.

Fig. 5.8 shows the influence of $\theta(\zeta)$ with increment in Q_E. $\theta(\zeta)$ rise with enhance in Q_E due to the presence of an additional heat source. Fig. 5.9 illustrates the trend of $\theta(\zeta)$ with R. $\theta(\zeta)$ improves with an increase in R. An increment in R applies more heat flux on the fluid and therefore, the temperature of the fluid enhances (see (L. Zhang et al., 2021)). The trend of fluid flow over both vertical and inclined plates is qualitatively similar but a greater velocity profile is observed in the case of the fluid flow over a vertical plate. It is because the buoyancy force exerted on the fluid past an inclined plate is much higher than that on the vertical plate. It is also inferred from these figures that, the temperature of the nanofluid is increasing functions of α.

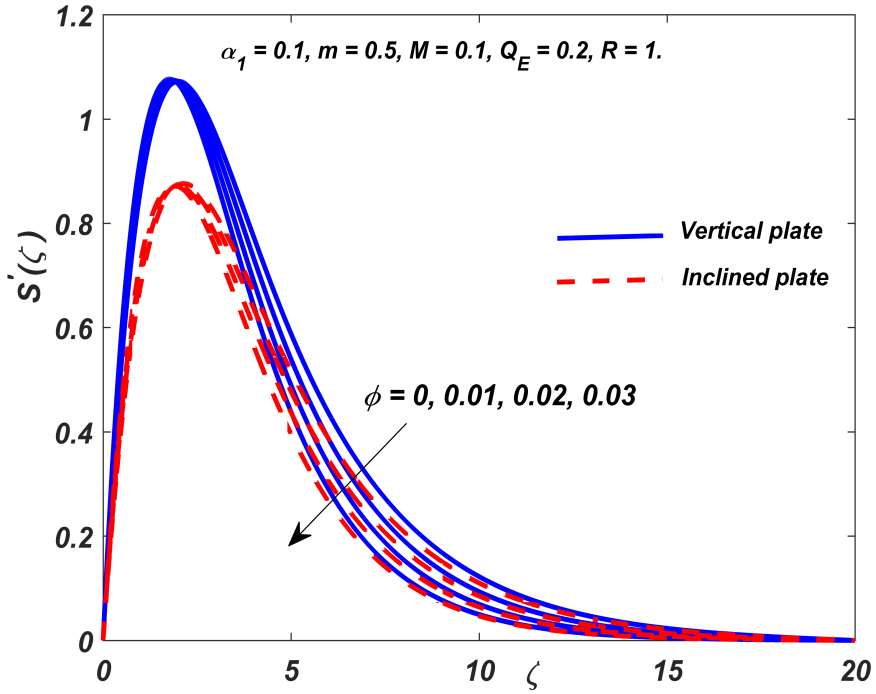

Figure 5.2: *Variation of $S'(\zeta)$ for distinct values of ϕ.*

Figs. 5.10 to 5.13 illustrate the simultaneous effects of pertinent parameters on the dependent variable studied. The change in the skin friction coefficient Cf_X with variations in α_1 and ϕ is described in Fig. 5.10. It can be observed that Cf_X is

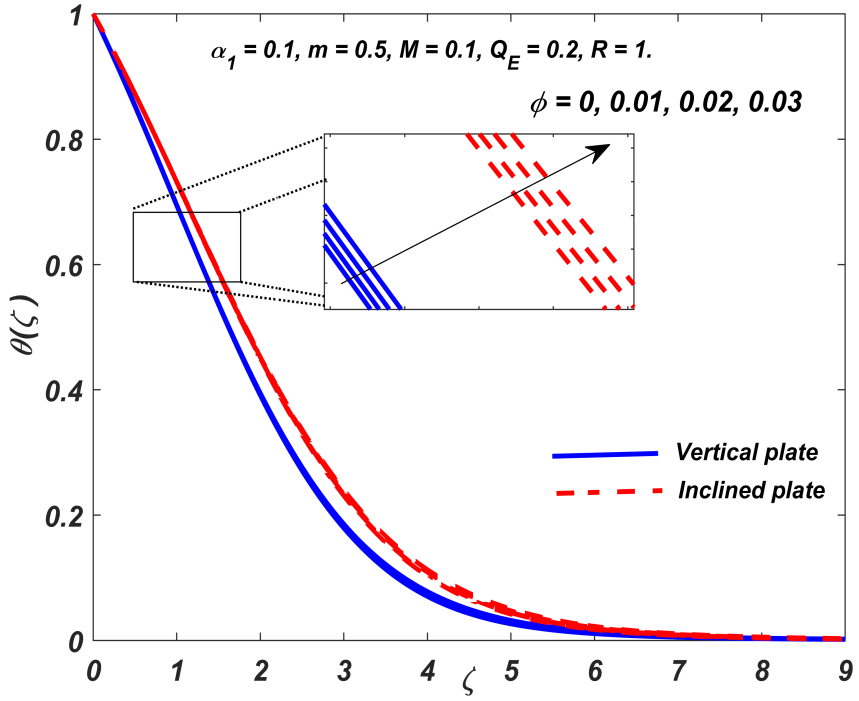

Figure 5.3: *Variation of $\theta(\zeta)$ for distinct values of ϕ.*

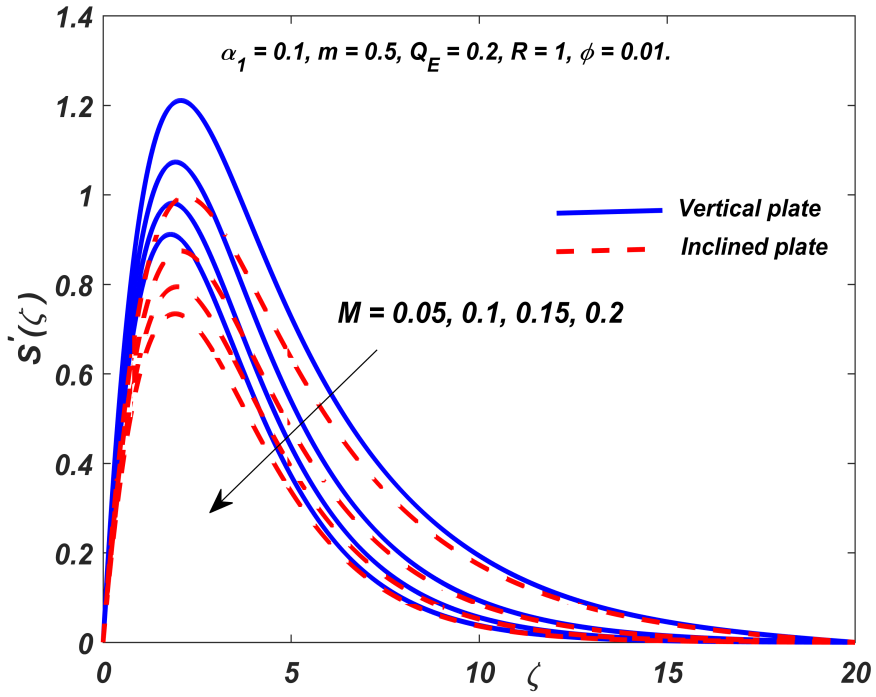

Figure 5.4: *Variation of $S'(\zeta)$ for distinct values of M.*

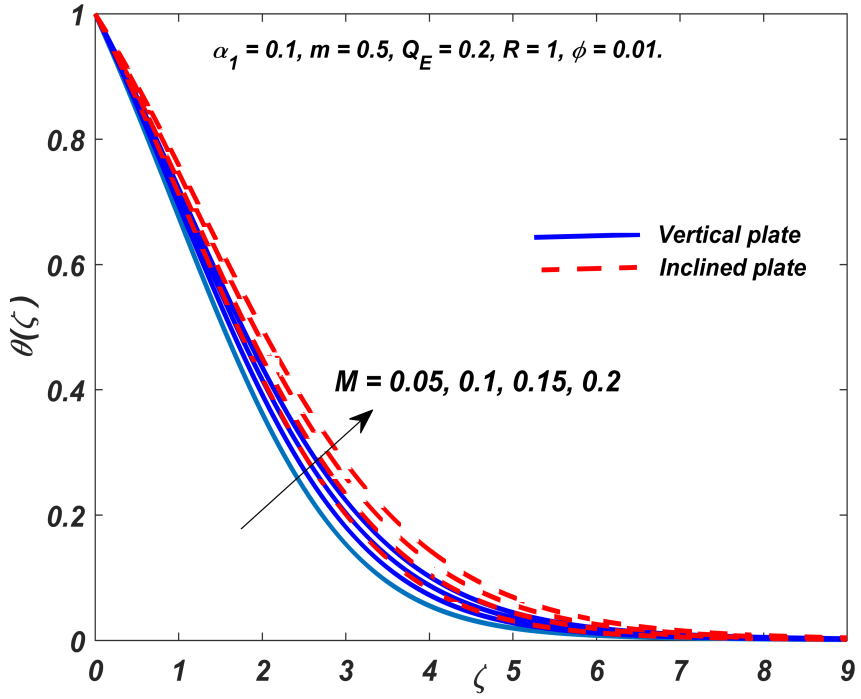

Figure 5.5: *Variation of $\theta(\zeta)$ for distinct values of M.*

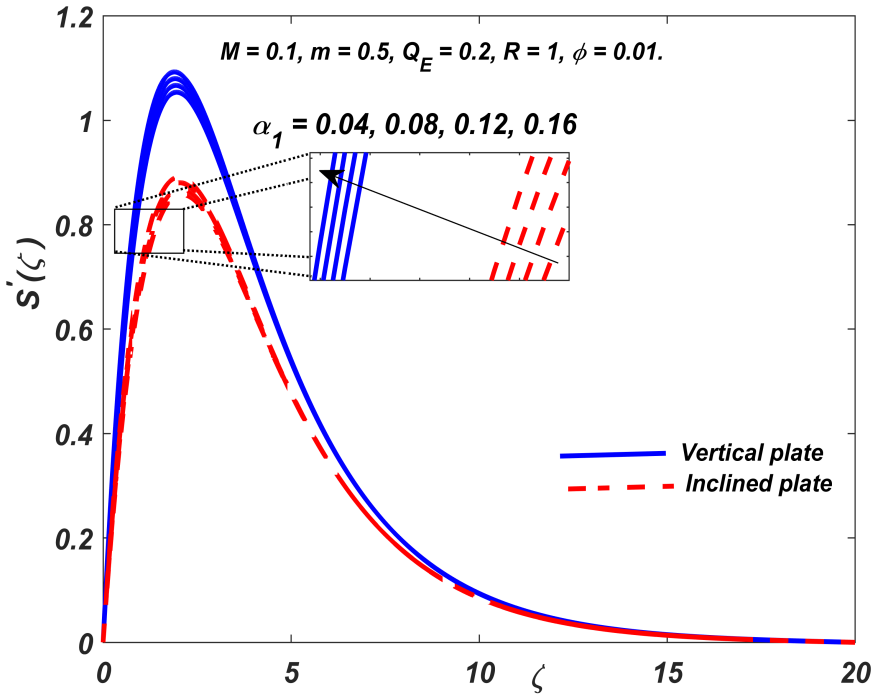

Figure 5.6: *Variation of $S'(\zeta)$ for distinct values of α_1.*

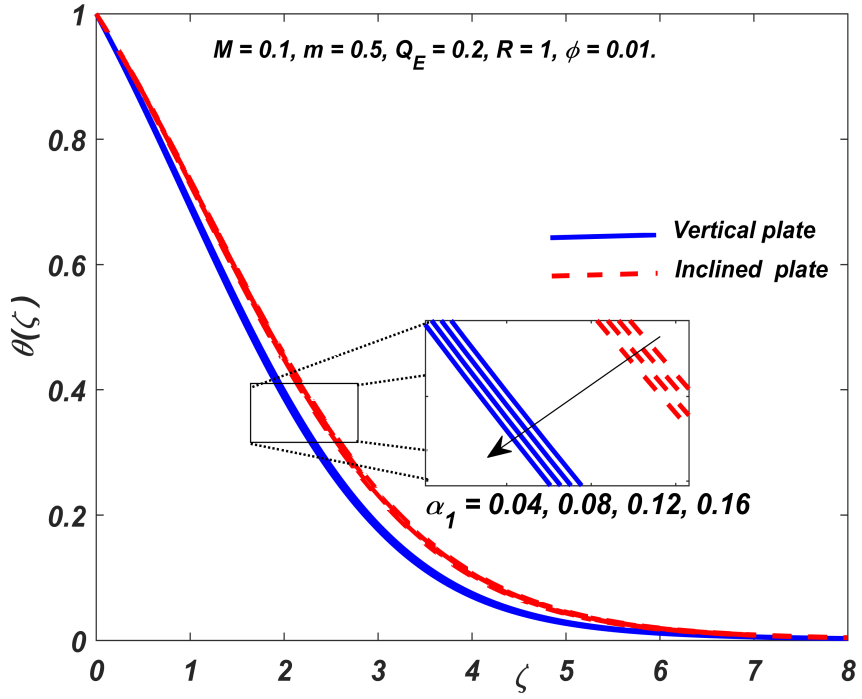

Figure 5.7: *Variation of* $\theta(\zeta)$ *for distinct values of* α_1.

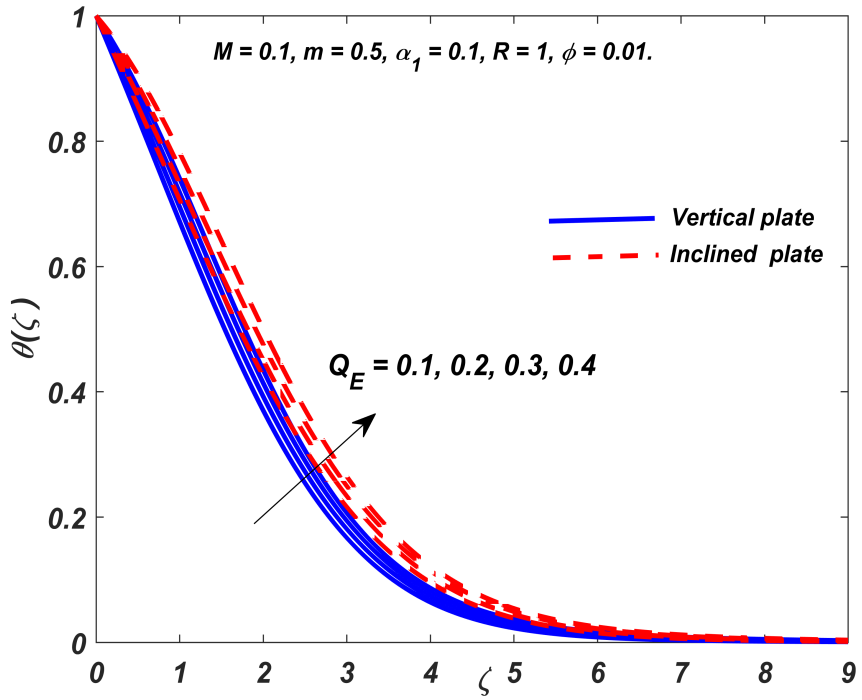

Figure 5.8: *Variation of* $\theta(\zeta)$ *for distinct values of* Q_E.

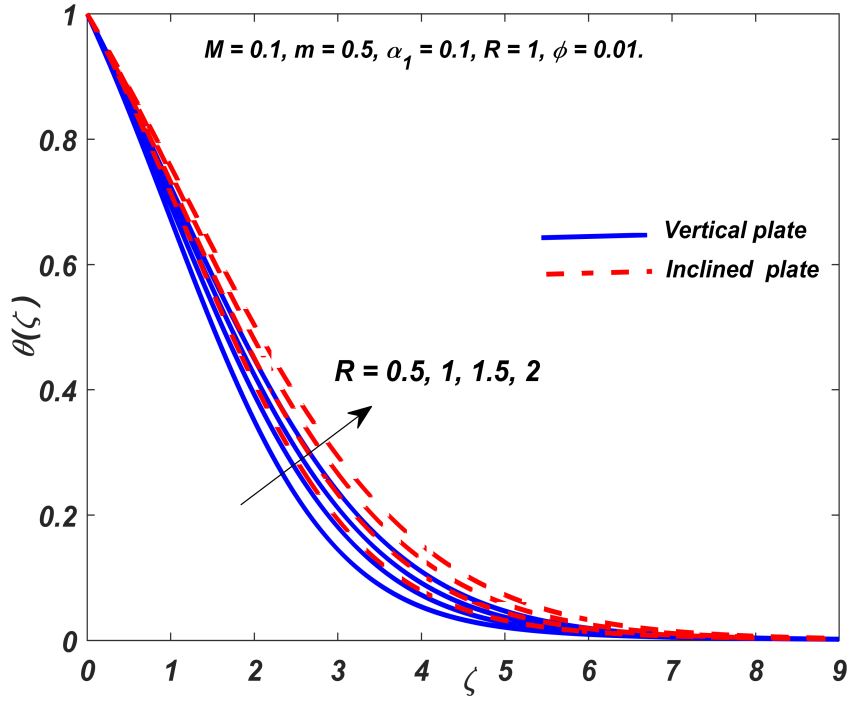

Figure 5.9: *Variation of $\theta(\zeta)$ for distinct values of R.*

an increasing function of α_1 and a decreasing function of ϕ. Maximum drag force is obtained at minimum α and M values as shown in Fig. 5.11. Physically, this is due to the effect of Lorentz and buoyancy forces near the surface. Fig. 5.12 delineates the influence of α and M on the heat transfer coefficient. It can be seen that the heat flux has a relatively small change by the increase in α and M. The heat transfer attains maximum for low values of α and M. (see (Acharya, Das, & Kundu, 2018)).Fig. 5.13 shows the variation in heat transfer with an increase in α_1 and ϕ. Maximum heat flux is observed for high α_1 and ϕ values.

5.5 Response Surface Methodology (RSM)

The RSM is a statistical and mathematical design-based tool to explore the interactive impact of pertinent parameters on a response variable of interest and to optimize it. Here, a full quadratic model is considered as follows:

$$\begin{aligned} Response = \chi_1 X_1 + \chi_2 X_2 + \chi_3 X_3 + \chi_4 X_1 X_2 + \chi_5 X_1 X_3 + \chi_6 X_2 X_3 \\ + \chi_7 X_1^2 + \chi_8 X_2^2 + \chi_9 X_3^2 + \chi_{10}. \end{aligned} \tag{5.5.1}$$

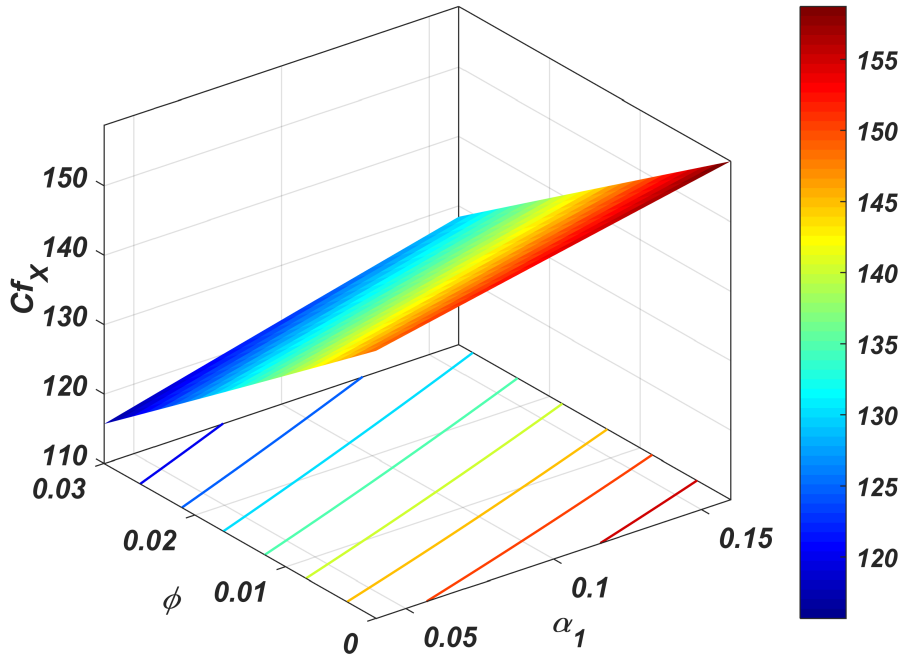

Figure 5.10: *Surface plot of Cf_X for variation of α_1 and ϕ .*

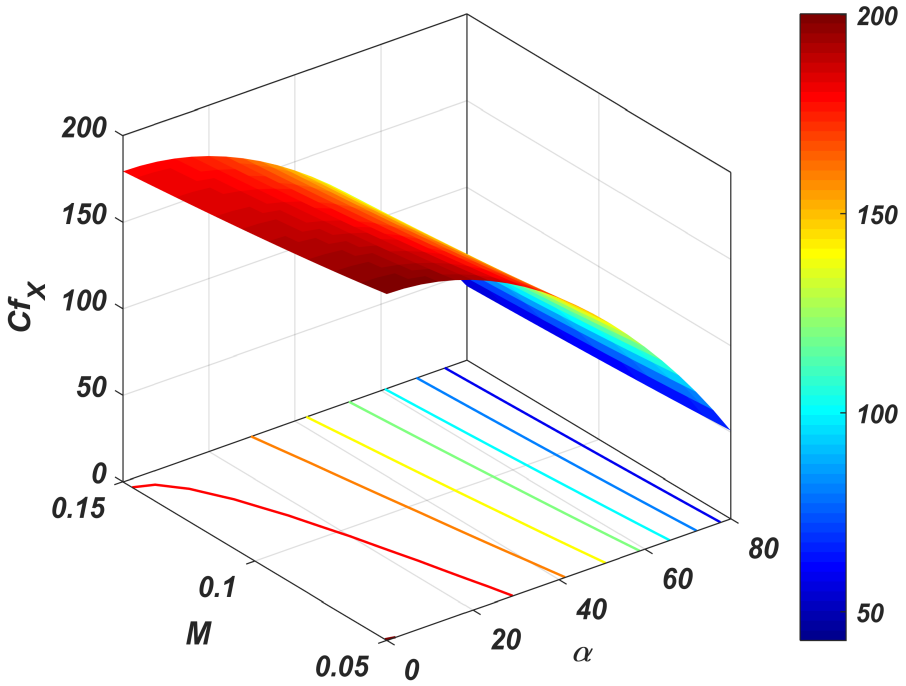

Figure 5.11: *Surface plot of Cf_X for variation of α and M*

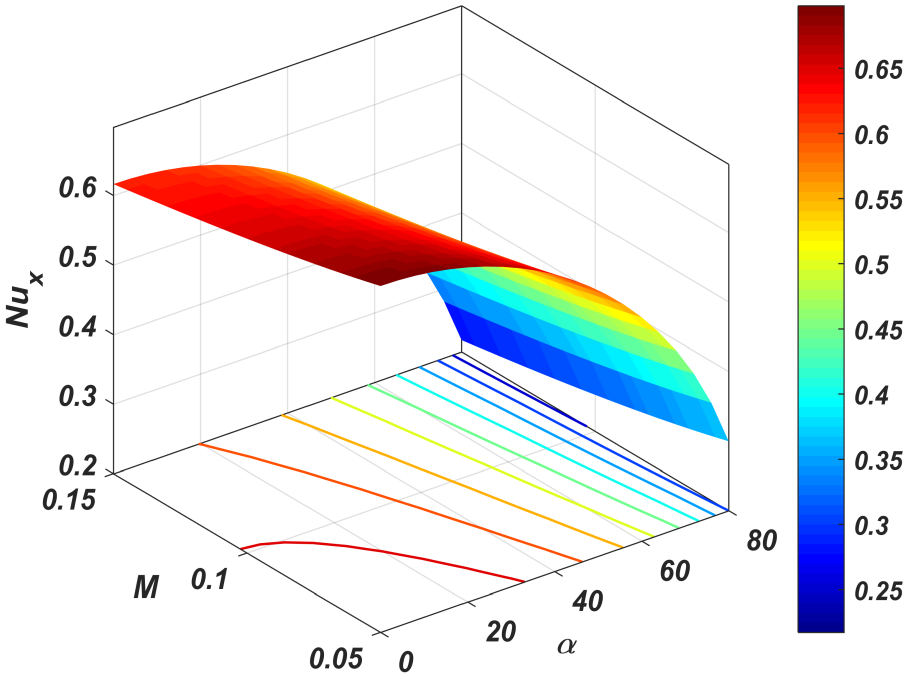

Figure 5.12: *Surface plot of Nu_X for variation of α and M .*

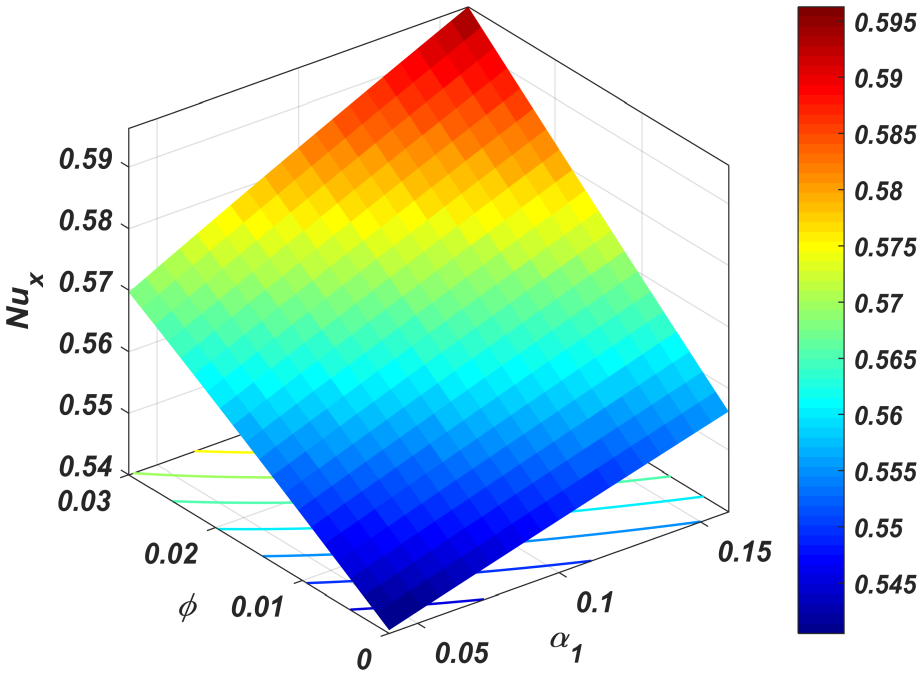

Figure 5.13: *Surface plot of Nu_X for variation of α_1 and ϕ .*

Table 5.5: *The effective levels of parameters*

Parameters	Coded Symbols	Levels		
		-1 (Low)	0 (Medium)	1 (High)
α	X_1	30^0	45^0	60^0
Q_E	X_2	0.15	0.2	0.25
R	X_3	0.8	1	1.2

Here, χ_i denotes the regression coefficients. The parameters α $\left(30^0 \leq \alpha \leq 60^0\right)$, Q_E $(0.15 \leq Q_E \leq 0.25$) and R $(0.8 \leq R \leq 1.2)$ are inducted for the analysis. Heat transfer coefficient (Nu_X) is the response variable. Here, a face-centered central composite design (CCD) is adopted for interpreting the influence of parameters on the response variable. The statistical technique involves 20 runs based on the face (P)- factor (F) relation $(2^F + 2F + P)$. It contains 8 factorial, 6 axial, and 6 centre points. The parameters α, Q_E and R are coded as X_1, X_2, and X_3 respectively. The effective levels of parameters are described in Table 5.5. Fig. 5.14 shows the precision

Table 5.6: *ANOVA table*

Source	**Deg. of Freedom**	**Adj. Sum of Squares**	**Adj. Mean Squares**	**F-value**	**p-value**
Model	9	0.107255	0.011917	46593.65	< 0.001
Linear terms	3	0.10564	0.035213	137676.2	< 0.001
α	1	0.047442	0.047442	185487.28	< 0.001
Q_E	1	0.026774	0.026774	104680.6	< 0.001
R	1	0.031424	0.031424	122860.73	< 0.001
Square terms	3	0.00137	0.000457	1784.96	< 0.001
α^2	1	0.000712	0.000712	2781.96	< 0.001
Q_E^2	1	0	0	0.14	**0.713**
R^2	1	0.000002	0.000002	8.11	0.017
Interaction terms	3	0.000245	0.000082	319.77	< 0.001
$\alpha.Q_E$	1	0.000031	0.000031	120.82	< 0.001
$\alpha.R$	1	0.000208	0.000208	811.71	< 0.001
$Q_E.R$	1	0.000007	0.000007	26.79	< 0.001
Errors	10	0.000003	0		
Lack-of-Fit	5	0.000003	0.000001	*	*
Pure Error	5	0	0		
Total	19	0.107258			
Coefficient of determination $\mathcal{R}^2 = 99.98\%$					

of the model. It is observed from the normal probability plot that data points are aligned along a straight line. The bell-shaped residual histogram concludes that residuals follow a normal distribution. The magnitude of residual against the fitted value and the residual against observation order plots are less than 0.001. It can be observed from the ANOVA table in Table 5.6 that the square term of Q_E is not significant as the p value is greater than 0.05. The coefficient of determination ($\mathcal{R}^2$) computes the variation in the response variable as explained by the independent variables taken in the model. It also explains the accuracy of the model. Here, $\mathcal{R}^2$ is found to be 99.98% and it guarantees the accuracy of the model.

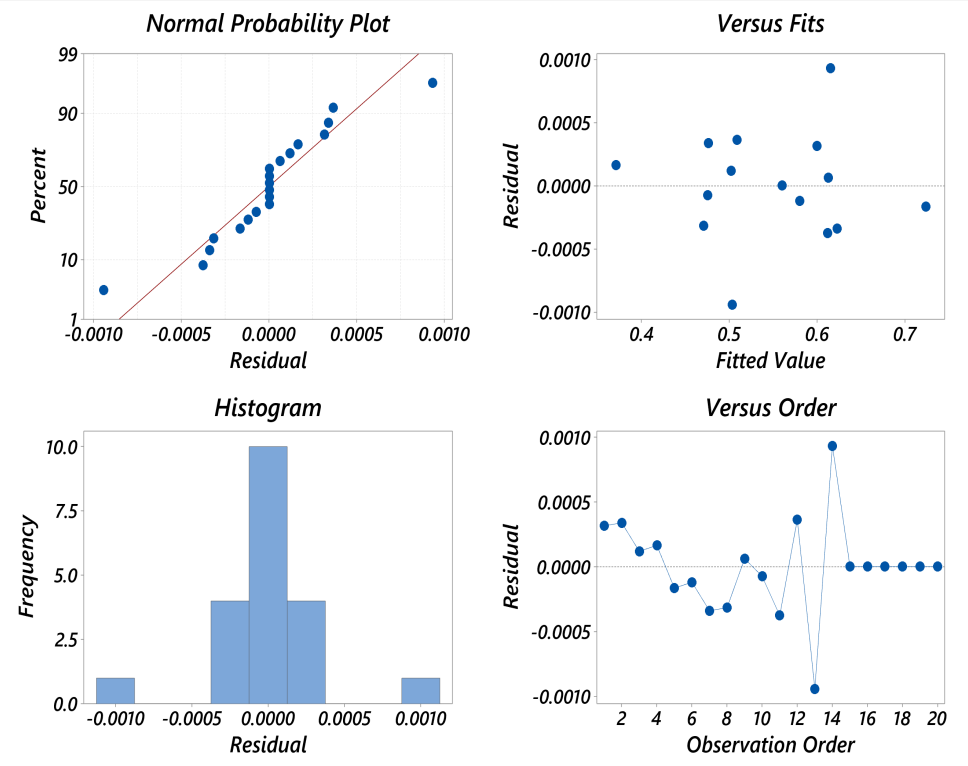

Figure 5.14: *Residual plots for Nu_X.*

5.5.1 Statistical Analysis

The full quadratic model for the wall heat flux by considering uncoded parameter values are

$$Nu_X = 0.41028 + 0.004064\ \alpha - 0.8429\ Q_E + 0.4186\ R - 0.000071\ \alpha^2 - 0.02171\ R^2 - 0.002621\ \alpha Q_E - 0.001698\ \alpha R - 0.0925\ Q_E R \tag{5.5.2}$$

The above relation can be used to estimate Nu_X accurately for the parameters in the given ranges. Fig. 5.15 (a) to (f) display the simultaneous impact of parameters on the heat transfer coefficient utilizing contour and surface plots. Variation in heat transfer coefficient with two parameters is considered by holding the third parameter at the medium level. It can be inferred from Fig. 5.15 (a)-5.15(b) that an increment in α reduces Nu_X also, Nusselt number is maximum for low values of α and Q_E. The Nusselt number with variation in R and α and R and Q_E is described in Figs. 5.15 (c) to 5.15 (f) respectively. These figures illustrate that the heat transfer coefficient is a decreasing function of α and an increasing function of R and similar trends are observed for Q_E and R. The interactive effects on the heat transfer coefficient can also be observed from Fig. 5.15.

5.6 Sensitivity analysis

The sensitivity of the heat flux is computed by using the coded coefficients of the full quadratic model as given below.

$$Nu_X = 0.560098 - 0.068878\ X_1 - 0.051744\ X_2 + 0.056057\ X_3 - 0.016085\ X_1^2 - 0.000868\ X_3^2 - 0.001965\ X_1X_2 - 0.005094\ X_1X_3 - 0.000925\ X_2X_3 \tag{5.6.1}$$

Sensitivity functions are estimated by computing the partial derivatives in a full quadratic model concerning the coded variables as follows:

$$\frac{\partial Nu_X}{\partial X_1} = -0.068878 - 0.03217\ X_1\ - 0.001965\ X_2 - 0.005094\ X_3, \tag{5.6.2}$$

$$\frac{\partial Nu_X}{\partial X_2} = -0.051744 - 0.001965\ X_1 - 0.000925\ X_3, \tag{5.6.3}$$

$$\frac{\partial Nu_X}{\partial X_3} = 0.056057 - 0.001736\ X_3 - 0.005094\ X_1 - 0.000925\ X_2. \tag{5.6.4}$$

The sensitivity of the heat transfer coefficient is visualized using bar chart (see Figure 5.16). The nature of the sensitivity is indicated by a positive or negative sign which means that the response term is positively or negatively correlated with the change in the effective parameter values. The magnitude of sensitivity indicates the intensity of this relationship. Here, the sensitivity of heat transfer coefficient (Nu_X) is computed by assuming a medium inclination angle ($\alpha = 45°$). Table 5.7 and Fig. 5.16 explains the sensitivities of Nu_X at different effective parameter levels.

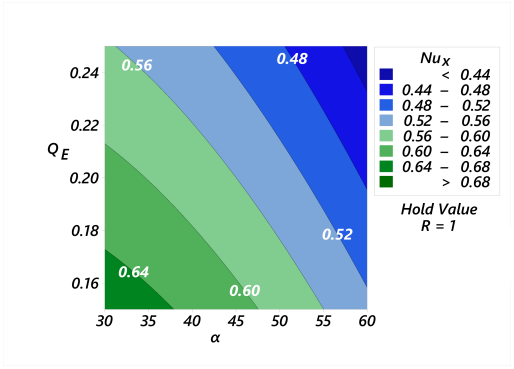

(a) *Contour plot of Nu_X for variation of α and Q_E*

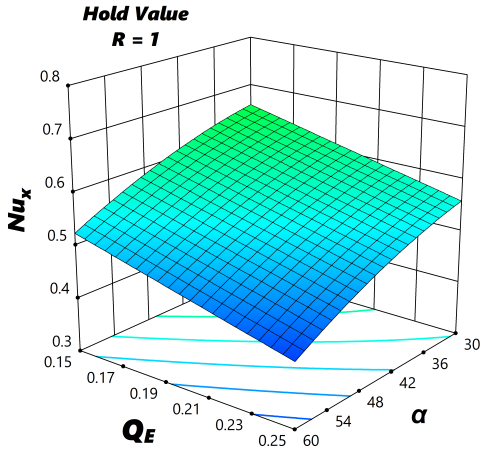

(b) *Response surface plot of Nu_X for variation of α and Q_E*

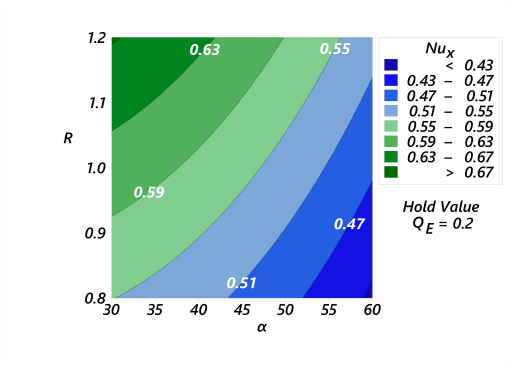

(c) *Contour plot of Nu_X for variation of α and R*

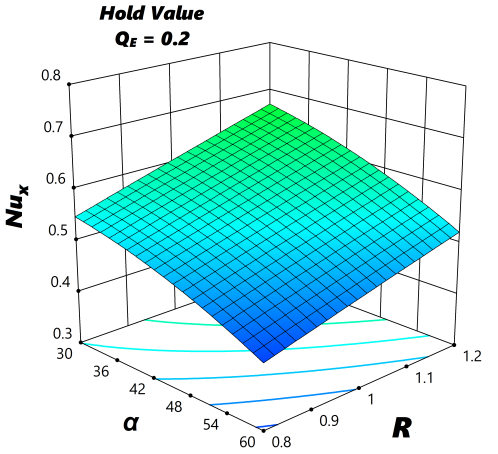

(d) *Response surface plot of Nu_X for variation of α and R*

Figure 5.15: *Contour plots and Response surface plots of Nu_X for all combinations of α, Q_E and R.*

Nu_X is negative sensitive towards α, Q_E and positive sensitive towards R. For a fixed value of Q_E at the low level ($X_2 = -1$) the magnitude of the sensitivity of Nusselt number enhances towards α and Q_E with an increment in the level of R whereas the sensitivity magnitude towards R reduces. A similar trend is noted for the medium and high levels of X_2. Further, the sensitivity towards α is more when compared to Q_E and R (due to the highest sensitivity magnitude). Additionally, the augmentation rate of the sensitivity magnitude for incrementing the levels of R are tabulated in the Table 5.7. This provides the rate at which the sensitivity is augmented for varying the levels of R which led to the following results:

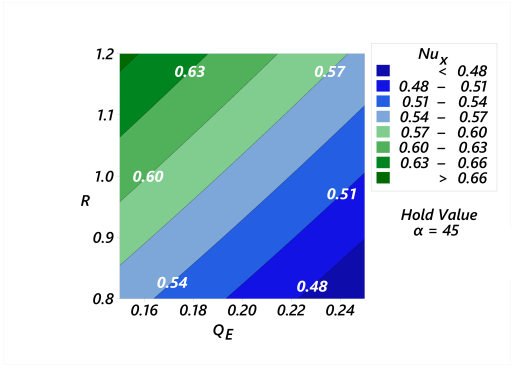

(e) *Contour plot of Nu_X for variation of Q_E and R*

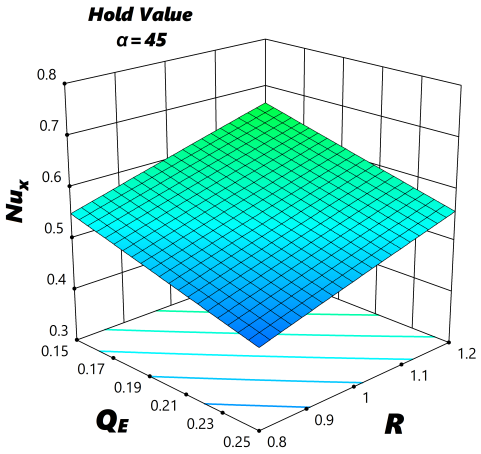

(f) *Response surface plot of Nu_X for variation of Q_E and R*

Figure 5.15: *Contour plots and Response surface plots of Nu_X for all combinations of α, Q_E and R.*

Table 5.7: *The sensitivity values of the response Nu_X when $X_1 = 0$*

B	C	Sensitivity values		
		$\frac{\partial Nu_X}{\partial X_1}$	$\frac{\partial Nu_X}{\partial X_2}$	$\frac{\partial Nu_X}{\partial X_3}$
-1	-1	-0.061819	-0.050819	0.058718
	0	-0.066913	-0.051744	0.056982
	1	-0.072007	-0.052669	0.055246
Rate of change		0.005094	0.000925	-0.001736
0	-1	-0.063784	-0.050819	0.057793
	0	-0.068878	-0.051744	0.056057
	1	-0.073972	-0.052669	0.054321
Rate of change		0.005094	0.000925	-0.001736
1	-1	-0.065749	-0.050819	0.056868
	0	-0.070843	-0.051744	0.055132
	1	-0.075937	-0.052669	0.053396
Rate of change		0.005094	0.000925	-0.001736

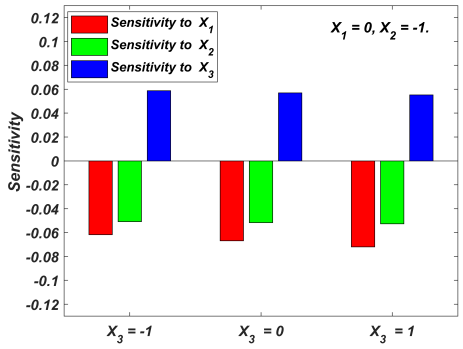

(a) *Bar charts depicting the sensitivity of* Nu_X *with* $X_2 = -1$

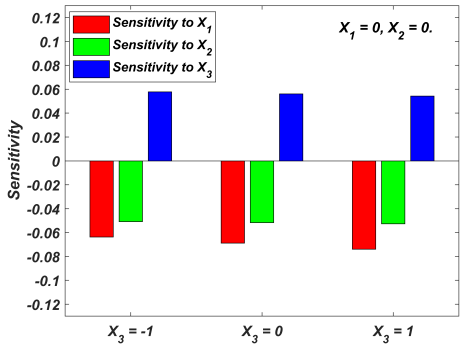

(b) *Bar charts depicting the sensitivity of* Nu_X *with* $X_2 = 0$

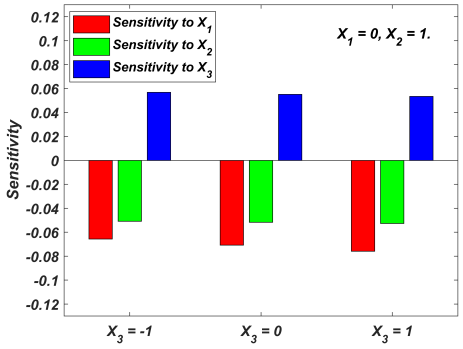

(c) *Bar charts depicting the sensitivity of* Nu_X *with* $X_2 = 1$

Figure 5.16: *Bar charts depicting the sensitivity of* Nu_X *with* $X_2 = -1$,$X_2 = 0$,*and* $X_2 = 1$

- The sensitivity towards α changes at the rate 0.5094
- The sensitivity towards Q_E changes at the rate 0.0925
- The sensitivity towards R changes at the rate -0.1736

This implies that the interactive effect on heat flux by the angle of inclination is predominant.

5.7 Conclusions

The hydromagnetic nanofluid flow past an inclined plate is explored with aggregation kinematics and significant buoyancy forces. The Runge-Kutta-based shooting method is adopted for the numerical computations. The limiting case of the present problem was found to be in good agreement with the literature. Sensitivity analysis based on the Response Surface model was conducted for a detailed study of the wall heat

flux. The present study includes potential applications in flat plate solar collectors and heat exchangers. The major conclusions of the present work are as given below:

- The aggregation kinematic aspect enhances the temperature field due to the improved thermal conductivity of the nanofluid.
- The velocity retards due to variation in Hartmann number and an opposite trend is exhibited for temperature. It is due to the generated opposing force, namely the Lorentz force.
- The temperature profile enhances with more thermal radiation and exponential heat source effects. Physically, these parameters contribute more energy to the fluid
- The surface drag force is an increasing function of quadratic thermal convection aspect.
- Maximum heat transfer occurs at the highest level of quadratic thermal convection and nanoparticle volume fraction parameters.
- The heat flux is more sensitive to the inclination angle when compared to other parameter values. This sensitivity augments at a rate 0.5094% for the increment in R.
- An accurate quadratic model is estimated for the wall heat flux with $\mathcal{R}^2 = 99.98\%$.
- The wall shear stress decrements by 41.1388 % when the inclination of the plate is changed from 60^0 to 75^0.

This work can be further explored by the inclusion of dissipation effects and the utilization of a suitable non-Newtonian fluid model, based on the practical applicability.

Chapter 6

MHD Darcy-Forchheimer hybrid nanoliquid flow over an elongated permeable sheet in a porous medium with hydrodynamic slip constraint *

6.1 Introduction

Modified Buongiorno nanoliquid model (MBNM) extends the traditional Buongiorno model by considering the effectual slip mechanisms along with the effective properties of a nanofluid. The dynamics of hydromagnetic Darcy-Forchheimer hybrid nanoliquid flow over an elongated permeable sheet with hydrodynamic slip constraint has been studied. The passive control of nanoparticle volume fraction at the boundary yields a realistic and practical model. In addition, the introduction of the modified Buongiorno model makes the present work different from the existing literature. The statistical scrutinization on the surface drag involving injection/suction effects, with the aid of regression analysis, enhances the novelty and uniqueness of the current exploration. The current study finds its applications in astronomical disciplines, fuel injection, thermal protection, and aerodynamics . A comparative analysis of the velocity profile on the two-dimensional and axisymmetric flows in the presence of slip and no-slip constraints has also been presented. The main objectives of the current study are to:

*Published in: Waves in Random and Complex Media (Taylor & Francis), 2022; (early access)

- Construct a mathematical model to study the dynamics of hydromagnetic Darcy-Forchheimer hybrid nanoliquid flow over an elongated permeable sheet in the presence of hydrodynamic slip using MBNM and passive control of nanoparticles.
- Conduct a comparative analysis on the nanoliquid flow by examining the injection and suction effect.
- Explore the influence of pertinent parameters on flow profiles.
- Utilize regression analysis to obtain a correlation between the influential parameters and the drag coefficient.

6.2 Mathematical formulation

A three-dimensional steady laminar incompressible and electrically conducting viscous nanofluid flow past a lengthening sheet in a Dacry-Forchheimer porous medium is analyzed. Let (u, v, w) be the velocity components along (x, y, z) directions. The sheet is stretched with velocities $U_w = ax$ and $V_w = by$ along x- and y- directions, respectively. Partial velocity slip with slip coefficient N_1 is considered at the boundary. A permeable sheet with mass flux velocity $w_0 > 0$ (for injection) and $w_0 < 0$ (for suction) is considered. A magnetic field of uniform strength B_0 is considered along the z-direction. The induced magnetic field was neglected due to the small magnetic Reynolds number. The hybrid nanoliquid flow is modeled using MBNM and a physically more realistic boundary condition that passively controls the volume fraction of nanoparticles. The convective boundary constraint that creates a significant relation between thermal difference and heat flux at the surface (see (Zhao et al., 2022)) is also incorporated. The temperature at the sheet is regulated with a convective heating condition by utilizing hot fluid. The physical configuration of the model is illustrated in Fig 6.1.

The boundary layer equations describing the fluid flow are as follows (see (Kumar et al., 2021), (Jusoh, Nazar, & Pop, 2018), (P. Rana, Mahanthesh, Mackolil, & Al-Kouz, 2021), (Muhammad, Alsaedi, Hayat, & Shehzad, 2017)):

$$u_x + v_y + w_z = 0 \tag{6.2.1}$$

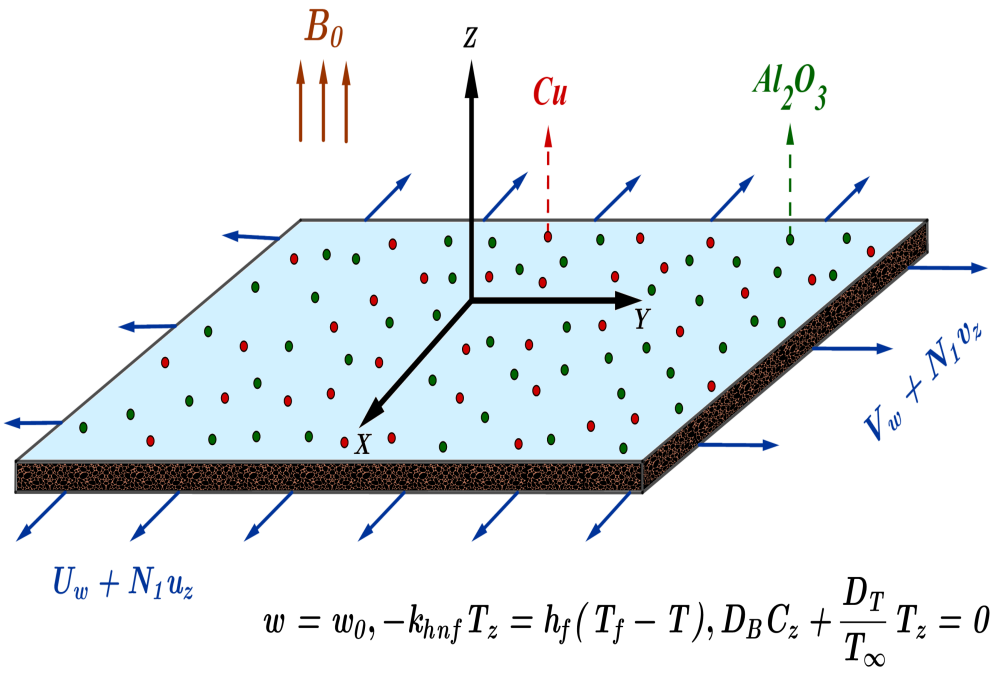

Figure 6.1: *Physical configuration.*

$$\rho_{hnf}\left(uu_x + vu_y + wu_z\right) = \mu_{hnf}\left(u_{zz} - \frac{u}{K_p}\right) - \sigma_{hnf} B_0^2 u - \frac{\rho_{hnf}\, C_b^* u^2}{x\sqrt{K_p}} \tag{6.2.2}$$

$$\rho_{hnf}\left(uv_x + vv_y + wv_z\right) = \mu_{hnf}\left(v_{zz} - \frac{v}{K_p}\right) - \sigma_{hnf} B_0^2 v - \frac{\rho_{hnf}\, C_b^* v^2}{y\sqrt{K_p}} \tag{6.2.3}$$

$$uT_x + vT_y + wT_z = \frac{k_{hnf}}{(\rho C_p)_{hnf}} T_{zz} + \frac{(\rho C_p)_p}{(\rho C_p)_{hnf}}\left\{\frac{D_T}{T_\infty} T_z^2 + D_B T_z \mathcal{C}_Z\right\} \tag{6.2.4}$$

$$u\mathcal{C}_x + v\mathcal{C}_y + w\mathcal{C}_z = D_B \mathcal{C}_{zz} + \frac{D_T}{T_\infty} T_{zz} \tag{6.2.5}$$

with the corresponding boundary conditions:

$$\left.\begin{aligned} u = ax + N_1 u_z \ ,\ v = by + N_1 v_z \ ,\ w = w_0 \ , \\ -k_{hnf} T_z = h_f\left(T_f - T\right) \ ,\ \tfrac{D_T}{T_\infty} T_z + D_B \mathcal{C}_z = 0 \ . \end{aligned}\right\} \ at\ z = 0 \tag{6.2.6}$$

$$u \to 0 \ ,\ v \to 0 \ ,\ T \to T_\infty \ ,\ \mathcal{C} \to \mathcal{C}_\infty \ . \qquad as\ z \to \infty. \tag{6.2.7}$$

The quantities of physical interest are the skin friction coefficients (Cf_x and Cf_y) and the Nusselt number (Nu_x) quantifying the surface drag and rate of heat transfer at the sheet, respectively are given by (see (Jusoh et al., 2018), (Yusuf, Mabood, Khan, & Gbadeyan, 2020)):

$$Cf_x = \frac{\tau_{wx}}{\rho_f U_w^2} = \frac{\mu_{hnf}\left(\frac{\partial u}{\partial z}\right)_{z=0}}{\rho_f U_w^2} \ , \tag{6.2.8}$$

$$Cf_y = \frac{\tau_{wy}}{\rho_f V_w^2} = \frac{\mu_{hnf}\left(\frac{\partial v}{\partial z}\right)_{z=0}}{\rho_f V_w^2} \ , \tag{6.2.9}$$

$$Nu_x = \frac{x q_w}{k_f\left(T_f - T_\infty\right)} = \frac{-x\ k_{hnf}\left(\frac{\partial T}{\partial z}\right)_{z=0}}{k_f\left(T_f - T_\infty\right)} \ . \tag{6.2.10}$$

where τ_{wx} , τ_{wy} , and q_w are the shear stress along the x- and y- directions and the heat flux from the surface, respectively.

The effective thermophysical properties of the hybrid nanoliquid (with alumina as nanoparticle 1 and copper as nanoparticle 2) are given by table 6.1 (see (Mathew et al., 2021), (Aladdin et al., 2020)):

Now consider the following similarity variables (see (Muhammad et al., 2017)):

$$\left.\begin{array}{c} u = axf'\left(\zeta\ \right)\ ,\ v = ayg'\left(\zeta\ \right)\ ,\ w = -\sqrt{a\nu_f}\left(f\left(\zeta\ \right) + g\left(\zeta\right)\right)\ , \\ \zeta = \sqrt{\frac{a}{\nu_f}}\ z\ ,\ \theta\left(\zeta\right) = \frac{T-T_\infty}{T_f - T_\infty}\ ,\ \phi\left(\zeta\right) = \frac{\mathcal{C}-\mathcal{C}_\infty}{\mathcal{C}_\infty}\ . \end{array}\right\} \tag{6.2.11}$$

In view of equation (6.2.11) and the thermophysical properties, one can get the following from equations (6.2.1)-(6.2.10):

$$f''' - \left(\frac{A_2}{A_1}\right)\left\{\left(1 + Fr\right) f'^2 - \left(f + g\right) f''\right\} - \left(\frac{A_3}{A_1} M + K_1\right) f' = 0 \tag{6.2.12}$$

$$g''' - \left(\frac{A_2}{A_1}\right)\left\{\left(1 + Fr\right) g'^2 - \left(f + g\right) g''\right\} - \left(\frac{A_3}{A_1} M + K_1\right) g' = 0 \tag{6.2.13}$$

$$\theta'' + \frac{Pr}{A_4}\left\{A_5\ \left(f + g\right)\theta' + Nt\ \theta'^2 + Nb\ \theta'\phi'\right\} = 0 \tag{6.2.14}$$

$$\phi'' + \left\{Sc\left(f + g\right)\phi' + \frac{Nt}{Nb}\theta''\right\} = 0 \tag{6.2.15}$$

Table 6.1: *The effective thermophysical properties of the hybrid nanoliquid (with alumina as nanoparticle 1 and copper as nanoparticle 2)*

Effective Dynamic Viscosity	$\frac{\mu_{hnf}}{\mu_f} = \frac{1}{\left(1-\phi_{Al_2O_3}\right)^{2.5}(1-\phi_{Cu})^{2.5}} = A_1.$
Effective Density	$\frac{\rho_{hnf}}{\rho_f} = (1-\phi_{Cu})\left((1-\phi_{Al_2O_3}) + \phi_{Al_2O_3}\,\frac{\rho_{s_1}}{\rho_f}\right) + \phi_{Cu}\frac{\rho_{s_2}}{\rho_f} = A_2$
Effective Electrical Conductivity	$\frac{\sigma_{hnf}}{\sigma_f} = 1 + \frac{3\left(\frac{\phi_{Al_2O_3}\sigma_{s_1}+\phi_{Cu}\sigma_{s_2}}{\sigma_f} - \left(\phi_{Al_3O_3}+\phi_{Cu}\right)\right)}{2+\left(\frac{\phi_{Al_2O_3}\sigma_{s_1}+\phi_{Cu}\sigma_{s_2}}{\left(\phi_{Al_2O_3}+\phi_{Cu}\right)\sigma_f}\right) - \left(\frac{\phi_{Al_2O_3}\sigma_{s_1}+\phi_{Cu}\sigma_{s_2}}{\sigma_f} - \left(\phi_{Al_2O_3}+\phi_{Cu}\right)\right)} = A_3$
Effective Thermal Conductivity	$\frac{k_{hnf}}{k_f} = A_4$, where $\frac{k_{hnf}}{k_{nf}} = \frac{k_{s_2}+2k_{nf}-2\phi_{Cu}\left(k_{nf}-k_{s_2}\right)}{k_{s_2}+2k_{nf}+\phi_{Cu}\left(k_{nf}-k_{s_2}\right)}$ and $\frac{k_{nf}}{k_f} = \frac{k_{s_1}+2k_f-2\phi_{Al_2O_3}\left(k_f-k_{s_1}\right)}{k_{s_1}+2k_f+\phi_{Al_2O_3}\left(k_f-k_{s_1}\right)}$
Effective Specific Heat	$\frac{(\rho C_p)_{hnf}}{(\rho C_p)_f} = (1-\phi_{Cu})\left(1-\phi_{Al_2O_3}+\phi_{Al_2O_3}\frac{(\rho C_p)_{s1}}{(\rho C_p)_f}\right) + \phi_{Cu}\frac{(\rho C_p)_{s_2}}{(\rho C_p)_f} = A_5\ .$

with

$$\left.\begin{array}{c} f(0)+g(0)=\lambda\ ,\quad f^{'}(0)=1+b_1 f''(0)\ ,\ g'(0)=\delta+b_1 g''(0)\ , \\ A_4\theta'(0)=Bi\left(\theta(0)-1\right)\ ,\ \phi'(0)+\frac{Nt}{Nb}\theta'(0)=0. \end{array}\right\} \tag{6.2.16}$$

$$f'(\infty\ )\to 0\ ,\ g'(\infty)\to 0\ ,\ \theta(\infty)\to 0\ ,\ \phi(\infty)\to 0 \tag{6.2.17}$$

The subsequent physical quantities are yielded as:

$$Re_x^{\frac{1}{2}}\ \ Cf_x = A_1 f''(0)\ \ ;where\ \ Re_x = \frac{U_w\ x}{\nu_f}\ .. \tag{6.2.18}$$

$$Re_y^{\frac{1}{2}}\ Cf_y = A_1(\delta)^{-\frac{3}{2}} g''(0)\ \ ;where\ \ Re_y = \frac{V_w\ y}{\nu_f}\ . \tag{6.2.19}$$

$$Re_x^{-\ \frac{1}{2}}\ Nu_x = -A_4\theta'(0)\ \ ;\ where\ \ Re_x = \frac{U_w\ x}{\nu_f}\ . \tag{6.2.20}$$

where M (Hartmann number)$= \frac{\sigma_f B_0^2}{a\rho_f}$, K_1 (porosity parameter)$= \frac{\nu_f}{aK_p}$, Nb (Brownian motion parameter)$= \frac{\tau D_B \mathcal{C}_\infty}{\nu_f}$, Pr (Prandtl number)$= \frac{(\mu C)_f}{k_f}$, Fr (Forchheimer parameter)=

$\frac{C_b^*}{\sqrt{K_p}}$, Sc (Schmidt number)= $\frac{\nu_f}{D_B}$, Nt (thermophoresis parameter)= $\frac{\tau D_T\left(T_f - T_\infty\right)}{T_\infty \nu_f}$, τ (effective heat capacity ratio) = $\frac{(\rho C_p)_p}{(\rho C_p)_f}$,b_1 (hydrodynamic slip parameter)= $N_1\sqrt{\frac{a}{\nu_f}}$,
δ (stretching ratio parameter)= $\frac{b}{a}$, Bi (Biot number)= $\frac{h}{k_f}\sqrt{\frac{\nu_f}{a}}$, and λ (suction/injection parameter)= $-\frac{w_0}{\sqrt{a\nu_f}}$ are the non-dimensional parameters.

Table 6.2: *Thermophysical properties of water, alumina, and copper (Aziz et al., 2021), (Aaiza et al., 2015), (Hussanan et al., 2017)*

Property	Base fluid(H_2O)	Nanoparticle 1 (Al_2O_3)	Nanoparticle 2(Cu)
ρ	997.1	3970	8933
C_p	4179	765	385
k	0.613	40	401
σ	0.05	3.5×10^7	5.96×10^7 .

6.3 Numerical solution

The highly nonlinear ODEs given in Eqns. (6.2.12)-(6.2.17) are reduced to a system of single-order ODEs by setting:
$f = y_1, f' = y_2, f'' = y_3,\ g = y_4, g' = y_5,\ g'' = y_6,$
$\theta = y_7,\ \theta' = y_8,\ \psi = y_9, \psi' = y_{10}$ The subsequent system of first-order ODEs is given by:

$$\left.\begin{array}{c} y_1' = y_2\ ,\ y_2' = y_3\ ,\ y_3' = \left(\frac{A_2}{A_1}\right)\left\{(1+Fr)\,y_2^2 - (y_1+y_4)\,y_3\right\} + \left(\frac{A_3}{A_1}M + K_1\right)y_2\ , \\ y_4' = y_5\ ,\ y_5' = y_6\ ,\ y_6' = \left(\frac{A_2}{A_1}\right)\left\{(1+Fr)\,y_5^2 - (y_1+y_4)\,y_6\right\} + \left(\frac{A_3}{A_1}M + K_1\right)y_5\ , \\ y_7' = y_8\ ,\ y_8' = -\frac{Pr}{A_4}\left\{A_5\ (y_1+y_4)\,y_8 + Nty_8^2 + Nb\ y_8 y_{10}\right\}\ ,\ y_9' = y_{10}\ , \\ y_{10}' = -\left\{Sc\,(y_1+y_4)\,y_{10} - \left(\frac{Nt}{Nb}\frac{Pr}{A_4}\right)\left\{A_5\ (y_1+y_4)\,y_8 + Nty_8^2 + Nb\ y_8 y_{10}\right\}\right\} \end{array}\right\} \tag{6.3.1}$$

with

$$\left.\begin{array}{c} y_1(0) + y_4(0) = \lambda\ ,\ y_2(0) = 1 + b_1\ y_3(0)\ \ ,\ y_5(0) = \delta + b_1\ y_6(0)\ , \\ A_4\ y_8(0) = Bi\,(y_7(0) - 1)\ \ ,\ y_{10}(0) + \frac{Nt}{Nb}\ y_8(0) = 0\ . \end{array}\right\} \tag{6.3.2}$$

$$y_2(\infty) \to 0\ ,\ y_5(\infty) \to 0\ ,\ y_7(\infty) \to 0\ ,\ y_9(\infty) \to 0 \tag{6.3.3}$$

The reduced system of first-order ODES is resolved using the bvp5c routine with an error tolerance of 10^{-6}. The bvp5c routine (an efficient built-in MATLAB code

Table 6.3: *Resemblance of* $-Re_x^{\frac{1}{2}}\ Cf_x$ *and* $-Re_y^{\frac{1}{2}}\ Cf_y$ *for differing values of* K_1 , Fr , *and* δ *when* $M = Nt = \lambda = \phi_{Al_2O_3} = \phi_{Cu} = b_1 = Bi = 0$, $Pr = Sc = 1$, *and* $Nb \to 0$.

K_1	Fr	δ	Present study		(Muhammad et al., 2017)	
			$-Re_x^{\frac{1}{2}}Cf_x$	$-Re_y^{\frac{1}{2}}Cf_y$	$-Re_x^{\frac{1}{2}}Cf_x$	$-Re_y^{\frac{1}{2}}Cf_y$
0	0.1	0.2	1.06954	1.67611	1.06945	1.67684
0.1	0.1	0.2	1.11475	1.81692	1.11471	1.81669
0.2	0.1	0.2	1.15832	1.94732	1.15830	1.94722
0.2	0	0.2	1.13043	1.93424	1.13041	1.93414
0.2	0.1	0.2	1.15832	1.94732	1.15830	1.94722
0.2	0.2	0.2	1.18563	1.96045	1.18561	1.96037
0.2	0.1	0.1	1.14163	2.5425	1.14160	2.54234
0.2	0.1	0.3	1.17451	1.7024	1.17449	1.70234
0.2	0.1	0.5	1.20565	1.47624	1.20563	1.47621

Table 6.4: *Resemblance of* $Re_x^{-\frac{1}{2}}\ Nu_x$ *for differing values of* K_1 , Fr , *and* δ *when* $M = \lambda = \phi_{Al_2O_3} = \phi_{Cu} = b_1 = 0$, $Pr = Sc = 1$, $Bi = 0.3$, $Nt = 0.2$, *and* $Nb = 0.5$.

K_1	Fr	δ	$Re_x^{-\frac{1}{2}}\ Nu_x$	
			Present study	(Muhammad et al., 2017)
0	0.1	0.2	0.2045108	0.20448
0.2	0.1	0.2	0.2025510	0.20248
0.2	0	0.2	0.2028408	0.20278
0.2	0.2	0.2	0.2022676	0.20220
0.2	0.1	0	0.1947498	0.19458
0.2	0.1	0.3	0.2056478	0.20560

used for numerical computation) is a finite-difference based code that implements the Lobatto IIIa formula of sixth-order in four steps. ζ_∞ has been restricted to 7 to get an asymptotic solution. The accuracy of the adopted numerical method has been validated through a restrictive correspondence with the previously published results by (Muhammad et al., 2017) and a commendable agreement is observed (see Tables 6.3 and 6.4).

6.4 Results and discussion

The consequence of pertinent parameters on physical quantities, x-directional velocity ($f'(\zeta)$), y-directional velocity ($g'(\zeta)$), temperature ($\theta(\zeta)$), and concentration ($\phi(\zeta)$) profiles are illustrated with the aid of graphs (see Figs. 6.2-6.18) and tables (see Tables 6.5 and 6.6). The Prandtl number (Pr) and Schmidt number (Sc) are set at

6.2 and 2.4, respectively. The thermophysical properties of base fluid (water), Al_2O_3 (nanoparticle 1), and Cu (nanoparticle 2) are given in Table 6.2. The results are presented to compare the flow phenomenon for injection ($\lambda < 0$) and suction ($\lambda > 0$) cases. It is observed that the suction case exhibits lower temperature and velocity profiles which are in perfect harmony with the findings of (Hussanan, Salleh, Khan, & Shafie, 2018). By increasing λ values, the boundary layer thickness diminishes thereby lowering the velocity. Furthermore, a progressive thinning of the thermal boundary layer is noted with an increase in λ values due to the introduction of cold ambient fluid near the sheet.

An increase in ϕ_{Cu} escalates the viscosity of fluid that demotes the velocity profile (see Fig. 6.2). Fig. 6.3 depicts the negative impact of M on $f'(\zeta)$, meaning an increase in M descends the x-directional velocity. This decrease in velocity is due to the generation of Lorentz force. The decreasing nature of $f'(\zeta)$ with Fr has been elucidated in Fig. 6.4. Augmentation in Fr ascends the resistance experienced in the fluid motion and hence $f'(\zeta)$ reduces. Fig. 6.5 describes the decreasing nature of K_1 on $f'(\zeta)$. Fig. 6.6 bespeaks the deviations in $f'(\zeta)$ with respect to b_1. It can be perceived that $f'(\zeta)$ decreases as b_1 values increase. Physically, the hydrodynamic slip parameter reduces the fluid movement due to the roughness of the sheet.

The generation of Lorentz force due to augmenting values of M reduces the y-directional velocity (see Fig. 6.7). The influence of K_1 on $g'(\zeta)$ is analyzed by means of Fig. 6.8. K_1 tends to decrease $g'(\zeta)$ which can be physically attributed to the fact that augmentation in the porosity parameter elevates the resistance of the porous medium. Fig. 6.9 displays the positive impact of δ on $g'(\zeta)$. Physically, increment in the stretching rate enhances the momentum associated with the boundary layer that swells the y-directional velocity.

Fig. 6.10 reflects the rise in $\theta(\zeta)$ due to mounting ϕ_{Cu} values. This is because an increase in ϕ_{Cu} improves the thermal conductivity of the hybrid nanoliquid which triggers an improvement in $\theta(\zeta)$. Fig. 6.11 describes the deviations in $\theta(\zeta)$ concerning M. The applied magnetic field generates a Lorentz force that ascends the temperature profile. The increase in $\theta(\zeta)$ with respect to augmentation in Bi values is described in Fig. 6.12. Physically, augmentation in the Biot number implies increased convection which enhances the hybrid nanoliquid temperature.

Fig. 6.13 elucidates the consequence of M on $\phi(\zeta)$. An increase in M tends to

increase $\phi(\zeta)$. The enhancement in $\phi(\zeta)$ due to an increase in K_1 has been graphed in Fig. 6.14. Furthermore, a dual nature is observed for augmenting λ values. For larger values of ζ, a decrease in $\phi(\zeta)$ is noted.

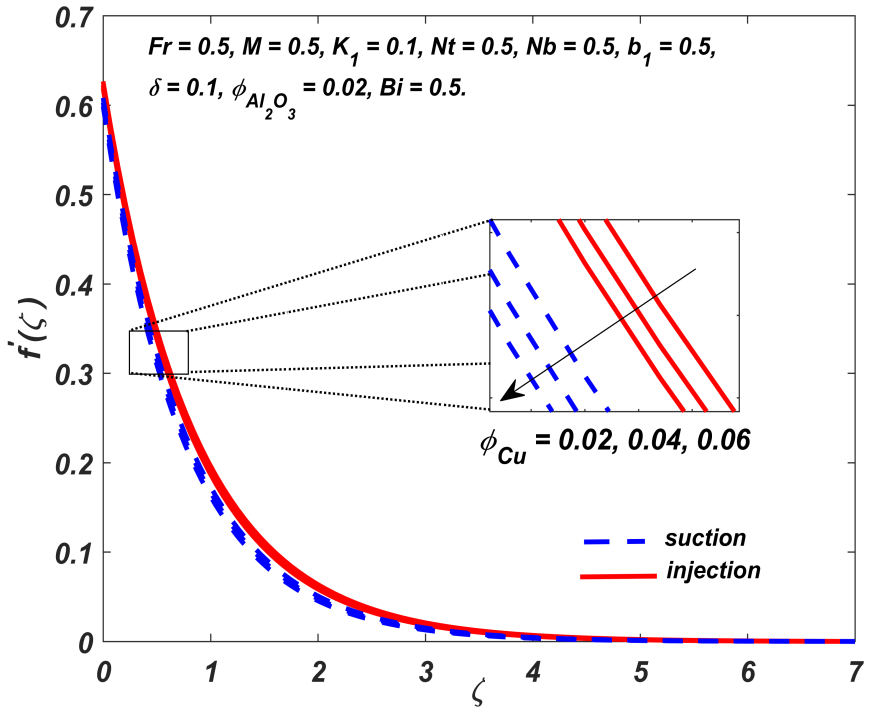

Figure 6.2: *Change in* $f'(\zeta)$ *for differing* ϕ_{Cu} *values.*

The simultaneous effect of two parameters on $Nu_x(Re_x)^{-\frac{1}{2}}$ is analysed with the aid of three-dimensional surface plots which have been graphed in Figs. 6.15 to 6.18. A comparative study between the suction and injection cases is also carried out. It can be perceived that the heat transfer rate is higher for the suction case in comparison with the injection case. From Figs. 6.15 to 6.18, it is seen that ϕ_{Cu} and Bi ascends $Nu_x(Re_x)^{-\frac{1}{2}}$ whereas Nt and M demotes the heat transfer rate. The key observations drawn from Tables 6.5 and 6.6 are:

- The drag coefficients $\left(Re_x^{\frac{1}{2}}\ Cf_x \text{ and } Re_y^{\frac{1}{2}}\ Cf_y\right)$ are directly proportional to b_1 and inversely proportional to M, K_1, and ϕ_{Cu}.
- $Re_x^{\frac{1}{2}}\ Cf_x$ is a decreasing function of Fr whereas $Re_y^{\frac{1}{2}}\ Cf_y$ is an increasing

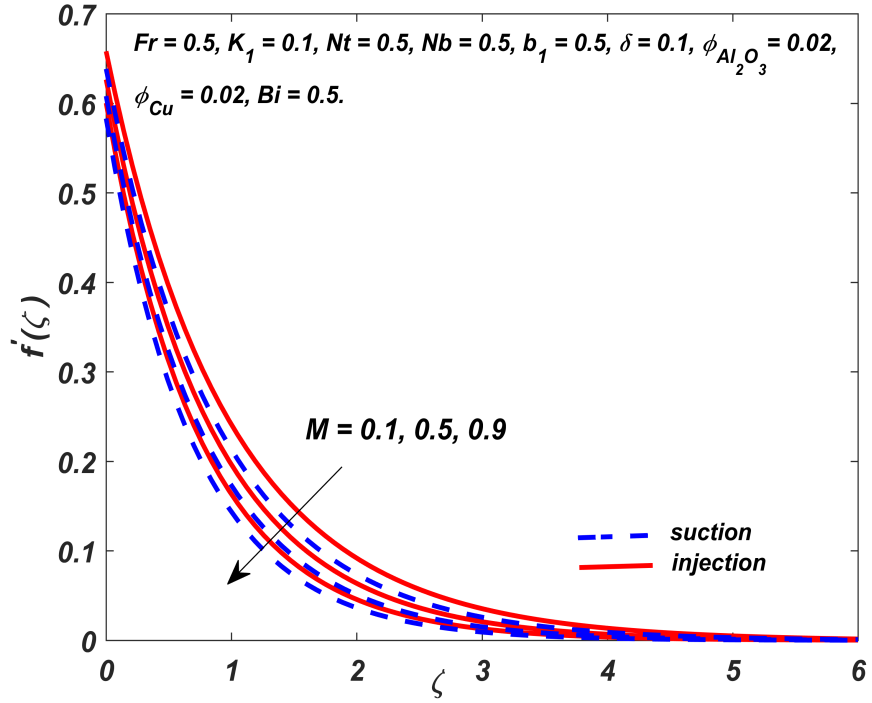

Figure 6.3: *Change in $f'(\zeta)$ for differing M values.*

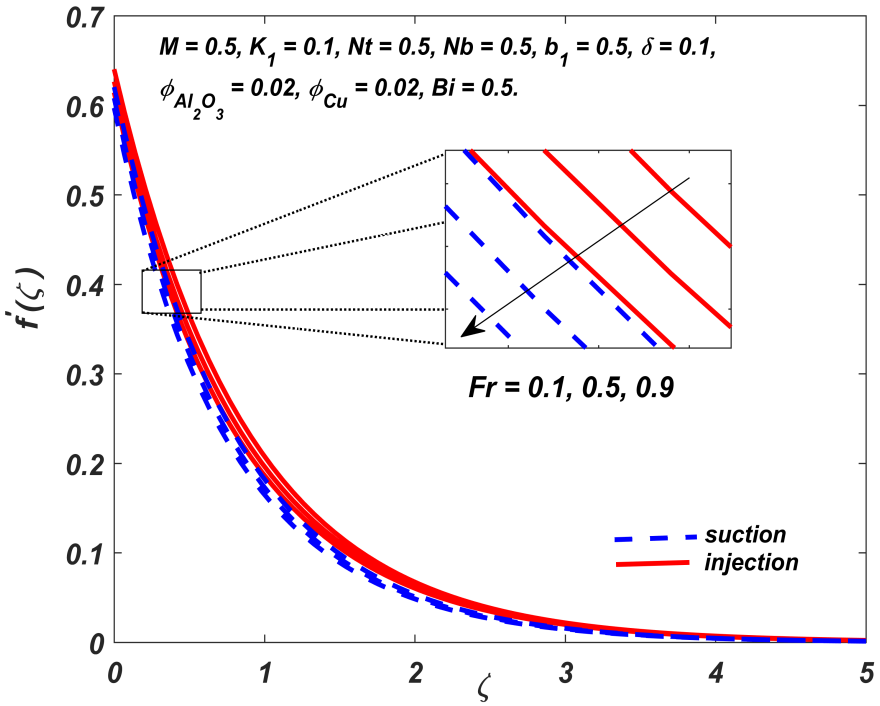

Figure 6.4: *Change in $f'(\zeta)$ for differing Fr values.*

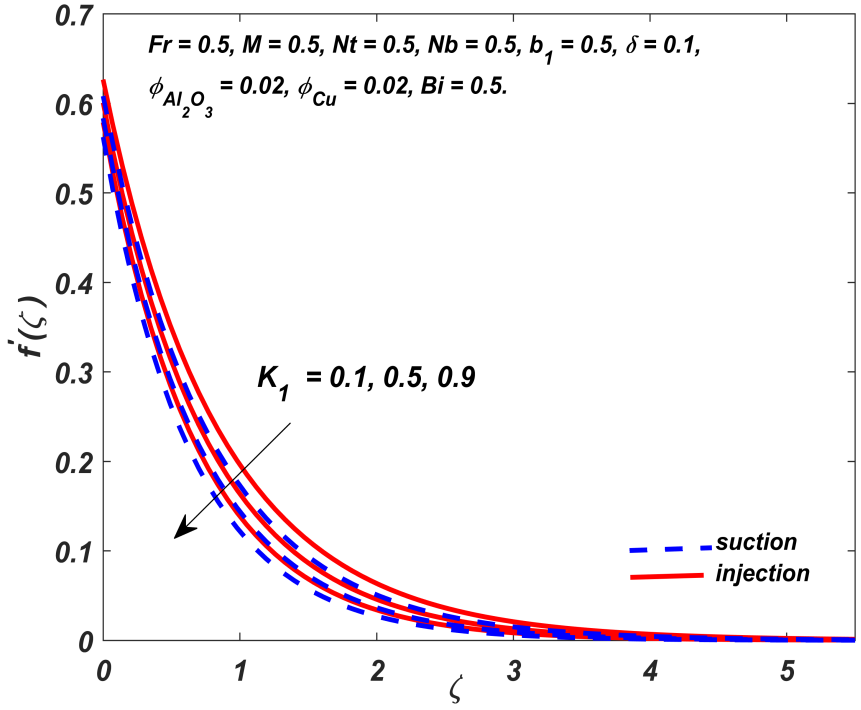

Figure 6.5: *Change in $f'(\zeta)$ for differing K_1 values.*

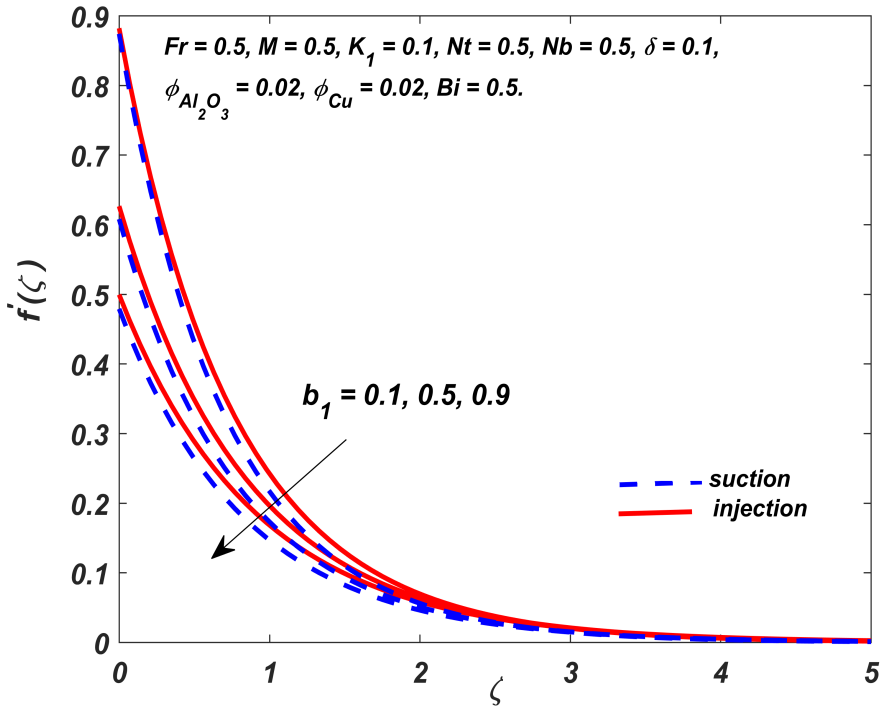

Figure 6.6: *Change in $f'(\zeta)$ for differing b_1 values.*

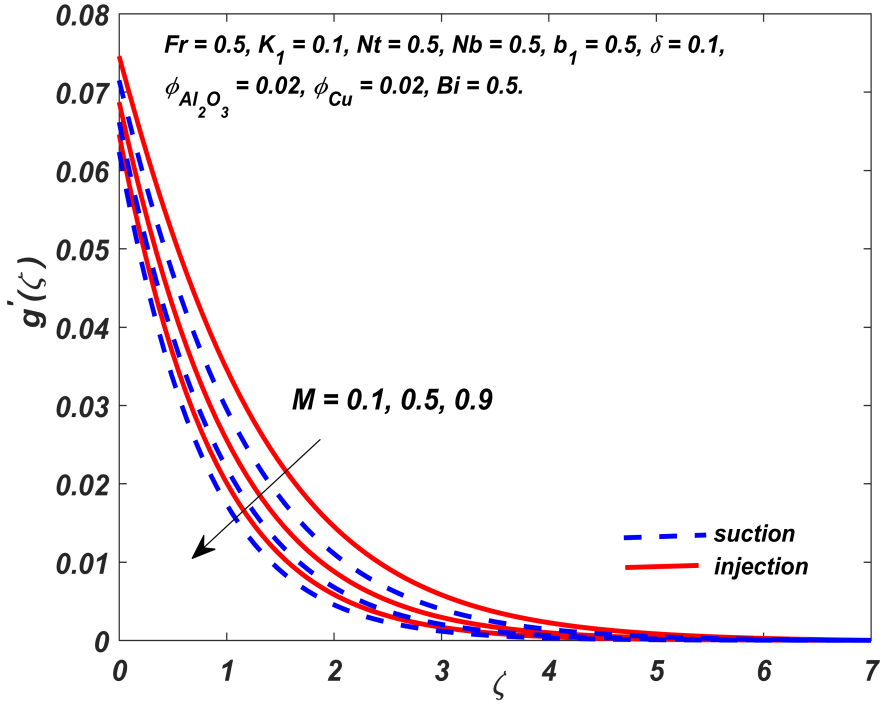

Figure 6.7: *Change in $g'(\zeta)$ for differing M values.*

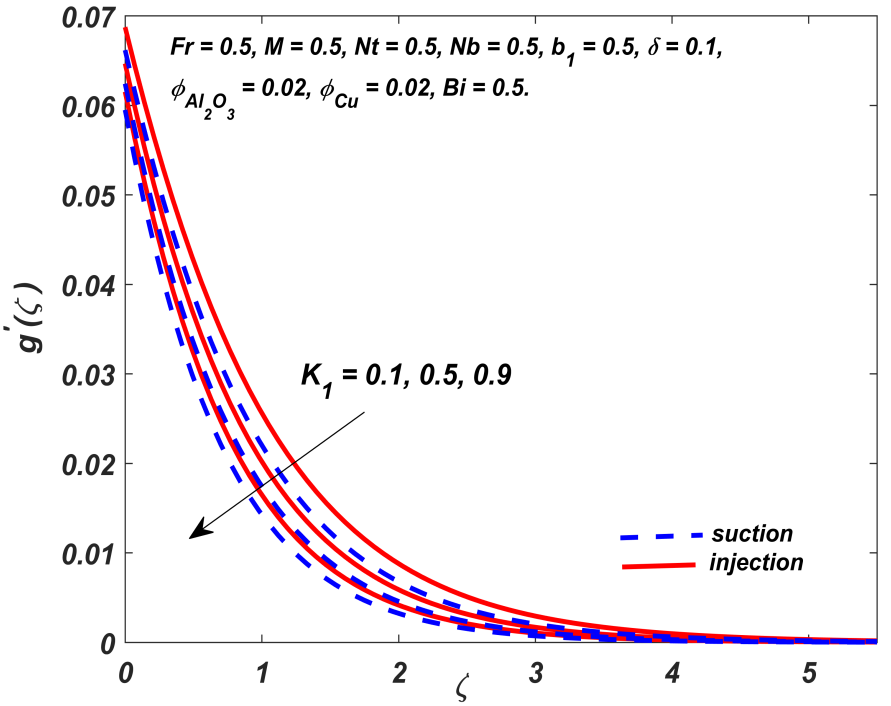

Figure 6.8: *Change in $g'(\zeta)$ for differing K_1 values.*

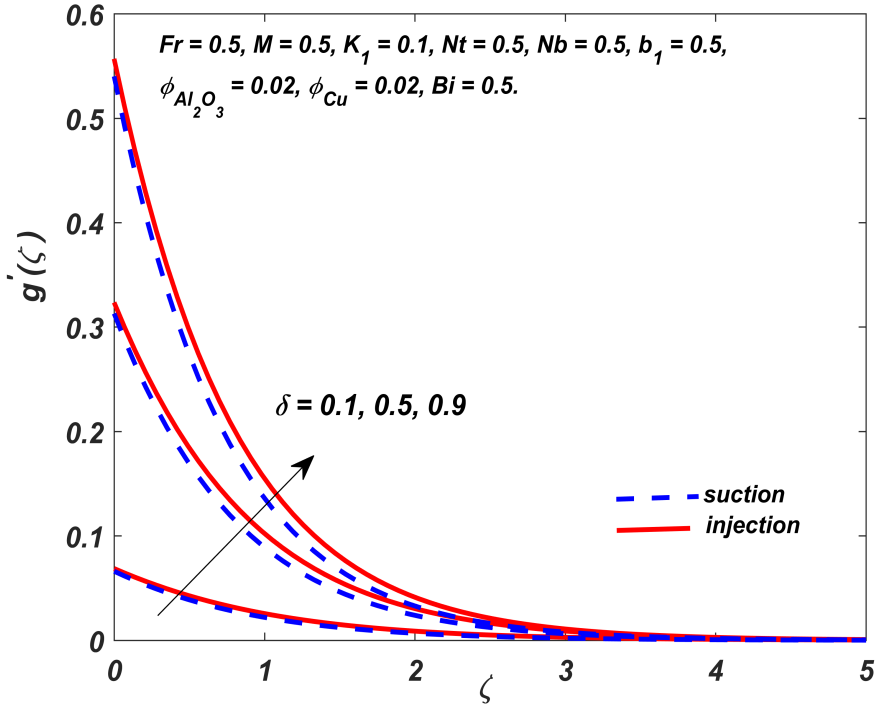

Figure 6.9: *Change in $g'(\zeta)$ for differing δ values.*

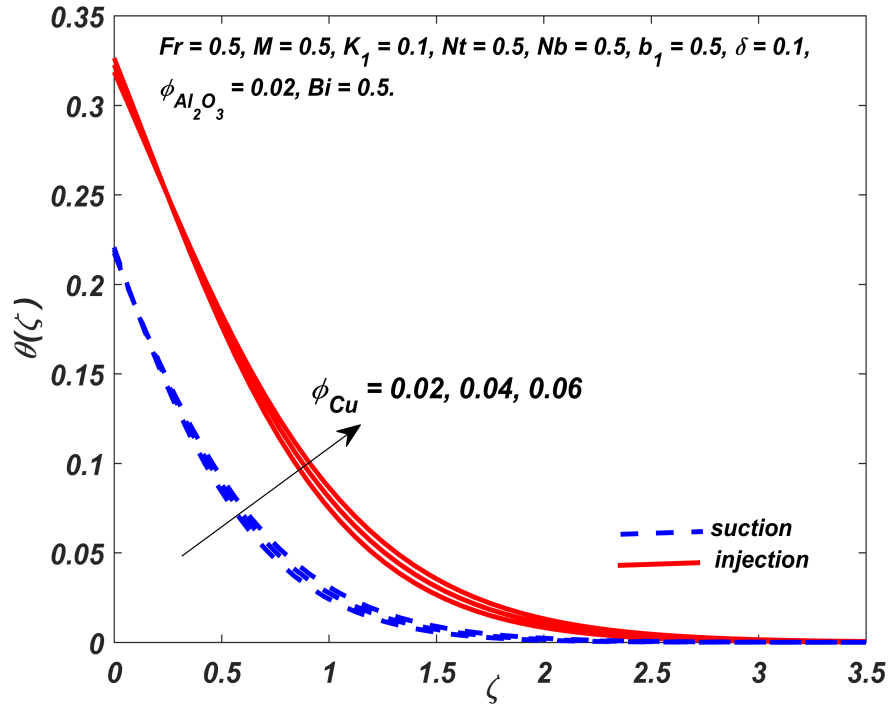

Figure 6.10: *Change in $\theta(\zeta)$ for differing ϕ_{Cu} values.*

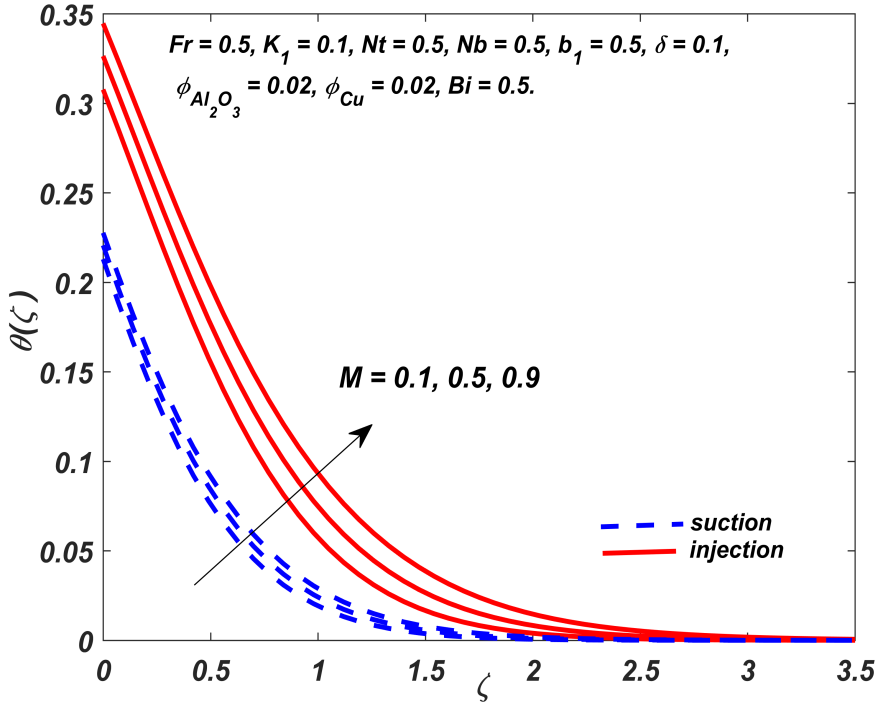

Figure 6.11: *Change in $\theta(\zeta)$ for differing M values.*

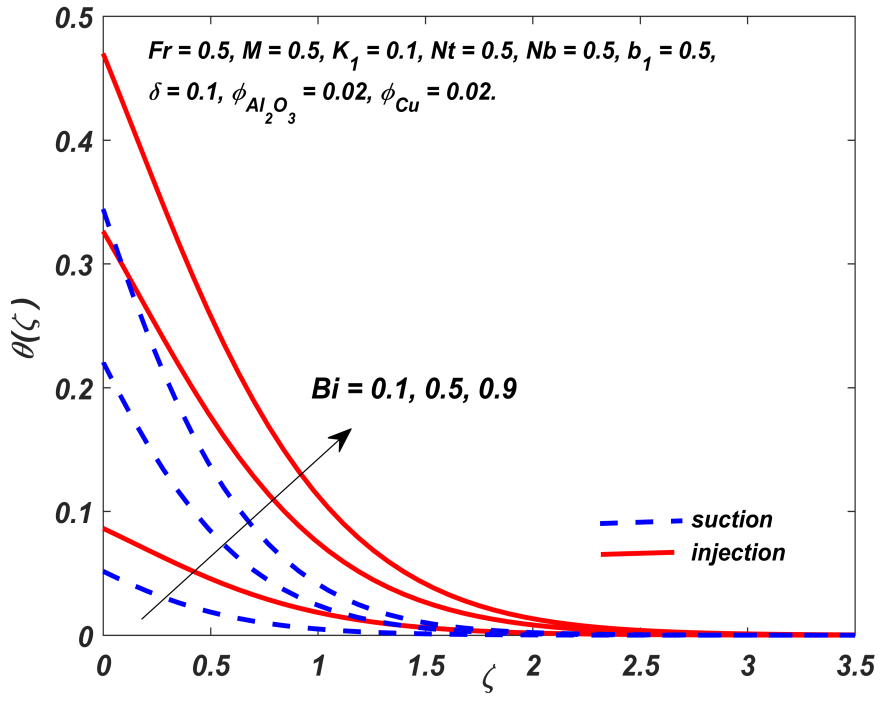

Figure 6.12: *Change in $\theta(\zeta)$ for differing Bi values.*

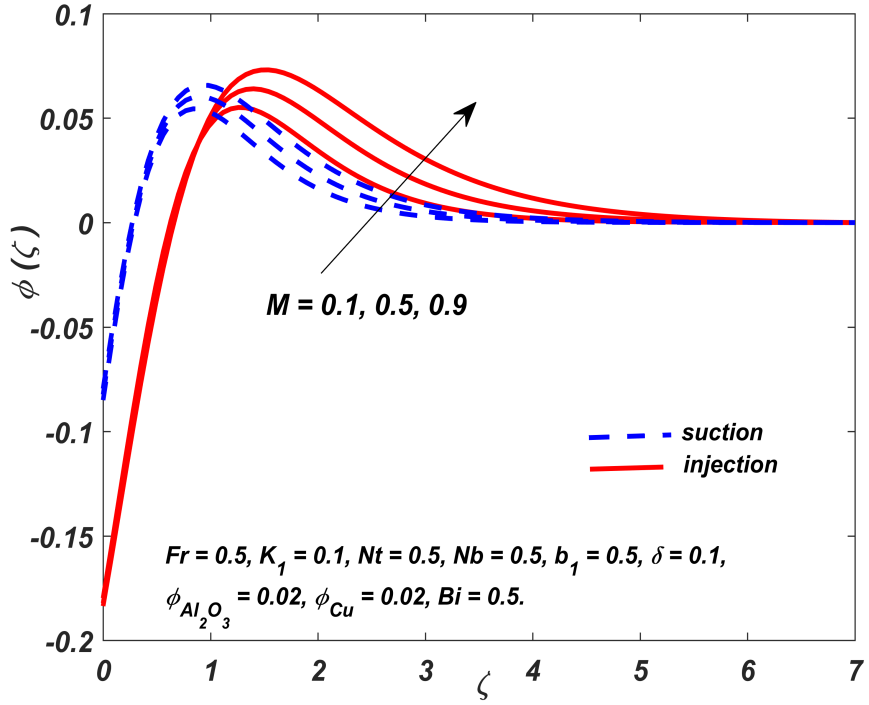

Figure 6.13: *Change in* $\phi(\zeta)$ *for differing* M *values.*

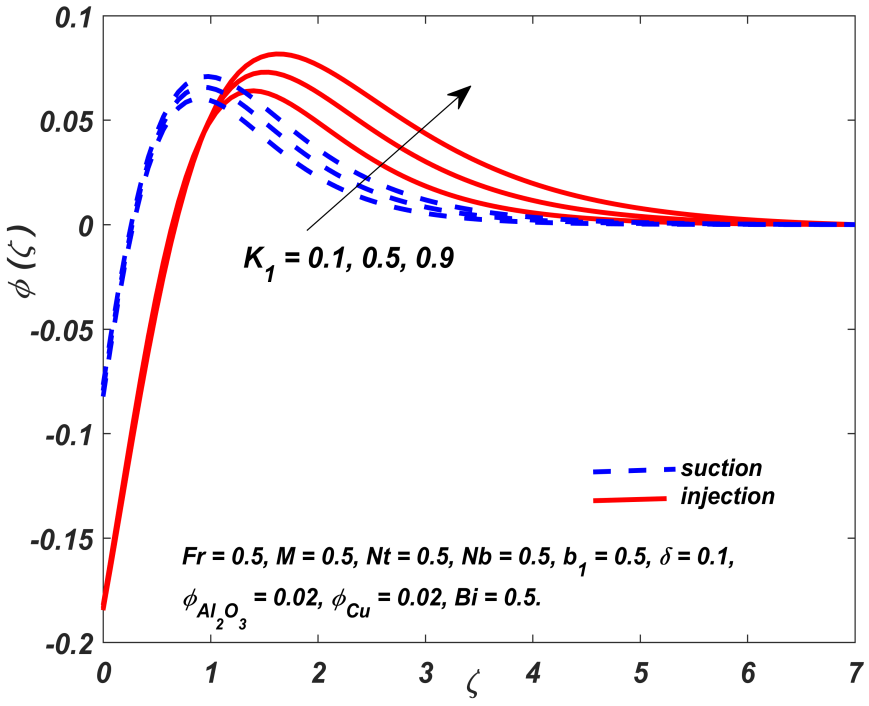

Figure 6.14: *Change in* $\phi(\zeta)$ *for differing* K_1 *values.*

Table 6.5: *Comparison on* $Re_x^{\frac{1}{2}}\ Cf_x$ *for differing values of* $Fr,\ M,\ K_1,\ \phi_{Cu}$, *and* b_1 *when* $Nt = 0.5,\ Nb = 0.5, \delta = 0.1, Bi = 0.5, \phi_{Al_2O_3} = 0.02$

					$Re_x^{\frac{1}{2}}\ Cf_x$	
Fr	M	K_1	ϕ_{Cu}	b_1	$\lambda = -0.1$	$\lambda = 0.1$
0.5	0.5	0.1	0.02	0.5	-0.82645	-0.86720
0.6	0.5	0.1	0.02	0.5	-0.83347	-0.87355
0.7	0.5	0.1	0.02	0.5	-0.84029	-0.87972
0.8	0.5	0.1	0.02	0.5	-0.84691	-0.88573
0.9	0.5	0.1	0.02	0.5	-0.85335	-0.89159
0.5	0.1	0.1	0.02	0.5	-0.75660	-0.80000
0.5	0.3	0.1	0.02	0.5	-0.79327	-0.83533
0.5	0.5	0.1	0.02	0.5	-0.82645	-0.86720
0.5	0.7	0.1	0.02	0.5	-0.85668	-0.89618
0.5	0.9	0.1	0.02	0.5	-0.88442	-0.92272
0.5	0.5	0.1	0.02	0.5	-0.82645	-0.86720
0.5	0.5	0.3	0.02	0.5	-0.85620	-0.89572
0.5	0.5	0.5	0.02	0.5	-0.88353	-0.92188
0.5	0.5	0.7	0.02	0.5	-0.90878	-0.94602
0.5	0.5	0.9	0.02	0.5	-0.93223	-0.96842
0.5	0.5	0.1	0.02	0.5	-0.82645	-0.86720
0.5	0.5	0.1	0.035	0.5	-0.86654	-0.91058
0.5	0.5	0.1	0.05	0.5	-0.90787	-0.95520
0.5	0.5	0.1	0.065	0.5	-0.95063	-1.00126
0.5	0.5	0.1	0.08	0.5	-0.99499	-1.04893
0.5	0.5	0.1	0.02	0.5	-0.82645	-0.86720
0.5	0.5	0.1	0.02	0.6	-0.76009	-0.79558
0.5	0.5	0.1	0.02	0.7	-0.70426	-0.73557
0.5	0.5	0.1	0.02	0.8	-0.65655	-0.68446
0.5	0.5	0.1	0.02	0.9	-0.61526	-0.64036

function of δ.

- Similar results are obtained for suction and injection cases.
- Higher drag coefficients are observed in the injection case when compared with the suction case.

6.5 Special Cases

In this section, a restrictive analysis on the velocity profile has been elucidated. The heat and concentration equations have been ignored for this purpose. A comparative analysis on the two-dimensional and axisymmetric flows considering slip and no-slip

Table 6.6: *Comparison on* $Re_y^{\frac{1}{2}}\ Cf_y$ *for differing values of* $M,\ K_1,\ \phi_{Cu},\ b_1$ *and* δ *when* $Nt = 0.5,\ Nb = 0.5, Fr = 0.5, Bi = 0.5, \phi_{Al_2O_3} = 0.02$.

					$Re_y^{\frac{1}{2}}\ Cf_y$	
M	K_1	ϕ_{Cu}	b_1	δ	λ = -0.1	$\lambda = 0.1$.
0.1	0.1	0.02	0.5	0.1	-1.77802	-1.99400
0.3	0.1	0.02	0.5	0.1	-2.00464	-2.19939
0.5	0.1	0.02	0.5	0.1	-2.18844	-2.36760
0.7	0.1	0.02	0.5	0.1	-2.34321	-2.51015
0.9	0.1	0.02	0.5	0.1	-2.47692	-2.63389
0.5	0.1	0.02	0.5	0.1	-2.18844	-2.36760
0.5	0.3	0.02	0.5	0.1	-2.34083	-2.50795
0.5	0.5	0.02	0.5	0.1	-2.47276	-2.63003
0.5	0.7	0.02	0.5	0.1	-2.58907	-2.73804
0.5	0.9	0.02	0.5	0.1	-2.69305	-2.83487
0.5	0.1	0.02	0.5	0.1	-2.18844	-2.36760
0.5	0.1	0.035	0.5	0.1	-2.28573	-2.48110
0.5	0.1	0.05	0.5	0.1	-2.38688	-2.59846
0.5	0.1	0.065	0.5	0.1	-2.49229	-2.72008
0.5	0.1	0.08	0.5	0.1	-2.60233	-2.84636
0.5	0.1	0.02	0.5	0.1	-2.18844	-2.36760
0.5	0.1	0.02	0.6	0.1	-2.04495	-2.20318
0.5	0.1	0.02	0.7	0.1	-1.92046	-2.06148
0.5	0.1	0.02	0.8	0.1	-1.81124	-1.93790
0.5	0.1	0.02	0.9	0.1	-1.71453	-1.82904
0.5	0.1	0.02	0.5	0.1	-2.18844	-2.36760
0.5	0.1	0.02	0.5	0.3	-1.35288	-1.44597
0.5	0.1	0.02	0.5	0.5	-1.10429	-1.17061
0.5	0.1	0.02	0.5	0.7	-0.97353	-1.02581
0.5	0.1	0.02	0.5	0.9	-0.88932	-0.93275

constraints is presented through Figs. 6.19 and 6.20.

6.5.1 Two-dimensional flow

The momentum equation of a two-dimensional flow ($g = 0$ and $\delta = 0$) is given by:

$$\left.\begin{array}{c} f''' - \left(\frac{A_2}{A_1}\right)\left\{(1+Fr)\,f'^2 - ff''\right\} - \left(\frac{A_3}{A_1}M + \lambda\right)f' = 0. \\ f'(0) = 1, f(0) = \lambda, f'(\infty) \to 0 \ \ (no\ slip\ condition) \\ f'(0) = 1 + b_1 f''(0), f(0) = \lambda, f'(\infty) \to 0 \ \ (\ slip\ condition) \end{array}\right\} \tag{6.5.1}$$

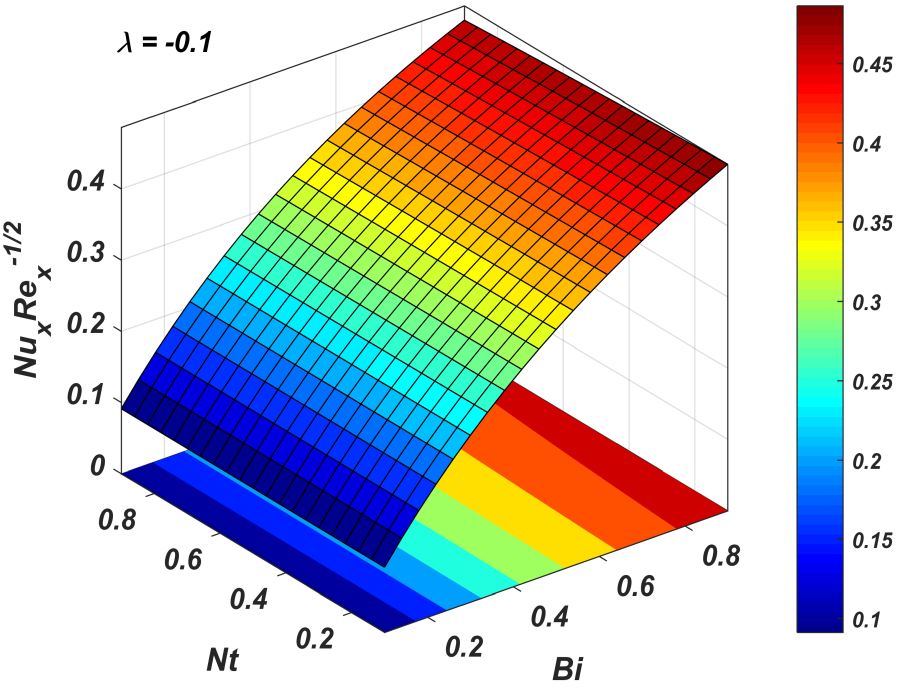

Figure 6.15: *Change in* $Nu_x(Re_x)^{-\frac{1}{2}}$ *for differing* Nt *and* Bi *with* $\lambda = -0.1$.

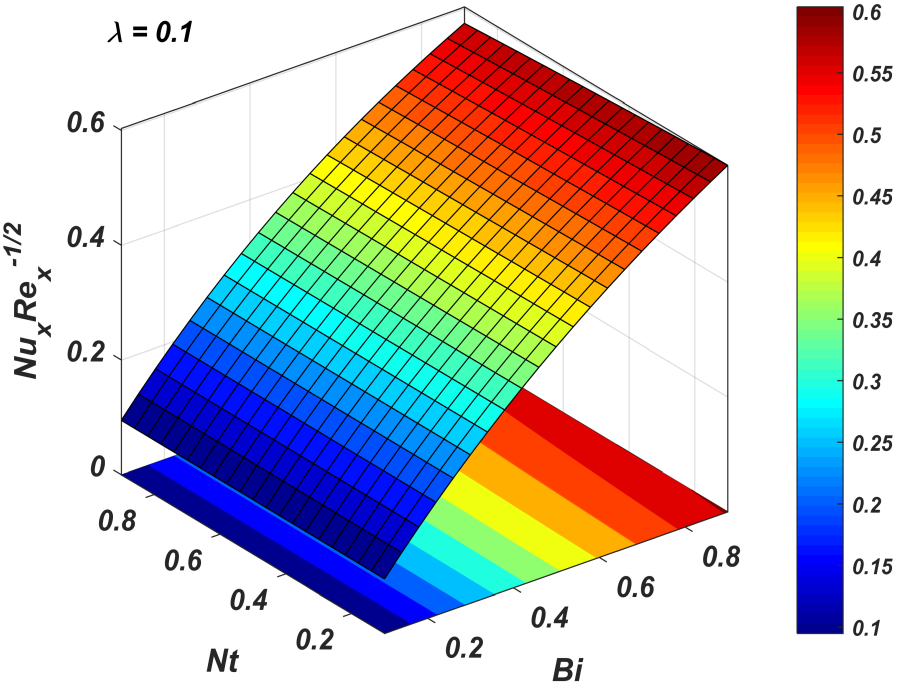

Figure 6.16: *Change in* $Nu_x(Re_x)^{-\frac{1}{2}}$ *for differing* Nt *and* Bi *with* $\lambda = 0.1$.

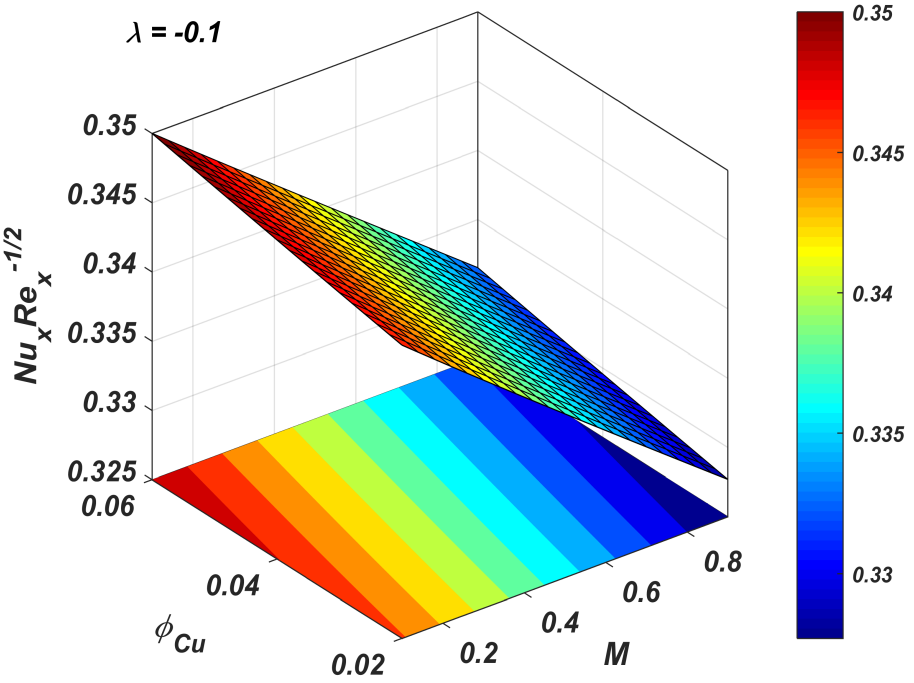

Figure 6.17: *Change in* $Nu_x(Re_x)^{-\frac{1}{2}}$ *for differing* ϕ_{Cu} *and* M *with* $\lambda = -0.1$.

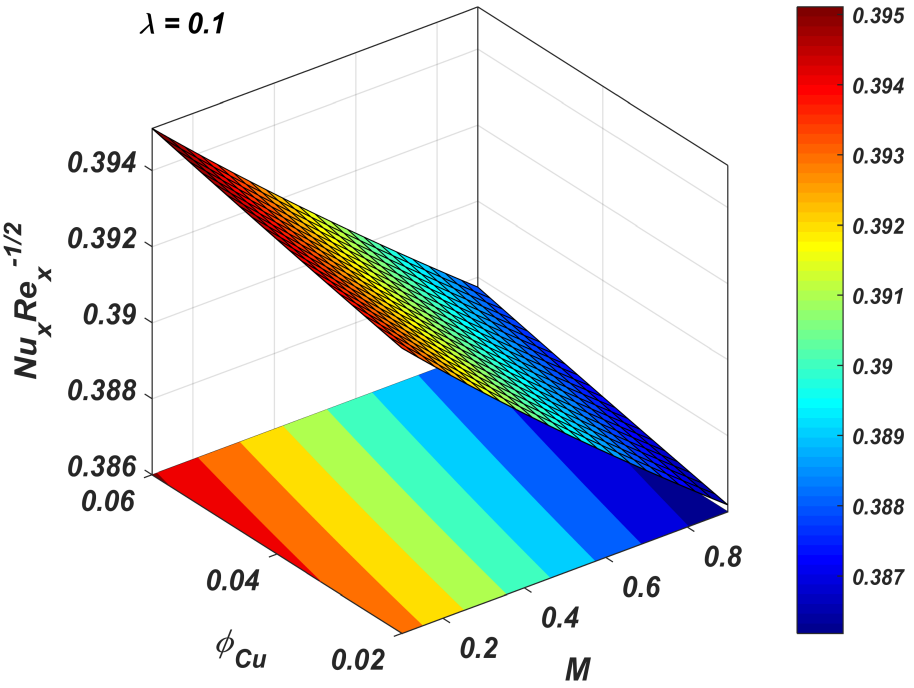

Figure 6.18: *Change in* $Nu_x(Re_x)^{-\frac{1}{2}}$ *for differing* ϕ_{Cu} *and* M *with* $\lambda = 0.1$.

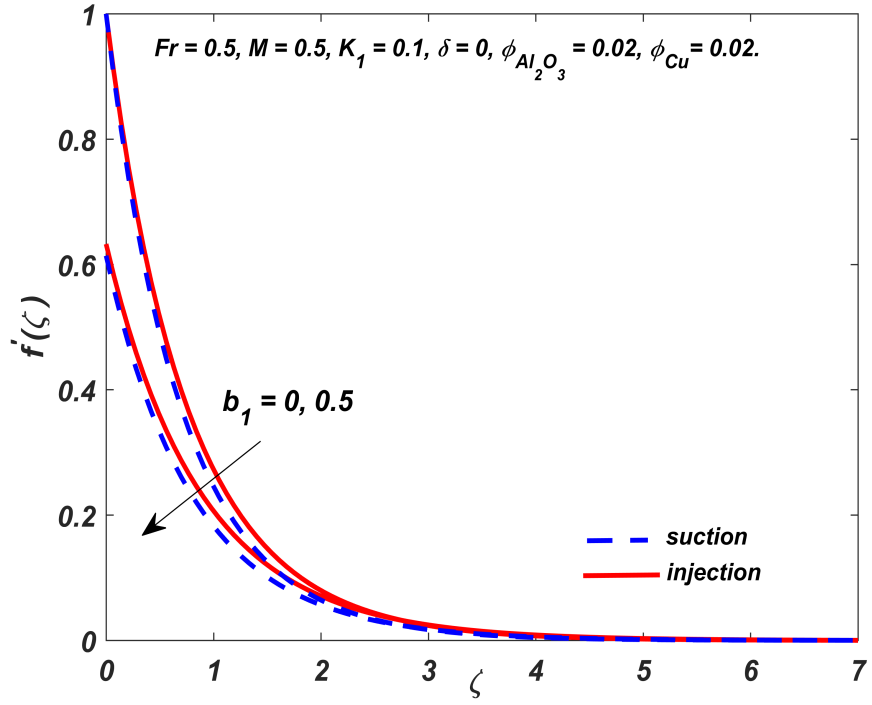

Figure 6.19: *Change in $f'(\zeta)$ of the two-dimensional flow for differing b_1 values.*

6.5.2 Axisymmetric flow

The momentum equation of an axisymmetric flow ($f = g$ and $\delta = 1$) is given by:

$$\left.\begin{array}{c} f''' - \left(\frac{A_2}{A_1}\right)\left\{(1+Fr)\,f'^2 - 2ff''\right\} - \left(\frac{A_3}{A_1}M + \lambda\right)f' = 0. \\ f'(0) = 1, f(0) = \lambda, f'(\infty) \to 0 \ \ (no\ slip\ condition) \\ f'(0) = 1 + b_1 f''(0), f(0) = \lambda, f'(\infty) \to 0 \ \ (\ slip\ condition) \end{array}\right\} \tag{6.5.2}$$

Fig. 6.19 depicts the effect of b_1 and λ on the two-dimensional flow. A higher velocity profile is observed in the case of injection and no-slip conditions. The impact of b_1 and λ on the axisymmetric flow have been illustrated using Fig. 6.20. A lower velocity profile is observed in the case of suction and slip conditions.

6.6 Regression Analysis

Regression analysis helps in establishing the relationship between a dependent and one or more independent variables . In this study, the relationship between the drag coefficients and the pertinent parameters for suction ($\lambda = 0.1$) and injection

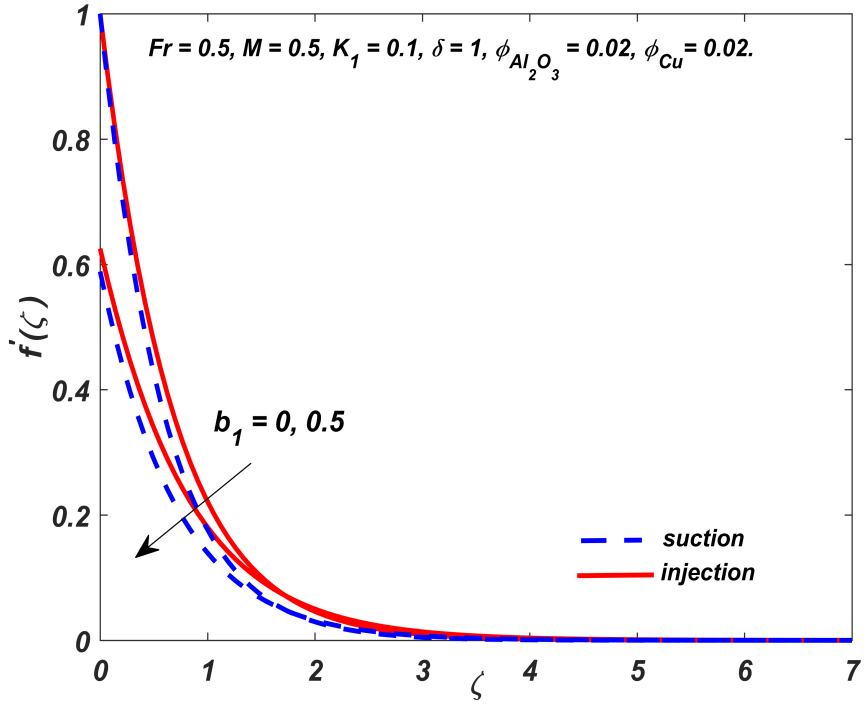

Figure 6.20: *Change in* $f'(\zeta)$ *of the axisymmetric flow for differing* b_1 *values.*

($\lambda = -0.1$) cases has been statistically modelled. The general form for the estimated model is given by:

$$Re_x^{\frac{1}{2}} \; Cf_x \; = r_{Fr}Fr + r_M M + r_{K_1}K_1 + r_{\phi_{Cu}}\phi_{Cu} + r_{b_1}b_1 + c \tag{6.6.1}$$

$$Re_y^{\frac{1}{2}} \; Cf_y \; = r_M M + r_{K_1}K_1 + r_{\phi_{Cu}}\phi_{Cu} + r_{b_1}b_1 + r_\delta \delta + c \tag{6.6.2}$$

where r_{Fr}, r_M, r_{K_1}, $r_{\phi_{Cu}}$, r_{b_1}, r_δ and c are the estimated regression coefficients. The drag coefficients are estimated using the 25 sets of values chosen in the range $[0.1, 0.9]$ for δ, $[0.5, 0.9]$ for b_1 , $[0.1, 0.9]$ for K_1, $[0.02, 0.08]$ for ϕ_{Cu} , $[0.5, 0.9]$ for Fr, and $[0.1, 0.9]$ for M and the regression coefficients are found using the MATLAB software. The estimated regression models are given by:

$$\begin{aligned} Re_x^{\frac{1}{2}} \; {Cf_x}^{\lambda=-0.1} \; &= -0.07585 \; Fr - 0.15952 \; M - 0.13964 \; K_1 - 2.82993 \; \phi_{Cu} \\ &\quad +0.547116 \; b_1 - \; 0.90938 \end{aligned} \tag{6.6.3}$$

$$Re_y^{\frac{1}{2}}\ Cf_y{}^{\lambda=-0.1} = -0.86819\ M - 0.74863\ K_1 - 8.02595\ \phi_{Cu} + 1.052088\ b_1 + 1.882442\ \delta - 2.17821 \tag{6.6.4}$$

$$Re_x^{\frac{1}{2}}\ Cf_x{}^{\lambda=0.1} = -0.06984\ Fr - 0.15314\ M - 0.13403\ K_1 - 3.05209\ \phi_{Cu} + 0.588495\ b_1 - 0.97302 \tag{6.6.5}$$

$$Re_y^{\frac{1}{2}}\ Cf_y{}^{\lambda=0.1} = -0.79527\ M - 0.70502\ K_1 - 9.18266\ \phi_{Cu} + 1.211844\ b_1 + 2.082646\ \delta - 2.47155 \tag{6.6.6}$$

The sign of the estimated regression coefficient denotes the nature of the relationship for the corresponding parameter on the dependent variable and the magnitude of the estimated regression coefficient corresponds to the intensity of this relationship. From the estimated models it is conclusive that the relationship experienced by the influential parameters on the drag coefficients are in present harmony with the observations derived from Tables 6.5 and 6.6. Figs. 6.21 to 6.24 illustrate the accuracy of the regression model for the chosen sample. A commendable agreement is noted between the actual and estimated values.

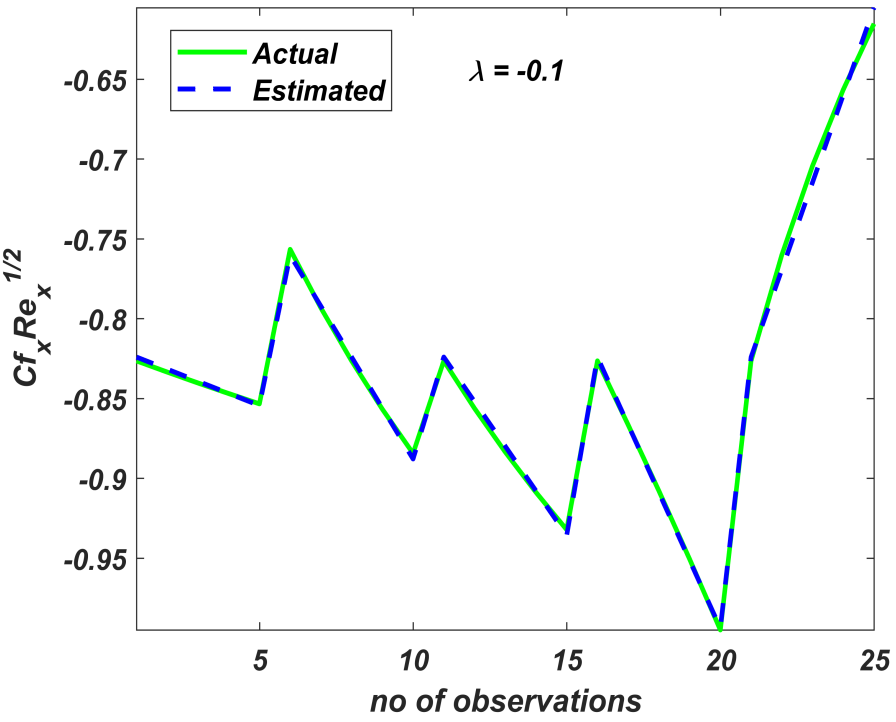

Figure 6.21: *Actual* $Re_x^{\frac{1}{2}} Cf_x$ *versus Estimated* $Re_x^{\frac{1}{2}} Cf_x$ *with* $\lambda = -0.1$.

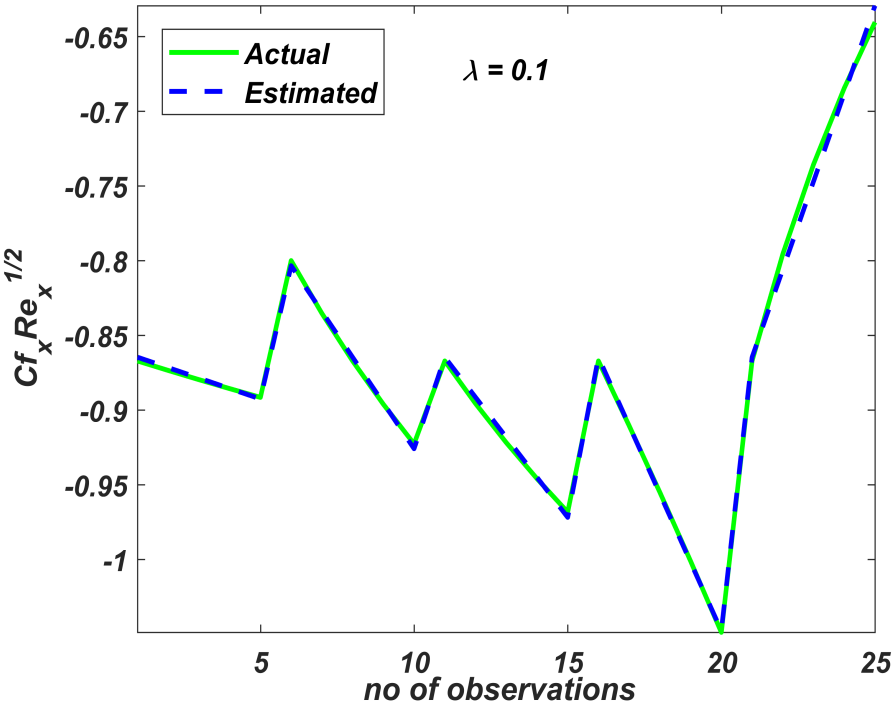

Figure 6.22: *Actual* $Re_x^{\frac{1}{2}} Cf_x$ *versus Estimated* $Re_x^{\frac{1}{2}} Cf_x$ *with* $\lambda = 0.1$.

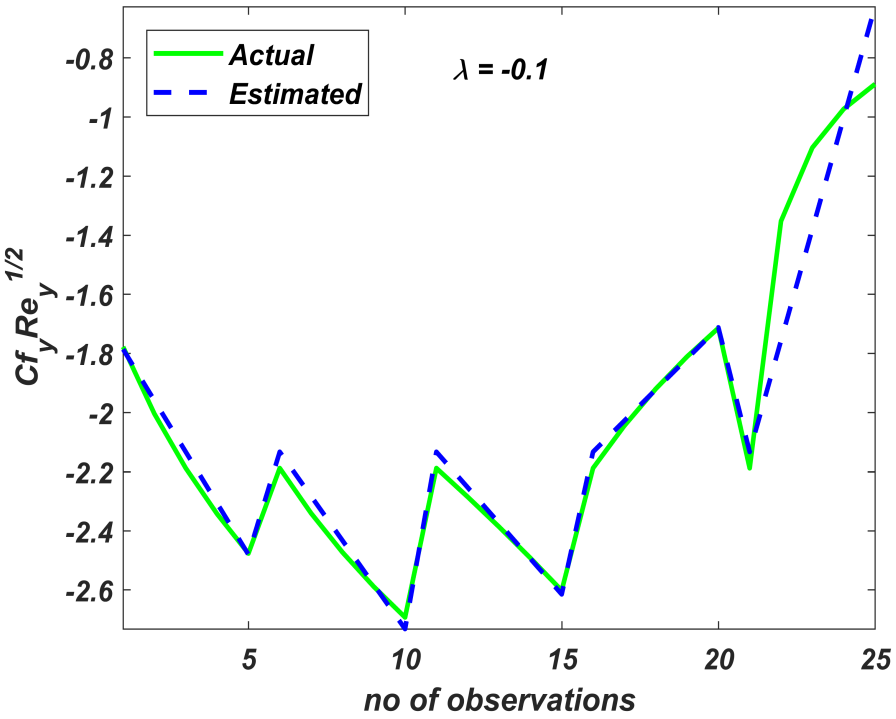

Figure 6.23: *Actual* $Re_y^{\frac{1}{2}} Cf_y$ *versus Estimated* $Re_y^{\frac{1}{2}} Cf_y$ *with* $\lambda = -0.1$.

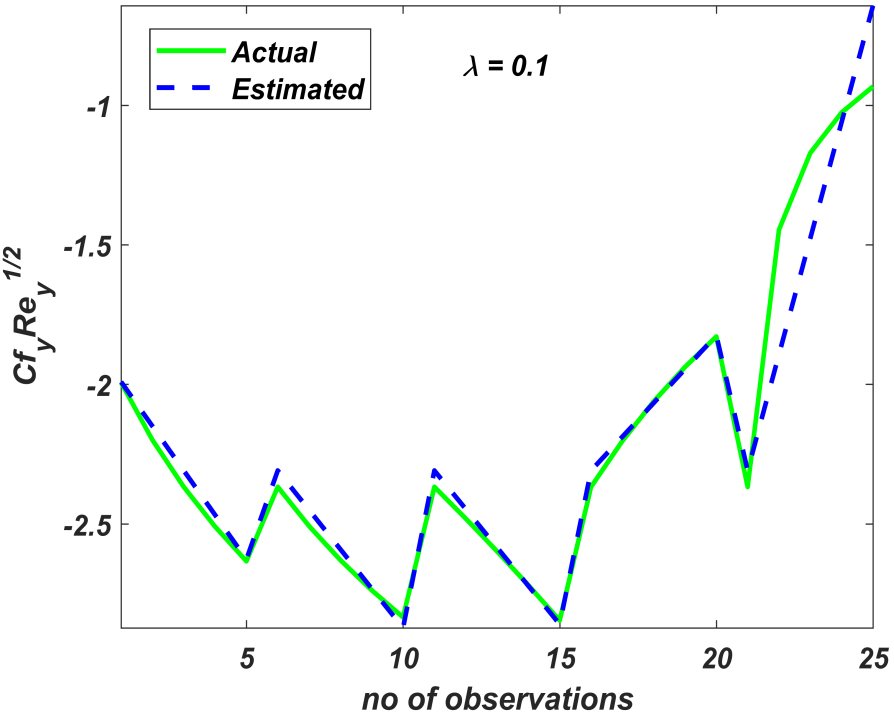

Figure 6.24: *Actual* $Re_y^{\frac{1}{2}}Cf_y$ *versus Estimated* $Re_y^{\frac{1}{2}}Cf_y$ *with* $\lambda = 0.1$.

6.7 Conclusions

For its applications in astronomical disciplines, fuel injection, solar collector plate, thermal protection, and aerodynamics; the MHD Darcy-Forchheimer hybrid nanoliquid flow over an elongated permeable sheet in a porous medium with hydrodynamic slip and Newtonian boundary constraints have been examined. A realistic model is used by considering the passive control of nanoparticles and the modified Buongiorno nanoliquid model. The consequence of effectual parameters on the flow profiles has been numerically investigated using the bvp5c routine. A comparative analysis of the velocity profile on the two-dimensional and axisymmetric flows in the presence of slip and no-slip constraints has also been presented. Further, the relationship between the pertinent parameters and the drag coefficients has been statistically scrutinized utilizing regression analysis. The major conclusions drawn from the study are:

- The x-directional velocity descends with the Forchheimer number and hydrodynamic slip parameter.

- The y-directional velocity ascends with the stretching parameter.
- The suction case exhibits lowered temperature and velocity profiles in correspondence with the injection case.
- The Biot number and the volume fraction of copper nanoparticles have a constructive effect on the hybrid nanoliquid temperature.
- The heat transfer rate is higher for the suction case in comparison with the injection case.
- The heat transfer rate is higher for lower values of magnetic field parameter and higher values of Biot number and volume fraction of copper nanoparticles.
- The drag coefficients increase with hydrodynamic slip parameter and decrease for higher values of magnetic field and porosity parameters.
- Higher drag coefficients are observed in the case of injection when compared with the suction case.
- A commendable agreement is noted between the numerical and statistical results.

Chapter 7

Reiner-Rivlin nanoliquid flow past a spinning disk with Joule heating and non-uniform heat source using Bulirsch-Stoer algorithm *

7.1 Introduction

The current study is conducted to investigate the hydromagnetic flow of Reiner-Rivlin nanoliquids due to a rotating disk with non-uniform heat source and Joule heating effects inorder to optimize the heat transfer rate through Response surface methodology. The volume fraction of the nanoparticles on the disk surface is passively controlled by a realistic boundary condition. Using numerical and statistical methods, this work addresses the following research questions:

- How do the flow profiles vary due to the non-Newtonian nature?
- What effect does Joule heating have on the thermal boundary layer?
- How do temperature and space-dependent heat source parameters affect the heat transport phenomenon?
- How can the heat transfer rate be regulated by varying the influential effects?
- What is the sensitivity of the heat transport against the key factors?

*Published in: Waves in Random and Complex Media (Taylor & Francis), 2022; (early access)

7.2 Mathematical formulation

An electrically conducting non-transient Reiner-Rivlin nanofluid flow past a rotating disk is considered (see Fig. 7.1). The nanoliquid is present in the region above $z > 0$ and is incompressible. The axisymmetric spinning of the disk about the vertical axis ignores the derivatives along with tangential directions. The uniform spinning of the disk (with an angular velocity Ω) in the plane $z = 0$ imparts a swirling flow in the adjacent fluid layers. Here, $(u,\ v,\ w)$ are respectively the components of velocity vector projections along the radial (r), azimuthal (φ), and axial (z) directions. Let the temperature at the surface of the disk be T_w. Furthermore, T_∞ and C_∞ represent the ambient temperature and volume fraction of nanoparticles far from the disk. The centrifugal fan-like behaviour of the disk preserves the mass conservation principle by drawing the nanoliquid in the axial direction. The heterogeneous two-phase model is utilized to model the nanoliquid. Also, the fluid properties are considered to be constant in the system. The fluid is exposed to a uniform magnetic field of intensity B_0 along the axial direction and Joule heating effects are accounted. The governing equations to model the above problem are given below (see (Tabassum & Mustafa, 2018), (Imtiaz, Kiran, Hayat, & Alsaedi, 2019), (Lin, Ghaffari, et al., 2021)):

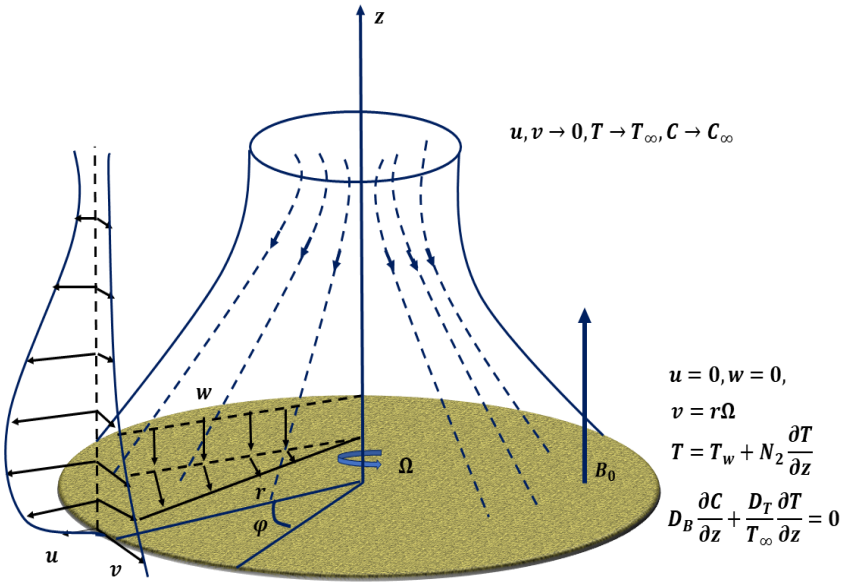

Figure 7.1: *Physical configuration*

$$\frac{\partial u}{\partial r} + \frac{u}{r} + \frac{\partial w}{\partial z} = 0, \tag{7.2.1}$$

$$\rho_f\left(u\frac{\partial u}{\partial r}+w\frac{\partial u}{\partial z}-\frac{v^2}{r}\right)=\frac{\partial \tau_{rr}}{\partial r}+\frac{\partial \tau_{zr}}{\partial z}+\frac{(\tau_{rr}-\tau_{\varphi\varphi})}{r}-\sigma_f B_0^2 u, \tag{7.2.2}$$

$$\rho_f\left(u\frac{\partial v}{\partial r}+w\frac{\partial v}{\partial z}+\frac{uv}{r}\right)=\frac{1}{r^2}\frac{\partial}{\partial r}\left(r^2\tau_{r\varphi}\right)+\frac{\partial \tau_{z\varphi}}{\partial z}+\frac{(\tau_{r\varphi}-\tau_{\varphi r})}{r}-\sigma_f B_0^2 v, \tag{7.2.3}$$

$$\rho_f\left(u\frac{\partial w}{\partial r}+w\frac{\partial w}{\partial z}\right)=\frac{1}{r}\frac{\partial}{\partial r}\left(r\tau_{rz}\right)+\frac{\partial \tau_{zz}}{\partial z}, \tag{7.2.4}$$

$$\begin{aligned} u\tfrac{\partial T}{\partial r}+w\tfrac{\partial T}{\partial z}=\alpha_m\left(\tfrac{\partial^2 T}{\partial r^2}+\tfrac{1}{r}\tfrac{\partial T}{\partial r}+\tfrac{\partial^2 T}{\partial z^2}\right)+\tfrac{(\rho c)_p}{(\rho c)_f}\left\{D_B\left(\tfrac{\partial T}{\partial r}\tfrac{\partial C}{\partial r}+\tfrac{\partial T}{\partial z}\tfrac{\partial C}{\partial z}\right)\right. \\ \left.+\tfrac{D_T}{T_\infty}\left(\left(\tfrac{\partial T}{\partial r}\right)^2+\left(\tfrac{\partial T}{\partial z}\right)^2\right)\right\}+\tfrac{1}{(\rho c)_f}q'''+\tfrac{\sigma_f B_0^2}{(\rho c)_f}\left(u^2+v^2\right), \end{aligned} \tag{7.2.5}$$

$$u\frac{\partial C}{\partial r}+w\frac{\partial C}{\partial z}=D_B\left(\frac{\partial^2 C}{\partial r^2}+\frac{1}{r}\frac{\partial C}{\partial r}+\frac{\partial^2 C}{\partial z^2}\right)+\frac{D_T}{T_\infty}\left(\frac{\partial^2 T}{\partial r^2}+\frac{1}{r}\frac{\partial T}{\partial r}+\frac{\partial^2 T}{\partial z^2}\right), \tag{7.2.6}$$

q''' is the non-uniform heat generation /absorption term that is modeled as $q'''=\frac{k_f\Omega}{\nu_f}\left[\frac{A(T_w-T_\infty)}{\Omega r}u+B\ (T-T_\infty)\right]$, where A and B denote respectively the space-dependent and temperature-dependent heat source/sink parameters. The internal heat generation mechanism without an external heat source has a major role in medical and industrial applications. Current flow in a conducting fluid augments the temperature of the fluid and therefore, the Joule heating effect is incorporated via the last term in Eqn. 7.2.5. The nanoparticle volume fraction at the surface of the disk is passively controlled. The disk is rigid which does not allow fluid penetration and viscous dissipative forces are ignored due to negligible effects. The thermal disparity between the disk and the nanoliquid associated with the surface is incorporated through the thermal jump condition.

Boundary conditions:

$$\left.\begin{aligned} &\text{At } z=0:\ u=0, && v=v_w=r\Omega, && w=0,\\ &T=T_w+N_2\tfrac{\partial T}{\partial z}\ , && D_B\tfrac{\partial C}{\partial z}+\tfrac{D_T}{T_\infty}\tfrac{\partial T}{\partial z}=0\ . \end{aligned}\right\} \tag{7.2.7}$$

$$As\ \ z\to\infty: u\to 0, \qquad v\to 0, \qquad T\to T_\infty, \qquad C\to C_\infty, \qquad p\to p_\infty. \tag{7.2.8}$$

Due to the stress tensor symmetry, the second last term in Eqn. 7.2.3 is ignored. The following constitutive relation is used to model the rheological properties of the Reiner-Rivlin nanoliquid:

$$\tau_{ij}=-p\delta_{ij}+\mu_f e_{ij}+\mu_c e_{ik}e_{kj}(e_{jj}=0).(see(Tabassum\ \&Mustafa,2018)): \tag{7.2.9}$$

The influence of stress across velocity gradients leads to cross-viscosity, a property of the Reiner-Rivlin nanofluid considered in the study. Here, the rate of strain (deformation) tensor is denoted by $e_{ij} = \frac{\partial u_i}{\partial x_j} + \frac{\partial u_j}{\partial x_i}$, Kronecker delta symbol is denoted by δ_{ij}, cross$-$viscosity coefficient is denoted by μ_c, coefficient of viscosity is denoted by μ_f and pressure is denoted by p. The stress tensors (τ_{ij}) of this liquid are given as follows (see (Tabassum & Mustafa, 2018)):

$$\tau_{rr} = -p + \mu_f \left(2\frac{\partial u}{\partial r}\right) + \mu_c \left\{4\left(\frac{\partial u}{\partial r}\right)^2 + \left(\frac{\partial v}{\partial r} - \frac{v}{r}\right)^2 + \left(\frac{\partial u}{\partial z} + \frac{\partial w}{\partial r}\right)^2\right\}, \quad (7.2.10)$$

$$\begin{aligned}\tau_{zr} = \mu_f \left(\tfrac{\partial u}{\partial z} + \tfrac{\partial w}{\partial r}\right) + \mu_c \left\{\left(2\tfrac{\partial u}{\partial r}\right)\left(\tfrac{\partial u}{\partial z} + \tfrac{\partial w}{\partial r}\right) + \left(\tfrac{\partial v}{\partial r} - \tfrac{v}{r}\right)\left(\tfrac{\partial v}{\partial z}\right)\right\} + \\ \mu_c \left\{\left(\tfrac{\partial u}{\partial z} + \tfrac{\partial w}{\partial r}\right)\left(2\tfrac{\partial w}{\partial z}\right)\right\},\end{aligned} \quad (7.2.11)$$

$$\tau_{\varphi\varphi} = -p + \mu_f \left(\frac{2u}{r}\right) + \mu_c \left\{\frac{4u^2}{r^2} + \left(\frac{\partial v}{\partial r} - \frac{v}{r}\right)^2 + \left(\frac{\partial v}{\partial z}\right)^2\right\}, \quad (7.2.12)$$

$$\begin{aligned}\tau_{r\varphi} = \mu_f \left(\tfrac{\partial v}{\partial r} - \tfrac{v}{r}\right) + \mu_c \left\{\left(2\tfrac{\partial u}{\partial r}\right)\left(\tfrac{\partial v}{\partial r} - \tfrac{v}{r}\right) + \left(\tfrac{\partial v}{\partial r} - \tfrac{v}{r}\right)\left(\tfrac{2u}{r}\right)\right\} + \\ \mu_c \left\{\left(\tfrac{\partial u}{\partial z} + \tfrac{\partial w}{\partial r}\right)\left(\tfrac{\partial v}{\partial z}\right)\right\},\end{aligned} \quad (7.2.13)$$

$$\tau_{z\varphi} = \mu_f \frac{\partial v}{\partial z} + \mu_c \left\{\left(\frac{\partial v}{\partial r} - \frac{v}{r}\right)\left(\frac{\partial u}{\partial z} + \frac{\partial w}{\partial r}\right) + 2\left(\frac{u}{r}\right)\left(\frac{\partial v}{\partial z}\right) + 2\left(\frac{\partial v}{\partial z}\right)\left(\frac{\partial w}{\partial z}\right)\right\}, \quad (7.2.14)$$

$$\tau_{zz} = -p + \mu_f \left(2\frac{\partial w}{\partial z}\right) + \mu_c \left\{\left(\frac{\partial u}{\partial z} + \frac{\partial w}{\partial r}\right)^2 + \left(\frac{\partial v}{\partial z}\right)^2 + 4\left(\frac{\partial w}{\partial z}\right)^2\right\} \quad (7.2.15)$$

The axial, radial, and azimuthal velocity components rely upon radial and normal spatial coordinates (r and z). Pressure along z-direction is considered in the system. The well-known von-Karman similarity variables are adopted as follows (see (Tabassum & Mustafa, 2018)):

$$(u, v, w) = \left(r\Omega F'(\zeta), r\Omega G(\zeta), -2\sqrt{\nu_f \Omega}\, F(\zeta)\right), \ \zeta = \frac{z}{r} Re^{1/2}, \quad (7.2.16)$$

$$(p, T, C) = (p_\infty - \Omega \mu_f P(\zeta), T_\infty + (T_w - T_\infty)\theta(\zeta), C_\infty + C_\infty \phi(\zeta)) \quad (7.2.17)$$

Thereby, the following equations are obtained:

$$F''' - F'^2 + 2FF'' + G^2 - K\left[2F'F''' - F''^2 + G'^2\right] - MF' = 0, \quad (7.2.18)$$

$$G'' - 2F'G + 2G'F - 2K\left[F'G'' - F^{''}G'\right] - MG = 0, \tag{7.2.19}$$

$$P' - 2F'' - 4FF' + 28\ KF'F'' + 2Re\ K\left\{F''F''' + G'G''\right\} = 0 \tag{7.2.20}$$

$$\theta'' + Pr_f\left[2\theta'F + Nb\ \theta'\phi' + Nt\ \theta'^2 + Ec\ M\left(F'^2 + G^2\right)\right] + A\ F' + B\ \theta = 0, \tag{7.2.21}$$

$$\phi'' + \frac{Nt}{Nb}\theta'' + 2Sc\ F\phi' = 0. \tag{7.2.22}$$

With the following conditions:

$$\left.\begin{array}{c} \text{At } \zeta = 0: \ F = 0,\ F' = 0,\ G = 1, \\ \theta = 1 + \gamma\theta',\ \phi' + \frac{Nt}{Nb}\theta' = 0. \end{array}\right\} \tag{7.2.23}$$

$$As\ \ \zeta \to \infty : F' \to 0, G \to 0, \theta \to 0, \phi \to 0,\ P \to 0. \tag{7.2.24}$$

It can be noted that Eqn. 7.2.1 describes a self-satisfying continuity equation and Eqn. 7.2.20 can be used to analyze the pressure distribution, but this is beyond the scope of the current study. The following are the dimensionless parameters of the current study:
$Sc = \frac{\nu_f}{D_B}$ (Schmidt number), $Pr_f = \frac{\nu_f}{\alpha_m}$ (Prandtl number), $K = \frac{\mu_c\Omega}{\mu_f}$ (Reiner-Rivlin material parameter), $\gamma = \left(\frac{\Omega}{\nu_f}\right)^{\frac{1}{2}} N_2$ (Thermal slip parameter), $M = \frac{\sigma_f B_0^2}{\rho_f\Omega}$ (Hartmann number), $Ec = \frac{v_w^2}{c_f(T_w - T_\infty)}$ (Eckert number), $Nb = \frac{(\rho c)_p D_B C_\infty}{(\rho c)_f \nu_f}$ (Brownian motion parameter), $Nt = \frac{(\rho c)_p D_T (T_w - T_\infty)}{(\rho c)_f T_\infty \nu_f}$ (Thermophoresis parameter), and $Re = \frac{\Omega r^2}{\nu_f}$ (Local Reynolds number).
Nu_r indicates the reduced Nusselt number which measures the convective to conductive heat transfer ratio. Also, a resistive force (friction) by the relative movement of fluid layers at the rotating disk causes surface drag which is measured using skin friction coefficient (C_f). The Nusselt number (N_u) and skin friction given as follows ((Tabassum & Mustafa, 2018)):

$$\left.\begin{array}{c} Nu = \frac{rq_w}{k_f(T_w - T_\infty)}, \\ C_f = \frac{\sqrt{\tau_r^2 + \tau_\varphi^2}}{\rho_f v_w^2}. \end{array}\right\} \tag{7.2.25}$$

where heat flux is denoted by q_w, radial wall stress by τ_r, and azimuthal wall stress by τ_φ. Using the Eqns. (7.2.16-7.2.17), Eqn. (7.2.25) yields the reduced Nusselt number (Nu_r) and skin friction coefficient (Cf_r) as follows:

$$\left.\begin{aligned} Nu_r = Re^{-\frac{1}{2}} Nu = -\theta'(0), \\ Cf_r = Re^{\frac{1}{2}} C_f = \sqrt{(F''(0))^2 + (G'(0))^2}. \end{aligned}\right\} \tag{7.2.26}$$

7.3 Numerical solution

The equations (7.2.18)-(7.2.19) and (7.2.21)-(7.2.22) is a boundary value problem (BVP) which does not possess an analytical solution. So, the Bulirsch-Stoer algorithm and Newton-Raphson method are employed. By substituting $y_1 = F, y_2 = F', y_3 = F'', y_4 = G, y_5 = G', y_6 = \theta, y_7 = \theta', y_8 = \phi, y_9 = \phi'$, one can get the following equations:

$$\left.\begin{aligned} y_1' &= y_2, \\ y_2' &= y_3, \\ y_3' &= \tfrac{y_2^2 - 2y_1y_3 - y_4^2 - Ky_3^2 + Ky_5^2 + My_2}{1 - 2Ky_2}, \\ y_4' &= y_5, \\ y_5' &= \tfrac{2y_2y_4 - 2y_1y_5 - 2Ky_3y_5 + My_4}{1 - 2Ky_2}, \\ y_6' &= y_7, \\ y_7' &= \{-Pr_f\,[2y_1y_7 + Nb\; y_7y_9 + Nt\; y_7^2 + Ec\; M\;\; (y_2^2 + y_4^2)] \\ &\quad -Ay_2 - By_6\}, \\ y_8' &= y_9, \\ y_9' &= \left\{-\left(\tfrac{N_t}{N_b}\right) y_7' - 2Sc\; y_1\; y_9\right\}. \end{aligned}\right\} \tag{7.3.1}$$

The following initial conditions are considered:

$$\left.\begin{aligned} y_1(0) = 0, y_2(0) = 0,\;\; y_3(0) = h_1, y_4(0) = 1, y_5(0) = h_2, \\ y_6(0) = 1 + \gamma\; h_3,\;\; y_7(0) = h_3, y_8(0) = h_4,\;\; y_9(0) = -\tfrac{Nt}{Nb}\; h_3. \end{aligned}\right\} \tag{7.3.2}$$

where $h_1, h_2, h_3,$ and h_4 are calculated by utilizing the Newton-Raphson method by using suitable guess values. Numerical solutions are generated with an error tolerance of 10^{-6} and step size of 0.01. ζ_∞ has been restricted to 15 as the further increment of the domain has a negligible effect. The accuracy of the adopted numerical method has been validated by comparing the limiting case of the present problem (see Table 7.1) with the previously published results by Turkyilmazoglu and Senel (Turkyilmazoglu & Senel, 2013).

Table 7.1: *Comparison of* $F''(0), G'(0), F(\infty)$, *and*$-\theta'(0)$ *with* $K = 0,\ M = 0,\ Ec = 0,\ A = 0,\ B = 0,\ Nt = 0, Sc = 0, Nb \to 0\ , Pr_f = 0.72^a$, *and* $Pr_f = 6^b$.

	Runge-Kutta-4 method (Turkyilmazoglu & Senel, 2013)	Bulirsch-Stoer algorithm
$F''(0)$	0.51023262	0.51023239
$G'(0)$	-0.61592201	-0.61592187
$F(\infty)$	0.44223705	0.44221609
$-\theta'(0)^a$	0.3285701	0.32861104
$-\theta'(0)^b$	0.92118503	0.92123523

7.4 Results and Discussion

The impact of the Reiner-Rivlin material parameter (K), Hartmann number(M), Schmidt number (Sc), thermophoresis parameter (Nt), Space-dependent heat source parameter (A), Eckert number (Ec), thermal slip parameter (γ), and temperature-dependent heat source parameter (B) is studied on the radial velocity ($F'(\zeta)$), azimuthal velocity ($G(\zeta)$), temperature ($\theta(\zeta)$) and volume fraction of nanoparticles ($\phi(\zeta)$) profiles respectively. The Prandtl number is chosen as 7 throughout the analysis.

Fig. 7.2-7.5 depicts the impression of M on $F'(\zeta)$, $G(\zeta)$, $\theta(\zeta)$ and $\phi(\zeta)$ profiles. An increase in M generates a Lorentz force, a resistive force against the fluid flow that retards the nanoliquid flow in radial and azimuthal directions. The drag coefficient at the surface of the disk grows due to the opposing force that enhances the fluid temperature (see Fig. 7.4). Fig. 7.5 displays a mixed response in nanoparticle volume fraction with magnification in M.

Fig. 7.6-7.9 reveals the response in $F'(\zeta)$, $G(\zeta), \theta(\zeta)$, and $\phi(\zeta)$ profiles concerning K. Viscoelastic nature of the nanoliquid enhances with increment in K. Fig. 7.6 depicts a negative impact in radial velocity profile with growing values of K and the trend reverses far from the disk. The peak in the velocity curve is due to weak non-Newtonian characteristics. Axial flow reduces due to the viscoelastic nature of

the nanoliquid and a small amount of fluid is drawn in the radial direction even though centrifugal force works. Rotation inertial effects get stronger with mounting values of K that elevate the azimuthal velocity profile (See Fig. 7.7). Fig. 7.8 delineates an increase in temperature with augmenting values of K. Less amount of cold ambient fluid is drawn towards the disk which rises the nanoliquid temperature. The nanoparticle volume fraction of the nanoliquid shows a dual nature as shown in Fig. 7.9. Maximum nanoparticle volume fraction is noticed far from the disk.

Fig. 7.10 shows a positive impact of Ec on $\theta(\zeta)$. Joule heating has a predom-

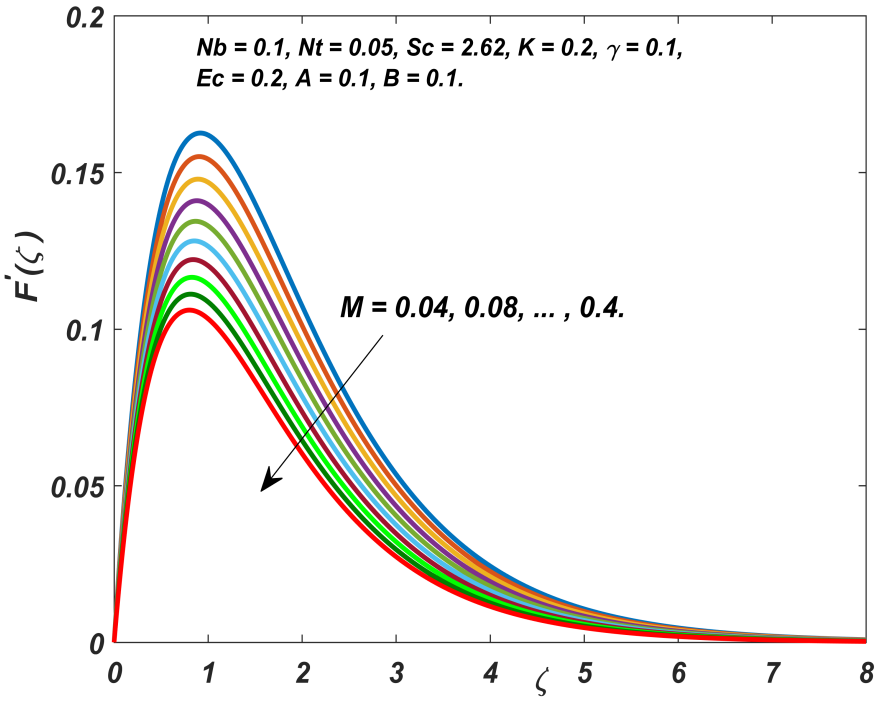

Figure 7.2: *Response in $F'(\zeta)$ for distinct M.*

inant impact on the thermal boundary layer thickness. Kinetic energy enhances with Ec that fuels the internal friction of nanoparticles followed by a rise in the temperature profile. Fig. 7.11 explains a mixed impact of Sc with $\phi(\eta)$. Nanoparticle volume fraction profile decreases with Sc far from the disk and it depicts an increasing functional relationship near the disk. Physically, it is due to depletion in molecular diffusion and migration of nanoparticles with magnification in Sc. Fig. 7.12 delineates a positive response of A & B on $\theta(\zeta)$. Temperature profile enhances with augmentation in A & B. An increase in the space and temperature-dependent heat source (A & B) produces additional heat energy to the nano liquid flow which

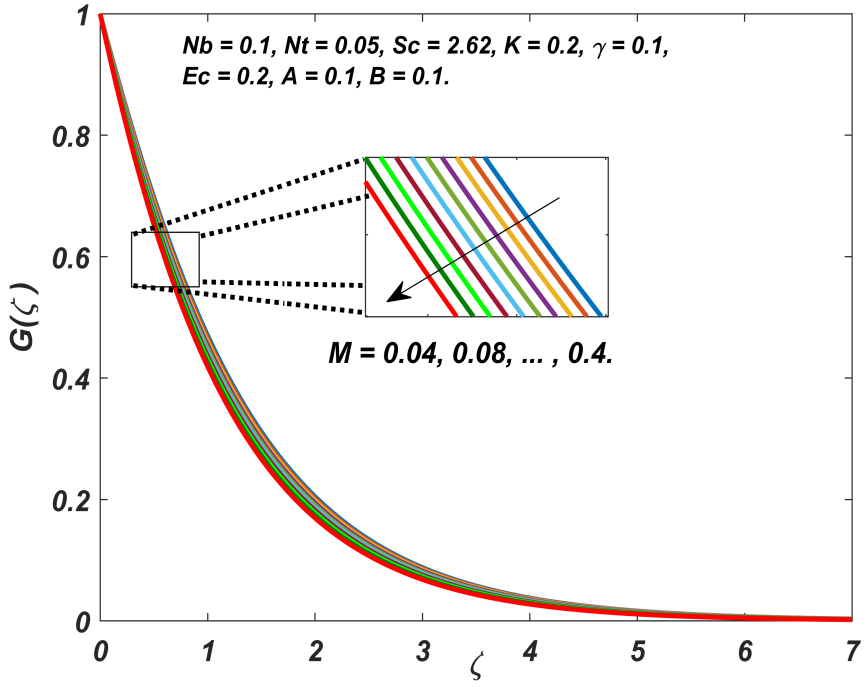

Figure 7.3: *Response in $G(\zeta)$ for distinct M.*

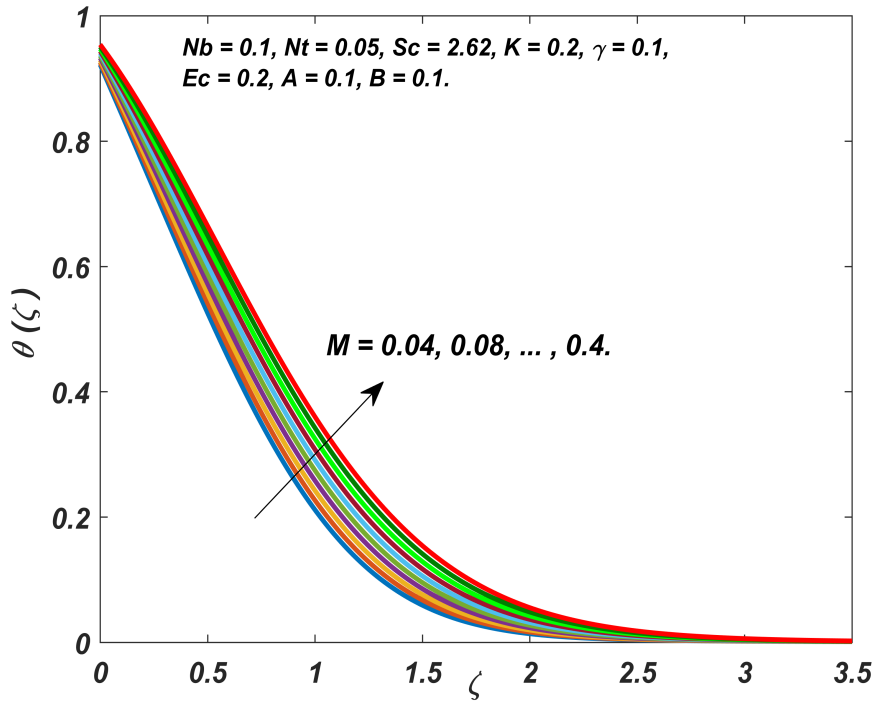

Figure 7.4: *Response in $\theta(\zeta)$ for distinct M.*

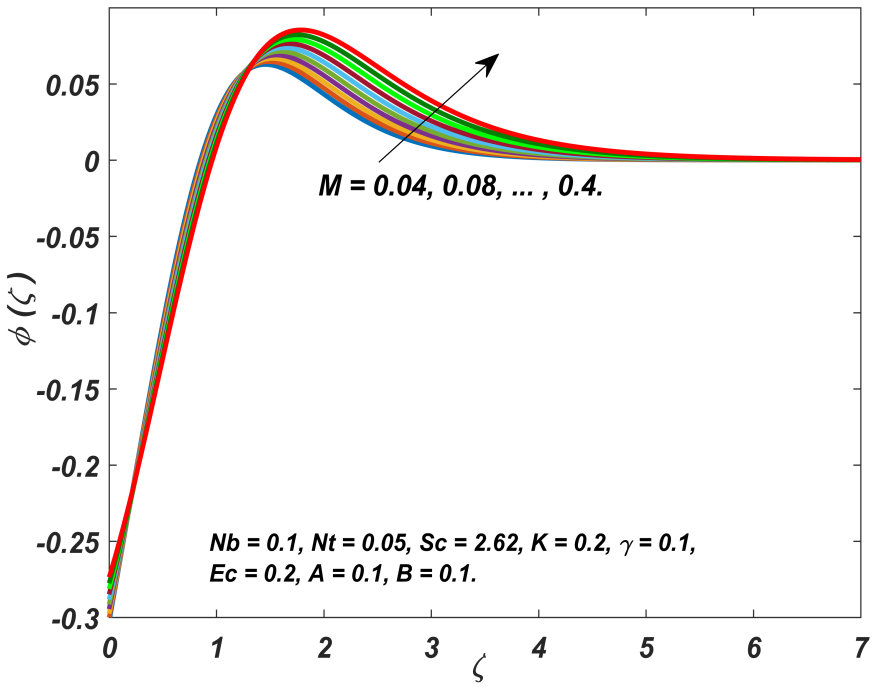

Figure 7.5: *Response in $\phi(\zeta)$ for distinct M.*

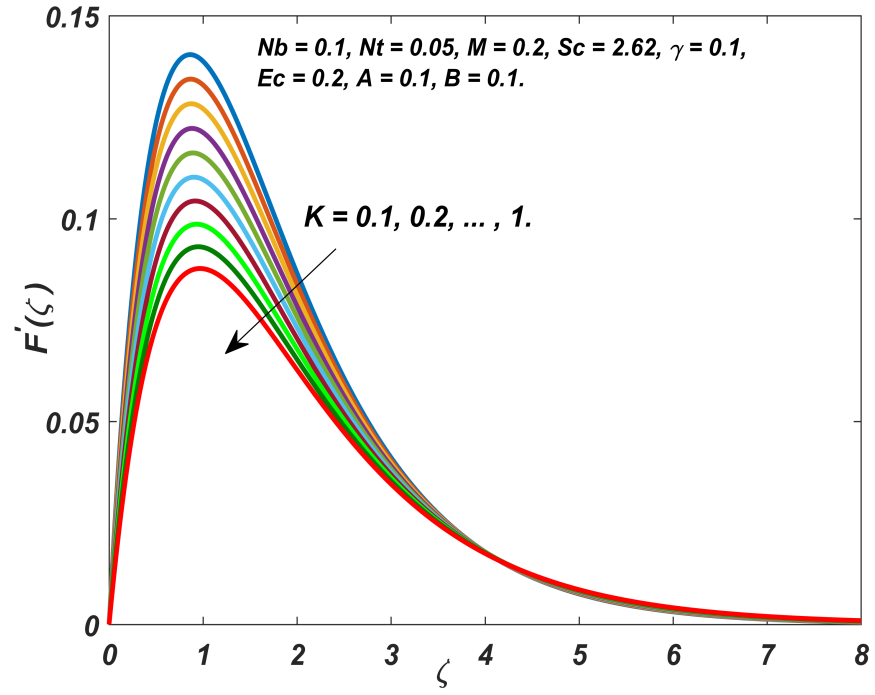

Figure 7.6: *Response in $F'(\zeta)$ for distinct K.*

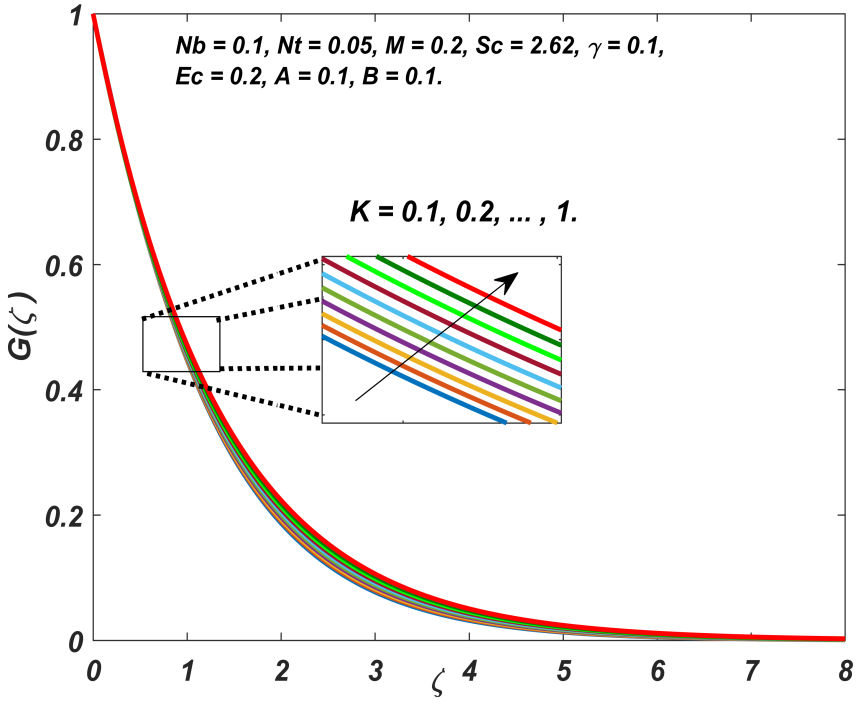

Figure 7.7: *Response in $G(\zeta)$ for distinct K.*

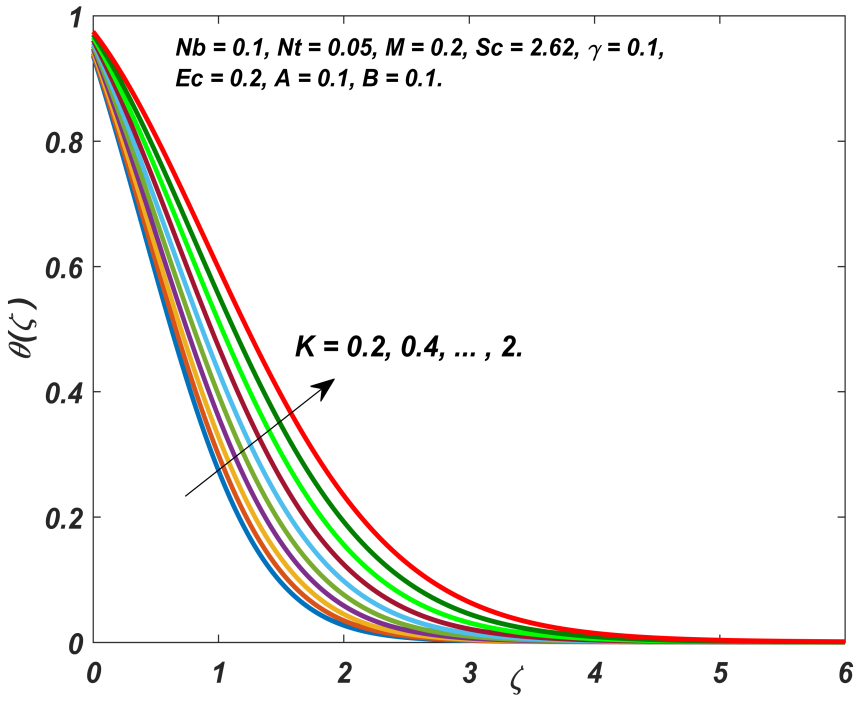

Figure 7.8: *Response in $\theta(\zeta)$ for distinct K.*

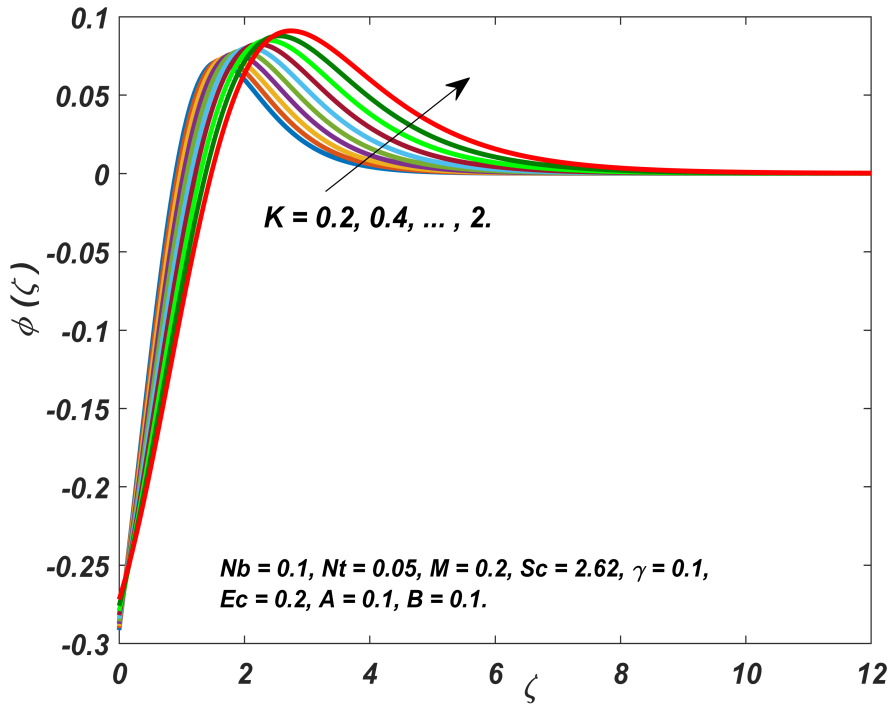

Figure 7.9: *Response in* $\phi(\zeta)$ *for distinct* K.

escalates the thermal boundary layer thickness.

Fig. 7.13-7.14 discloses the influence of Nt on $\theta(\zeta)$ and $\phi(\zeta)$ profiles. Augmentation in Nt elevates the temperature whereas the nanoparticle volume fraction profile shows a mixed character with Nt. A negative impact of nanoparticle volume fraction with Nt is observed near the disk and the nature reverses far from the disk. Physically, an increment in Nt produces thermophoresis force which moves the hot fluid particles to the colder ambient region. Fig. 7.15 juxtaposes the consequence of $\theta(\zeta)$ with variation in γ. An increase in thermal slip parameter extrapolates interfacial fluid temperature followed by a thermal resistance which depreciates further thermal transport in fluids and hence $\theta(\zeta)$ lowers.

Three-dimensional plots are used to examine the simultaneous impact of two parameters on the frictional drag and heat transfer rate as depicted in Figs. 7.16-7.19. A maximum frictional drag was observed for low K and high M values. Physically, it is due to high Lorentz force and minimum cross-viscosity. The highest heat transfer rate occurs at low A and B parameter values (see Fig. 7.17). Augmentation in A & B supplements additional heat energy to the nanoliquid that in turn minimizes the thermal difference. Fig. 7.18 delineates the discrepancy of Nusselt number with

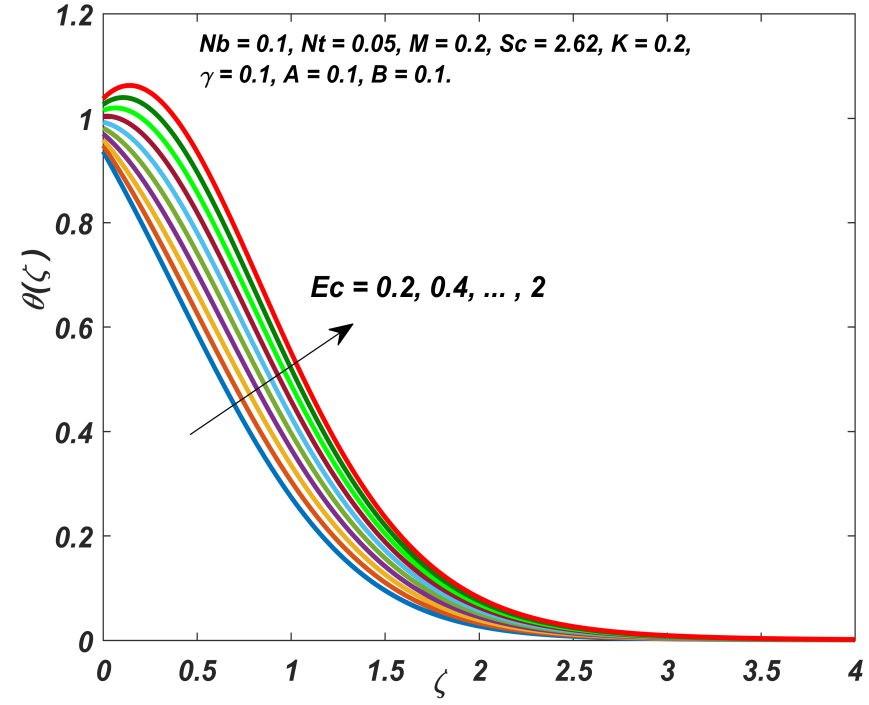

Figure 7.10: *Response in $\theta(\zeta)$ for distinct Ec.*

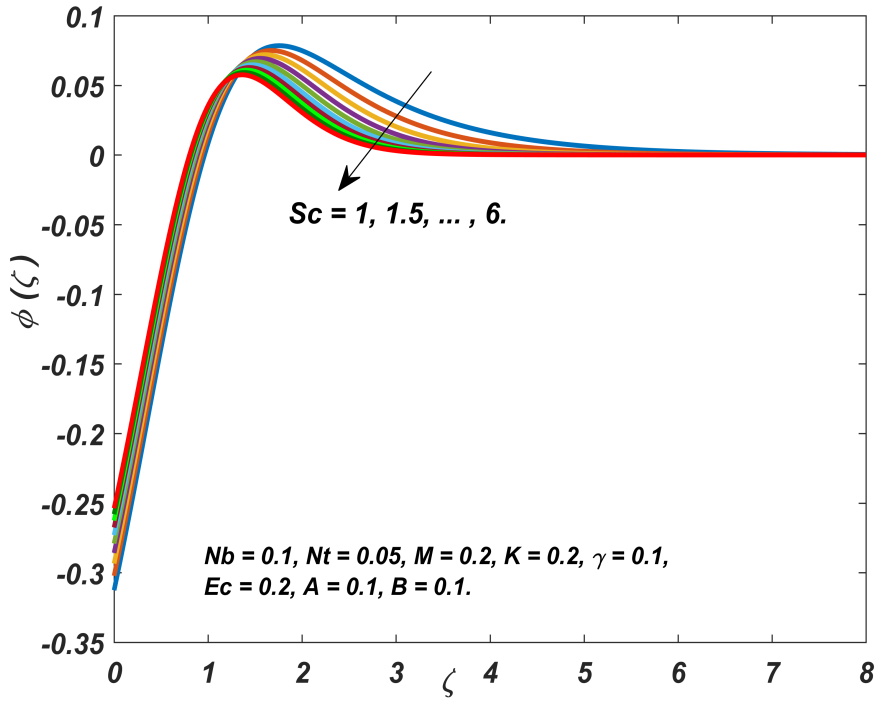

Figure 7.11: *Response in $\phi(\zeta)$ for distinct Sc.*

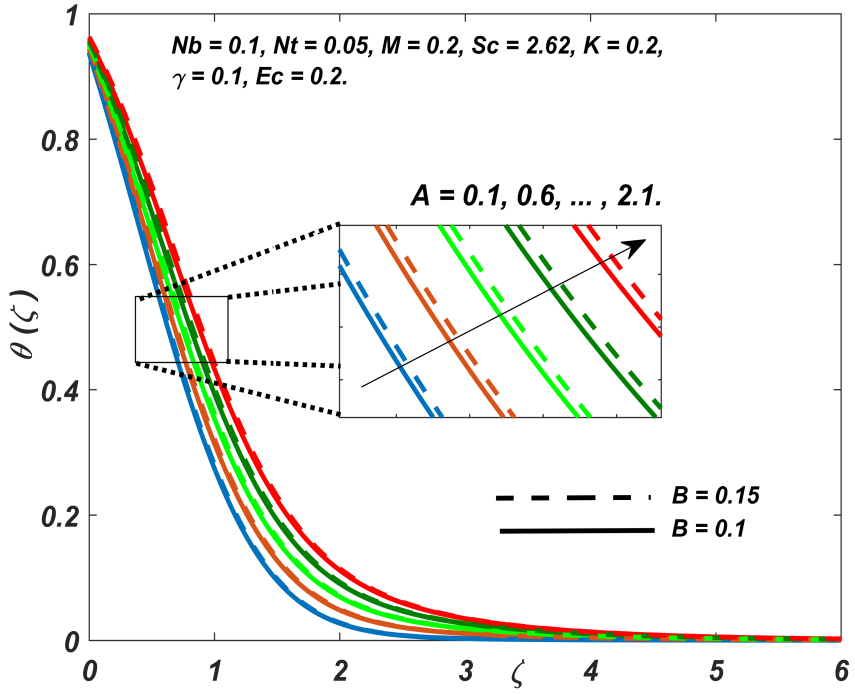

Figure 7.12: *Response in* $\theta(\zeta)$ *for distinct* $A \quad \& \quad B$.

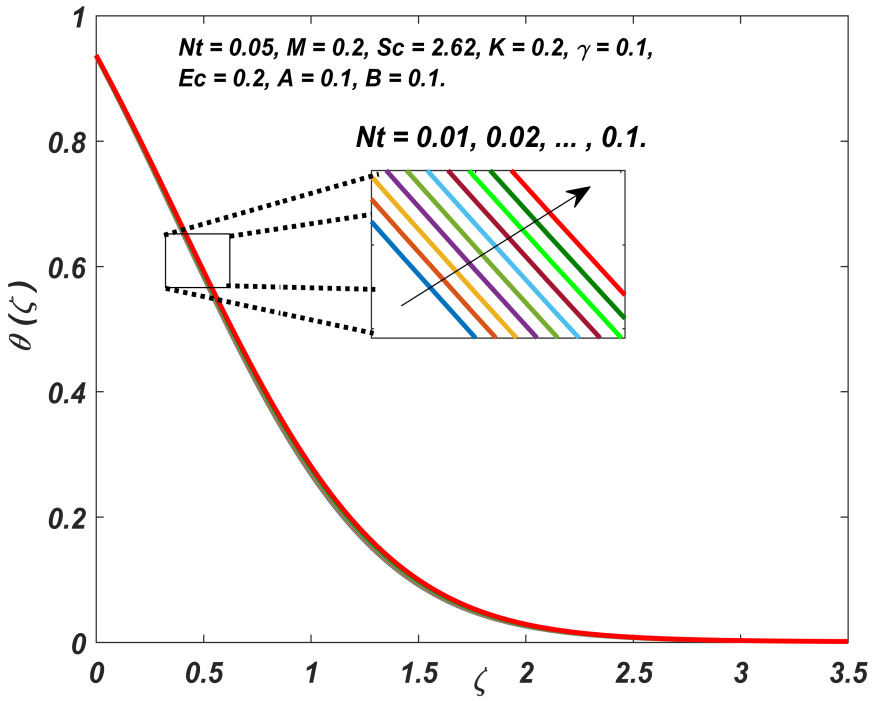

Figure 7.13: *Response in* $\theta(\zeta)$ *for distinct* Nt.

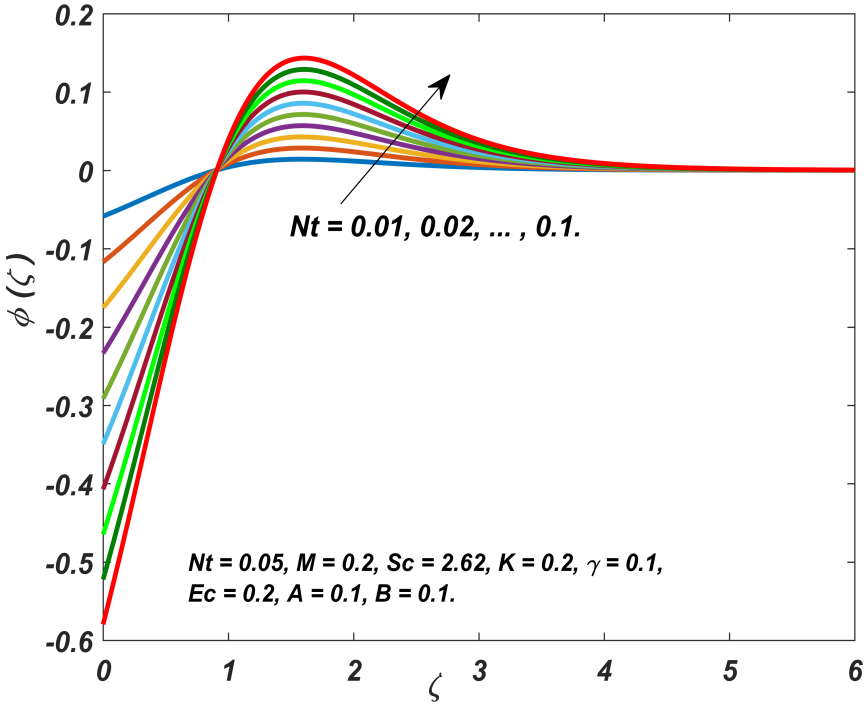

Figure 7.14: *Response in $\phi(\zeta)$ for distinct Nt.*

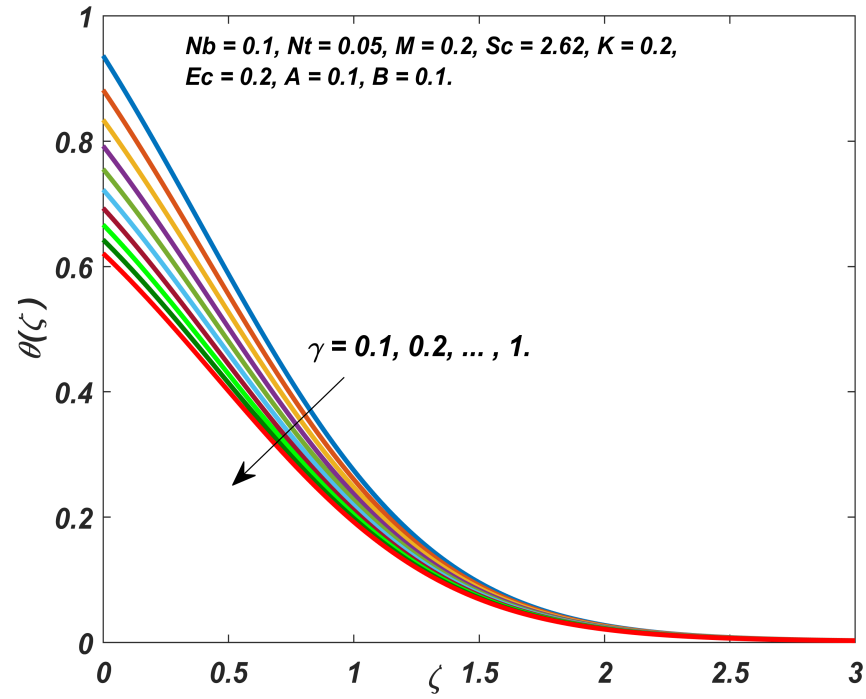

Figure 7.15: *Response in $\theta(\zeta)$ for distinct γ.*

Ec & Sc. Heat transfer rate is maximum for low Ec values. An increment in Ec escalates the temperature of the nanoliquid near the disk and hence it lowers the heat transfer rate. Heat transfer rate decreases with larger Nt (see Fig. 7.19). Physically, it is due to thermophoresis effects.

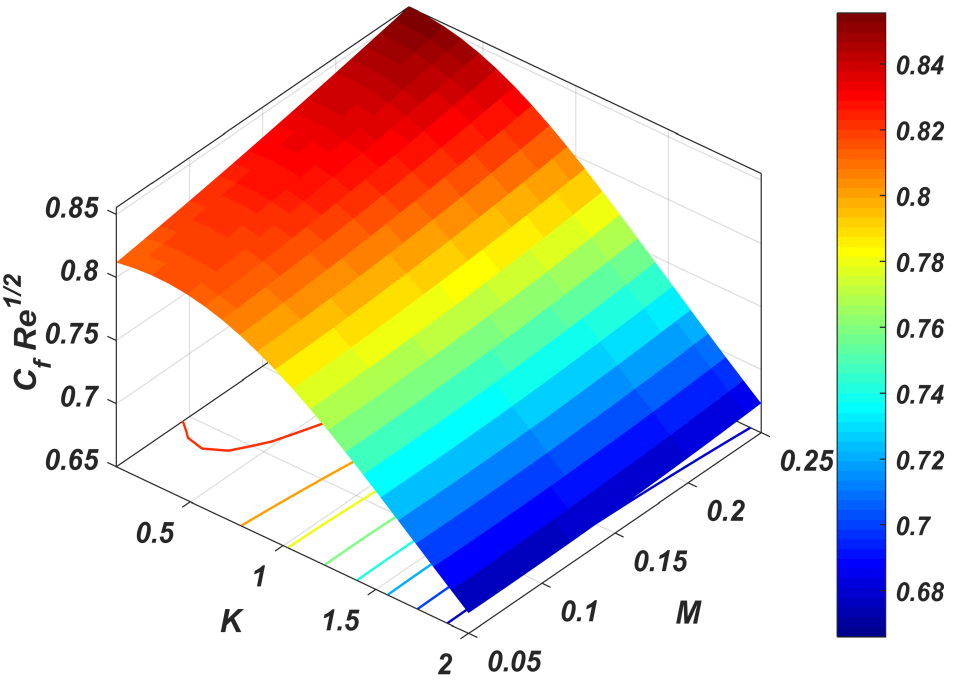

Figure 7.16: *Surface plot of* $C_f Re^{\frac{1}{2}}$ *for variation of* K *and* M.

7.5 Response Surface Methodology (RSM)

RSM is an experimental design-based statistical technique that illustrates the impact of influential parameters (independent variables) and their interactive effects on the physical quantity of choice (dependent or response variable). Experimental trials are time-consuming and costly whereas RSM reduces the number of trials and optimizes the response variable. RSM using the Central Composite Design (CCD) is a suitable sequential experimentation method which is incorporated in the present study with 20 ($2^j + 2j + o,\ j\ = 3, o = 6$) runs, here o denotes the number of faces and j denotes the number of factors. The relation involves 2^3 factorial 6 center and 6 axial points. A full quadratic 3 level factorial design is adopted in the study as follows

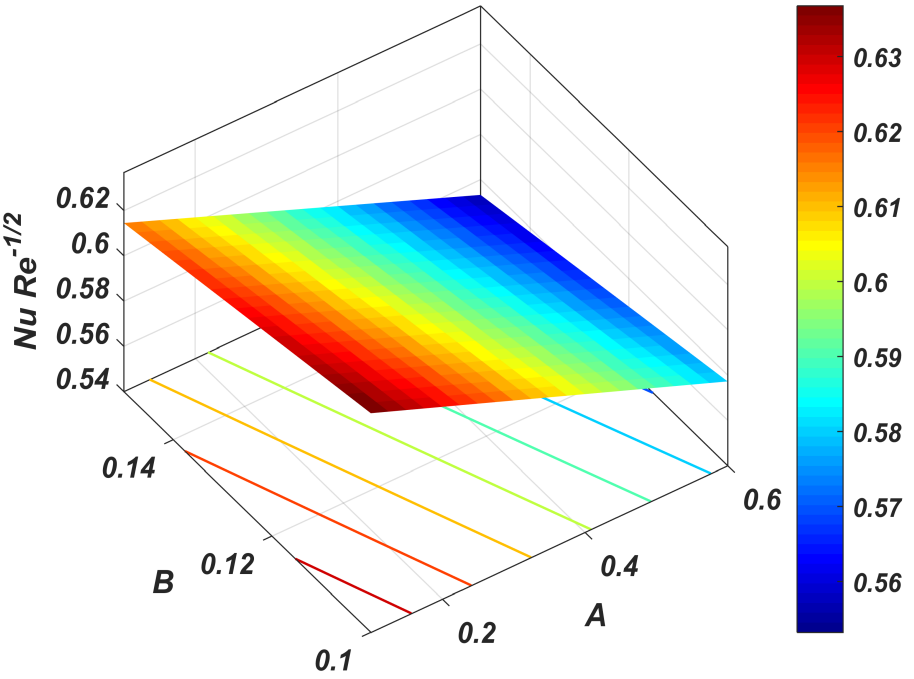

Figure 7.17: *Surface plot of* $NuRe^{-\frac{1}{2}}$ *for variation of* A *and* B.

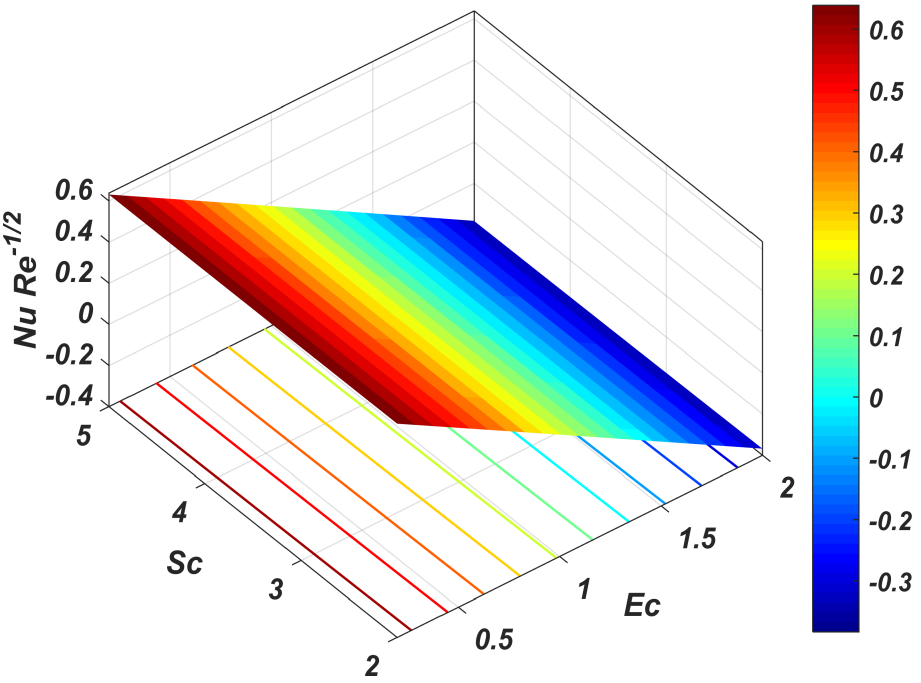

Figure 7.18: *Surface plot of* $NuRe^{-\frac{1}{2}}$ *for variation of* Sc *and* Ec.

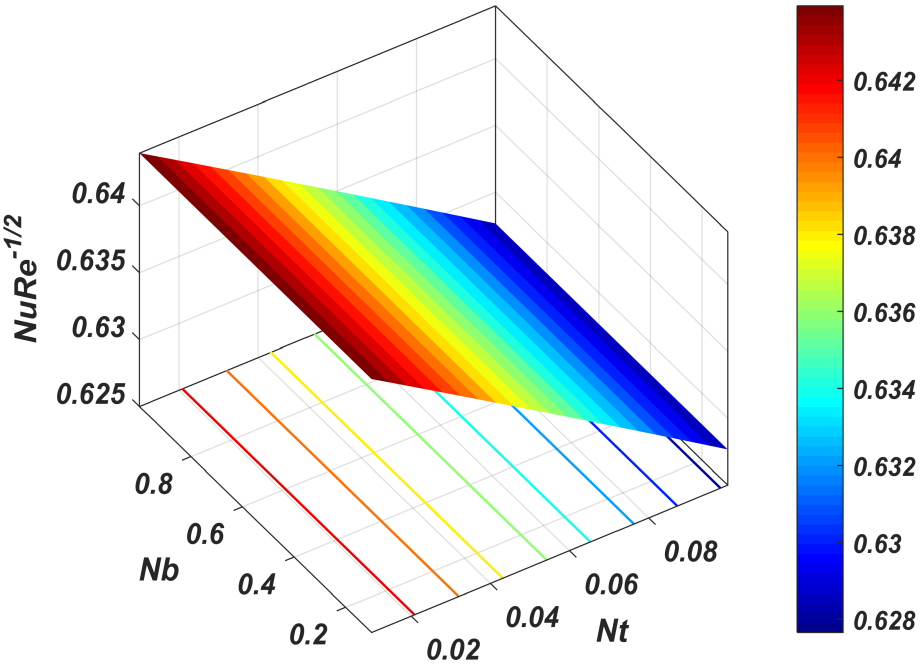

Figure 7.19: *Surface plot of* $NuRe^{-\frac{1}{2}}$ *for variation of* Nb *and* Nt.

$$\begin{aligned} Response\ (Y) = \ & L_1X_1 + L_2X_2 + L_3X_3 + L_4X_1X_2 + L_5X_2X_3 + L_6X_1X_3 + \\ & L_7X_1^2 + L_8X_2^2 + L_9X_3^2 + L_{10}. \end{aligned} \tag{7.5.1}$$

Here, L_i $(i = 1,\ 2,\ \ldots,\ 10)$ denote the regression coefficients. The RSM techniquie becomes advantageous in finding the levels of the parameters that optimize the response. In processes involving heat transfer, the maximization of the heat transfer is carried such that the desirability factor is maximized. If the lowest and highest response are respectively denoted by Y_l and Y_h, then the desirability factor is calculated as follows:

$$\begin{aligned} d &= 0, && Y \le Y_l \\ d &= \tfrac{Y - Y_l}{Y_h - Y_l}, && Y_l \le Y \le Y_h \\ d &= 1, && Y \ge Y_h \end{aligned} \tag{7.5.2}$$

For the present analysis, Nu_r is chosen as the response variable and the parameters inducted for the design are M $(0.15 \le M \le 2.5)$, K $(0.15 \le K \le 2.5)$, and γ $(0.05 \le \gamma \le 0.15\ )$ respectively. Also, the influential parameters M, K,

and γ are coded as X_1, X_2, and X_3 respectively (see Table 7.2). The numerical experimental design involving 20 runs (based on the face-centered CCD design) is given in Table 7.3.

The ANOVA table as described in Table 7.4 evaluates the quality of the fitted

Table 7.2: *The effectual levels of parameters.*

Parameters	Coded Symbols	Levels		
		-1 (Low)	0 (Medium)	1 (High)
M	X_1	0.15	0.2	0.25
K	X_1	0.15	0.2	0.25
γ	X_1	0.05	0.1	0.15

Table 7.3: *Experimental (numerical) design.*

Runs	Coded Values			Real values			Response
	X_1	X_2	X_3	M	K	γ	Nu_r
1	-1	-1	-1	0.15	0.15	0.05	0.716786
2	1	-1	-1	0.25	0.15	0.05	0.623955
3	-1	1	-1	0.15	0.25	0.05	0.700967
4	1	1	-1	0.25	0.25	0.05	0.604885
5	-1	-1	1	0.15	0.15	0.15	0.663199
6	1	-1	1	0.25	0.15	0.15	0.579336
7	-1	1	1	0.15	0.25	0.15	0.649497
8	1	1	1	0.25	0.25	0.15	0.562579
9	-1	0	0	0.15	0.2	0.1	0.681731
10	1	0	0	0.25	0.2	0.1	0.592045
11	0	-1	0	0.2	0.15	0.1	0.644742
12	0	1	0	0.2	0.25	0.1	0.628525
13	0	0	-1	0.2	0.2	0.05	0.661615
14	0	0	1	0.2	0.2	0.15	0.613698
15	0	0	0	0.2	0.2	0.1	0.636765
16	0	0	0	0.2	0.2	0.1	0.636765
17	0	0	0	0.2	0.2	0.1	0.636765
18	0	0	0	0.2	0.2	0.1	0.636765
19	0	0	0	0.2	0.2	0.1	0.636765
20	0	0	0	0.2	0.2	0.1	0.636765

quadratic model in a reliable way. The significance of linear, quadratic, and interactive regression terms of M,K, and γ are computed statistically using a high F value with p-value < 0.05. All the regression terms in the fitted model are significant (see Table 7.4). Fig. 7.20 is used to explain the accuracy of the fitted model. In

Table 7.4: *ANOVA table*

Source	Deg. of Freedom	Adj. Sum of Squares	Adj. Mean Squares	F-value	p-value
Model	9	0.026667	0.002963	827176.7	< 0.001
Linear terms	3	0.026615	0.008872	2476641	<0.001
M	1	0.020194	0.020194	5637544	< 0.001
K	1	0.000665	0.000665	185731.8	< 0.001
γ	1	0.005755	0.005755	1606648	< 0.001
Square terms	3	0.000004	0.000001	373.57	< 0.001
M^2	1	0	0	11.83	0.006
K^2	1	0	0	13.09	0.005
γ^2	1	0.000002	0.000002	611.68	< 0.001
Interaction terms	3	0.000049	0.000016	4515.58	< 0.001
$M \times K$	1	0.000005	0.000005	1387.84	< 0.001
$M \times \gamma$	1	0.000041	0.000041	11473.87	< 0.001
$K \times \gamma$	1	0.000002	0.000002	685.03	<0.001
Errors	10	0	0		
Lack-of-Fit	5	0	0	*	*
Pure Error	5	0	0		
Total	19	0.026667			
Coefficient of determination $\mathcal{R}^2 = 99.99$ %					

the normal probability plot against residuals, the data points are aligned along a straight line and the histogram has a bell shape. Therefore, the residuals follow a normal distribution. The maximum error entailed in the residual versus fitted value plots of the model is 0.00010. The coefficient of determination ($\mathcal{R}^2$) indicates the change in response variable for a chosen set of independent variables and the relevance of the model. The empirical model gives a good fit if $\mathcal{R}^2$ value is very close to 1. Here, $\mathcal{R}^2$ is found to be 99.99 % which guarantees the precision of the model.

7.5.1 Statistical Analysis

The fitted model of the response function Nu_r in terms of uncoded significant influential parameters is given below

$$\begin{aligned} Nu_r = \; & 0.910541 - \; 0.94622\; M - \; 0.10133\; K - \; 0.77684\; \gamma + \; 0.0497\; M^2 \; - \; 0.0522\; K^2 \\ & + 0.3570\; \gamma^2 \; - \; 0.31532\; M\; K \; + \; 0.90665\; M\; \gamma \; + \; 0.22153\; K\; \gamma \end{aligned} \tag{7.5.3}$$

The regression coefficients of M, K *and* γ are negative. These parameters have a negative impact with Nu_r. This indicates that heat transfer rate demotes an enhance in these parameters.

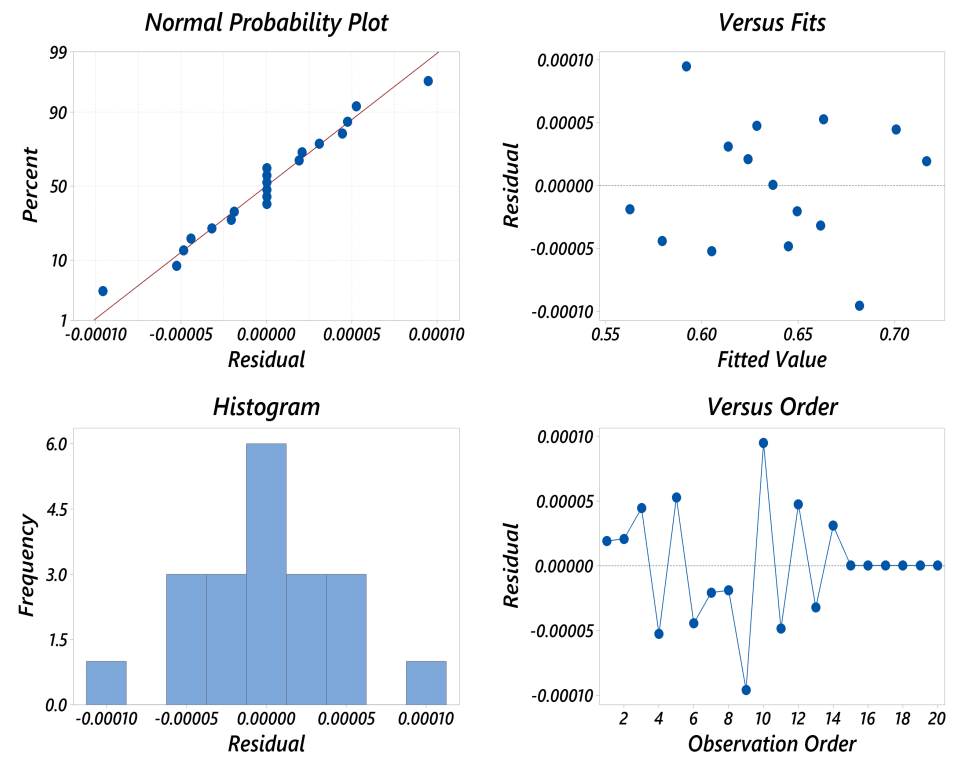

Figure 7.20: *Residual plots for* Nu_r.

Fig. 7.21-7.23 depict the simultaneous effect of pertinent parameters on Nu_r using contour and 3-D plots. The heat transfer coefficient is investigated by studying the interaction of two parameters while keeping the third parameter at a medium level. It can be noticed from Fig. 7.21 -7.23 that heat transfer coefficient is a decreasing function of M, K, and γ.

The optimization of heat transfer rate in practical applications implies the maximization of Nu_r, Therefore, the levels of the parameters that maximize the heat transfer rate are estimated to be $M = 0.15$ (low level), $K = 0.15$ (low level), and $\gamma = 0.05$ (low level). The maximized Nu_r value is estimated to be 0.7168 with a desirability of 0.9999.

7.5.2 Sensitivity analysis

The sensitivity of the heat transfer coefficient is estimated using the the full quadratic model with the coded coefficients given below:

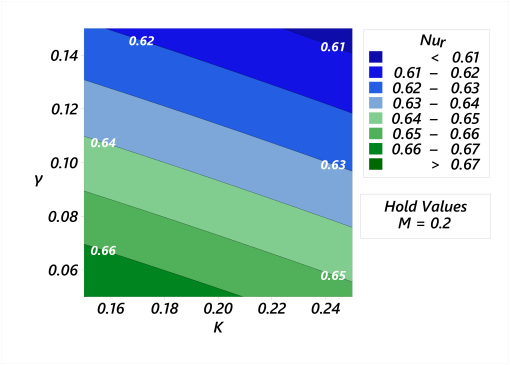

(a) *Contour plot of Nu_r for combinations of γ, K .*

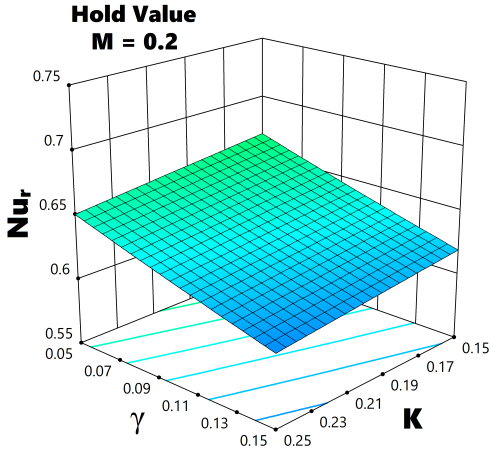

(b) *Response surface plot of Nu_r for combinations of γ, K .*

Figure 7.21: *Contour and response surface plot of Nu_r for combinations of γ, K .*

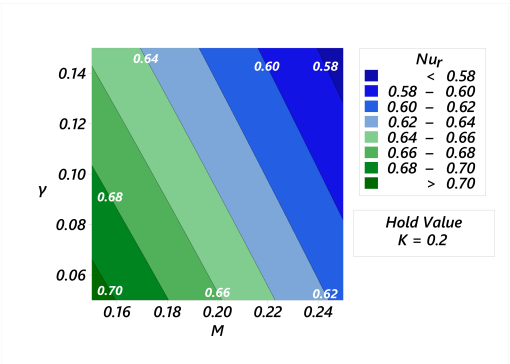

(a) *Contour plot of Nu_r for combinations of γ, M .*

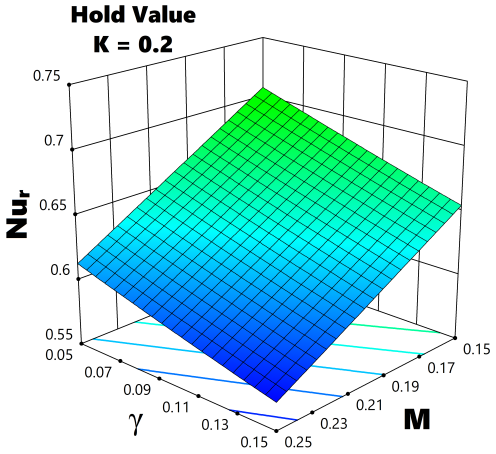

(b) *Response surface plot of Nu_r for combinations of γ, M .*

Figure 7.22: *Contour and response surface plot of Nu_r for combinations of γ, M .*

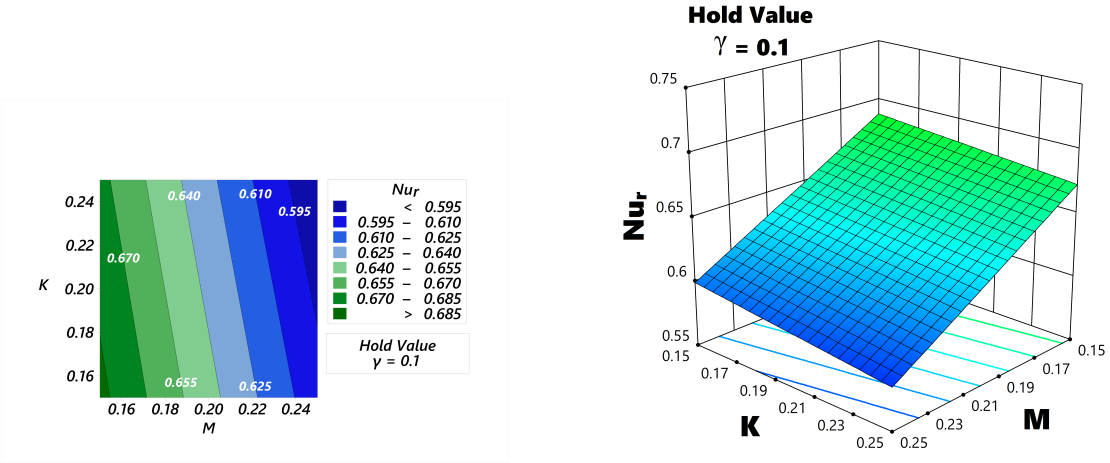

(a) *Contour plot of Nu_r for combinations of M, K .*

(b) *Response surface plot of Nu_r for combinations of M, K .*

Figure 7.23: *Contour and response surface plot of Nu_r for combinations of M, K .*

$$\begin{aligned} Nu_r = 0.636764 - 0.044938\ X_1 - 0.008157\ X_2 - 0.023990\ X_3 \\ +0.000124\ X_1^2 - 0.000131\ X_2^2 + 0.000893\ X_3^2 - 0.000788\ X_1X_2 \\ +0.002267\ X_1X_3 + 0.000554\ X_2X_3, \end{aligned} \tag{7.5.4}$$

The partial derivatives of the full quadratic model with the coded variables are computed to find the sensitivity functions as follows:

$$\frac{\partial Nu_r}{\partial X_1} = -0.044938 + 0.000248\ X_1 - 0.000788\ X_2 + 0.002267\ X_3, \tag{7.5.5}$$

$$\frac{\partial Nu_r}{\partial X_2} = -0.008157 - 0.000262\ X_2 - 0.000788\ X_1 + 0.000554\ X_3, \tag{7.5.6}$$

$$\frac{\partial Nu_r}{\partial X_3} = -0.023990 + 0.001786\ X_3 + 0.002267\ X_1 + 0.000554\ X_2. \tag{7.5.7}$$

Bar charts in Fig. 7.24 visualize the heat transfer coefficient sensitivity. Sensitivity is a measurement that interprets the level of change in response variables with variation in independent variables. The positive or negative sign in the sensitivity function indicates the nature of the sensitivity and its magnitude delineates the intensity of the relationship. The sensitivity of Nu_r is computed by assuming $M = 0.2$. Nu_r is negative sensitive towards M, K and γ. For a fixed value of K magnitude of sensitivity towards M, K and γ reduce with an increase in γ and the intensity of the relationship is maximum for M when compared to other variables. Further, the

sensitivity intensity augments with an increase in K. The change in the sensitivity rate with varying levels of γ is described as follows (see Table 7.5):

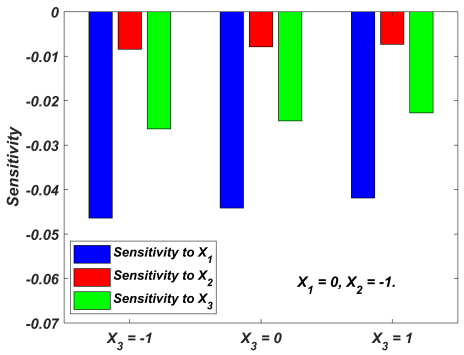

(a) *Bar charts depicting the sensitivity of Nu_r with $X_1 = 0, X_2 = -1$.*

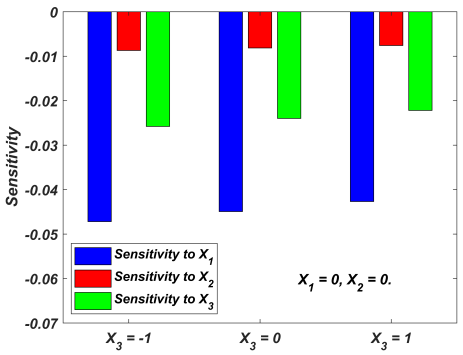

(b) *Bar charts depicting the sensitivity of Nu_r with $X_1 = 0, X_2 = 0$.*

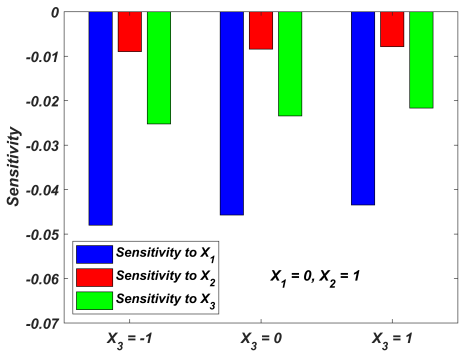

(c) *Bar charts depicting the sensitivity of Nu_r $X_1 = 0, X_2 = 1$.*

Figure 7.24: *Bar charts depicting the sensitivity of Nu_r*

- The sensitivity towards M varies at the rate of -0.2267%.

- The sensitivity towards K varies at the rate of -0.0554%.

- The sensitivity towards γ varies at the rate of -0.1786%.

Table 7.5: *The sensitivity values of the response Nu_r when $X_1 = 0$*

X_2	X_3	**Sensitivity values**		
		$\frac{\partial Nu_r}{\partial X_1}$	$\frac{\partial Nu_r}{\partial X_2}$	$\frac{\partial Nu_r}{\partial X_3}$
-1	-1	-0.046417	-0.008449	-0.02633
	0	-0.04415	-0.007895	-0.024544
	1	-0.041883	-0.007341	-0.022758
Rate of change		**-0.002267**	**-0.000554**	**-0.001786**
0	-1	-0.047205	-0.008711	-0.025776
	0	-0.044938	-0.008157	-0.02399
	1	-0.042671	-0.007603	-0.022204
Rate of change		**-0.002267**	**-0.000554**	**-0.001786**
1	-1	-0.047993	-0.008973	-0.025222
	0	-0.045726	-0.008419	-0.023436
	1	-0.043459	-0.007865	-0.021650
Rate of change		**-0.002267**	**-0.000554**	**-0.001786**

7.6 Conclusions

An electrically conducting Reiner Rivlin nanoliquid flow past a rotating disk is considered in the study. A uniform magnetic field of intensity B_0 is applied along the axial direction. The volume fraction of the nanoparticles on the surface of the disk is passively controlled by a realistic boundary condition . In addition, thermal jump conditions and Joule heating effects are accounted. In the presence of a space-dependent and temperature- dependent heat source effects the conclusions of the present work are summarized below:

- Radial and azimuthal velocities demote with an increment in magnetic field due to the presence of Lorentz force.
- Radial velocity and surface drag decrease with augmentation in Reiner-Rivlin fluid parameter. It is due to an elevation in the cross-viscosity coefficient.
- The temperature profile increases due to both temperature and space-dependent heat sources. An opposite trend is noted in the heat transfer rate.
- Joule heating has a positive influence on the thermal boundary layer. The heat transfer rate lowers with an increment in the Eckert number.
- Hartmann number, Reiner-Rivlin fluid parameter, and thermal slip parameter show a negative response with heat transfer coefficient.

- The heat transfer sensitivity towards the Hartmann number decreases at the rate of 0.2267% and the sensitivity towards the Reiner-Rivlin fluid parameter decreases at the rate of 0.0554% when thermal slip is incremented.

Chapter 8

Significance of nanoparticle shape effect on MHD convective alumina-water nanofluid flow over a rotating rigid disk *

8.1 Introduction

This work aims in the numerical exploration of the hydromagnetic alumina–water nanofluid flow due to a rotating rigid disk. The nano fluid flow considering different nanoparticle shapes (namely sphere, platelet, cylinder, and brick) and the thermo-hydrodynamic slip constraints have been modeled utilizing the modified Buongiorno model. Modified Buongiorno model modifies the conventional two-phase Buongiorno model by additionally considering the volume fraction dependent nanoparticle properties. The present study has many applications in both engineering and industrial fields like spin coating, extrusion process, aerodynamics, etc. Von Kármán's similarity transformations are exercised in the transmutation of the mathematically modelled equations into a system of first-order ODE's and treated numerically using the generalized differential quadrature method. The consequence of effectual parameters on the physical quantities and the flow profiles is explained with the aid of graphs and tables.

8.2 Mathematical formulation

A steady hydromagnetic incompressible and axisymmetric alumina-water nanofluid flow due to a circular rigid disk placed at $z = 0$ has been considered (see Fig. 8.1). The flow is due to a constant rotation (Ω) of the disk which establishes a

*Published in: International Communications in Heat and Mass Transfer (Elsevier), 2022 (129); 105711

swirling flow in the neighbouring nanofluid layers. Let $(u,\ v,\ w)$ be the velocity components along $(r,\ \varphi,\ z)$ directions. Also, let $(T,\ T_W,\ T_\infty)$ be the nanofluid temperature, nanofluid temperature near the disk, and nanofluid temperature far from the disk, correspondingly and $(C,\ C_W,\ C_\infty)$ be the nanofluid concentration, nanofluid concentration near the disk, and nanofluid concentration far from the disk, respectively. An external magnetic field (of uniform intensity B_0) is applied along the axial direction. Using the two-phase modified Buongiorno nanofluid model (Yang et al., 2013), the governing equations take the form (see (Mustafa, 2017), (U. Khan, Bilal, Zaib, Makinde, & Wakif, 2022), (Mustafa et al., 2018)):

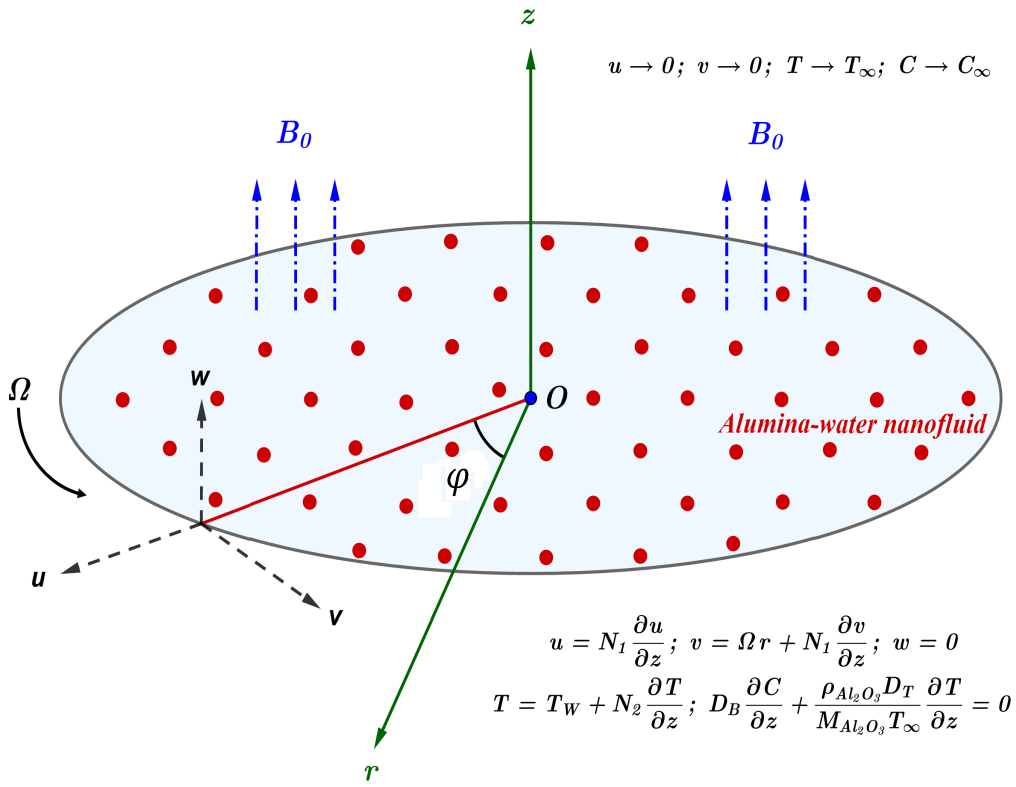

Figure 8.1: *Physical configuration*

$$\frac{\partial u}{\partial r}+\frac{u}{r}+\frac{\partial w}{\partial z}=0, \tag{8.2.1}$$

$$\rho_{nf}\left(u\frac{\partial u}{\partial r}-\frac{v^2}{r}+w\frac{\partial u}{\partial z}\right)=-\frac{\partial p}{\partial r}+\mu_{nf}\left(\frac{\partial^2 u}{\partial r^2}+\frac{1}{r}\frac{\partial u}{\partial r}-\frac{u}{r^2}+\frac{\partial^2 u}{\partial z^2}\right)-\sigma_{nf}B_o^2 u, \tag{8.2.2}$$

$$\rho_{nf}\left(u\frac{\partial v}{\partial r}+\frac{uv}{r}+w\frac{\partial v}{\partial z}\right)=\mu_{nf}\left(\frac{\partial^2 v}{\partial r^2}+\frac{1}{r}\frac{\partial v}{\partial r}-\frac{v}{r^2}+\frac{\partial^2 v}{\partial z^2}\right)-\sigma_{nf}B_o^2 v, \tag{8.2.3}$$

$$\rho_{nf}\left(u\frac{\partial w}{\partial r}+w\frac{\partial w}{\partial z}\right)=-\frac{\partial p}{\partial z}+\mu_{nf}\left(\frac{\partial^2 w}{\partial r^2}+\frac{1}{r}\frac{\partial w}{\partial r}+\frac{\partial^2 w}{\partial z^2}\right), \tag{8.2.4}$$

$$\begin{gathered}\left(\rho C_p\right)_{nf}\left(u\tfrac{\partial T}{\partial r}+w\tfrac{\partial T}{\partial z}\right)=k_{nf}\left(\tfrac{\partial^2 T}{\partial r^2}+\tfrac{1}{r}\tfrac{\partial T}{\partial r}+\tfrac{\partial^2 T}{\partial z^2}\right)+\\ \left(\rho C_p\right)_p\left\{\tfrac{D_B M_{Al_2O_3}}{\rho_{Al_2O_3}}\left(\tfrac{\partial T}{\partial z}\tfrac{\partial C}{\partial z}+\tfrac{\partial T}{\partial r}\tfrac{\partial C}{\partial r}\right)+\tfrac{D_T}{T_\infty}\left[\left(\tfrac{\partial T}{\partial z}\right)^2+\left(\tfrac{\partial T}{\partial r}\right)^2\right]\right\}\end{gathered} \tag{8.2.5}$$

$$u\frac{\partial C}{\partial r}+w\frac{\partial C}{\partial z}=D_B\left(\frac{\partial^2 C}{\partial z^2}+\frac{1}{r}\frac{\partial C}{\partial r}+\frac{\partial^2 C}{\partial r^2}\right)+\frac{\rho_{Al_2O_3}D_T}{M_{Al_2O_3}T_\infty}\left(\frac{\partial^2 T}{\partial r^2}+\frac{1}{r}\frac{\partial T}{\partial r}+\frac{\partial^2 T}{\partial z^2}\right), \tag{8.2.6}$$

subject to the following boundary conditions

$$\left.\begin{gathered}u=N_1\tfrac{\partial u}{\partial z},\ v=r\Omega+N_1\tfrac{\partial v}{\partial z},w=0,\\ T=T_w+N_2\tfrac{\partial T}{\partial z},D_B\tfrac{\partial C}{\partial z}+\tfrac{\rho_{Al_2O_3}D_T}{M_{Al_2O_3}T_\infty}\tfrac{\partial T}{\partial z}=0\end{gathered}\right\}\ \text{at}\ \ z=0 \tag{8.2.7}$$

$$u\to 0\ ,\ v\to 0\ ,\ T\to T_\infty\ ,\ C\to C_\infty\ \ \text{as}\ \ z\to\infty \tag{8.2.8}$$

Physical quantities of interest are (see (Mustafa et al., 2018)):
Local Skin friction coefficient :

$$C_f=\frac{\sqrt{\tau_r^2+\tau_\varphi^2}}{\rho_f(r\Omega)^2}\ ;\tau_r=\mu_{nf}\left.\frac{\partial u}{\partial z}\right|_{z=0}\ \ \&\ \ \tau_\varphi=\mu_{nf}\left.\frac{\partial v}{\partial z}\right|_{z=0}. \tag{8.2.9}$$

Local Nusselt number:

$$Nu=\frac{rq_w}{k_f\left(T_W-T_\infty\right)}\ ;q_w=k_{nf}\left.\frac{\partial T}{\partial z}\right|_{z=0}. \tag{8.2.10}$$

Introducing the following similarity transformations (see (Mahanthesh, Lorenzini, Oudina, & Animasaun, 2020)) into equations (8.2.1) to (8.2.10)
$\zeta=z\sqrt{\frac{\Omega}{\nu_f}},\ u=\ \Omega r\ F\left(\zeta\right)\ ,$
$v=\ \Omega r\ G\left(\zeta\right)\ ,w=\sqrt{\nu_f\Omega}\ H\left(\zeta\right)\ ,p=p_\infty-2\Omega\ \mu_f\ P\left(\zeta\right)\ ,$
$T=T_\infty+\left(\mathrm{T}_w-T_\infty\right)\ \theta\left(\zeta\right)\ ,C=C_\infty+\left(C_W-C_\infty\right)\ \phi\left(\zeta\right)$
The reduced governing equations are given by:

$$2F+H_\zeta=0 \tag{8.2.11}$$

$$F_{\zeta\zeta}-\frac{A_3}{A_1}MF+\frac{A_2}{A_1}\left(G^2-F^2-F_\zeta H\right)=0 \tag{8.2.12}$$

$$G_{\zeta\zeta} - \frac{A_3}{A_1} MG - \frac{A_2}{A_1} \left(2FG + G_\zeta H\right) = 0 \tag{8.2.13}$$

$$\theta_{\zeta\zeta} + \frac{Pr}{A_4} \left(Nb\chi_\zeta \theta_\zeta + Nt\theta_\zeta^2 - A_5 H\theta_\zeta\right) = 0 \tag{8.2.14}$$

$$\phi_{\zeta\zeta} + \frac{Nt}{Nb}\theta_{\zeta\zeta} - ScH\phi_\zeta = 0 \tag{8.2.15}$$

with

$$\begin{gathered} F\left(0\right) = b_1\ F_\zeta\left(0\right)\ ,\ G\left(0\right) = 1 + b_1\ G_\zeta\left(0\right)\ ,\ H\left(0\right) = 0\ , \\ \theta\left(0\right) = 1 + \gamma\ \theta_\zeta\left(0\right)\ ,\ \chi_\zeta\left(0\right) + \tfrac{Nt}{Nb}\theta_\zeta\left(0\right) = 0\ ,\ F\left(\zeta \to \infty\right) \to 0, \\ G\left(\zeta \to \infty\right) \to 0\ ,\ \theta\left(\zeta \to \infty\right) \to 0\ ,\ \phi\left(\zeta \to \infty\right) \to 0\ . \end{gathered} \tag{8.2.16}$$

The physical quantities in their reduced form are:

$$C_{fr} = C_f\ Re^{1/2} = A_1\ \sqrt{F_\zeta^2\left(0\right) + G_\zeta^2\left(0\right)}\ . \tag{8.2.17}$$

$$Nu_r = Nu\ Re^{-1/2}\ = -A_4\ \theta_\zeta\left(0\right)\ . \tag{8.2.18}$$

where M (magnetic field parameter)$= \frac{\sigma_f B_0^2}{\rho_f \Omega}$, τ (effective heat capacity ratio)$= \frac{\left(\rho C_P\right)_p}{\left(\rho C_P\right)_f}$, Pr (Prandtl number)$= \frac{\left(\mu C_P\right)_f}{\kappa_f}$, Nt (thermophoresis parameter)$= \frac{\tau\ D_T(T_w - T_\infty)}{T_\infty \nu_f}$, Nb (Brownian motion parameter)$= \frac{\tau\ M_{Al_2O_3} D_B (C_w - C_\infty)}{\rho_{Al_2O_3} \nu_f}$, Sc (Schmidt number)$= \frac{\nu_f}{D_B}$, b_1 (hydrodynamic slip parameter)$= N_1 \left(\frac{\Omega}{\nu_f}\right)^{\frac{1}{2}}$, γ (thermal slip parameter)$= N_2 \left(\frac{\Omega}{\vartheta_f}\right)^{\frac{1}{2}}$, and Re (local Reynold's number)$= \frac{\Omega r^2}{\nu_f}$ are the nondimensional quantities. The nanofluid models, thermophysical properties and the nanoparticle shape characteristics are described in Tables 8.1, 8.2 and 8.3 respectively.

Table 8.1: *Effective nanofluid constants see (Timofeeva et al., 2009),(Mustafa et al., 2018),(Brinkman, 1952).*

Non-spherical Nanoparticles	Spherical Nanoparticles
$A_1 = \frac{\mu_{nf}}{\mu_f} = 1 + a_1\phi_{Al_2O_3} + a_2\phi_{Al_2O_3}^2$	$A_1 = \frac{\mu_{nf}}{\mu_f} = \frac{1}{\left(1-\phi_{Al_2O_3}\right)^{2.5}}$
$A_2 = \frac{\rho_{nf}}{\rho_f} = \left(1 - \phi_{Al_2O_3}\right) + \phi_{Al_2O_3}\left(\frac{\rho_{Al_2O_3}}{\rho_f}\right)$	
$A_3 = \frac{\sigma_{nf}}{\sigma_f} = 1 + \frac{3\left(\frac{\sigma_{Al_2O_3}}{\sigma_f} - 1\right)\phi_{Al_2O_3}}{\left(\frac{\sigma_{Al_2O_3}}{\sigma_f} + 2\right) - \left(\frac{\sigma_{Al_2O_3}}{\sigma_f} - 1\right)\phi_{Al_2O_3}}$	
$A_4 = \frac{k_{nf}}{k_f} = \frac{k_{Al_2O_3} + (\widetilde{n_s} - 1)k_f - (\widetilde{n_s} - 1)\varphi\left(k_f - k_{Al_2O_3}\right)}{k_{Al_2O_3} + (\widetilde{n_s} - 1)k_f + \phi_{Al_2O_3}\left(k_f - k_{Al_2O_3}\right)}$	
$A_5 = \frac{\left(\rho C_P\right)_{nf}}{\left(\rho C_P\right)_f} = \left(1 - \phi_{Al_2O_3}\right) + \phi_{Al_2O_3}\frac{\left(\rho C_p\right)_{Al_2O_3}}{\left(\rho C_p\right)_f}$	

Table 8.2: *Thermophysical Properties of water and Al_2O_3 (see (Wakif & Sehaqui, 2022)).*

Physical Properties	Water	Al_2O_3
$\rho\ (kg/m^3)$	997.1	3970
$k\ (W/m.K)$	0.613	40
$\sigma\ (S/m)$	0.05	10^{-10}
$C_P\ (J/kg.K)$	4179	765
$\mu\ (Pa.s)$	89 $\times 10^{-5}$	—

8.3 Numerical solution

Generalized differential quadrature method (GDQM) acts as a powerful numerical collocation method for tackling linear and nonlinear physical problems due to its high flexibility and higher accuracy levels. More description on the solving procedure for the proposed GDQM can be seen in (Thumma, Wakif, & Animasaun, 2020), (Nayak, Wakif, Animasaun, & Alaoui, 2020). Fig. 8.2 depicts a brief outline on the steps involved in adopted numerical procedure. The conversion of the infinite physical domain $[0, \infty]$ to the finite computational domain $[0, 1]$ is achieved with the aid of the following transformations:

$$\left.\begin{array}{c} \zeta = \zeta_\infty\ \eta \\ F(\zeta) = F(\zeta_\infty\ \eta) = \tilde{F}(\eta) \\ G(\zeta) = G(\zeta_\infty\ \eta) = \tilde{G}(\eta) \\ H(\zeta) = H(\zeta_\infty\ \eta) = \tilde{H}(\eta) \\ \theta(\zeta) = \theta(\zeta_\infty\ \eta) = \tilde{\theta}(\eta) \\ \phi(\zeta) = \phi(\zeta_\infty\ \eta) = \tilde{\phi}(\eta) \end{array}\right\} \tag{8.3.1}$$

where ζ_∞ is the appropriate asymptotical value taken by the boundary layer thickness.

The reduced ODE's, boundary conditions, and physical quantities are transformed (using equation (8.3.1)) into:

$$2\ \zeta_\infty\ \tilde{F} + \tilde{H}_\eta = 0 \tag{8.3.2}$$

$$\tilde{F}_{\eta\eta} - \frac{A_3}{A_1}\ \zeta_\infty^2\ M\ \tilde{F} + \frac{A_2}{A_1}\left(\ \zeta_\infty^2\ \tilde{G}^2 -\ \zeta_\infty^2\ \tilde{F}^2 -\ \zeta_\infty\ \tilde{F}_\eta\ \tilde{H}\right) = 0 \tag{8.3.3}$$

$$\tilde{G}_{\eta\eta} - \frac{A_3}{A_1}\ \zeta_\infty^2\ M\ \tilde{G} - \frac{A_2}{A_1}\left(2\ \zeta_\infty^2\ \tilde{F}\ \tilde{G} +\ \zeta_\infty\ \tilde{G}_\eta\ \tilde{H}\right) = 0 \tag{8.3.4}$$

Table 8.3: *Nanoparticle shape properties of Al_2O_3 (see (Timofeeva et al., 2009)).*

Characteristics of nanoparticles	Sphere	Platelet	Cylinder	Brick
a_1	——	37.1	13.5	1.9
a_2	——	612.6	904.4	471.4
Sphericity χ	1	0.52	0.62	0.81
Shape factor $\widetilde{n_s} = \frac{3}{\chi}$	3	5.7	4.9	3.7

$$\tilde{\theta}_{\eta\eta} + \frac{Pr}{A_4}\left(Nb\ \tilde{\theta}_\eta\ \tilde{\chi}_\eta + Nt\ \tilde{\theta}_\eta^2 - A_5\ \zeta_\infty\ \tilde{H}\ \tilde{\theta}_\eta\right) = 0 \tag{8.3.5}$$

$$\tilde{\phi}_{\eta\eta} + \frac{Nt}{Nb}\ \tilde{\theta}_{\eta\eta} - Sc\ \zeta_\infty\ \tilde{H}\ \tilde{\phi}_\eta = 0 \tag{8.3.6}$$

with

$$\left.\begin{array}{c} \tilde{F}(0) = \frac{b_1}{\zeta_\infty}\ \tilde{F}_\eta(0)\ ,\ \tilde{G}(0) = 1 + \frac{b_1}{\zeta_\infty}\ \tilde{G}_\eta(0)\ ,\ \tilde{H}(0) = 0\ , \\ \tilde{\theta}(0) = 1 + \frac{\gamma}{\zeta_\infty}\ \tilde{\theta}_\eta(0)\ ,\ \tilde{\phi}_\eta(0) + \frac{Nt}{Nb}\tilde{\theta}_\eta(0) = 0\ , \\ \tilde{F}(\eta \to 1) \to 0\ ,\ \tilde{G}(\eta \to 1) \to 0\ ,\ \tilde{\theta}(\eta \to 1) \to 0\ ,\ \tilde{\phi}(\eta \to 1) \to 0\ . \end{array}\right\} \tag{8.3.7}$$

$$Re^{1/2}C_{fr}\ = \frac{A_1}{\zeta_\infty}\ \sqrt{\tilde{F}_\eta^2(0) + \tilde{G}_\eta^2(0)} \tag{8.3.8}$$

$$Re^{-1/2}Nu_r = -\frac{A_4}{\zeta_\infty}\ \tilde{\theta}_\eta(0) \tag{8.3.9}$$

In order to achieve a higher level of accuracy, the transformed ODEs are spatially discretized utilizing the modified Gauss-Lobatto grid points $\left\{\eta_i \mid 0 \leq \eta_i\ \leq 1 \quad \& \quad 1 \leq i \leq \tilde{N}\right\}$ given by

$$\eta_i = \frac{1}{2} - \frac{1}{2}cos\left(\frac{\pi(i-1)}{\tilde{N}-1}\right) \tag{8.3.10}$$

where $\tilde{N}$ is the total number of collocation points. The numerical discretization of the space derivative for a continuous function $T(\eta)$ at any collocation point η_i is given by

$$T^{(\tilde{n})}(\eta_i) = \sum_{j=1}^{\tilde{N}} d_{ij}^{(\tilde{n})}\ T_j \tag{8.3.11}$$

where $T_j = T(\eta_j) \quad \& \quad 1 \leq i,\ j \leq \tilde{N}$ are the weighting coefficients for the $\tilde{n}^{th}$-order derivative.

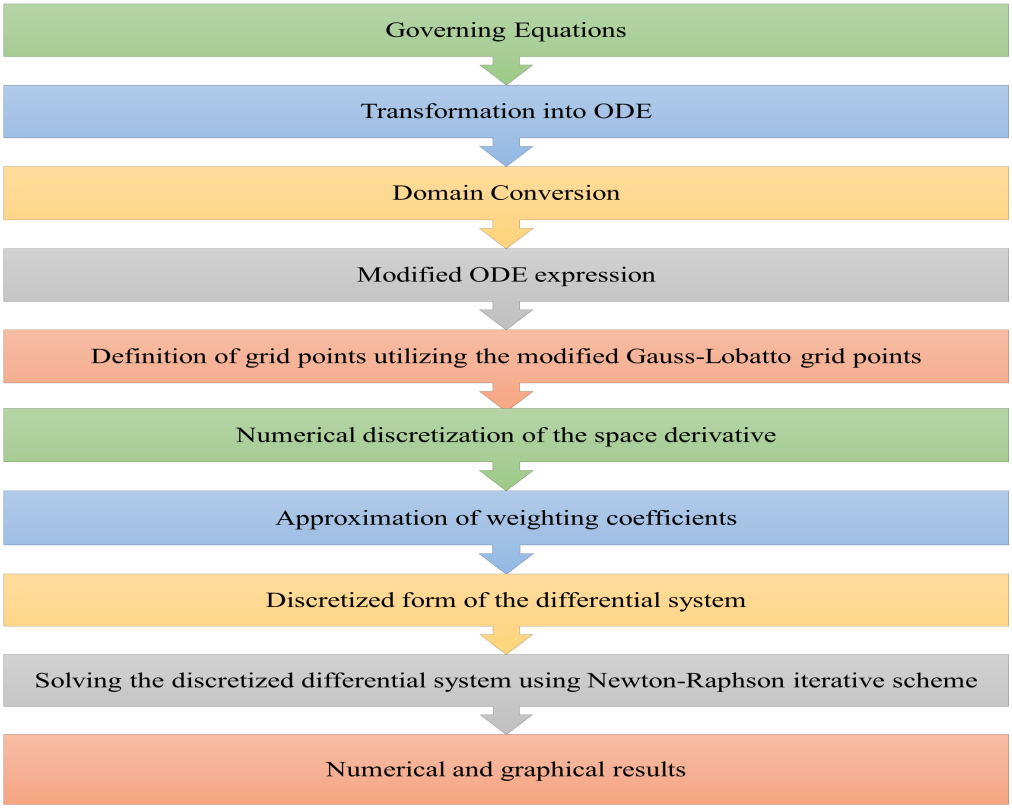

Figure 8.2: *Flowchart depicting the numerical scheme.*

According to (Shu, 2012) and (X. Wang, 2015), the coefficients $d_{ij}^{(\tilde{n})}$ are explicitly defined as:

$$\left.\begin{aligned} d_{ij}^{(1)} &= \frac{\prod_{k=1,k\neq i}^{\tilde{N}}(\eta_i-\eta_k)}{(\eta_i-\eta_j)\prod_{k=1,k\neq j}^{\tilde{N}}(\eta_j-\eta_k)} \quad for\ i\neq j,\ 1\leq i,\ j\leq \tilde{N}.\\ d_{ij}^{(1)} &= \sum_{k=1,k\neq i}^{\tilde{N}} d_{ik}^{(1)} \quad for\ i=j,\ 1\leq i,\ j\leq \tilde{N}.\\ d_{ij}^{(\tilde{n})} &= \tilde{n}\left[d_{ii}^{(\tilde{n}-1)}d_{ij}^{(1)} - \frac{d_{ij}^{(\tilde{n}-1)}}{\eta_i-\eta_j}\right] \quad for\ i\neq j,\ 1\leq i,\ j\leq \tilde{N} \quad \& \quad \tilde{n}\geq 2.\\ d_{ij}^{(\tilde{n})} &= -\sum_{k=1,\ k\neq i}^{\tilde{N}} d_{ik}^{(\tilde{n})} \quad for\ i=j,\ 1\leq i,\ j\leq \tilde{N} \quad \& \quad \tilde{n}\geq 2. \end{aligned}\right\} \tag{8.3.12}$$

Applying GDQM approximation to equations (8.3.2)-(8.3.7), the discretized nonlinear differential system is given by:

$$NDS:$$

$$\tilde{F}_i - \tfrac{b_1}{\zeta_\infty} \sum_{j=1}^{\tilde{N}} d_{ij}^{(1)}\ \tilde{F}_j = 0, \quad for\ i = 1,$$

$$\tfrac{A_2}{A_1}\left(\zeta_\infty^2\ \tilde{G}_i^2 - \ \zeta_\infty^2\ \tilde{F}_i^2 - \ \zeta_\infty \sum_{j=1}^{\tilde{N}} d_{ij}^{(1)}\ \tilde{H}_i\ \tilde{F}_j \right)$$

$$+\sum_{j=1}^{\tilde{N}} d_{ij}^{(2)}\ \tilde{F}_j - \tfrac{A_3}{A_1}\ \zeta_\infty^2\ M\ \tilde{F}_i = 0 \quad for \quad i = 2 \leq i \leq \tilde{N} - 1.$$

$$\tilde{F}_i = 0,\ for\ i = \tilde{N},.$$

$$\tilde{G}_i - \left(1 + \tfrac{b_1}{\zeta_\infty} \sum_{j=1}^{\tilde{N}} d_{ij}^{(1)}\ \tilde{G}_j \right) = 0,\ for\ i = 1,$$

$$\sum_{j=1}^{\tilde{N}} d_{ij}^{(2)}\ \tilde{G}_j - \tfrac{A_2}{A_1}\left(2\ \zeta_\infty^2\ \tilde{F}_i\ \tilde{G}_i + \ \zeta_\infty \sum_{j=1}^{\tilde{N}} d_{ij}^{(1)}\ \tilde{H}_i\ \tilde{G}_j \right)$$

$$-\tfrac{A_3}{A_1}\ \zeta_\infty^2\ M\ \tilde{G}_i = 0,\ for\ i = 2 \leq i \leq \tilde{N} - 1,$$

$$\tilde{G}_i = 0, \quad for\ i = \tilde{N},$$

$$\tilde{H}_i = 0, \quad for\ i = 1,$$

$$2\ \zeta_\infty\ \tilde{F}_i + \sum_{j=1}^{\tilde{N}} d_{ij}^{(1)}\ \tilde{H}_j = 0, \quad for\ i = 2 \leq i \leq \tilde{N} - 1,$$

$$\tilde{\theta}_i - \left(1 + \tfrac{\gamma}{\zeta_\infty} \sum_{j=1}^{\tilde{N}} d_{ij}^{(1)}\ \tilde{\theta}_j \right) = 0,\ for\ i = 1,$$

$$\tfrac{Pr}{A_4}\left(Nb \sum_{j=1}^{\tilde{N}} d_{ij}^{(1)}\ \tilde{\theta}_j \sum_{j=1}^{\tilde{N}} d_{ij}^{(1)}\ \tilde{\phi}_j + Nt \left(\sum_{j=1}^{\tilde{N}} d_{ij}^{(1)}\ \tilde{\theta}_j \right)^2 - A_5\ \zeta_\infty \ \sum_{j=1}^{\tilde{N}} d_{ij}^{(1)}\ \tilde{H}_i\ \tilde{\theta}_j \right)$$

$$+\sum_{j=1}^{\tilde{N}} d_{ij}^{(2)}\ \tilde{\theta}_j = 0, \quad for\ i = 2 \leq i \leq \tilde{N} - 1,$$

$$\tilde{\theta}_i = 0,\ for\ i = \tilde{N},$$

$$\sum_{j=1}^{\tilde{N}} d_{ij}^{(1)}\ \tilde{\phi}_j + \tfrac{Nt}{Nb} \sum_{j=1}^{\tilde{N}} d_{ij}^{(1)}\ \tilde{\theta}_j = 0,\ for\ i = 1,$$

$$\sum_{j=1}^{\tilde{N}} d_{ij}^{(2)}\ \tilde{\phi}_j + \tfrac{Nt}{Nb} \sum_{j=1}^{\tilde{N}} d_{ij}^{(2)}\ \tilde{\theta}_j - Sc\ \zeta_\infty \ \sum_{j=1}^{\tilde{N}} d_{ij}^{(1)}\ \tilde{H}_i\ \tilde{\phi}_j = 0,\ \text{for } i = 2 \leq i \leq \tilde{N} - 1,$$

$$\tilde{\phi}_i = 0\ for\ i = \tilde{N}.$$

The above non-linear algebraic system (NDS) is solved iteratively utilizing Newton-Raphson method and by taking $\left(\zeta_\infty\ , \tilde{N}\right) = (30, 100)$ as the best key values with an accuracy of 10^{-11}. After accurate generation of the discrete solutions $\left\{ \tilde{F}\left(\eta_i\right)\ ,\ \tilde{G}\left(\eta_i\right)\ ,\ \tilde{\theta}\left(\eta_i\right)\ ,\ \tilde{\phi}\left(\eta_i\right)\ \mid 1 \leq i \leq \tilde{N} \right\}$ locally, the flow profiles and the physical quantities can be deduced as:

$$F\left(\zeta_i\right) = \tilde{F}\left(\eta_i\right) \tag{8.3.13}$$

$$G\left(\zeta_i\right) = \tilde{G}\left(\eta_i\right), \tag{8.3.14}$$

$$H\left(\zeta_i\right) = \tilde{H}\left(\eta_i\right), \tag{8.3.15}$$

$$\theta\left(\zeta_i\right) = \tilde{\theta}\left(\eta_i\right) \tag{8.3.16}$$

$$\phi\left(\zeta_i\right) = \tilde{\phi}\left(\eta_i\right), \tag{8.3.17}$$

$$C_{fr} = \frac{A_1}{\zeta_\infty} \sqrt{\left(\sum_{j=1}^{\tilde{N}} d_{1j}^{(1)}\ \tilde{F}_j\right)^2 + \left(\sum_{j=1}^{\tilde{N}} d_{1j}^{(1)}\ \tilde{G}_j\right)^2} \tag{8.3.18}$$

$$Nu_r = -\frac{A_4}{\zeta_\infty} \sum_{j=1}^{\tilde{N}} d_{1j}^{(1)}\ \tilde{\theta}_j \tag{8.3.19}$$

The veracity of the code and the validation of the current problem have been adjudged through a restrictive comparison with already published works (see Tables 8.4 and 8.5).

Table 8.4: *Validation for regular fluids ($Pr = 6.2$, $\phi_{Al_2O_3} = 0$, $M = 0$, $b_1 = 0$, $\gamma = 0$, $\zeta_\infty = 30$, $\tilde{N} = 100$)*

Physical Quantities	(Turkyilmazoglu, 2014)	(J. A. Khan, Mustafa, Hayat, & Alsaedi, 2018)	Present Results
$F_\zeta(0)$	0.51023262	0.510232	0.510232619
$-G_\zeta(0)$	0.61592201	0.615923	0.615922014
$-H(\infty)$	0.88447411	0.88462	0.88447411
$-\theta_\zeta(0)$.	0.93387794	0.933877	0.93387794

Table 8.5: *Validation for nanofluids ($Pr = 7$, $A_1 = A_2 = A_3 = A_4 = A_5 = 1$, $Sc = 5$, $Nb = 0.5$, $Nt = 0.5$, $b_1 = 0$, $\gamma = 0$, $\zeta_\infty = 15$, $\tilde{N} = 100$)*

M	(J. A. Khan et al., 2018)		Present Results	
	$-\theta_\zeta(0)$	$\sqrt{F_\zeta^2(0) + G_\zeta^2(0)}$	$-\theta_\zeta(0)$	$\sqrt{F_\zeta^2(0) + G_\zeta^2(0)}$
0.5	———	0.93201894	0.642783196	0.932018932
1	0.50409254	1.1128862	0.504092494	1.112886149
1.5	———	1.2929102	0.392295982	1.292910169
2	———	1.4604084	0.306400265	1.460408379
2.5	———	1.6148965	0.242922257	1.614896532

8.4 Results and Discussion

The consequence of pertinent parameters over the radial velocity ($F(\zeta)$), azimuthal velocity ($G(\zeta)$), nanofluid temperature profile ($\theta(\zeta)$), and nanofluid concentration profiles ($\phi(\zeta)$) has been depicted through Figs. 8.3-8.23. The Prandtl number and infinity are chosen as 6.2 and 8, respectively. The thermophysical properties of water and alumina nanoparticles are identified in Table 8.2. The base values for the effectual parameters are fixed at $\phi_{Al_2O_3} = 0.02$, $M = 0.2$, $Sc = 5$, $Nb = 0.2$, $Nt = 0.1$, $b_1 = 0.25$, $\gamma = 0.25$. Further, the impact of nanoparticle shape factor on the physical quantities is elucidated in Tables 8.6 and 8.7.

Figs. 8.3 and 8.4 display the variation in $F(\zeta)$ and $G(\zeta)$ for differing values of $\phi_{Al_2O_3}$, respectively. Both $F(\zeta)$ and $G(\zeta)$ elevates with augmentation in $\phi_{Al_2O_3}$. The radial velocity profile attains the maximum value after travelling a distance from the disk and finally converges asymptotically whereas the azimuthal velocity profile achieves the highest magnitude near the disk and reduces subsequently. The elevation in $\theta(\zeta)$ due to an increment in $\phi_{Al_2O_3}$ is depicted in Fig. 8.5. This escalation in the nanofluid temperature is due to the enhanced thermal conductivity and also due to the increased frictional drag initiated by the hike in nanofluid viscosity.

The influence of M on the radial and azimuthal velocity profiles is shown in

Table 8.6: *Numerical estimation of Cf_r for various shapes of nanoparticles ($M = 0.2$, $Sc = 5$, $Nb = 0.2$, $Nt = 0.1$, $b_1 = 0.25$, $\gamma = 0.25$, $\zeta_\infty = 30$, $\tilde{N} = 100$)*

$\widetilde{n}_s$	Cf_r				Slope of $Cf_r = f(\widetilde{n}_s, \phi_{Al_2O_3})$
	$\phi_{Al_2O_3} = 0.01$	$\phi_{Al_2O_3} = 0.02$	$\phi_{Al_2O_3} = 0.03$	$\phi_{Al_2O_3} = 0.04$	
3	0.70204642	0.719531478	0.737435414	0.7557736	1.79085
3.7	0.718533752	0.788333074	0.889210514	1.015145323	9.90712
4.9	0.780370295	0.931753125	1.122969268	1.342003469	18.76115
5.7	0.855189646	1.043874203	1.245861103	1.458150886	20.1087

Figs. 8.6 and 8.7, respectively. An increment in M retards both the velocity profiles. Physically, an augmentation in M enhances the Lorentz force (a conflicting force) that brings down the velocity. In addition, Lorentz force fuels a frictional force that leads to an escalation in the nanofluid temperature. Hence, $\theta(\zeta)$ increases with M (shown in Fig 8.8). The magnetic field parameter has a mixed impact on the nanofluid concentration (see Fig 8.9). Initially, $\phi(\zeta)$ decreases with M and gradually

Table 8.7: *Numerical estimation of Nu_r for various shapes of nanoparticles ($M = 0.2$, $Sc = 5$, $Nb = 0.2$, $Nt = 0.1$, $b_1 = 0.25$, $\gamma = 0.25$, $\zeta_\infty = 30$, $\tilde{N} = 100$.*

$\widetilde{n}_s$	Nu_r				Slope of $Nu_r = f(\widetilde{n}_s, \phi_{Al_2O_3})$
	$\phi_{Al_2O_3} = 0.01$	$\phi_{Al_2O_3} = 0.02$	$\phi_{Al_2O_3} = 0.03$	$\phi_{Al_2O_3} = 0.04$	
3	0.761567002	0.77656073	0.791540424	0.806513545	1.49819
3.7	0.763692739	0.778935228	0.791999253	0.802907625	1.30708
4.9	0.765231559	0.779448063	0.78971431	0.797404207	1.06784
5.7	0.763684413	0.777463582	0.789397437	0.800430499	1.22172

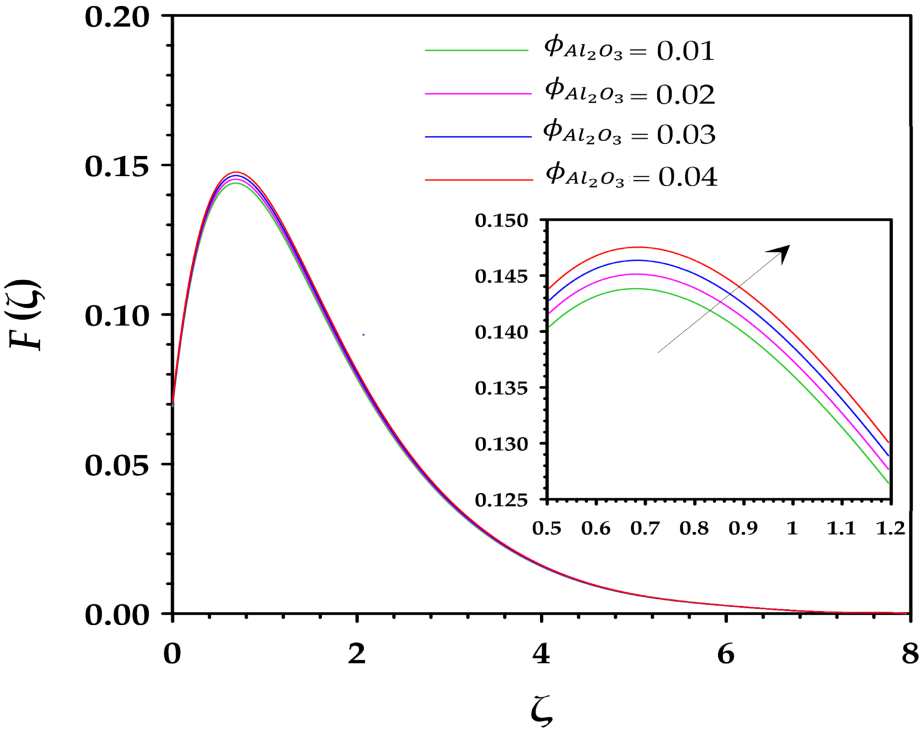

Figure 8.3: *Impact of $\phi_{Al_2O_3}$ on $F(\zeta)$.*

the trend reverses.

Figs. 8.10 and 8.11 depicts the consequence of b_1 on $F(\zeta)$ and $G(\zeta)$, respectively. An augmentation in b_1 transfers the stretching effects onto the fluid layers in the radial and azimuthal direction that decelerates the fluid flow. The positive impact of b_1 on the $\theta(\zeta)$ and $\phi(\zeta)$ has been illustrated in Figs. 8.12 and 8.13, respectively.

Fig. 8.14 elucidates the drop in $\theta(\zeta)$ due to escalating γ values. This is physically associated to the fact that mounting values of γ decreases the reactivity of fluid flow within the boundary layer, which reduces the amount of heat processed and thus

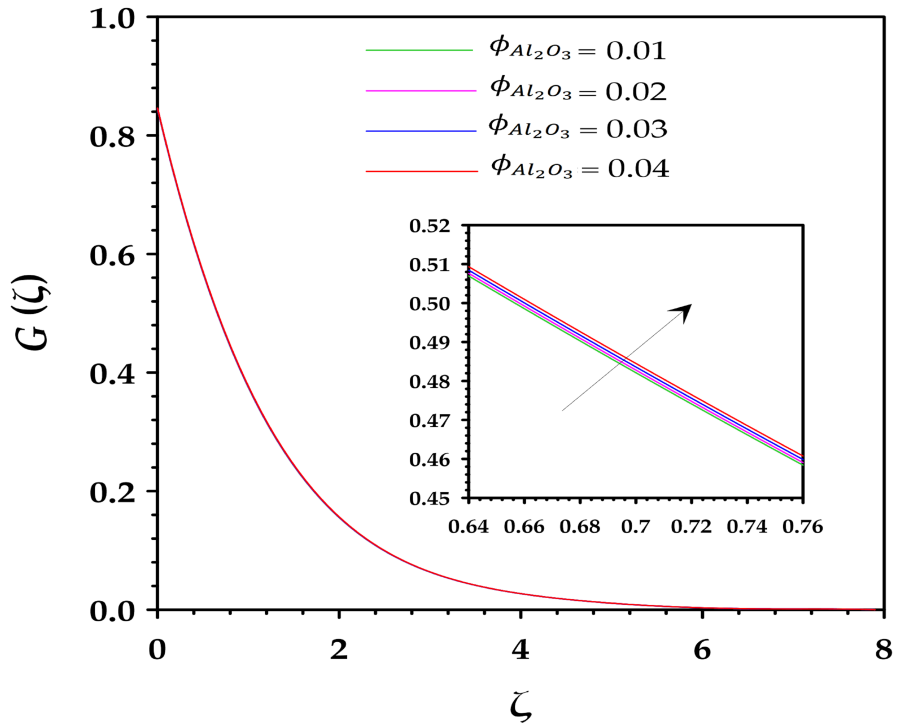

Figure 8.4: *Impact of* $\phi_{Al_2O_3}$ *on* $G(\zeta)$.

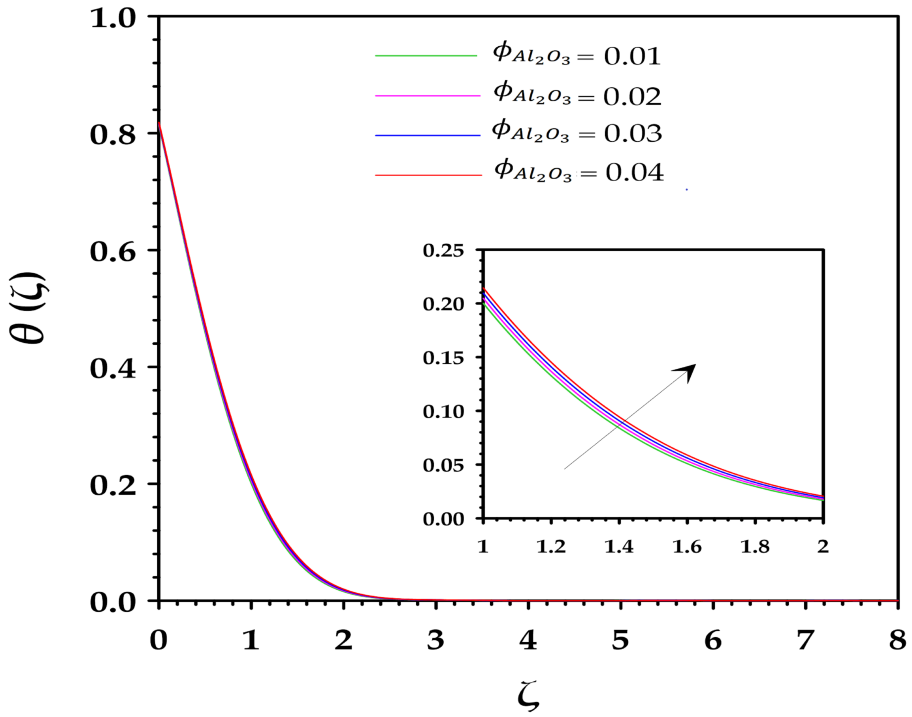

Figure 8.5: *Impact of* $\phi_{Al_2O_3}$ *on* $\theta(\zeta)$.

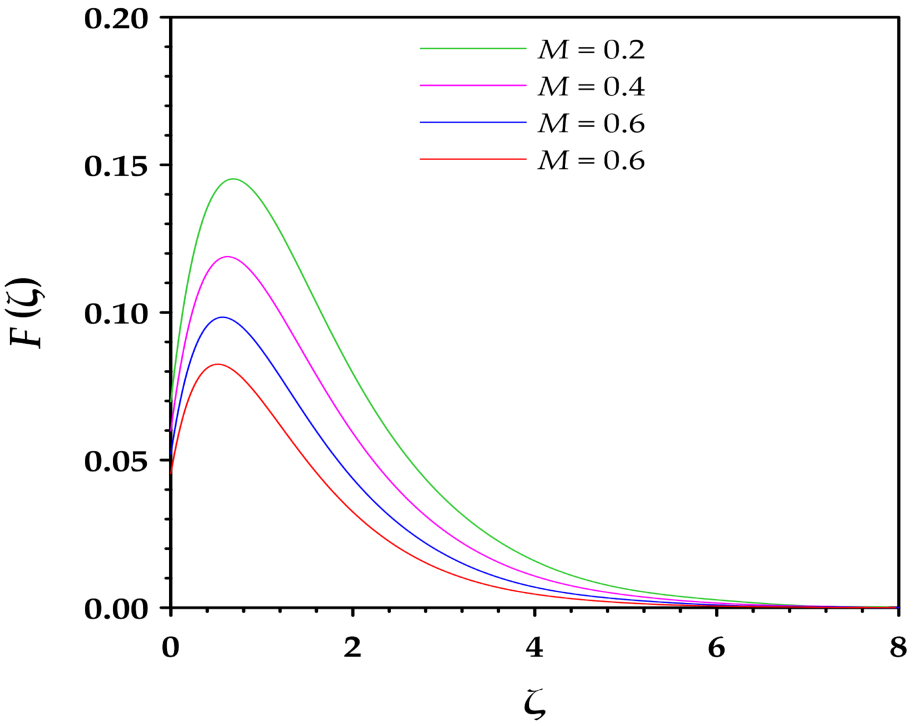

Figure 8.6: *Impact of* M *on* $F(\zeta)$.

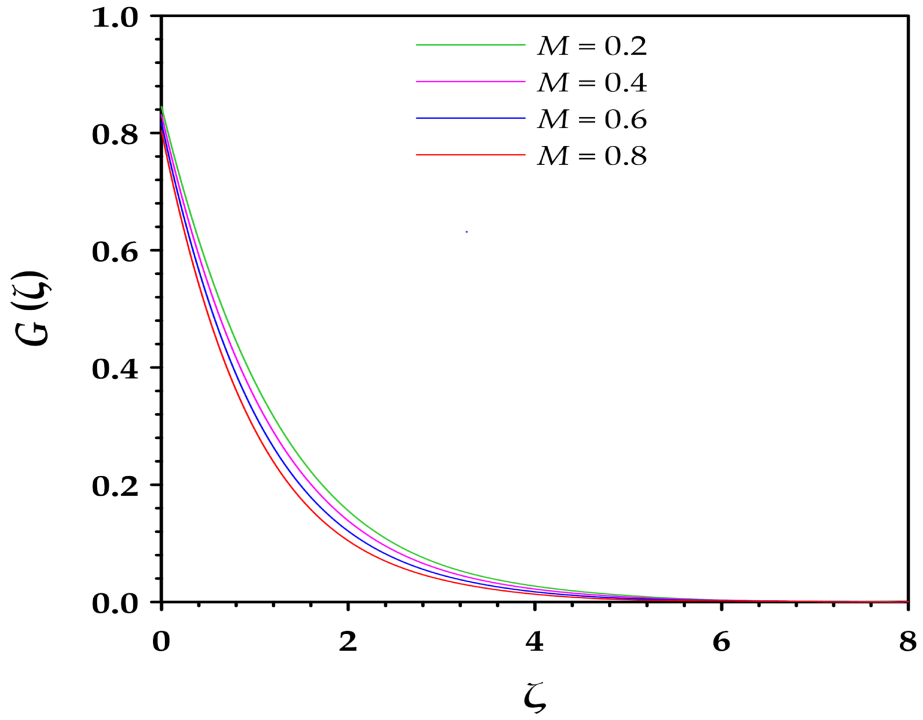

Figure 8.7: *Impact of* M *on* $G(\zeta)$.

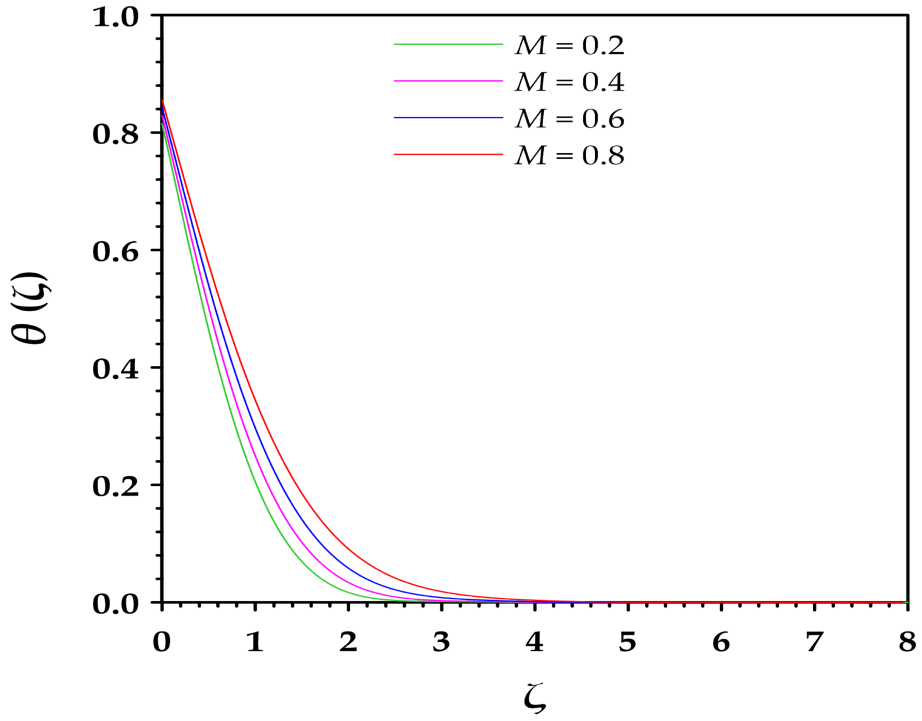

Figure 8.8: *Impact of* M *on* $\theta(\zeta)$.

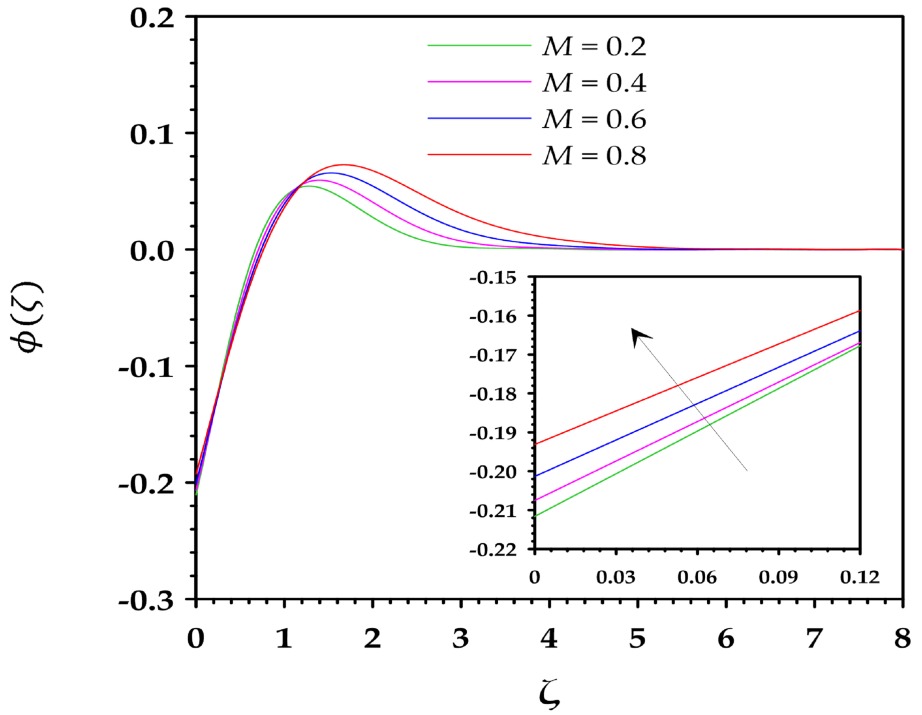

Figure 8.9: *Impact of* M *on* $\phi(\zeta)$.

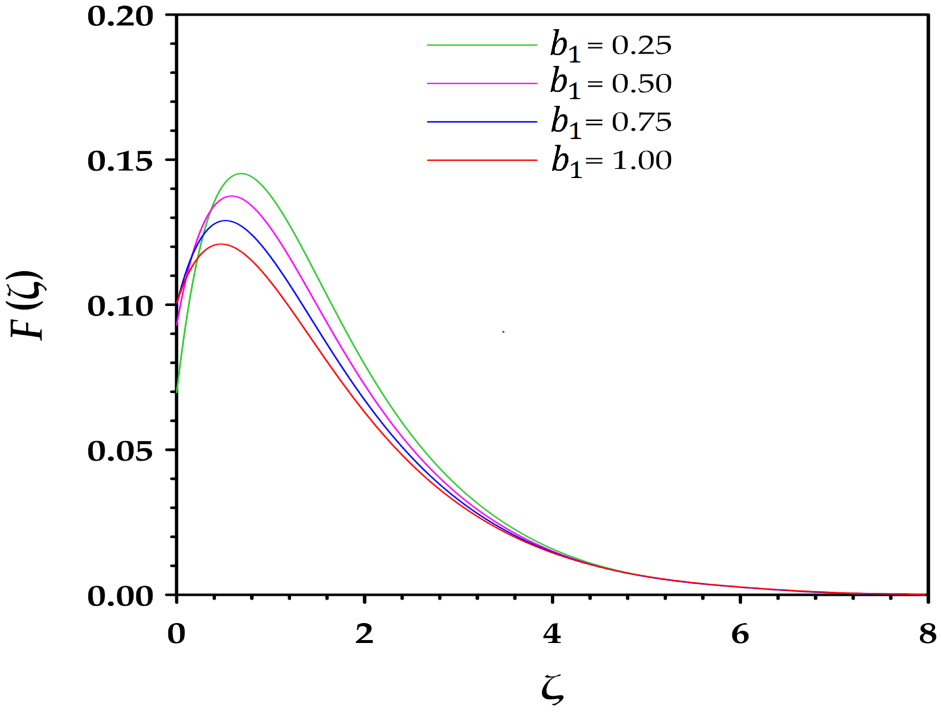

Figure 8.10: *Impact of* b_1 *on* $F(\zeta)$.

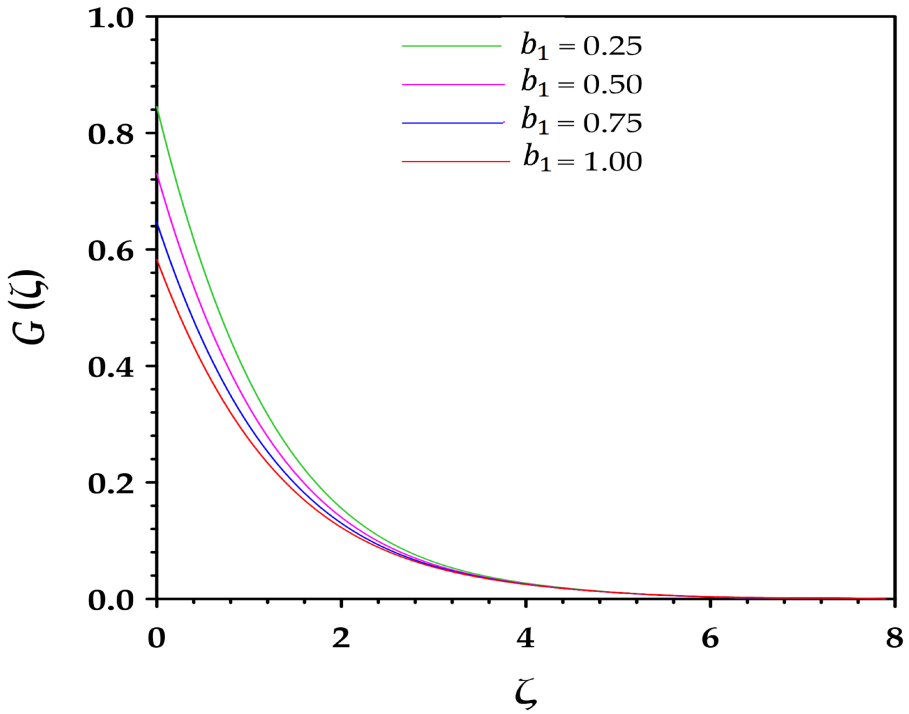

Figure 8.11: *Impact of* b_1 *on* $G(\zeta)$.

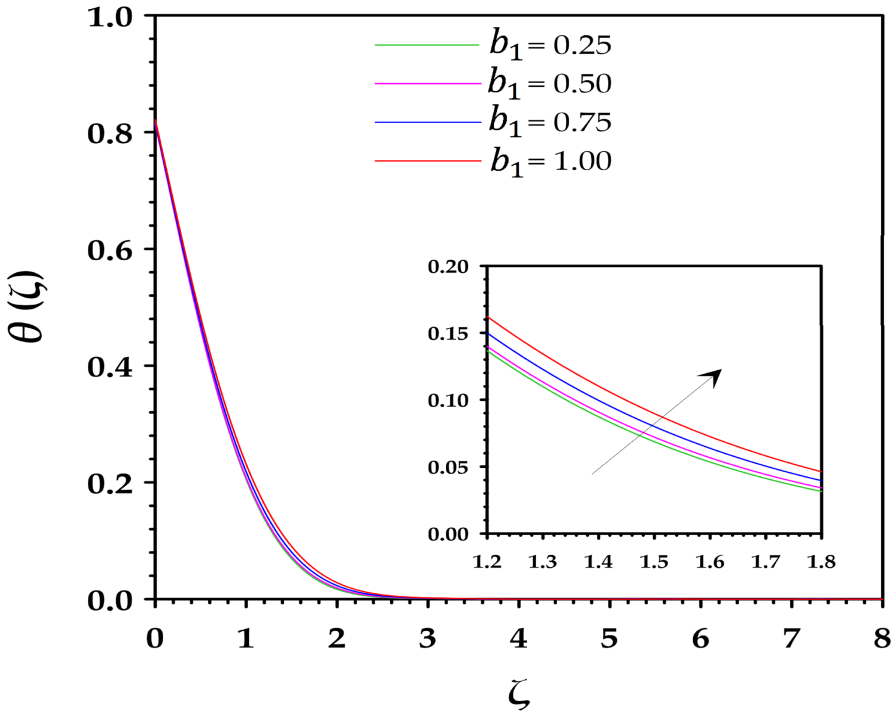

Figure 8.12: *Impact of* b_1 *on* $\theta(\zeta)$.

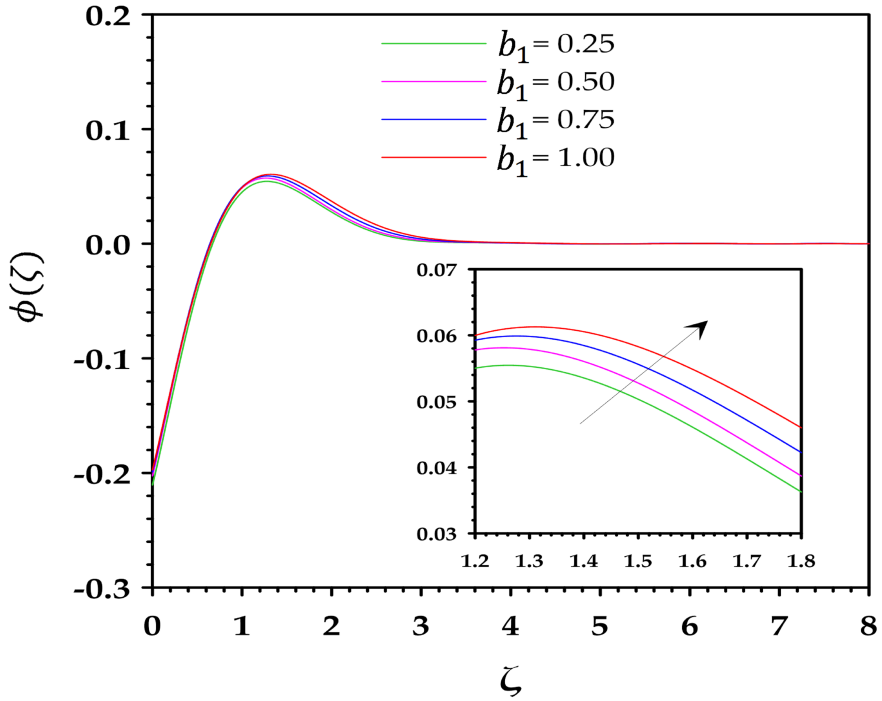

Figure 8.13: *Impact of* b_1 *on* $\phi(\zeta)$.

descends the nanofluid temperature. In addition, $\phi(\zeta)$ enhances near the disk and $\phi(\zeta)$ depletes away from the disk for augmenting values of γ (see Fig. 8.15). The flow rate is maximal away from the disk relative to the boundary layer which is the reason behind the decrease in nanofluid concentration.

The effect of Nt on $\theta(\zeta)$ and $\phi(\zeta)$ profiles are displayed in Figs. 8.16 and 8.17,

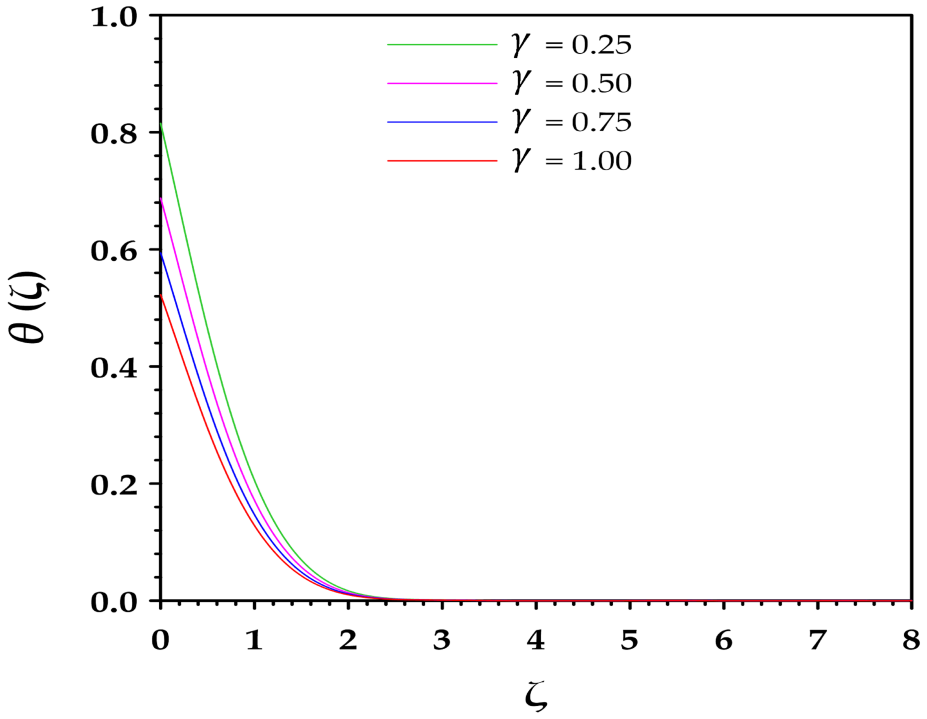

Figure 8.14: *Impact of* γ *on* $\theta(\zeta)$.

respectively. $\theta(\zeta)$ escalates with mounting Nt values and $\phi(\zeta)$ exhibits a negative impact near the disk which gradually transits into a positive impact (away from the disk). A rise in Nt accelerates the movement of hot fluid particles to the cold regions which enhances the thermal gradient and therefore the nanofluid temperature increases. Further, the increase in the nanofluid concentration away from the disk is due to improved mass transport caused by the movement of fluid particles from the disk to the ambient region.

Fig 8.18 elucidates the mixed impact of Nb on $\phi(\zeta)$. $\phi(\zeta)$ demotes near the disk and enhances away from the disk. Physically, an increment in Nb promotes the haphazard motion of nanoparticles that leads to increased collision near the disk (relative to away from the disk) caused by a large centrifugal force.

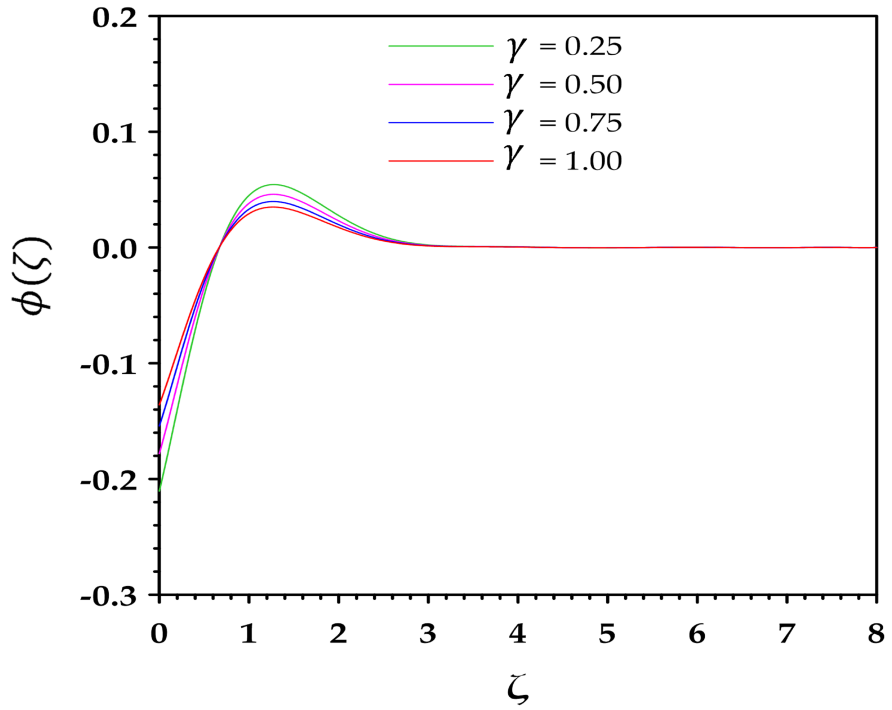

Figure 8.15: *Impact of* γ *on* $\phi(\zeta)$.

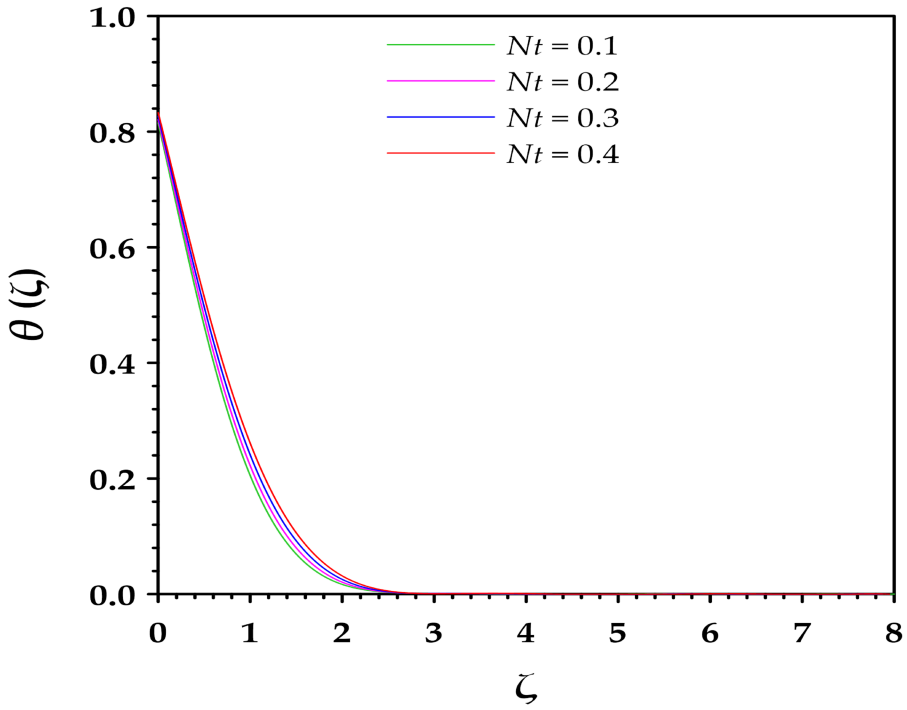

Figure 8.16: *Impact of* Nt *on* $\theta(\zeta)$.

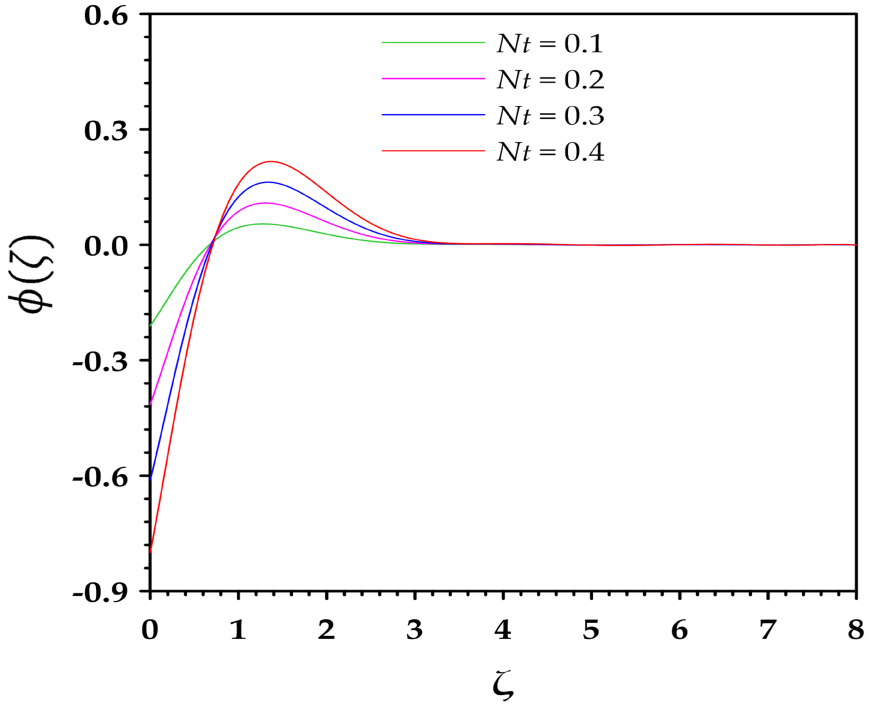

Figure 8.17: *Impact of* Nt *on* $\phi(\zeta)$.

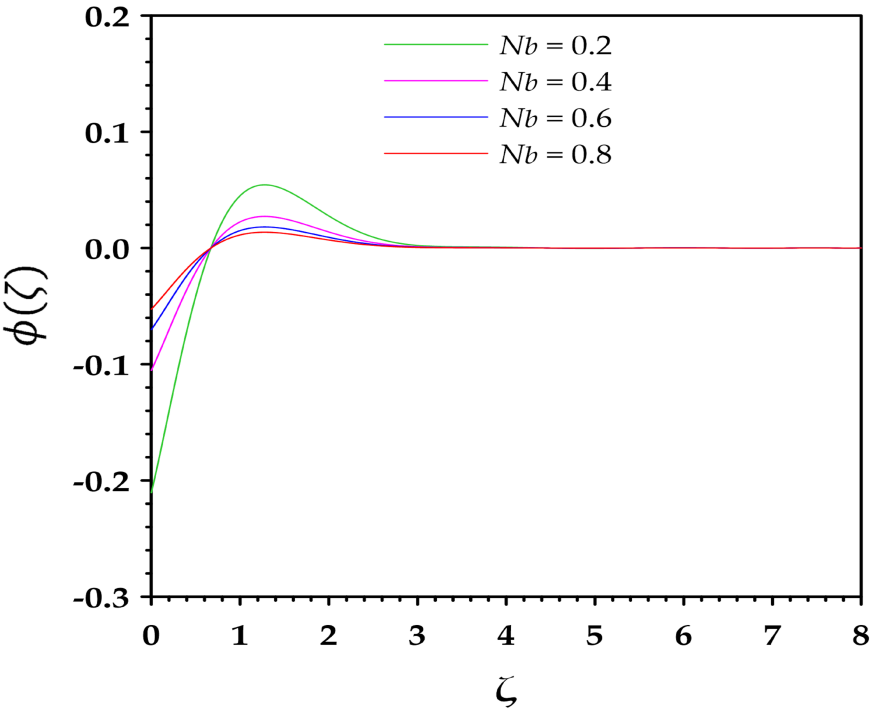

Figure 8.18: *Impact of* Nb *on* $\phi(\zeta)$.

Fig 8.19 depicts the influence of Sc on $\phi(\zeta)$. $\phi(\zeta)$ reduces near the disk and increases far from the disk. This is due to a mild diffusivity that encourages the nanoparticle migration from the hot disk towards the cold ambient fluid.

Figs. 8.20-8.23 illustrates significance of nanoparticle shape factor on $F(\zeta)$,

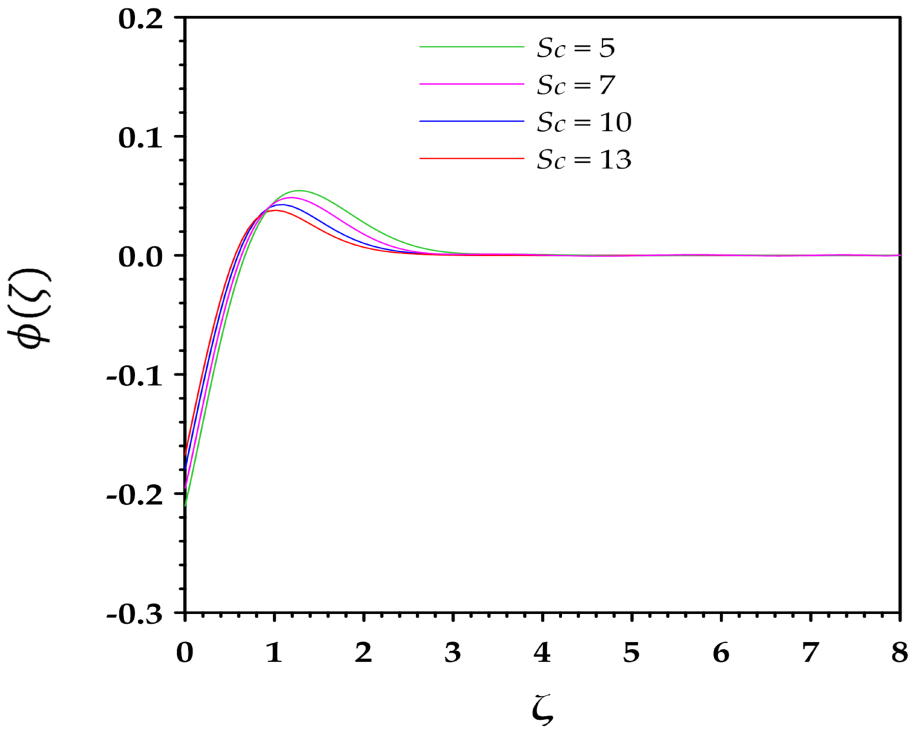

Figure 8.19: *Impact of Sc on $\phi(\zeta)$.*

$G(\zeta)$, $\theta(\zeta)$, and $\phi(\zeta)$, respectively. Initially, $F(\zeta)$ retards near the disk and gradually reverses the trend. In addition, $G(\zeta)$ and $\theta(\zeta)$ are increasing functions in $\widetilde{n_s}$ whereas $\phi(\zeta)$ is a reducing function of $\widetilde{n_s}$. Sphericity explores the resemblance of an object with a perfect sphere and the nanoparticle shape factor is inversely proportional to sphericity. An increment in the nanoparticle shape factor elevates the fluid flow in azimuthal direction due to the rotational effect. Further, augmenting $\widetilde{n_s}$ values exert more friction in the radial direction (near the disk) that helps in enhancing the nanofluid temperature. Tables 8.6 and 8.7 describe the influence of nanoparticle shape on the drag coefficient and the heat transfer rate, respectively. The highest drag is exhibited by platelet-shaped alumina nanoparticles followed by cylinder-, brick-, and sphere-shaped alumina nanoparticles. From Table 8.7, it can be concluded that heat transfer rate ascends with an increase in $\phi_{Al_2O_3}$.

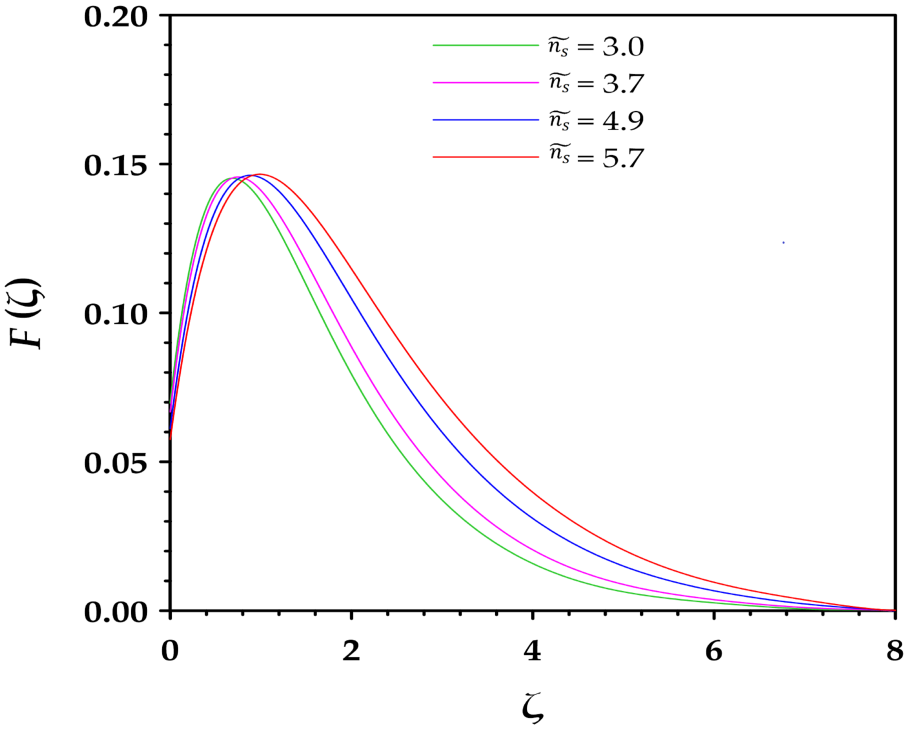

Figure 8.20: *Impact of* $\widetilde{n_s}$ *on* $F(\zeta)$.

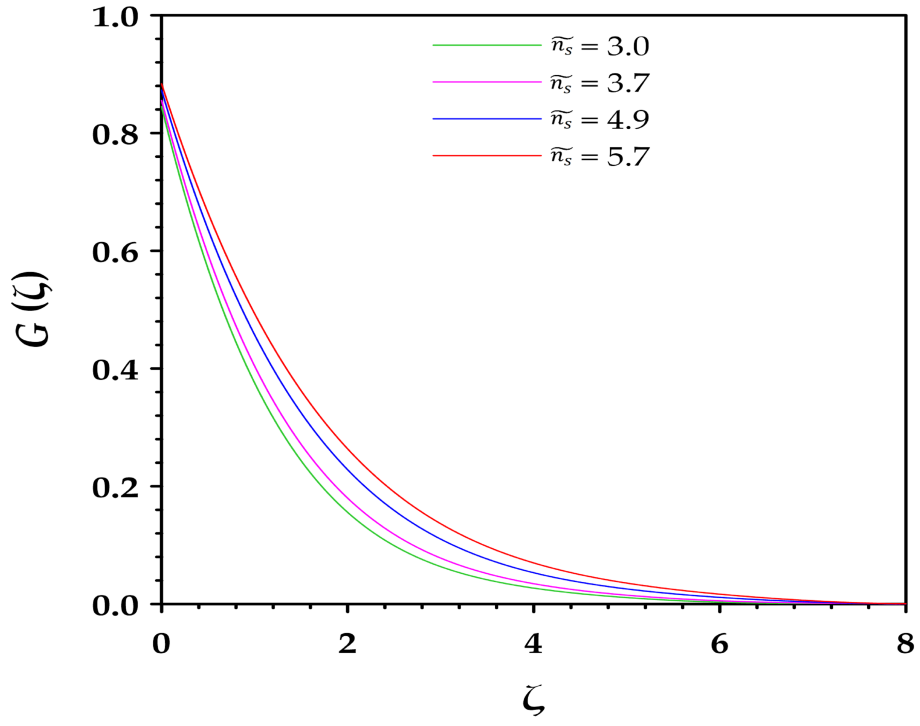

Figure 8.21: *Impact of* $\widetilde{n_s}$ *on* $G(\zeta)$.

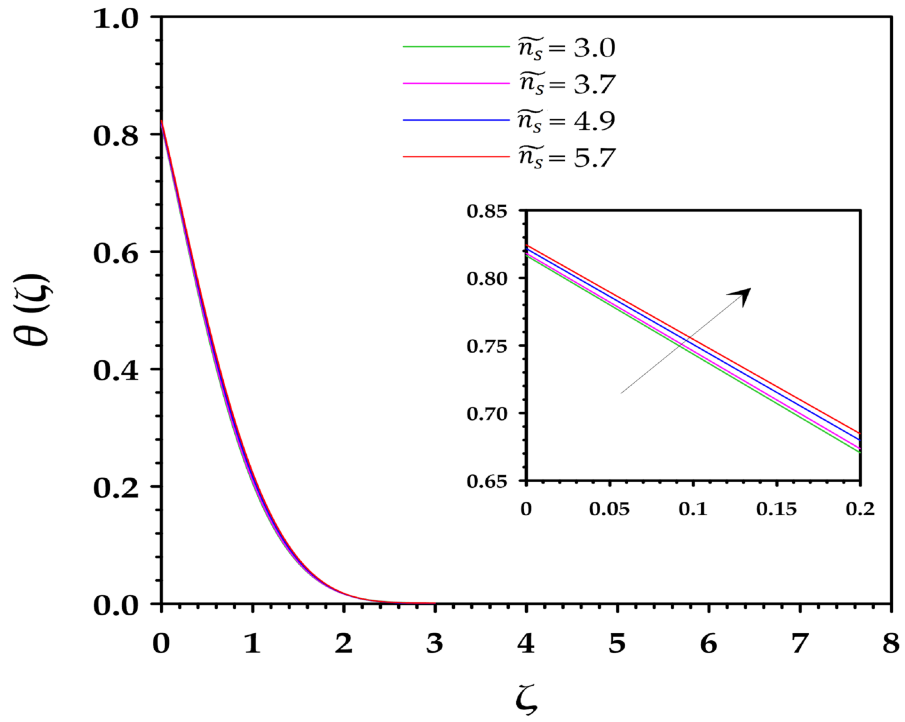

Figure 8.22: *Impact of* $\widetilde{n}_s$ *on* $\theta(\zeta)$.

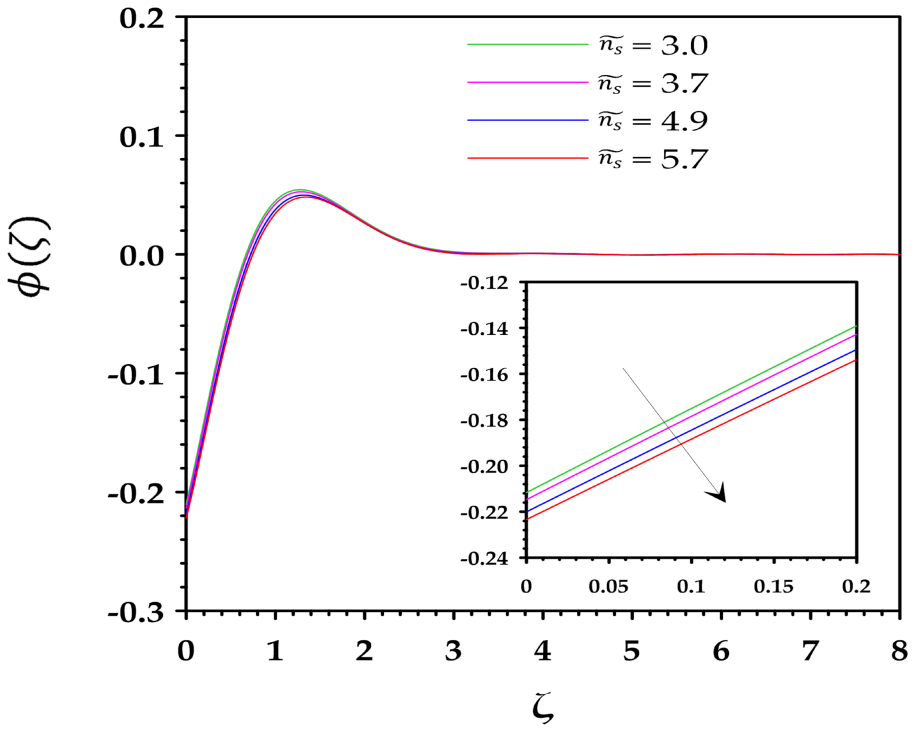

Figure 8.23: *Impact of* $\widetilde{n}_s$ *on* $\phi(\zeta)$.

8.5 Conclusions

The hydromagnetic alumina-water nanofluid flow past a rotating rigid disk has been theoretically investigated. The nanofluid flow considering different nanoparticle shapes (namely sphere, platelet, cylinder, and brick) and the thermo-hydrodynamic slip constraints have been modeled utilizing the modified Buongiorno model. The mathematically modeled equations are transmuted into a system of first-order ODEs using Von Kármán's similarity transformations and then resolved numerically by employing generalized differential quadrature method. The key conclusions of the present study are:

- The azimuthal velocity is inversely proportional to the hydrodynamic slip parameter.
- The nanofluid temperature ascends with the hydrodynamic slip parameter and descends with the thermal slip parameter.
- The nanofluid temperature is an increasing function of nanoparticle shape factor whereas the nanofluid concentration is a reducing function of nanoparticle shape factor.
- The heat transfer rate ascends with an increase in the volume fraction of alumina nanoparticle.
- The highest drag is exhibited by platelet-shaped alumina nanoparticles followed by cylinder-, brick-, and sphere-shaped alumina nanoparticles.

Chapter 9

Conclusive remarks and future scope

Various mathematical models were used in the thesis to numerically and statistically examine the flow of hydromagnetic nanofluid. The study examines the applicability of nanofluids by including the impacts of various parameters on different hydromagnetic fluids. In the thesis, aggregation kinematics and nanoparticle shape effects are taken into account. Utilizing three-dimensional surface plots and statistical techniques, a study on the augmentation of the heat transfer and optimization of the drag coefficient is undertaken. The use of graphs allows for the comparison of numerical and statistical values. Following is a summary of the overall findings.

- Hall current and injection/suction parameter plays a crucial role in amplifying the velocity profile.
- The temperature and velocity profiles are directly proportional to the heat source parameter, S.
- Angle of inclination, α has a constructive effect on the velocity profiles.
- The volume fraction of the nanoparticles, ϕ enhances the concentration profiles but reduces the temperature and velocity profiles.
- The Soret effect has a destructive impact on concentration profiles.
- Heat source and hall current has a negative impact on skin friction.
- An increase of 0.982513 per unit S (heat source) is noted due to the impact of heat source on Nusselt number.

- Soret number has a negative impact (a decrease of 1.853334359 per unit S_o) on Sherwood number.
- The velocity profiles are directly proportional to the viscosity ratio parameter in shear thinning case and inversely proportional in shear thickening case.
- Weissenberg number enhances the velocity profiles in case of shear thickening fluids and retards the velocity profiles for shear thinning fluids.
- An exponential increase is observed in the temperature profile due to an increase in Biot number, heat generation/absorption and thermophoresis parameters.
- Increase in the stretching ratio parameter improves the Y directional velocity profile.
- The concentration profile is enhanced and depleted with increasing thermophoresis and Brownian motion effects, respectively.
- The regression models are found to be in synchronization with the numerical results for the chosen values of parameters.
- Exponential space-based heat source (ESHS) and linear heat source (LHS) parameters exhibit a constructive behaviour on the temperature profile.
- Slip effect decreases the velocity and temperature profiles.
- Weissenberg number exhibits a differing nature on the velocity profile based on the nature of fluid; velocity is reduced when $n < 1$ and increased when $n > 1$.
- Velocity slip increases the drag coefficient whereas Hartmann number decreases the drag coefficient.
- Heat transfer rate lowers with ESHS, LHS and temperature slip parameters.
- Mass transfer rate is inversely proportional to concentration slip parameter.
- Nusselt number has been faultlessly estimated using multiple linear regression.
- The aggregation kinematic aspect enhances the temperature field due to the improved thermal conductivity of the nanofluid.

- The velocity retards due to variation in Hartmann number and an opposite trend is exhibited for temperature. It is due to the generated opposing force, namely the Lorentz force.
- The temperature profile enhances with more thermal radiation and exponential heat source effects. Physically, these parameters contribute more energy to the fluid
- The surface drag force is an increasing function of quadratic thermal convection aspect.
- Maximum heat transfer occurs at the highest level of quadratic thermal convection and nanoparticle volume fraction parameters.
- The heat flux is more sensitive to the inclination angle when compared to other parameter values. This sensitivity augments at a rate 0.5094% for the increment in R.
- An accurate quadratic model is estimated for the wall heat flux with $\mathcal{R}^2 = 99.98\%$.
- The wall shear stress decrements by 41.1388 % when the inclination of the plate is changed from 60^0 to 75^0.
- The x-directional velocity descends with the Forchheimer number and hydrodynamic slip parameter.
- The y-directional velocity ascends with the stretching parameter.
- The suction case exhibits lowered temperature and velocity profiles in correspondence with the injection case.
- The Biot number and the volume fraction of copper nanoparticles have a constructive effect on the hybrid nanoliquid temperature.
- The heat transfer rate is higher for the suction case in comparison with the injection case.
- The heat transfer rate is higher for lower values of magnetic field parameter and higher values of Biot number and volume fraction of copper nanoparticles.

- The drag coefficients increase with hydrodynamic slip parameter and decrease for higher values of magnetic field and porosity parameters.
- Higher drag coefficients are observed in the case of injection when compared with the suction case.
- A commendable agreement is noted between the numerical and statistical results.
- Radial and azimuthal velocities demote with an increment in magnetic field due to the presence of Lorentz force.
- Radial velocity and surface drag decrease with augmentation in Reiner-Rivlin fluid parameter. It is due to an elevation in the cross-viscosity coefficient.
- The temperature profile increases due to both temperature and space-dependent heat sources. An opposite trend is noted in the heat transfer rate.
- Joule heating has a positive influence on the thermal boundary layer. The heat transfer rate lowers with an increment in the Eckert number.
- Hartmann number, Reiner-Rivlin fluid parameter, and thermal slip parameter show a negative response with heat transfer coefficient.
- The heat transfer sensitivity towards the Hartmann number decreases at the rate of 0.2267% and the sensitivity towards the Reiner-Rivlin fluid parameter decreases at the rate of 0.0554% when thermal slip is incremented.
- The azimuthal velocity is inversely proportional to the hydrodynamic slip parameter.
- The nanofluid temperature ascends with the hydrodynamic slip parameter and descends with the thermal slip parameter.
- The nanofluid temperature is an increasing function of nanoparticle shape factor whereas the nanofluid concentration is a reducing function of nanoparticle shape factor.
- The heat transfer rate ascends with an increase in the volume fraction of alumina nanoparticle.

- The highest drag is exhibited by platelet-shaped alumina nanoparticles followed by cylinder-, brick-, and sphere-shaped alumina nanoparticles.

The basic concepts and knowledge of fluid mechanics and modelling problems are essential for analyzing a system working in a fluid medium. Nanofluids enhances the conventional fluid (e.g., water, kerosene, Ethylene glycol, and oil) with nanotechnology that made a drastic change in Engineering, industry medical, and Economic fields. Theoretical models lessen risk, conserve resources, and add more concepts to the experimental design. Hydromagnetic stagnation point flow over a stretchable disk is in initial stage. There are so many work to be done in the area. The mathematical models described in this work can be expanded in the following ways in the future.

- Entropy generation in MHD convective nanofluid flow with more than one nanoparticles.
- Optimising the drag coefficient of MHD convective nanofluid flow with microorganisms.
- Enhancing heat transport of MHD convective nanofluid flow in the presence of electric field and non linear Boussinesq approximation.
- To study convective flow in the presence of induced magnetic field.

Publications in journals and presentations

Publications:

1. Sabu, A. S., Mathew, A., Neethu, T. S., & George, K. A. (2021). Statistical analysis of MHD convective ferro-nanofluid flow through an inclined channel with hall current, heat source and soret effect. Thermal Science and Engineering Progress, 22, 100816. https://doi.org/10.1016/j.tsep.2020.100816

2. Sabu, A. S., Areekara, S., & Mathew, A. (2021). Statistical analysis on three-dimensional MHD convective Carreau nanofluid flow due to bilateral nonlinear stretching sheet with heat source and zero mass flux condition. Heat Transfer, 50(4), 3641-3660. https://doi.org/10.1002/htj.22045

3. Sabu, A. S., Areekara, S., & Mathew, A. (2021). Effects of multislip and distinct heat source on MHD Carreau nanofluid flow past an elongating cylinder using the statistical method. Heat Transfer, 50(6), 5652-5673. https://doi.org/10.1002/htj.22142

4. Sabu, A. S., Mackolil, J., Mahanthesh, B., & Mathew, A. (2022). Nanoparticle aggregation kinematics on the quadratic convective magnetohydrodynamic flow of nanomaterial past an inclined flat plate with sensitivity analysis. Proceedings of the Institution of Mechanical Engineers, Part E: Journal of Process Mechanical Engineering, 236(3), 1056-1066. https://doi.org/10.1177/09544089211056235

5. Sabu, A. S., Areekara, S., & Mathew, A. (2022). Regression analysis on MHD Darcy-Forchheimer hybrid nanoliquid flow over an elongated permeable sheet in a porous medium with hydrodynamic slip constraint: a realistic two-phase

modified Buongiorno model. Waves in Random and Complex Media, 1-24. https://doi.org/10.1080/17455030.2022.2086318

6. Sabu, A. S., Mackolil, J., Mahanthesh, B., & Mathew, A. (2022). Numerical study of Reiner-Rivlin nanoliquid flow due to a rotating disk with Joule heating and non-uniform heat source using Bulirsch-Stoer algorithm. Waves in Random and Complex Media, 1-23. https://doi.org/10.1080/17455030.2022.2111476

7. Sabu, A. S., Wakif, A., Areekara, S., Mathew, A., & Shah, N. A. (2021). Significance of nanoparticles' shape and thermo-hydrodynamic slip constraints on MHD alumina-water nanoliquid flows over a rotating heated disk: The passive control approach. International Communications in Heat and Mass Transfer, 129, 105711. https://doi.org/10.1016/j.icheatmasstransfer.2021.105711.

Presentations:

1. Presented a paper entitled "MHD nanofluid flow past a stretching sheet containing different shapes of nanoparticles with thermal radiation and Chemical reaction", in the 28th International conference (Virtual) of forum for Interdisciplinary Mathematics, Synergies in Computational, Mathematical, Statistical and Physical sciences (FIM 28, SCMSPS 2020), organized by FIM Stella Maris College (Autonomous),Chennai, and Sri Sivasubramaniya Nadar College of Engineering (Autonomous) Tamilnadu during 23-27 November 2020.

2. Presented a paper entitled "MHD nanofluid flow containing various shapes of nano particles in a rotating porous channel with chemical reaction and radiation", in the international conference on Mathematics 2018, organized by department of Mathematics, St Thomas College (Autonomous) Thrissur, Kerala and International multidisciplinary research foundation (IMRF), during 29-30 June 2018.

3. Presented a paper entitled " Radiative MHD flow of nano fluids in a vertical channel with hall current" in the International conference on Mathematical Impacts in science and technology (BIT MIST-2017), organised by Department of Mathematics, Bannari Amman Institute of technology (Autonomous), Sathyamangalam, Tamilnadu during 17-18 November 2017.

References

Aaiza, G., Khan, I., & Shafie, S. (2015). Energy transfer in mixed convection mhd flow of nanofluid containing different shapes of nanoparticles in a channel filled with saturated porous medium. *Nanoscale Research Letters*, *10*(1), 1–14.

Abbas, T., Rehman, S., Shah, R. A., Idrees, M., & Qayyum, M. (2020). Analysis of mhd carreau fluid flow over a stretching permeable sheet with variable viscosity and thermal conductivity. *Physica A: Statistical Mechanics and its Applications*, *551*, 124225.

Abdal, S., Mariam, A., Ali, B., Younas, S., Ali, L., & Habib, D. (2021). Implications of bioconvection and activation energy on reiner–rivlin nanofluid transportation over a disk in rotation with partial slip. *Chinese Journal of Physics*, *73*, 672–683.

Abdo, S., & Saidani-Scott, H. (2021). Effect of using saturated hydrogel beads with alumina water-based nanofluid for cooling solar panels: Experimental study with economic analysis. *Solar Energy*, *217*, 155–164.

Acharya, N., Das, K., & Kundu, P. K. (2017). Cattaneo–christov intensity of magnetised upper-convected maxwell nanofluid flow over an inclined stretching sheet: a generalised fourier and fick's perspective. *International Journal of Mechanical Sciences*, *130*, 167–173.

Acharya, N., Das, K., & Kundu, P. K. (2018). Rotating flow of carbon nanotube over a stretching surface in the presence of magnetic field: a comparative study. *Applied Nanoscience*, *8*(3), 369–378.

Acharya, N., Das, K., & Kundu, P. K. (2019). Effects of aggregation kinetics on nanoscale colloidal solution inside a rotating channel. *Journal of Thermal Analysis and Calorimetry*, *138*(1), 461–477.

Acharya, N., Maity, S., & Kundu, P. K. (2020). Influence of inclined magnetic field on the flow of condensed nanomaterial over a slippery surface: the hybrid visualization. *Applied Nanoscience*, *10*(2), 633–647.

Ahmed, A., Khan, M., Hafeez, A., & Ahmed, J. (2020). Thermal analysis in unsteady radiative maxwell nanofluid flow subject to heat source/sink. *Applied Nanoscience*, *10*(12), 5489–5497.

Ahmed, S. E., & Rashed, Z. (2019). Mhd natural convection in a heat generating

porous medium-filled wavy enclosures using buongiorno's nanofluid model. *Case Studies in Thermal Engineering*, *14*, 100430.

Akcay, S., Akdag, U., & Palancioglu, H. (2020). Experimental investigation of mixed convection on an oscillating vertical flat plate. *International Communications in Heat and Mass Transfer*, *113*, 104528.

Aladdin, N. A. L., Bachok, N., & Pop, I. (2020). Cu-al2o3/water hybrid nanofluid flow over a permeable moving surface in presence of hydromagnetic and suction effects. *Alexandria Engineering Journal*, *59*(2), 657–666.

Alfvén, H. (1942). Existence of electromagnetic-hydrodynamic waves. *Nature*, *150*(3805), 405–406.

Ali, A. R. I., & Salam, B. (2020). A review on nanofluid: preparation, stability, thermophysical properties, heat transfer characteristics and application. *SN Applied Sciences*, *2*(10), 1–17.

Ali, M., Shahzad, M., Sultan, F., & Khan, W. A. (2020). Numerical analysis of chemical reaction and non-linear radiation for magneto-cross nanofluid over a stretching cylinder. *Applied Nanoscience*, *10*(8), 3259–3267.

Alsagri, A. S., Hassanpour, A., & Alrobaian, A. A. (2019). Simulation of mhd nanofluid flow in existence of viscous dissipation by means of adm. *Case Studies in Thermal Engineering*, *14*, 100494.

Aly, E. H., & Pop, I. (2020). Mhd flow and heat transfer near stagnation point over a stretching/shrinking surface with partial slip and viscous dissipation: Hybrid nanofluid versus nanofluid. *Powder Technology*, *367*, 192–205.

Alzahrani, A. K., Ullah, M. Z., Alshomrani, A. S., & Gul, T. (2021). Hybrid nanofluid flow in a darcy-forchheimer permeable medium over a flat plate due to solar radiation. *Case Studies in Thermal Engineering*, *26*, 100955.

Aminfar, H., Mohammadpourfard, M., & Mohseni, F. (2012). Two-phase mixture model simulation of the hydro-thermal behavior of an electrical conductive ferrofluid in the presence of magnetic fields. *Journal of Magnetism and Magnetic Materials*, *324*(5), 830–842.

Areekara, S., Mackolil, J., Mahanthesh, B., Mathew, A., & Rana, P. (2022). A study on nanoliquid flow with irregular heat source and realistic boundary conditions: A modified buongiorno model for biomedical applications. *ZAMM-Journal of Applied Mathematics and Mechanics/Zeitschrift für Angewandte Mathematik*

und Mechanik, *102*(3), e202100167.

Aziz, A., Jamshed, W., Aziz, T., Bahaidarah, H., & Ur Rehman, K. (2021). Entropy analysis of powell–eyring hybrid nanofluid including effect of linear thermal radiation and viscous dissipation. *Journal of Thermal Analysis and Calorimetry*, *143*(2), 1331–1343.

Aziz, A., & Khan, W. (2012). Natural convective boundary layer flow of a nanofluid past a convectively heated vertical plate. *International Journal of Thermal Sciences*, *52*, 83–90.

Bahiraei, M., Monavari, A., & Moayedi, H. (2020). Second law assessment of nanofluid flow in a channel fitted with conical ribs for utilization in solar thermal applications: Effect of nanoparticle shape. *International Journal of Heat and Mass Transfer*, *151*, 119387.

Balvinder, P. G., Krishan, D. S., & Bansal, A. (2014). Hall current effect on viscoelastic (walter's liquid model-b) mhd oscillatory convective channel flow through a porous medium with heat radiation. *Kragujevac Journal of Science*(36), 19–32.

Basha, H. T., Sivaraj, R., Prasad, V. R., & Beg, O. A. (2021). Entropy generation of tangent hyperbolic nanofluid flow over a circular cylinder in the presence of nonlinear boussinesq approximation: a non-similar solution. *Journal of Thermal Analysis and Calorimetry*, *143*(3), 2273–2289.

Bejan, A., & Lage, J. (1991). Heat transfer from a surface covered with hair. In *Convective heat and mass transfer in porous media* (pp. 823–845). Springer.

Benkhedda, M., Boufendi, T., Tayebi, T., & Chamkha, A. J. (2020). Convective heat transfer performance of hybrid nanofluid in a horizontal pipe considering nanoparticles shapes effect. *Journal of Thermal analysis and Calorimetry*, *140*(1), 411–425.

Bilal, M., Sagheer, M., & Hussain, S. (2018). Numerical study of magnetohydrodynamics and thermal radiation on williamson nanofluid flow over a stretching cylinder with variable thermal conductivity. *Alexandria engineering journal*, *57*(4), 3281–3289.

Brinkman, H. C. (1949). A calculation of the viscous force exerted by a flowing fluid on a dense swarm of particles. *Flow, Turbulence and Combustion*, *1*(1), 27–34.

Brinkman, H. C. (1952). The viscosity of concentrated suspensions and solutions. *The Journal of chemical physics*, *20*(4), 571–571.

Bulirsch, R., Stoer, J., & Stoer, J. (2002). *Introduction to numerical analysis* (Vol. 3). Springer.

Carreau, P. J. (1972). Rheological equations from molecular network theories. *Transactions of the Society of Rheology*, *16*(1), 99–127.

Chamkha, A. J., Jena, S. K., & Mahapatra, S. K. (2015). Mhd convection of nanofluids: a review. *Journal of Nanofluids*, *4*(3), 271–292.

Chen, H., Ding, Y., He, Y., & Tan, C. (2007). Rheological behaviour of ethylene glycol based titania nanofluids. *Chemical physics letters*, *444*(4-6), 333–337.

Choi, S. U., & Eastman, J. A. (1995). *Enhancing thermal conductivity of fluids with nanoparticles* (Tech. Rep.). Argonne National Lab.(ANL), Argonne, IL (United States).

Das, A., & Sahoo, B. (2018). Flow of a reiner-rivlin fluid between two infinite coaxial rotating disks. *Mathematical Methods in the Applied Sciences*, *41*(14), 5602–5618.

Das, K., Duari, P. R., & Kundu, P. K. (2014). Nanofluid flow over an unsteady stretching surface in presence of thermal radiation. *Alexandria engineering journal*, *53*(3), 737–745.

Das, S., Jana, R., & Makinde, O. (2016). Transient natural convection in a vertical channel filled with nanofluids in the presence of thermal radiation. *Alexandria Engineering Journal*, *55*(1), 253–262.

De, P. (2019a). Impact of dual solutions on nanofluid containing motile gyrotactic micro-organisms with thermal radiation. *BioNanoScience*, *9*(1), 13–20.

De, P. (2019b). Soret-dufour effects on unsteady flow of convective eyring-powell magneto nanofluids over a semi-infinite vertical plate. *BioNanoScience*, *9*(1), 7–12.

De, P., & Gorji, M. R. (2020). Activation energy and binary chemical reaction on unsteady mhd williamson nanofluid containing motile gyrotactic micro-organisms. *Heat Transfer*, *49*(5), 3030–3043.

Deymi-Dashtebayaz, M., Akhoundi, M., Ebrahimi-Moghadam, A., Arabkoohsar, A., Jabari Moghadam, A., & Farzaneh-Gord, M. (2021). Thermo-hydraulic analysis and optimization of cuo/water nanofluid inside helically dimpled heat

exchangers. *Journal of Thermal Analysis and Calorimetry*, *143*(6), 4009–4024.

Drew, D. A., & Passman, S. L. (2006). *Theory of multicomponent fluids* (Vol. 135). Springer Science & Business Media.

Eastman, J. A., Choi, U., Li, S., Thompson, L., & Lee, S. (1996). Enhanced thermal conductivity through the development of nanofluids. *MRS Online Proceedings Library (OPL)*, *457*.

Eid, M. R., Mahny, K., Dar, A., & Muhammad, T. (2020). Numerical study for carreau nanofluid flow over a convectively heated nonlinear stretching surface with chemically reactive species. *Physica A: Statistical Mechanics and its Applications*, *540*, 123063.

Eid, M. R., & Nafe, M. A. (2022). Thermal conductivity variation and heat generation effects on magneto-hybrid nanofluid flow in a porous medium with slip condition. *Waves in Random and Complex Media*, *32*(3), 1103–1127.

Elshehabey, H. M., Raizah, Z., Öztop, H. F., & Ahmed, S. E. (2020). Mhd natural convective flow of fe3o4- h2o ferrofluids in an inclined partial open complex-wavy-walls ringed enclosures using non-linear boussinesq approximation. *International Journal of Mechanical Sciences*, *170*, 105352.

Erkan, A., Tüccar, G., Tosun, E., & Özgür, T. (2021). Comparison of effects of nanofluid utilization (al2o3, sio2, tio2) with reference water in automotive radiators on exergetic properties of diesel engines. *SN Applied Sciences*, *3*(3), 1–13.

Faisal, M., Ahmad, I., & Javed, T. (2021). Keller–box simulation for nonzero and zero mass fluxes of nanofluid flow impinging over a bi-directional stretching sheet: An unsteady mathematical model. *International Journal of Modern Physics C*, *32*(04), 2150052.

Fauzan, M. Y., Muyeen, S., & Islam, S. (2021). Enhanced power extraction from thermoelectric generators considering non-uniform heat distribution. *Energy Conversion and Management*, *246*, 114565.

Fisher, R. A., et al. (1921). 014: On the" probable error" of a coefficient of correlation deduced from a small sample.

Ganapathirao, M., Chamkha, A., & Srinivasa Rao, N. (2019). Effects of non-uniform slot suction/injection and chemical reaction on mixed convective mhd flow along a vertical wedge embedded in a porous medium. *Frontiers in Heat and*

Mass Transfer (FHMT), *13*.

Gangadhar, K., Bhargavi, D. N., Kannan, T., Venkata Subba Rao, M., & Chamkha, A. J. (2020). Transverse mhd flow of al2o3-cu/h2o hybrid nanofluid with active radiation: a novel hybrid model. *Mathematical Methods in the Applied Sciences*.

Ganguly, S., Basu, S., & Sikdar, S. (2012). Determination of the aggregate fractal dimensions in colloidal nanofluids. *Proceedings of the Institution of Mechanical Engineers, Part N: Journal of Nanoengineering and Nanosystems*, *226*(1), 3–7.

Gayatri, M., Jayarami Reddy, K., & Jayachandra Babu, M. (2020). Slip flow of carreau fluid over a slendering stretching sheet with viscous dissipation and joule heating. *SN Applied Sciences*, *2*(3), 1–11.

Gholinia, M., Armin, M., Ranjbar, A., & Ganji, D. (2019). Numerical thermal study on cnts/c2h6o2–h2o hybrid base nanofluid upon a porous stretching cylinder under impact of magnetic source. *Case Studies in Thermal Engineering*, *14*, 100490.

Gireesha, B., Nagaraja, B., Sindhu, S., & Sowmya, G. (2020). Consequence of exponential heat generation on non-darcy-forchheimer flow of water based carbon nanotubes driven by a curved stretching sheet. *Applied Mathematics and Mechanics*, *41*(11), 1723–1734.

Gireesha, B., Srinivasa, C., Shashikumar, N., Macha, M., Singh, J., & Mahanthesh, B. (2019). Entropy generation and heat transport analysis of casson fluid flow with viscous and joule heating in an inclined porous microchannel. *Proceedings of the Institution of Mechanical Engineers, Part E: Journal of Process Mechanical Engineering*, *233*(5), 1173–1184.

Goyal, M., & Bhargava, R. (2018). Simulation of natural convective boundary layer flow of a nanofluid past a convectively heated inclined plate in the presence of magnetic field. *International Journal of Applied and Computational Mathematics*, *4*(2), 1–24.

Gul, A., Khan, I., Shafie, S., Khalid, A., & Khan, A. (2015). Heat transfer in mhd mixed convection flow of a ferrofluid along a vertical channel. *PloS one*, *10*(11), e0141213.

Hafeez, A., Khan, M., & Ahmed, J. (2020). Stagnation point flow of radiative

oldroyd-b nanofluid over a rotating disk. *Computer Methods and Programs in Biomedicine*, *191*, 105342.

Haile, E., & Shankar, B. (2014). Heat and mass transfer through a porous media of mhd flow of nanofluids with thermal radiation, viscous dissipation and chemical reaction effects. *American Chemical Science Journal*, *4*(6), 828–846.

Hall, E. H., et al. (1879). On a new action of the magnet on electric currents. *American Journal of Mathematics*, *2*(3), 287–292.

Hamilton, R. L., & Crosser, O. (1962). Thermal conductivity of heterogeneous two-component systems. *Industrial & Engineering chemistry fundamentals*, *1*(3), 187–191.

Hasnain, J., Abbas, Z., & Sajid, M. (2015). Effects of porosity and mixed convection on mhd two phase fluid flow in an inclined channel. *PloS one*, *10*(3), e0119913.

Hayat, T., Ahmed, B., Alsaedi, A., & Abbasi, F. (2018). Numerical study for peristalsis of carreau-yasuda nanomaterial with convective and zero mass flux condition. *Results in physics*, *8*, 1168–1177.

Hayat, T., Aslam, N., Khan, M. I., Khan, M. I., & Alsaedi, A. (2019). Physical significance of heat generation/absorption and soret effects on peristalsis flow of pseudoplastic fluid in an inclined channel. *Journal of Molecular Liquids*, *275*, 599–615.

Hayat, T., Aziz, A., Muhammad, T., & Alsaedi, A. (2019). Numerical simulation for three-dimensional flow of carreau nanofluid over a nonlinear stretching surface with convective heat and mass conditions. *Journal of the Brazilian Society of Mechanical Sciences and Engineering*, *41*(1), 1–11.

Hayat, T., Qayyum, S., Alsaedi, A., & Ahmad, B. (2020). Entropy generation minimization: Darcy-forchheimer nanofluid flow due to curved stretching sheet with partial slip. *International Communications in Heat and Mass Transfer*, *111*, 104445.

Hayat, T., Riaz, R., Aziz, A., & Alsaedi, A. (2020). Influence of arrhenius activation energy in mhd flow of third grade nanofluid over a nonlinear stretching surface with convective heat and mass conditions. *Physica A: Statistical Mechanics and its Applications*, *549*, 124006.

Hayat, T., Shehzad, S., & Alsaedi, A. (2012). Soret and dufour effects on magnetohydrodynamic (mhd) flow of casson fluid. *Applied Mathematics and Mechanics*,

33(10), 1301–1312.

Ho, C., Cheng, C.-Y., Yang, T.-F., Rashidi, S., & Yan, W.-M. (2021). Experimental study on cooling performance of nanofluid flow in a horizontal circular tube. *International Journal of Heat and Mass Transfer*, *169*, 120961.

Hossain, M., & Takhar, H. (1996). Radiation effect on mixed convection along a vertical plate with uniform surface temperature. *Heat and Mass transfer*, *31*(4), 243–248.

Hu, J., Wang, J., Liu, S., Zhang, Z., Zhang, H., Cai, X., ... Liu, J. (2018). Effect of tio2 nanoparticle aggregation on marine microalgae isochrysis galbana. *Journal of environmental sciences*, *66*, 208–215.

Hussain, S., Mehmood, K., Sagheer, M., & Farooq, A. (2017). Entropy generation analysis of mixed convective flow in an inclined channel with cavity with al2o3-water nanofluid in porous medium. *International Communications in Heat and Mass Transfer*, *89*, 198–210.

Hussain, Z., Hayat, T., Alsaedi, A., & Ahmad, B. (2018). Three-dimensional convective flow of cnts nanofluids with heat generation/absorption effect: a numerical study. *Computer Methods in Applied Mechanics and Engineering*, *329*, 40–54.

Hussain, Z., Hayat, T., Alsaedi, A., & Ahmed, B. (2018). Darcy forhheimer aspects for cnts nanofluid past a stretching cylinder; using keller box method. *Results in Physics*, *11*, 801–816.

Hussanan, A., Salleh, M. Z., Khan, I., & Shafie, S. (2017). Convection heat transfer in micropolar nanofluids with oxide nanoparticles in water, kerosene and engine oil. *Journal of Molecular Liquids*, *229*, 482–488.

Hussanan, A., Salleh, M. Z., Khan, I., & Shafie, S. (2018). Analytical solution for suction and injection flow of a viscoplastic casson fluid past a stretching surface in the presence of viscous dissipation. *Neural computing and applications*, *29*(12), 1507–1515.

Ibrahim, M. (2020). Numerical analysis of time-dependent flow of viscous fluid due to a stretchable rotating disk with heat and mass transfer. *Results in Physics*, *18*, 103242.

Imtiaz, M., Kiran, A., Hayat, T., & Alsaedi, A. (2019). Joule heating and mhd effects in flow of second-grade fluid due to a rotating disk with variable thickness.

Physica Scripta, *94*(8), 085203.

Iqbal, Z., Khan, M., Ahmed, A., & Nadeem, S. (2020). Features of thermophoretic and brownian forces in burgers fluid flow subject to joule heating and convective conditions. *Physica Scripta*, *96*(1), 015211.

Jafar, A. B., Shafie, S., & Ullah, I. (2020). Mhd radiative nanofluid flow induced by a nonlinear stretching sheet in a porous medium. *Heliyon*, *6*(6), e04201.

Jawad, M., Saeed, A., Khan, A., & Islam, S. (2021). Mhd bioconvection darcy-forchheimer flow of casson nanofluid over a rotating disk with entropy optimization. *Heat Transfer*, *50*(3), 2168–2196.

Jha, B. K., & Sarki, M. N. (2020). Chemical reaction and dufour effects on nonlinear free convection heat and mass transfer flow near a vertical moving porous plate. *Heat Transfer*, *49*(2), 984–999.

Joseph, D. D., Nield, D. A., & Papanicolaou, G. (1982). Nonlinear equation governing flow in a saturated porous medium. *Water Resources Research*, *18*(4), 1049–1052.

Joshi, N., Upreti, H., & Pandey, A. K. (2022). Mhd darcy-forchheimer cu-ag/h2o-c2h6o2 hybrid nanofluid flow via a porous stretching sheet with suction/blowing and viscous dissipation. *International Journal for Computational Methods in Engineering Science and Mechanics*, 1–9.

Jusoh, R., Nazar, R., & Pop, I. (2018). Three-dimensional flow of a nanofluid over a permeable stretching/shrinking surface with velocity slip: A revised model. *Physics of Fluids*, *30*(3), 033604.

Kameswaran, P., Narayana, M., Sibanda, P., & Murthy, P. (2012). Hydromagnetic nanofluid flow due to a stretching or shrinking sheet with viscous dissipation and chemical reaction effects. *International Journal of Heat and Mass Transfer*, *55*(25-26), 7587–7595.

Kandasamy, R., Dharmalingam, R., & Prabhu, K. S. (2018). Thermal and solutal stratification on mhd nanofluid flow over a porous vertical plate. *Alexandria engineering journal*, *57*(1), 121–130.

Kempannagari, A. K., Buruju, R. R., Naramgari, S., & Vangala, S. (2020). Effect of joule heating on mhd non-newtonian fluid flow past an exponentially stretching curved surface. *Heat Transfer*, *49*(6), 3575–3592.

Khademi, R., Razminia, A., & Shiryaev, V. I. (2020). Conjugate-mixed convection of

nanofluid flow over an inclined flat plate in porous media. *Applied Mathematics and Computation*, *366*, 124761.

Khan, I., Malik, M., Hussain, A., Khan, M., et al. (2017). Magnetohydrodynamics carreau nanofluid flow over an inclined convective heated stretching cylinder with joule heating. *Results in physics*, *7*, 4001–4012.

Khan, I., Ullah, S., Malik, M., & Hussain, A. (2018). Numerical analysis of mhd carreau fluid flow over a stretching cylinder with homogenous-heterogeneous reactions. *Results in Physics*, *9*, 1141–1147.

Khan, J. A., Mustafa, M., Hayat, T., & Alsaedi, A. (2014). On three-dimensional flow and heat transfer over a non-linearly stretching sheet: analytical and numerical solutions. *PloS one*, *9*(9), e107287.

Khan, J. A., Mustafa, M., Hayat, T., & Alsaedi, A. (2018). A revised model to study the mhd nanofluid flow and heat transfer due to rotating disk: numerical solutions. *Neural Computing and Applications*, *30*(3), 957–964.

Khan, M., Azam, M., & Alshomrani, A. (2017). Unsteady slip flow of carreau nanofluid over a wedge with nonlinear radiation and new mass flux condition. *Results in physics*, *7*, 2261–2270.

Khan, M., Hussain, A., Malik, M., Salahuddin, T., & Aly, S. (2019). Numerical analysis of carreau fluid flow for generalized fourier's and fick's laws. *Applied Numerical Mathematics*, *144*, 100–117.

Khan, M., Sardar, H., et al. (2018). Heat generation/absorption and thermal radiation impacts on three-dimensional flow of carreau fluid with convective heat transfer. *Journal of Molecular Liquids*, *272*, 474–480.

Khan, M. I. (2021). Transportation of hybrid nanoparticles in forced convective darcy-forchheimer flow by a rotating disk. *International Communications in Heat and Mass Transfer*, *122*, 105177.

Khan, M. I., Alzahrani, F., Hobiny, A., & Ali, Z. (2020). Estimation of entropy optimization in darcy-forchheimer flow of carreau-yasuda fluid (non-newtonian) with first order velocity slip. *Alexandria Engineering Journal*, *59*(5), 3953–3962.

Khan, S. A., Hayat, T., Khan, M. I., & Alsaedi, A. (2020). Salient features of dufour and soret effect in radiative mhd flow of viscous fluid by a rotating cone with entropy generation. *International Journal of Hydrogen Energy*, *45*(28),

14552–14564.

Khan, S. U., Waqas, H., Muhammad, T., Imran, M., & Aly, S. (2020). Simultaneous effects of bioconvection and velocity slip in three-dimensional flow of eyring-powell nanofluid with arrhenius activation energy and binary chemical reaction. *International Communications in Heat and Mass Transfer*, *117*, 104738.

Khan, U., Bilal, S., Zaib, A., Makinde, O., & Wakif, A. (2022). Numerical simulation of a nonlinear coupled differential system describing a convective flow of casson gold–blood nanofluid through a stretched rotating rigid disk in the presence of lorentz forces and nonlinear thermal radiation. *Numerical Methods for Partial Differential Equations*, *38*(3), 308–328.

Khan, W., & Pop, I. (2010). Boundary-layer flow of a nanofluid past a stretching sheet. *International journal of heat and mass transfer*, *53*(11-12), 2477–2483.

Khan, Z., Makinde, O., Hamid, M., Haq, R. U., & Khan, W. (2020). Hydromagnetic flow of ferrofluid in an enclosed partially heated trapezoidal cavity filled with a porous medium. *Journal of Magnetism and Magnetic Materials*, *499*, 166241.

Khanafer, K., Vafai, K., & Lightstone, M. (2003). Buoyancy-driven heat transfer enhancement in a two-dimensional enclosure utilizing nanofluids. *International journal of heat and mass transfer*, *46*(19), 3639–3653.

Khashi'ie, N. S., Arifin, N. M., Merkin, J. H., Yahaya, R. I., & Pop, I. (2021). Mixed convective stagnation point flow of a hybrid nanofluid toward a vertical cylinder. *International Journal of Numerical Methods for Heat & Fluid Flow*.

Kho, Y. B., Hussanan, A., Mohamed, M. K. A., & Salleh, M. Z. (2019). Heat and mass transfer analysis on flow of williamson nanofluid with thermal and velocity slips: Buongiorno model. *Propulsion and Power Research*, *8*(3), 243–252.

Kierzenka, J., & Shampine, L. F. (2008). A bvp solver that controls residual and error. *JNAIAM J. Numer. Anal. Ind. Appl. Math*, *3*(1-2), 27–41.

Kim, H. J., Lee, S.-H., Lee, J.-H., & Jang, S. P. (2015). Effect of particle shape on suspension stability and thermal conductivities of water-based bohemite alumina nanofluids. *Energy*, *90*, 1290–1297.

Kiusalaas, J. (2005). *Numerical methods in engineering with matlab*. Cambridge university press.

Krishna, M. V., Ahamad, N. A., & Chamkha, A. J. (2020). Hall and ion slip effects on unsteady mhd free convective rotating flow through a saturated

porous medium over an exponential accelerated plate. *Alexandria Engineering Journal*, *59*(2), 565–577.

Krishna, M. V., & Chamkha, A. J. (2019). Hall and ion slip effects on mhd rotating boundary layer flow of nanofluid past an infinite vertical plate embedded in a porous medium. *Results in Physics*, *15*, 102652.

Krishna, M. V., Swarnalathamma, B., & Chamkha, A. J. (2019). Investigations of soret, joule and hall effects on mhd rotating mixed convective flow past an infinite vertical porous plate. *Journal of Ocean Engineering and Science*, *4*(3), 263–275.

Kumar, R., Kumar, R., Shehzad, S. A., & Sheikholeslami, M. (2018). Rotating frame analysis of radiating and reacting ferro-nanofluid considering joule heating and viscous dissipation. *International Journal of Heat and Mass Transfer*, *120*, 540–551.

Kumar, R., Sharma, T., Kumar, R., Sheikholeslami, M., & Vajravelu, K. (2021). Stability analysis of multiple solutions in case of a stretched nanofluid flow obeying corcione's correlation: An extended darcy model. *ZAMM-Journal of Applied Mathematics and Mechanics/Zeitschrift für Angewandte Mathematik und Mechanik*, *101*(5), e202000172.

Kumar, R., Sood, S., Shehzad, S. A., & Sheikholeslami, M. (2017). Radiative heat transfer study for flow of non-newtonian nanofluid past a riga plate with variable thickness. *Journal of Molecular Liquids*, *248*, 143–152.

Kumar, R., Sood, S., Sheikholeslami, M., & Shehzad, S. A. (2017). Nonlinear thermal radiation and cubic autocatalysis chemical reaction effects on the flow of stretched nanofluid under rotational oscillations. *Journal of colloid and interface science*, *505*, 253–265.

Kuznetsov, A., & Nield, D. (2010). Natural convective boundary-layer flow of a nanofluid past a vertical plate. *International Journal of Thermal Sciences*, *49*(2), 243–247.

Kuznetsov, A., & Nield, D. (2013). The cheng–minkowycz problem for natural convective boundary layer flow in a porous medium saturated by a nanofluid: a revised model. *International Journal of Heat and Mass Transfer*, *65*, 682–685.

Kuznetsov, A., & Nield, D. (2014). Natural convective boundary-layer flow of a nanofluid past a vertical plate: A revised model. *International journal of*

thermal sciences, *77*, 126–129.

Leong, K. Y., Razali, I., Ahmad, K. K., Ong, H. C., Ghazali, M. J., & Rahman, M. R. A. (2018). Thermal conductivity of an ethylene glycol/water-based nanofluid with copper-titanium dioxide nanoparticles: an experimental approach. *International Communications in Heat and Mass Transfer*, *90*, 23–28.

Lin, P., Ghaffari, A., et al. (2021). Steady flow and heat transfer of the power-law fluid between two stretchable rotating disks with non-uniform heat source/sink. *Journal of Thermal Analysis and Calorimetry*, *146*(4), 1735–1749.

Lv, Y.-P., Gul, H., Ramzan, M., Chung, J. D., & Bilal, M. (2021). Bioconvective reiner–rivlin nanofluid flow over a rotating disk with cattaneo–christov flow heat flux and entropy generation analysis. *Scientific Reports*, *11*(1), 1–18.

Lv, Y.-P., Shaheen, N., Ramzan, M., Mursaleen, M., Nisar, K. S., & Malik, M. (2021). Chemical reaction and thermal radiation impact on a nanofluid flow in a rotating channel with hall current. *Scientific Reports*, *11*(1), 1–17.

Mabood, F., Ibrahim, S., Rashidi, M., Shadloo, M., & Lorenzini, G. (2016). Non-uniform heat source/sink and soret effects on mhd non-darcian convective flow past a stretching sheet in a micropolar fluid with radiation. *International Journal of Heat and Mass Transfer*, *93*, 674–682.

Mackolil, J., & Mahanthesh, B. (2019). Exact and statistical computations of radiated flow of nano and casson fluids under heat and mass flux conditions. *Journal of Computational Design and Engineering*, *6*(4), 593–605.

Mackolil, J., & Mahanthesh, B. (2021a). Heat transfer optimization and sensitivity analysis of marangoni convection in nanoliquid with nanoparticle interfacial layer and cross-diffusion effects. *International Communications in Heat and Mass Transfer*, *126*, 105361.

Mackolil, J., & Mahanthesh, B. (2021b). Sensitivity analysis of marangoni convection in tio2–eg nanoliquid with nanoparticle aggregation and temperature-dependent surface tension. *Journal of Thermal Analysis and Calorimetry*, *143*(3), 2085–2098.

Maghrebi, M. J., Nazari, M., & Armaghani, T. (2012). Forced convection heat transfer of nanofluids in a porous channel. *Transport in porous media*, *93*(3), 401–413.

Mahanthesh, B., Gireesha, B., & Gorla, R. S. R. (2017). Unsteady three-dimensional

mhd flow of a nano eyring-powell fluid past a convectively heated stretching sheet in the presence of thermal radiation, viscous dissipation and joule heating. *Journal of the Association of Arab Universities for Basic and Applied Sciences*, *23*, 75–84.

Mahanthesh, B., Gireesha, B., Shehzad, S., Rauf, A., & Kumar, P. S. (2018). Nonlinear radiated mhd flow of nanoliquids due to a rotating disk with irregular heat source and heat flux condition. *Physica B: Condensed Matter*, *537*, 98–104.

Mahanthesh, B., Lorenzini, G., Oudina, F. M., & Animasaun, I. L. (2020). Significance of exponential space-and thermal-dependent heat source effects on nanofluid flow due to radially elongated disk with coriolis and lorentz forces. *Journal of Thermal Analysis and Calorimetry*, *141*(1), 37–44.

Mahanthesh, B., & Mackolil, J. (2021). Flow of nanoliquid past a vertical plate with novel quadratic thermal radiation and quadratic boussinesq approximation: sensitivity analysis. *International Communications in Heat and Mass Transfer*, *120*, 105040.

Mahanthesh, B., Mackolil, J., & Mallikarjunaiah, S. (2021). Response surface optimization of heat transfer rate in falkner-skan flow of zno- eg nanoliquid over a moving wedge: Sensitivity analysis. *International Communications in Heat and Mass Transfer*, *125*, 105348.

Mahanthesh, B., Shashikumar, N. S., Gireesha, B. J., & Animasaun, I. L. (2019). Effectiveness of hall current and exponential heat source on unsteady heat transport of dusty tio2-eo nanoliquid with nonlinear radiative heat. *Journal of Computational Design and Engineering*, *6*(4), 551–561.

Mahanthesh, B., Shashikumar, N. S., & Lorenzini, G. (2021). Heat transfer enhancement due to nanoparticles, magnetic field, thermal and exponential space-dependent heat source aspects in nanoliquid flow past a stretchable spinning disk. *Journal of Thermal Analysis and Calorimetry*, *145*(6), 3339–3347.

Makinde, O., & Animasaun, I. (2016). Bioconvection in mhd nanofluid flow with nonlinear thermal radiation and quartic autocatalysis chemical reaction past an upper surface of a paraboloid of revolution. *International Journal of Thermal Sciences*, *109*, 159–171.

Makinde, O. D., Mahanthesh, B., Gireesha, B. J., Shashikumar, N., Monaledi, R., & Tshehla, M. (2018). Mhd nanofluid flow past a rotating disk with thermal radiation in the presence of aluminum and titanium alloy nanoparticles. In *Defect and diffusion forum* (Vol. 384, pp. 69–79).

Malashetty, M., & Umavathi, J. (1997). Two-phase magnetohydrodynamic flow and heat transfer in an inclined channel. *International Journal of Multiphase Flow*, *23*(3), 545–560.

Mandal, I. C., Mukhopadhyay, S., & Vajravelu, K. (2021). Melting heat transfer of mhd micropolar fluid flow past an exponentially stretching sheet with slip and thermal radiation. *International Journal of Applied and Computational Mathematics*, *7*(2), 1–18.

Mandal, S., & Shit, G. (2021). Entropy analysis on unsteady mhd biviscosity nanofluid flow with convective heat transfer in a permeable radiative stretchable rotating disk. *Chinese Journal of Physics*, *74*, 239–255.

Mathew, A., Neethu, T., & Areekara, S. (2021). Three-dimensional hydromagnetic hybrid nanoliquid flow and heat transfer between two vertical porous plates moving in opposite directions: Sensitivity analysis. *Heat Transfer*, *50*(7), 6548–6571.

Mir, N. A., Farooq, M., Rizwan, M., Ahmad, F., Ahmad, S., Ahmad, B., et al. (2020). Analysis of thermally stratified flow of sutterby nanofluid with zero mass flux condition. *Journal of Materials Research and Technology*, *9*(2), 1631–1639.

Mishra, A., & Kumar, M. (2020). Velocity and thermal slip effects on mhd nanofluid flow past a stretching cylinder with viscous dissipation and joule heating. *SN Applied Sciences*, *2*(8), 1–13.

Mohammadein, A., & El-Amin, M. (2000). Thermal radiation effects on power-law fluids over a horizontal plate embedded in a porous medium. *International communications in heat and mass transfer*, *27*(7), 1025–1035.

Mondal, H., Pal, D., Chatterjee, S., & Sibanda, P. (2018). Thermophoresis and soret-dufour on mhd mixed convection mass transfer over an inclined plate with non-uniform heat source/sink and chemical reaction. *Ain Shams Engineering Journal*, *9*(4), 2111–2121.

Muhammad, T., Alsaedi, A., Hayat, T., & Shehzad, S. A. (2017). A revised model

for darcy-forchheimer three-dimensional flow of nanofluid subject to convective boundary condition. *Results in physics*, *7*, 2791–2797.

Mustafa, M. (2017). Mhd nanofluid flow over a rotating disk with partial slip effects: Buongiorno model. *International Journal of Heat and Mass Transfer*, *108*, 1910–1916.

Mustafa, M., Khan, J. A., Hayat, T., & Alsaedi, A. (2018). Numerical solutions for radiative heat transfer in ferrofluid flow due to a rotating disk: Tiwari and das model. *International Journal of Nonlinear Sciences and Numerical Simulation*, *19*(1), 1–10.

Nadeem, S., Abbas, N., & Malik, M. (2020). Inspection of hybrid based nanofluid flow over a curved surface. *Computer Methods and Programs in Biomedicine*, *189*, 105193.

Nagaraja, B., & Gireesha, B. (2021). Exponential space-dependent heat generation impact on mhd convective flow of casson fluid over a curved stretching sheet with chemical reaction. *Journal of Thermal Analysis and Calorimetry*, *143*(6), 4071–4079.

Naga Santoshi, P., Venkata Ramana Reddy, G., & Padma, P. (2019). Numerical study of carreau nanofluid flow under slips. *International Journal of Applied and Computational Mathematics*, *5*(5), 1–25.

Nandeppanavar, M., & Siddalingappa, M. (2013). Effect of viscous dissipation and thermal radiation on heat transfer over a non-linearly stretching sheet through porous medium. *International journal of applied mechanics and engineering*, *18*(2).

Nandeppanavar, M. M., Kemparaju, M., & Shilpa, J. (2019). Heat and mass transfer analysis of carreau nanofluid over an exponentially stretching sheet in a saturated porous medium. *Journal of Nanofluids*, *8*(5), 990–997.

Nandi, S., & Kumbhakar, B. (2020). Unsteady mhd free convective flow past a permeable vertical plate with periodic movement and slippage in the presence of hall current and rotation. *Thermal Science and Engineering Progress*, *19*, 100561.

Naqvi, S. M. R. S., Kim, H. M., Muhammad, T., Mallawi, F., & Ullah, M. Z. (2020). Numerical study for slip flow of reiner-rivlin nanofluid due to a rotating disk. *International Communications in Heat and Mass Transfer*, *116*, 104643.

Nayak, M., Shaw, S., Pandey, V., & Chamkha, A. J. (2018). Combined effects of slip and convective boundary condition on mhd 3d stretched flow of nanofluid through porous media inspired by non-linear thermal radiation. *Indian Journal of Physics*, *92*(8), 1017–1028.

Nayak, M., Wakif, A., Animasaun, I., & Alaoui, M. (2020). Numerical differential quadrature examination of steady mixed convection nanofluid flows over an isothermal thin needle conveying metallic and metallic oxide nanomaterials: a comparative investigation. *Arabian Journal for Science and Engineering*, *45*(7), 5331–5346.

Nield, D. A., Bejan, A., et al. (2006). *Convection in porous media* (Vol. 3). Springer.

Ogunseye, H. A., Sibanda, P., & Mondal, H. (2019). Mhd mixed convective stagnation-point flow of eyring-powell nanofluid over stretching cylinder with thermal slip conditions. *Journal of Central South University*, *26*(5), 1172–1183.

Ouyang, C., Akhtar, R., Raja, M. A. Z., Touseef Sabir, M., Awais, M., & Shoaib, M. (2020). Numerical treatment with lobatto iiia technique for radiative flow of mhd hybrid nanofluid (al2o3—cu/h2o) over a convectively heated stretchable rotating disk with velocity slip effects. *AIP Advances*, *10*(5), 055122.

Pal, D., & Talukdar, B. (2013). Influence of hall current and thermal radiation on mhd convective heat and mass transfer in a rotating porous channel with chemical reaction. *International Journal of Engineering Mathematics*, *2013*, 1–13.

Parameshwaran, R., & Kalaiselvam, S. (2013). Effect of aggregation on thermal conductivity and heat transfer in hybrid nanocomposite phase change colloidal suspensions. *Applied Physics Letters*, *103*(19), 193113.

Patel, H. R., & Singh, R. (2019). Thermophoresis, brownian motion and non-linear thermal radiation effects on mixed convection mhd micropolar fluid flow due to nonlinear stretched sheet in porous medium with viscous dissipation, joule heating and convective boundary condition. *International Communications in Heat and Mass Transfer*, *107*, 68–92.

Pattnaik, P., Mishra, S., Mahanthesh, B., Gireesha, B., & Rahimi-Gorji, M. (2020). Heat transport of nano-micropolar fluid with an exponential heat source on a convectively heated elongated plate using numerical computation. *Multidisci-*

pline Modeling in Materials and Structures, *16*(5), 1295–1312.

Plant, R. D., Hodgson, G. K., Impellizzeri, S., & Saghir, M. Z. (2020). Experimental and numerical investigation of heat enhancement using a hybrid nanofluid of copper oxide/alumina nanoparticles in water. *Journal of Thermal Analysis and Calorimetry*, *141*(5), 1951–1968.

Rabbi, K. M., Sheikholeslami, M., Karim, A., Shafee, A., Li, Z., & Tlili, I. (2020). Prediction of mhd flow and entropy generation by artificial neural network in square cavity with heater-sink for nanomaterial. *Physica A: Statistical Mechanics and its Applications*, *541*, 123520.

Rafiq, T., Mustafa, M., & Khan, J. A. (2022). Rotationally symmetric flow of reiner-rivlin fluid over a heated porous wall using numerical approach. *Proceedings of the Institution of Mechanical Engineers, Part C: Journal of Mechanical Engineering Science*, *236*(6), 2803–2814.

Raju, C., Saleem, S., Al-Qarni, M., & Upadhya, S. M. (2019). Unsteady nonlinear convection on eyring–powell radiated flow with suspended graphene and dust particles. *Microsystem Technologies*, *25*(4), 1321–1331.

Raju, C., Sandeep, N., & Malvandi, A. (2016). Free convective heat and mass transfer of mhd non-newtonian nanofluids over a cone in the presence of non-uniform heat source/sink. *Journal of Molecular Liquids*, *221*, 108–115.

Ram, P., Singh, H., Kumar, R., Kumar, V., & Joshi, V. K. (2017). Free convective boundary layer flow of radiating and reacting mhd fluid past a cosinusoidally fluctuating heated plate. *International Journal of Applied and Computational Mathematics*, *3*(1), 261–294.

Ramya, D., Raju, R. S., Rao, J. A., & Chamkha, A. (2018). Effects of velocity and thermal wall slip on magnetohydrodynamics (mhd) boundary layer viscous flow and heat transfer of a nanofluid over a non-linearly-stretching sheet: a numerical study. *Propulsion and Power Research*, *7*(2), 182–195.

Ramzan, M., Riasat, S., Chung, J. D., Chu, Y.-M., Sheikholeslami, M., Kadry, S., & Howari, F. (2021). Upshot of heterogeneous catalysis in a nanofluid flow over a rotating disk with slip effects and entropy optimization analysis. *Scientific Reports*, *11*(1), 1–15.

Ramzan, M., Sheikholeslami, M., Saeed, M., & Chung, J. D. (2019). On the convective heat and zero nanoparticle mass flux conditions in the flow of 3d

mhd couple stress nanofluid over an exponentially stretched surface. *Scientific reports*, *9*(1), 1–13.

Rana, P., Mahanthesh, B., Mackolil, J., & Al-Kouz, W. (2021). Nanofluid flow past a vertical plate with nanoparticle aggregation kinematics, thermal slip and significant buoyancy force effects using modified buongiorno model. *Waves in Random and Complex Media*, 1–25.

Rana, P., Shukla, N., Bég, O. A., & Bhardwaj, A. (2021). Lie group analysis of nanofluid slip flow with stefan blowing effect via modified buongiorno's model: entropy generation analysis. *Differential Equations and Dynamical Systems*, *29*(1), 193–210.

Rana, P., Srikantha, N., Muhammad, T., & Gupta, G. (2021). Computational study of three-dimensional flow and heat transfer of 25 nm cu–h2o nanoliquid with convective thermal condition and radiative heat flux using modified buongiorno model. *Case Studies in Thermal Engineering*, *27*, 101340.

Rana, S., Mehmood, R., & Bhatti, M. (2021). Bioconvection oblique motion of magnetized oldroyd-b fluid through an elastic surface with suction/injection. *Chinese Journal of Physics*, *73*, 314–330.

Rashed, Z., Ahmed, S., & Sheremet, M. A. (2019). Mhd buoyancy flow of nanofluids over an inclined plate immersed in uniform porous medium in the presence of solar radiation. *Journal of Mechanics*, *35*(4), 563–576.

Rashid, M. U., & Mustafa, M. (2021). A study of heat transfer and entropy generation in von kármán flow of reiner-rivlin fluid due to a stretchable disk. *Ain Shams Engineering Journal*, *12*(1), 875–883.

Ray, A. K., Vasu, B., Bég, O. A., Gorla, R. S., & Murthy, P. (2019). Homotopy semi-numerical modeling of non-newtonian nanofluid transport external to multiple geometries using a revised buongiorno model. *Inventions*, *4*(4), 54.

Ray, A. K., Vasu, B., Murthy, P., & Gorla, R. S. (2020). Non-similar solution of eyring–powell fluid flow and heat transfer with convective boundary condition: Homotopy analysis method. *International Journal of Applied and Computational Mathematics*, *6*(1), 1–22.

Raza, J., Rohni, A. M., & Omar, Z. (2016). Mhd flow and heat transfer of cu–water nanofluid in a semi porous channel with stretching walls. *International Journal of Heat and Mass Transfer*, *103*, 336–340.

Reddy, P. S. A., & Chamkha, A. (2018). Heat and mass transfer characteristics of mhd three-dimensional flow over a stretching sheet filled with water-based alumina nanofluid. *International Journal of Numerical Methods for Heat & Fluid Flow*.

Reddy, S., Bala Anki Reddy, P., & Rashad, A. (2020). Activation energy impact on chemically reacting eyring–powell nanofluid flow over a stretching cylinder. *Arabian Journal for Science and Engineering*, *45*(7), 5227–5242.

Roşca, N., Roşca, A., Pop, I., & Merkin, J. (2020). Nanofluid flow by a permeable stretching/shrinking cylinder. *Heat and Mass Transfer*, *56*(2), 547–557.

Sadiq, M. A., Haider, F., Hayat, T., & Alsaedi, A. (2020). Partial slip in darcy-forchheimer carbon nanotubes flow by rotating disk. *International Communications in Heat and Mass Transfer*, *116*, 104641.

Sadiq, M. A., & Hayat, T. (2022). Entropy optimized flow of reiner-rivlin nanofluid with chemical reaction subject to stretchable rotating disk. *Alexandria Engineering Journal*, *61*(5), 3501–3510.

Sahoo, B., & Shevchuk, I. V. (2019). Heat transfer due to revolving flow of reiner-rivlin fluid over a stretchable surface. *Thermal Science and Engineering Progress*, *10*, 327–336.

Said, S., Habib, M., Badr, H., & Anwar, S. (2005). Numerical investigation of natural convection inside an inclined parallel-walled channel. *International Journal for numerical methods in fluids*, *49*(5), 569–582.

Saif, R. S., Muhammad, T., Sadia, H., & Ellahi, R. (2020). Boundary layer flow due to a nonlinear stretching curved surface with convective boundary condition and homogeneous-heterogeneous reactions. *Physica A: Statistical Mechanics and Its Applications*, *551*, 123996.

Salahuddin, T., Hussain, A., Malik, M., Awais, M., & Khan, M. (2017). Carreau nanofluid impinging over a stretching cylinder with generalized slip effects: using finite difference scheme. *Results in physics*, *7*, 3090–3099.

Salahuddin, T., Sakinder, S., Alharbi, S. O., & Abdelmalek, Z. (2021). A brief comparative study of gamma alumina–water and gamma alumina–eg nanofluids flow near a solid sphere. *Mathematics and Computers in Simulation*, *181*, 487–500.

Salehi, S., Nori, A., Hosseinzadeh, K., & Ganji, D. (2020). Hydrothermal analysis

of mhd squeezing mixture fluid suspended by hybrid nanoparticles between two parallel plates. *Case Studies in Thermal Engineering*, *21*, 100650.

Saranya, S., & Al-Mdallal, Q. M. (2021). Computational study on nanoparticle shape effects of al2o3-silicon oil nanofluid flow over a radially stretching rotating disk. *Case Studies in Thermal Engineering*, *25*, 100943.

Sarma, D., & Pandit, K. (2018). Effects of hall current, rotation and soret effects on mhd free convection heat and mass transfer flow past an accelerated vertical plate through a porous medium. *Ain Shams Engineering Journal*, *9*(4), 631–646.

Sekhar, K. R., Reddy, G. V., Raju, C. S., Pullepu, B., Kumar, R., & Shehzad, S. A. (2017). Aligned magnetic dipole in nonlinear radiative falkner-skan flow of casson fluid over a wedge containing suspension of nanoparticles and microorganisms. *International Journal of Nanoparticles*, *9*(4), 213–233.

Shahul Hameed, M., Suresh, S., & Singh, R. K. (2019). Comparative study of heat transfer and friction characteristics of water-based alumina–copper and alumina–cnt hybrid nanofluids in laminar flow through pipes. *Journal of Thermal Analysis and Calorimetry*, *136*(1), 243–253.

Shaiq, S., Maraj, E., & Iqbal, Z. (2019). A comparative analysis of shape factor and thermophysical properties of electrically conducting nanofluids tio2- eg and cu- eg towards stretching cylinder. *Chaos, Solitons & Fractals*, *118*, 290–299.

Shakunthala, S., & Nandeppanavar, M. (2019). Boundary layer flow and cattaneo-christov heat flux of a nonlinear stretching sheet with a suspended cnt. *Nanoscience & Nanotechnology-Asia*, *9*(4), 494–503.

Shankaralingappa, B., Gireesha, B., Prasannakumara, B., & Nagaraja, B. (2021). Darcy-forchheimer flow of dusty tangent hyperbolic fluid over a stretching sheet with cattaneo-christov heat flux. *Waves in Random and Complex Media*, 1–20.

Sharma, P. K., Sharma, B. K., & Chaudhary, R. (2007). Unsteady free covection oscillatory couette flow through a porous medium with periodic wall temperature. *TAMKANG journal of mathematics*, *38*(1), 93–102.

Sharma, V. K. (2009). Aggregation and toxicity of titanium dioxide nanoparticles in aquatic environment—a review. *Journal of Environmental Science and Health Part A*, *44*(14), 1485–1495.

Shehzad, S., Mabood, F., Rauf, A., & Tlili, I. (2020). Forced convective maxwell fluid flow through rotating disk under the thermophoretic particles motion. *International Communications in Heat and Mass Transfer*, *116*, 104693.

Shehzad, S., Sheikholeslami, M., Ambreen, T., Shafee, A., Babazadeh, H., & Ahmad, M. (2020). Heat transfer management of hybrid nanofluid including radiation and magnetic source terms within a porous domain. *Applied Nanoscience*, *10*(12), 5351–5359.

Sheikholeslami, M., Chamkha, A. J., Rana, P., & Moradi, R. (2017). Combined thermophoresis and brownian motion effects on nanofluid free convection heat transfer in an l-shaped enclosure. *Chinese journal of physics*, *55*(6), 2356–2370.

Sheikholeslami, M., & Ganji, D. D. (2014). Ferrohydrodynamic and magnetohydrodynamic effects on ferrofluid flow and convective heat transfer. *Energy*, *75*, 400–410.

Sheikholeslami, M., Hatami, M., & Ganji, D. (2013). Analytical investigation of mhd nanofluid flow in a semi-porous channel. *Powder Technology*, *246*, 327–336.

Sheikholeslami, M., Shah, Z., Shafee, A., Khan, I., & Tlili, I. (2019). Uniform magnetic force impact on water based nanofluid thermal behavior in a porous enclosure with ellipse shaped obstacle. *Scientific reports*, *9*(1), 1–11.

Sheriff, S., Mir, N. A., Ahmad, S., & Rafiq, N. (2021). Porosity and dissipative effects in peristalsis of hydro-magneto nanomaterial: Application of biomedical treatment. *Advances in Mechanical Engineering*, *13*(4), 16878140211011890.

Shojaei, A., Amiri, A. J., Ardahaie, S. S., Hosseinzadeh, K., & Ganji, D. (2019). Hydrothermal analysis of non-newtonian second grade fluid flow on radiative stretching cylinder with soret and dufour effects. *Case Studies in Thermal Engineering*, *13*, 100384.

Shu, C. (2012). *Differential quadrature and its application in engineering*. Springer Science & Business Media.

Sindhu, S., & Gireesha, B. (2020). Flow of colloidal suspension and irreversibility analysis with aggregation kinematics of nanoparticles in a microchannel. *Applied Mathematics and Mechanics*, *41*(11), 1671–1684.

Singh, K., & Kumar, R. (2009). Combined effects of hall current and rotation on free convection mhd flow in a porous channel.

Singh, K., & Mathew, A. (2012). An oscillatory free convective flow through porous medium in a rotating vertical porous channel. *Global J. Sci. Front. Res*, *12*(3), 51–64.

Sohail, M., & Naz, R. (2020). Modified heat and mass transmission models in the magnetohydrodynamic flow of sutterby nanofluid in stretching cylinder. *Physica A: Statistical Mechanics and its Applications*, *549*, 124088.

Song, Y.-Q., Hamid, A., Sun, T.-C., Khan, M. I., Qayyum, S., Kumar, R. N., ... Chinram, R. (2022). Unsteady mixed convection flow of magneto-williamson nanofluid due to stretched cylinder with significant non-uniform heat source/sink features. *Alexandria Engineering Journal*, *61*(1), 195–206.

Sravanthi, C. (2019). Effect of nonlinear thermal radiation on silver and copper water nanofluid flow due to a rotating disk with variable thickness in the presence of nonuniform heat source/sink using the homotopy analysis method. *Heat Transfer—Asian Research*, *48*(8), 4033–4048.

Sreedevi, P., Reddy, P. S., & Chamkha, A. J. (2018). Magneto-hydrodynamics heat and mass transfer analysis of single and multi-wall carbon nanotubes over vertical cone with convective boundary condition. *International journal of Mechanical sciences*, *135*, 646–655.

Sudarsana Reddy, P., & Sreedevi, P. (2021). Effect of zero mass flux condition on heat and mass transfer analysis of nanofluid flow inside a cavity with magnetic field. *The European Physical Journal Plus*, *136*(1), 1–24.

Sulochana, P., et al. (2014). Hall effects on unsteady mhd three dimensional flow through a porous medium in a rotating parallel plate channel with effect of inclined magnetic field. *American Journal of Computational Mathematics*, *4*(05), 396.

Sureshkumar, S., & Muthtamilselvan, M. (2016). A slanted porous enclosure filled with cu-water nanofluid. *The European Physical Journal Plus*, *131*(4), 1–19.

Tabassum, M., & Mustafa, M. (2018). A numerical treatment for partial slip flow and heat transfer of non-newtonian reiner-rivlin fluid due to rotating disk. *International Journal of Heat and Mass Transfer*, *123*, 979–987.

Tahat, M. S., & Benim, A. C. (2017). Experimental analysis on thermophysical properties of al2o3/cuo hybrid nano fluid with its effects on flat plate solar collector. In *Defect and diffusion forum* (Vol. 374, pp. 148–156).

Tarakaramu, N., & Narayan, P. S. (2017). Unsteady mhd nanofluid flow over a stretching sheet with chemical reaction. In *Iop conference series: Materials science and engineering* (Vol. 263, p. 062030).

Tassaddiq, A., Khan, S., Bilal, M., Gul, T., Mukhtar, S., Shah, Z., & Bonyah, E. (2020). Heat and mass transfer together with hybrid nanofluid flow over a rotating disk. *AIP Advances*, *10*(5), 055317.

Telionis, D. P., & Telionis, D. P. (1981). *Unsteady viscous flows* (Vol. 320). Springer.

Teng, T.-P., Hung, Y.-H., Teng, T.-C., Mo, H.-E., & Hsu, H.-G. (2010). The effect of alumina/water nanofluid particle size on thermal conductivity. *Applied Thermal Engineering*, *30*(14-15), 2213–2218.

Thumma, T., Wakif, A., & Animasaun, I. L. (2020). Generalized differential quadrature analysis of unsteady three-dimensional mhd radiating dissipative casson fluid conveying tiny particles. *Heat Transfer*, *49*(5), 2595–2626.

Timofeeva, E. V., Routbort, J. L., & Singh, D. (2009). Particle shape effects on thermophysical properties of alumina nanofluids. *Journal of applied physics*, *106*(1), 014304.

Tiwari, R. K., & Das, M. K. (2007). Heat transfer augmentation in a two-sided lid-driven differentially heated square cavity utilizing nanofluids. *International Journal of heat and Mass transfer*, *50*(9-10), 2002–2018.

Tlili, I., Bilal, M., Qureshi, M. Z. A., & Abdelmalek, Z. (2020). Thermal analysis of magnetized pseudoplastic nano fluid flow over 3d radiating non-linear surface with passive mass flux control and chemically responsive species. *Journal of Materials Research and Technology*, *9*(4), 8125–8135.

Tlili, I., Ramzan, M., Kadry, S., Kim, H.-W., & Nam, Y. (2020). Radiative mhd nanofluid flow over a moving thin needle with entropy generation in a porous medium with dust particles and hall current. *Entropy*, *22*(3), 354.

Turkyilmazoglu, M. (2014). Nanofluid flow and heat transfer due to a rotating disk. *Computers & Fluids*, *94*, 139–146.

Turkyilmazoglu, M., & Senel, P. (2013). Heat and mass transfer of the flow due to a rotating rough and porous disk. *International Journal of Thermal Sciences*, *63*, 146–158.

Uddin, I., Khan, M. A., Ullah, S., Islam, S., Israr, M., & Hussain, F. (2018). Characteristics of buoyancy force on stagnation point flow with magneto-

nanoparticles and zero mass flux condition. *Results in physics*, *8*, 160–168.

Ullah, M. Z., Muhammad, T., & Mallawi, F. (2021). On model for darcy–forchheimer 3d nanofluid flow subject to heat flux boundary condition. *Journal of Thermal Analysis and Calorimetry*, *143*(3), 2411–2418.

Unyong, B., Vadivel, R., Govindaraju, M., Anbuvithya, R., & Gunasekaran, N. (2022). Entropy analysis for ethylene glycol hybrid nanofluid flow with elastic deformation, radiation, non-uniform heat generation/absorption, and inclined lorentz force effects. *Case Studies in Thermal Engineering*, *30*, 101639.

Usman, M., Soomro, F. A., Haq, R. U., Wang, W., & Defterli, O. (2018). Thermal and velocity slip effects on casson nanofluid flow over an inclined permeable stretching cylinder via collocation method. *International Journal of Heat and Mass Transfer*, *122*, 1255–1263.

Vajravelu, K., & Sastri, K. (1977). Fully developed laminar free convection flow between two parallel vertical walls—i. *International Journal of Heat and Mass Transfer*, *20*(6), 655–660.

Vinita, V., & Poply, V. (2020). Impact of outer velocity mhd slip flow and heat transfer of nanofluid past a stretching cylinder. *Materials Today: Proceedings*, *26*, 3429–3435.

Von Kármán, T. (1921). Uber laminare und turbulente reibung. *Z. Angew. Math. Mech.*, *1*, 233–252.

Wakif, A., Chamkha, A., Animasaun, I., Zaydan, M., Waqas, H., & Sehaqui, R. (2020). Novel physical insights into the thermodynamic irreversibilities within dissipative emhd fluid flows past over a moving horizontal riga plate in the coexistence of wall suction and joule heating effects: a comprehensive numerical investigation. *Arabian Journal for Science and Engineering*, *45*(11), 9423–9438.

Wakif, A., Chamkha, A., Thumma, T., Animasaun, I., & Sehaqui, R. (2021). Thermal radiation and surface roughness effects on the thermo-magneto-hydrodynamic stability of alumina–copper oxide hybrid nanofluids utilizing the generalized buongiorno's nanofluid model. *Journal of Thermal Analysis and Calorimetry*, *143*(2), 1201–1220.

Wakif, A., & Sehaqui, R. (2022). Generalized differential quadrature scrutinization of an advanced mhd stability problem concerned water-based nanofluids with

metal/metal oxide nanomaterials: a proper application of the revised two-phase nanofluid model with convective heating and through-flow boundary conditions. *Numerical Methods for Partial Differential Equations*, *38*(3), 608–635.

Wang, B.-X., Zhou, L.-P., & Peng, X.-F. (2003). A fractal model for predicting the effective thermal conductivity of liquid with suspension of nanoparticles. *International Journal of Heat and Mass Transfer*, *46*(14), 2665–2672.

Wang, X. (2015). *Differential quadrature and differential quadrature based element methods: theory and applications*. Butterworth-Heinemann.

Waqas, H., Farooq, U., Naseem, R., Hussain, S., & Alghamdi, M. (2021). Impact of mhd radiative flow of hybrid nanofluid over a rotating disk. *Case Studies in Thermal Engineering*, *26*, 101015.

Wensel, J., Wright, B., Thomas, D., Douglas, W., Mannhalter, B., Cross, W., ... Roy, W. (2008). Enhanced thermal conductivity by aggregation in heat transfer nanofluids containing metal oxide nanoparticles and carbon nanotubes. *Applied Physics Letters*, *92*(2), 023110.

Xiong, P.-Y., Chu, Y.-M., Khan, M. I., Khan, S. A., & Abbas, S. (2021). Entropy optimized darcy-forchheimer flow of reiner-philippoff fluid with chemical reaction. *Computational and Theoretical Chemistry*, *1200*, 113222.

Xuan, Y., & Roetzel, W. (2000). Conceptions for heat transfer correlation of nanofluids. *International Journal of heat and Mass transfer*, *43*(19), 3701–3707.

Yang, C., Li, W., & Nakayama, A. (2013). Convective heat transfer of nanofluids in a concentric annulus. *International Journal of Thermal Sciences*, *71*, 249–257.

Yusuf, T., Mabood, F., Khan, W., & Gbadeyan, J. (2020). Irreversibility analysis of cu-tio2-h2o hybrid-nanofluid impinging on a 3-d stretching sheet in a porous medium with nonlinear radiation: Darcy-forchhiemer's model. *Alexandria Engineering Journal*, *59*(6), 5247–5261.

Zeeshan, A., Maskeen, M. M., & Mehmood, O. U. (2018). Hydromagnetic nanofluid flow past a stretching cylinder embedded in non-darcian forchheimer porous media. *Neural Computing and Applications*, *30*(11), 3479–3489.

Zhang, C., Zheng, L., Zhang, X., & Chen, G. (2015). Mhd flow and radiation heat transfer of nanofluids in porous media with variable surface heat flux and chemical reaction. *Applied Mathematical Modelling*, *39*(1), 165–181.

Zhang, L., Bhatti, M., Shahid, A., Ellahi, R., Beg, O. A., & Sait, S. M. (2021). Nonlinear nanofluid fluid flow under the consequences of lorentz forces and arrhenius kinetics through a permeable surface: A robust spectral approach. *Journal of the Taiwan Institute of Chemical Engineers*, *124*, 98–105.

Zhang, W. (2014). Nanoparticle aggregation: principles and modeling. *Nanomaterial*, 19–43.

Zhao, B., Li, K., Wang, Y., & Wang, Z. (2022). Theoretical analysis of convective heat flux structure in the incompressible turbulent boundary layer on a porous plate with uniform injection and suction. *International Journal of Thermal Sciences*, *171*, 107264.

Zhu, M., Wang, H., Keller, A. A., Wang, T., & Li, F. (2014). The effect of humic acid on the aggregation of titanium dioxide nanoparticles under different ph and ionic strengths. *Science of the Total Environment*, *487*, 375–380.